

Direct Search for Standard Model-Like Higgs Boson and Software Integration of Data Acquisition Cards

THÈSE N° 4686 (2010)

PRÉSENTÉE LE 6 MAI 2010

À LA FACULTÉ DES SCIENCES DE BASE
LABORATOIRE DE PHYSIQUE DES HAUTES ÉNERGIES
PROGRAMME DOCTORAL EN PHYSIQUE

ÉCOLE POLYTECHNIQUE FÉDÉRALE DE LAUSANNE

POUR L'OBTENTION DU GRADE DE DOCTEUR ÈS SCIENCES

PAR

Cédric POTTERAT

acceptée sur proposition du jury:

Prof. N. Baluc, présidente du jury
Prof. A. Bay, directeur de thèse
Dr N. Neufeld, rapporteur
Dr T. Shears, rapporteur
Prof. M. Q. Tran, rapporteur



ÉCOLE POLYTECHNIQUE
FÉDÉRALE DE LAUSANNE

Suisse
2010

Résumé

Le Grand Collisionneur de Hadrons (LHC) au CERN, près de Genève, est conçu pour faire entrer en collision des protons à une énergie dans le centre de masse de 14 TeV. Il a été testé à plus faible énergie en novembre 2009. Durant ces premiers jours, le LHC a établi un nouveau record du monde avec ces deux faisceaux de protons à l'énergie de 1180 MeV.

Le LHC a quatre points d'interaction pour les quatre grandes expériences que sont : ALICE, ATLAS, CMS et LHCb. Le détecteur LHCb est situé au point d'interaction P8 (France). C'est un spectromètre à bras unique dédié à la physique des hadrons contenant un quark b . Son but est l'étude des processus qui ne conservent pas la symétrie CP et ainsi que certaines désintégrations rares. Pour ce faire, le détecteur LHCb a la capacité de distinguer, avec une résolution de l'ordre d'une dizaine de microns, des vertex de désintégration dans la région d'interaction.

Durant cette thèse, deux sujets distincts ont été abordés. Dans le premier sujet, nous avons étudié la sensibilité de l'expérience LHCb à détecter un boson de Higgs du modèle standard (MS) dans les canaux $HW^\pm \rightarrow b\bar{b} + \ell^\pm \bar{\nu}_\ell$ et $HZ^0 \rightarrow b\bar{b} + \ell^+\ell^-$ (ou des événements ayant une topologie similaire). Le défi a été de discriminer les événements de signal par rapport aux grandes contributions des principales sources de bruit que sont les canaux $t\bar{t}$, Z^0W^\pm , Z^0Z^0 , $W^\pm + 2b$ et $\gamma^*/Z^0 + 2b$. Pour ce faire, plusieurs outils ont été conçus pour cette tâche qui demande la reconstruction de jets contenant un quark b . En particulier, nous avons optimisé un algorithme cherchant les b -jets, ainsi qu'un réseau de neurones destiné à la mesure de l'énergie de b -jets. Nous avons obtenu une résolution du pique de masse des dijets de 38 %. L'efficacité d'identification des b -jets est de 70 %, tout en rejetant 70 % des c -jets (90 % pour jets de quarks légers). La sélection des événements contenant un Higgs a été obtenue grâce à l'utilisation d'un second réseau de neurones basé sur la topologie de l'événement. En considérant cinq ans de prise de données, nous obtenons environ une cinquantaine d'événements et une signification statistique dans le spectre de masse du Higgs d'environ 1, en prenant pour compte une masse de 120 GeV/c² pour le Higgs. Cette statistique n'est en principe pas assez suffisante pour découvrir un MS higgs. Cependant, la possibilité qu'un nouveau mécanisme produisant des événements de topologie similaire pourrait aider cette découverte.

Le second sujet de cette thèse est porté sur l'intégration des cartes électroniques d'acquisition de donnée, développée et construite à Lausanne, (les cartes TELL1) dans le Système de Contrôle de l'Expérience (ECS). Le détecteur LHCb a environ un million de canaux de détection qui sont lus par 300 cartes TELL1. Un projet complet a été développé permettant de contrôler, interagir, surveiller et configurer les TELL1s depuis l'ECS. Ce projet est maintenant utilisé par tous les sous-détecteurs de l'expérience LHCb ayant des cartes d'acquisition TELL1.

Mots-clé : CERN, LHCb, Standard Model-Like Higgs, b -jets, TELL1, PVSS, DAQ, ECS

Abstract

The Large Hadron Collider (LHC) accelerator at CERN near Geneva is designed to collide protons with a centre-of-mass energy up to 14 TeV. It was tested at lower energy in November 2009. The world record collisions of beams of 1180 MeV was achieved.

The LHC has four interaction points for the four large experiments: ALICE, ATLAS, CMS, and LHCb. LHCb is the “LHC beauty” experiment, located at interaction point P8 (France). It is a single arm forward spectrometer dedicated to the b -hadron sector optimised to study CP-violating processes and rare decays. In particular the LHCb detector has the capability to measure decay vertices with a resolution of few tenths of microns.

Two topics have been addressed in this thesis. In the first part we study the LHCb sensitivity to detect a Standard Model Higgs boson in the $HW^\pm \rightarrow b\bar{b} + \ell^\pm \overset{(-)}{\nu}_\ell$ and $HZ^0 \rightarrow b\bar{b} + \ell^+\ell^-$ channels (or events with similar topologies). Here we face the challenge to discriminate signal events from the huge background sources which have been identified to be $t\bar{t}$, Z^0W^\pm , Z^0Z^0 , $W^\pm+2b$ and γ^*/Z^0+2b events. Several tools have been designed for this goal which requires the reconstruction of b -jets. In particular we have optimised a b -jet finder algorithm, and a Neural Network procedure for the b -jet energy measurement. We have achieved a dijet mass resolution (giving the Higgs mass) of 38 %. The efficiency to identify b -jets is 70 %, and we discard more than 70 % c -jets (90 % for lighter quark-jets). The Higgs event selection uses another Neural Network based on the event topology. If we consider 5 years of data taking we obtain about 50 events and a statistical significance in the Higgs mass spectrum of about 1, assuming a SM Higgs with a mass of 120 GeV/c². This statistics is in principle not enough to discover a SM Higgs. The only hope is that a new mechanism exists producing events with a similar topology.

The second part of this thesis is a contribution to the integration of the Data Acquisition electronics boards built in Lausanne (the TELL1 boards) into the Experiment Control System (ECS). The LHCb detector consists of roughly one million detector channels which are readout by about 300 TELL1 boards. A complete framework has been developed allowing to configure, control, interact, “spy” and check the TELL1s from the ECS. This project is now used by all the different LHCb subdetectors using TELL1 boards.

Keywords: CERN, LHCb, Standard Model-Like Higgs, b -jets, TELL1, PVSS, DAQ, ECS

Acknowledgements

Je tiens tout d'abord à exprimer mon immense gratitude envers Aurelio Bay, pour ces cinq années de totale confiance, de franchise, de soutiens multiples, de travail, de collaboration directe et complète, d'heures d'observation partagées dans la chasse du boson de Higgs, et finalement d'ouverture d'esprit. Grazie mille! Ce fut cinq années de pur plaisir au sein du Laboratoire de Physique des Hautes Énergie, un cadre idyllique, des membres-collègues-amis si chaleureux.

Je remercie également mon jury de thèse Nadine Baluc, Minh Quand Tran, Niko Neufeld et Tara Shears pour leurs suggestions et corrections à la lecture de mon manuscrit.

Un énorme merci à Erika Lüthi et Esther Hofman qui sont de loin les meilleures secrétaires que l'on puisse imaginer côtoyer. Guido Häfeli, merci d'avoir guidé les deux premières années de cette thèse sur tes TELL1s, guidé mes pas dans la course à pieds et de m'avoir fait gravir les pentes du marathon de la Jungfrau. Je tiens à remercier les deux précédents chercheurs du Higgs dans LHCb, mes amis, Laurent Locatelli et Victor Coco, ainsi que les membres du Jets WG. Merci à Stefan Köstner, Clara Gaspar, pour leurs aides précieuses dans l'achèvement du projet d'intégration des TELL1s. Je remercie encore Paul Szczypka et Vittoria Rezzonico pour avoir repris avec moi les rênes du cluster de calcul du laboratoire. Thomas Schietinger et Stefano Villa pour leurs conseils, et pour m'avoir proposé et convaincu de faire cette thèse. Olivier Schneider, Tatsuya Nakada, Minh Tâm Tran, Frédéric Blanc, Kim Vervink et les membres du LPHE, pour toutes ces discussions intéressées et leurs conseils avisés. Moltes gràcies a Neus March Lopez! Gràcies per l'ajuda i per a les discussions durant la redacció de les nostres tesis!

Marc-Olivier Bettler... que dire, à part le plus grand des mercis pour m'avoir obligé à rédiger cette thèse le 2 janvier 2010, merci! Merci encore pour les moments passés à rigoler, à courir au bord du lac au lieu de manger.

Dix ans ! Dix ans d'études ! Dix ans de rigolade ! Dix ans finalement trop courts ! 28 ans d'amitié ! Louis Nicolas, je te remercie pour tout ça et bien plus encore !

Samuel Monnier, mon *troisième* frère, et Jean-Yves Cavin, je vous remercie pour tout ce que vous avez fait pour moi, pour votre amitié inestimable, votre bonne humeur, votre présence et votre soutien inébranlable. Merci Céline Schmid, pour m'avoir poussé dans ma vie, d'avoir un immense, chaleureux et réconfortant soleil dans ton cœur, ta joie quotidienne et tes pensées magiques. Merci Joëlle Fellay, d'avoir toujours été là pour tendre bien plus qu'une oreille au moment opportun, d'avoir agrémenté tellement de journées de discussions intéressées et cela toujours d'un sourire rayonnant et enchanteur. Marjolaine Lamontagne-Pelletier, merci pour

cette année illuminée par ton si joli accent et pour tous ces moments inoubliables. François Gigante, merci pour ton soutien, ton aide, les terrasses ensoleillées et tout ces moments. Merci à Morgane et Mohéna Kühni pour les nombreuses discussions, conseils, cafés et autres repas partagés ici et là. Carole Brülhart pour avoir embelli bien des pensées, pour les douces discussions et ces petits moments échangés. Muchas gracias a Mara Paz Poblete Maureira, para todos los dulces y tiernos pensamientos que sobrevuelan los océanos.

Merci encore à Laura De Felicis, Arnaud Di Clemente, Gilles et Benoît Guignet, Olivier Allaz, Jonas et Dorianne Cuenoud, Astrid Marion, Amélie Kittel, Julien Monnier, Lionel Regamey, Fiona Rossi, Pauline Marie, Laurent Bigler et le Great Escape.

Mes amis, merci! Merci du fond du cœur

Finalement, je tiens à remercier ma famille, mes parents, Claire et Jean-François, mes frères, Guillaume et Nicolas, pour avoir toujours été derrière moi dans mes décisions, pour leur soutien et leur amour.

2005 – 2010
Cédric Potterat

Contents

Introduction	1
1 The Standard Model and the Higgs Boson Physics	3
1.1 Introduction to the Standard Model of Particle Physics	3
1.1.1 Elementary Particles	4
1.1.2 Leptons	4
1.1.3 Quarks and Hadrons	5
1.1.4 Fundamental Interactions and Bosons	5
1.1.5 Discrete Symmetries	6
1.2 The Standard Model and the Higgs Mechanism	7
1.2.1 Introduction to the Higgs Mechanism	8
1.2.2 The Goldstone Theorem and Spontaneous Symmetry Breaking	9
1.2.3 Higgs Mechanism in an Abelian Theory	11
1.2.4 Higgs Mechanism in the Standard Model	12
1.2.5 Fermion Masses	14
1.2.6 The Higgs Boson	15
1.2.7 Higgs Production in Hadron Colliders	17
1.2.8 Higgs Decays	18
1.2.9 Constraints on the Higgs Mass	21
2 CERN and the LHC	29
2.1 The European Organisation for Nuclear Research CERN	29
2.2 The LHC Machine	31
2.2.1 Accelerator and Energy	32
2.3 The Experiments on the LHC	33
2.4 Computing Solutions	36
3 The LHCb Experiment	37
3.1 Generalities on the LHCb Detector	37
3.2 LHCb layout	40
3.3 The Tracking System	40
3.3.1 Vertex Locator	41
3.3.2 Dipole Magnet	42
3.3.3 Silicon Trackers	43
3.3.4 Outer Tracker	44
3.3.5 Track Reconstruction and Performances	45
3.4 The Particle Identification Systems and Calorimetry	47
3.4.1 Ring Imaging Čerenkov Detectors	47
3.4.2 Calorimeters	49
3.4.3 Muon system	50
3.4.4 Particle Identification Performances	51

3.5	The Trigger System	53
3.5.1	Level-0 Trigger	53
3.5.2	HLT	55
3.6	Online System	55
3.6.1	Data Acquisition System	56
3.6.2	Timing and Fast Control	57
3.6.3	Experiment Control System	57
3.7	Computing and Resources	57
3.7.1	LHCb Computing Model	57
3.7.2	LHCb Software	58
4	Direct Search for Standard Model-Like Higgs Boson	61
4.1	Phenomenology and Topology	62
4.1.1	QCD, Asymptotic Freedom and Confinement	62
4.1.2	Hadronisation, Parton Shower and Jets in QCD	63
4.1.3	Signal $HW^\pm/Z^0 \rightarrow b\bar{b} + \ell$	64
4.1.4	Background: $t\bar{t}$, $Z^0 Z^0$, $W^\pm Z^0$, $Z^0 + b$ -jets, $W^\pm + b$ -jets,	67
4.2	Generation of the MONTE-CARLO Higgs and $t\bar{t}$ Events, and Single Quark Jets . .	68
4.3	Jet Algorithms and Beauty Tagging	70
4.3.1	The VV Seed Finder Algorithm	70
4.3.2	K_T Algorithm	86
4.3.3	Optimisation of b -jet Energy Measurement in LHCb	87
4.4	Lepton Selection	103
4.4.1	Lepton Generator Level Studies	103
4.4.2	Full Simulation	105
4.4.3	High- p_T Electrons	106
4.5	Higgs Selection	107
4.5.1	Dijet Mass Distribution	113
4.5.2	Higgs Selection Efficiency and Purity	115
4.6	Background Studies	117
4.6.1	$t\bar{t}$ Rejection	117
4.6.2	Z^0 Selection	124
4.7	Perspective	127
5	Software Integration of Data Acquisition Cards	131
5.1	Data Acquisition Cards: TELL1	133
5.1.1	The ECS Interface	136
5.1.2	Memory Map of the TELL1	137
5.2	Introduction to the PVSS SCADA System	140
5.2.1	Recipes	141
5.2.2	Finite State Machines	141
5.2.3	Distributed Information Management	144
5.3	fwTELL1: Integration of TELL1 into PVSS and ECS	146
5.3.1	Datapoint and Datapoint Type Descriptions	146
5.3.2	Graphical User Interfaces	150
5.3.3	Control Script and Check Functions	155
5.3.4	Recipes	156
5.3.5	FSM	159

Introduction

The Standard Model of Particle Physics was introduced and developed during the second half of the twentieth century. Since its introduction, the model has proved to be extremely successful and describes with great precision all the observed particle properties and their interactions. It has driven physics research and predicted the existence of particles that have since then been discovered. However the mass of the particles are arbitrary parameters of the model and its origin remains an open question. An elegant solution responsible for ElectroWeak symmetry breaking, called the Higgs mechanism, was proposed by theorists to solve the problem. The mechanism generates the mass of all the particles of the model, and also creates an associated particle, the Higgs boson. This key particle of the Standard Model has yet to be discovered, forty years after its prediction.

Direct and indirect searches have set limits on the Higgs particle mass. The LEP experiments have excluded a Higgs mass below $114.4 \text{ GeV}/c^2$ at 95 % confidence level and the latest results provided by the Tevatron experiments exclude a mass ranging between $163 \text{ GeV}/c^2$ and $166 \text{ GeV}/c^2$ at 95 % confidence level. The indirect searches set an upper limit for the Higgs mass of $157 \text{ GeV}/c^2$ at 95 % confidence level.

Chapter 1 sets the basis of the Standard Model of Particle Physics and introduces the Higgs mechanism and the Higgs boson physics.

In November 2009 CERN started to commission its new accelerator, the Large Hadron Collider (LHC). The LHC, which is described in Chapter 2, is designed to collide protons at a nominal centre-of-mass energy of $\sqrt{s} = 14 \text{ TeV}$. This energy opens up a new era of searches in particle physics and gives the potential to discover the Higgs boson in the near future.

The LHC beauty detector, detailed in Chapter 3, located at one of LHC's four collision points is dedicated to the study of the b -hadron physics and aims to study CP-violation processes and rare decays. The capability of the LHCb detector to distinguish displaced vertices with respect to the interaction point is mandatory to measure time of flight. This capability led the idea of using the LHCb detector to study the light Higgs sector, with the Higgs boson decaying into a $b\bar{b}$ quark-antiquark pair. The light Higgs, with a mass below $135 \text{ GeV}/c^2$, is predicted to decay predominately ($\sim 70\%$) into a $b\bar{b}$ pair. The decay into a $b\bar{b}$ pair could be an incentive to search for the Higgs boson within the LHCb experiment. On the other hand, this channel has a limited discovery potential at the two main general purpose detectors, ATLAS and CMS, which should be less precise to tag jets coming from b -quarks due to a larger background level.

Chapter 4 assesses the LHCb experiment discovery potential of the Higgs boson. This thesis presents a complete analysis for the light Standard Model-Like Higgs search within the LHCb experiment. In particular, a method to compute the energy and to tag the b -quark jets is introduced.

The first collisions were recorded at the LHCb detector at the end of 2009. These events have shown the first light quark jets. The reliability of the Experimental Control System (ECS) used by the experiment has also been tested. In order to control the detector, it was necessary to describe the whole experiment in one single Supervisory Control And Data Acquisition tool. Chapter 5 summarises the overall development performed during this thesis study for the software integration of Data Acquisition cards (TELL1) into the ECS of LHCb.

1

The Standard Model and Higgs Boson Physics



A STRONG INTERACTION

The Standard Model of Particle Physics is the theory that describes the elementary constituents of matter and their interactions. It was formulated from the 1960's with the consideration of the Quantum ElectroWeak and ChromoDynamics theories. In this chapter, an introduction to the Standard Model is presented, with a stress on the mechanism that generates the mass of particles. This mechanism, called the Higgs Mechanism, implies the existence of a new particle: the Higgs Boson.

1.1 Introduction to the Standard Model of Particle Physics

Particle Physics studies the elementary constituents of matter and their interactions. As knowledge has improved, the particles that are regarded as fundamental have changed with the time. Our current knowledge of the particles observed is summarised in the *Standard Model* (SM). This model was formulated in the 1960's and 1970's and attempts to explain all the phenomena of particle physics in terms of properties and interactions of a small number of "elementary" particles. The theory is very successful in that many Standard Model predictions have been experimentally confirmed precisely. An important objective in current particle physics studies is to measure the properties predicted by the SM. Any inconsistency found would hint at a sign of *New Physics* (NP), physics which is not described in the SM framework. The elementary particles described in the SM can be classified into two types: *fermions*, two spin- $\frac{1}{2}$ families, called *leptons* and *quarks* which constitute matter, and *bosons*, spin-1 particles, which act as the mediators of the fundamental forces in the theory. In addition to these observed particles, one spin-0 particle, called the *Higgs Boson* is postulated to explain the mass of the particles. All these particles are considered elementary and are treated as point particles without any internal structure. The Standard Model is mathematically based on Group theory.

1.1.1 Elementary Particles

These constituents of the matter can be divided in two groups: the leptons and the quarks which are summarised in Table 1.1. Both groups are divided into three families (or generations).

		Q [e]	m [MeV/ c^2]	L	B
Leptons	e^-	-1	0.511	+1	0
	ν_e	0	$< 2.2 \times 10^{-6}$	+1	0
	μ^-	-1	105.7	+1	0
	ν_μ	0	< 0.170	+1	0
	τ^-	-1	1.78×10^3	+1	0
	ν_τ	0	< 15.5	+1	0
Quarks	u	$+\frac{2}{3}$	1.5 - 3.3	0	$+\frac{1}{3}$
	d	$-\frac{1}{3}$	3.5 - 6.0	0	$+\frac{1}{3}$
	c	$+\frac{2}{3}$	$(1.27^{+0.07}_{-0.11}) \times 10^3$	0	$+\frac{1}{3}$
	s	$-\frac{1}{3}$	104^{+26}_{-34}	0	$+\frac{1}{3}$
	t	$+\frac{2}{3}$	$(171.2 \pm 2.1) \times 10^3$	0	$+\frac{1}{3}$
	b	$-\frac{1}{3}$	$(4.2^{+0.17}_{-0.07}) \times 10^3$	0	$+\frac{1}{3}$

Table 1.1: The Standard Model fundamental particles. The classification contains the three families of leptons and quarks with the electric charge Q , the mass m , the leptonic and baryonic numbers [1].

In addition, for each particle, there is an associated antiparticle with the same mass, spin, and lifetime, but with opposite quantum charges.

1.1.2 Leptons

The leptons are one of the three classes of fundamental particles and are indivisible particles. They are spin- $\frac{1}{2}$ fermions and obey the Fermi-Dirac statistics. They interact through the *weak interaction*, but are not affected by the *strong interaction*. There are six known leptons (see Table 1.1), which are distinguishable by their masses, electric charges and interaction modes. The three charged leptons are: the electron, e^- , the muon, μ^- , the tau, τ^- . They all carry the same negative elementary electric charge: $Q = -e$, where e is equal to 1.602×10^{-19} C.

They are associated to the three other neutral leptons, the *neutrinos* which are assumed to be massless in the Standard Model. However the phenomena of neutrino flavour oscillations between the three families requires to have at least two non-zero neutrino masses.

All these leptons can be divided into three *families* of *doublets*.

$$\begin{pmatrix} \nu_e \\ e^- \end{pmatrix}, \begin{pmatrix} \nu_\mu \\ \mu^- \end{pmatrix}, \begin{pmatrix} \nu_\tau \\ \tau^- \end{pmatrix} \quad (1.1)$$

A fourth generation with a “light” neutrino (one with a mass less than about 45 GeV/ c^2) has been ruled out by measurements of the widths of the Z^0 boson at CERN’s Large ElectronPositron Collider [2].

1.1.3 Quarks and Hadrons

$$\begin{pmatrix} u \\ d \end{pmatrix}, \begin{pmatrix} c \\ s \end{pmatrix}, \begin{pmatrix} t \\ b \end{pmatrix} \quad (1.2)$$

The quarks can also be grouped into three “families”. The first one is composed of the lightest quarks, the “up” u and the “down” d . They are the most abundant in nature and form the two nucleons: the proton, uud , and the neutron, udd . The two others families contain heavier quarks: the “charm” c and the “strange” s , and the “top” t and the “bottom” (or “beauty”) b . The quarks do not carry an entire electric charge as the leptons do, but u , c and t quarks have fractional electric charges $+\frac{2}{3}$ in units of the elementary charge e , while the three other quarks (d , s , b) have a fractional charge of $-\frac{1}{3} \cdot e$. The quarks also carry an additional quantum value, called the *colour*, and only the colour-charged particles are affected by the strong interaction.

Just like the leptons the quarks have corresponding anti-quarks

$$\begin{pmatrix} \bar{d} \\ \bar{u} \end{pmatrix}, \begin{pmatrix} \bar{s} \\ \bar{c} \end{pmatrix}, \begin{pmatrix} \bar{b} \\ \bar{t} \end{pmatrix} \quad (1.3)$$

Quarks are always found in groups of two or three and form particles called *hadrons*. There are two types of hadrons: *mesons* and *baryons*. Mesons are composed of a quark-antiquark pair ($q\bar{q}$), whereas the baryons are made of three quarks or three antiquarks (qqq , $\bar{q}\bar{q}\bar{q}$).

Quark masses are very difficult to measure due to the fact that the quarks cannot be observed alone. The strong interaction that binds the quarks together forbids that. Nevertheless it is possible to evaluate their masses by measuring the masses of particles that contains these quarks and by taking into account the contribution of the strong interaction.

1.1.4 Fundamental Interactions and Bosons

The four fundamental forces are briefly discussed here (except for the gravitation which is not included in the Standard Model). Particle interact though the exchange of mediators which “carry” the forces. These are particles called the *gauge bosons*.

Electromagnetic Interaction: As gravitation, the electromagnetic force is known from experience to have a very long range, hence the mass of the exchange boson must be very small. Quantum ElectroDynamic (QED) is the quantum field theory that describes the interaction between the charged particles. In QED, the charged particles are considered as matter fields and the mediator of the force is the photon.

Weak Interaction: Since the nuclear β decay was discovered and studied, the existence of a new type of interaction was an evidence. The weak interaction, responsible for the β -decay has an extremely short range, about 10^{-16} cm, which implies the mediators to be massive. The three gauge bosons associated to the weak force are the charged W^+ and W^- , and the neutral Z^0 . They have respectively a mass of about $80.4 \text{ GeV}/c^2$ for the W^\pm and about $91.2 \text{ GeV}/c^2$ for the Z^0 . The weak interaction allows decays that are forbidden by the electromagnetic or the strong interaction (like the flavour-changing and the CP -violation processes).

Strong Interaction: The strong interaction is the interaction which confines the quarks together in hadrons. It occurs between colour-charged particles. There are six types of strong charges: three colours and three anticolours ($r, g, b, \bar{r}, \bar{g}, \bar{b}$). The strong interaction is mediated by eight electrically neutral and massless gluons. The strong interaction does

not decrease with distance which has the consequence that free quarks have never been observed.

Table 1.2 presents a summary of the fundamental forces, and also the relative strengths of these interactions.

Interaction	Effective coupling	Bosons	Mass [GeV/c ²]	Range [fm]
Gravitation	10^{-39}	“graviton”	0	∞
Electromagnetism	1/137	photon	0	∞
Weak force	10^{-5}	W^{\pm}, Z^0	80.4 - 91.2	10^{-3}
Strong force	1	gluons	0	$< 1^{(a)}$

Table 1.2: Relative strengths and ranges of the fundamental interactions. The mediators and their masses are listed as well. (a) The range of the nuclear force, not that of the quark-quark force

1.1.5 Discrete Symmetries

The deep connection between symmetries and conservation laws in particle physics is fundamental [3]. In particle physics, considerations based on symmetries of the interactions determine the structure of the Hamiltonian. Some discrete transformations are particularly interesting. They are briefly described below with their effect on the quantum state $|f(\vec{p}, h)\rangle$ of a particle of momentum \vec{p} and helicity $h = \vec{s} \cdot \vec{p}/|\vec{p}|$, where \vec{s} is the spin of the particle:

Parity : it is the spatial inversion, described by the parity operator P:

$$P|f(\vec{p}, h)\rangle = \eta_P |f(-\vec{p}, -h)\rangle, \text{ where } \eta_P \text{ is the parity of the particle.}$$

Charge Conjugation : it is the exchange between particle and anti-particle, described by the charge conjugation operator C:

$$C|f(\vec{p}, h)\rangle = \eta_C |\bar{f}(\vec{p}, h)\rangle, \text{ where } \eta_C \text{ is a phase factor.}$$

Time Inversion : the direction of the time is reversed, described by the operator T:

$$T|f(\vec{p}, h)\rangle = \eta_T |f(-\vec{p}, h)\rangle^*, \text{ where } \eta_T \text{ is a phase factor depending on the spin.}$$

The three discrete symmetries C, P and T stay exact for strong and electromagnetic interactions, while for the weak interactions experimental observations show an obvious violation of the parity and charge conjugation. For the combined CP a slight violation has been observed. In particular this aspect has been pointed out in specific systems in sub-nuclear physics, as neutral K -mesons, for which the first observations date back to 1964 [4], and more recently, neutral B -mesons.

The Large Hadron Collider beauty experiment (LHCb) has been designed to perform precise measurements of the CP violation in the b -hadron sector.

The Standard Model predicts that the combination of the three symmetries (the combined operation of time reversal, space inversion and charge conjugation, CPT) to be a conserved fundamental symmetry: this has important and very general consequences [5]. In particular the mass and the lifetime of an elementary particle and its anti-particle must be equal. Up to now all the experimental observations obtained are consistent with CPT conservation.

1.2 The Standard Model and the Higgs Mechanism

The Standard Model of particle physics is a theory which describes the elementary particles and their interactions. It contains Quantum ChromoDynamics (QCD) and, through their unification into the ElectroWeak theory, the weak and electromagnetic interactions. This global quantum field theory is based on the gauge symmetry of $SU(3)_c \times SU(2)_L \times U(1)_Y$ and on the Spontaneous Symmetry Breaking $SU(2)_L \times U(1)_Y \rightarrow U(1)_Q$. A brief review of the Electroweak sector of the Standard Model is presented, including the Spontaneous Symmetry Breaking, and the Higgs Mechanism. The derivation of the formalism mainly follows the approach of Refs [6, 7].

The Electroweak theory, proposed by Glashow, Salam and Weinberg [8, 9, 10], is a non-abelian theory based on $SU(2)_L \times U(1)_Y$ that describes the electromagnetic and weak interactions between quarks and leptons. The weak interaction acts only on the left-handed fermions and hence the leptons are described as a doublet $(\ell, \nu_\ell)_L$ and a singlet ℓ_R which is not sensitive to the weak interaction in the $SU(2)_L$ gauge symmetry. To unify the weak and the electromagnetic interactions, the local symmetry group needs at least three vector bosons coupled to the electromagnetic (the photon) and weak currents (the intermediate vector bosons). From these currents, three charges can be defined, the electromagnetic charge Q and the weak charges I_+ and I_- . The simplest group with three generators is the $SU(2)_L$ group with I_+ , I_- and I_3 . But if the electric charge Q is one generator of $SU(2)_L$, it implies that the sum of the electric charges for the left-handed doublet is null. This is not the case for the leptons ($Q(\ell^-) + Q(\nu_\ell) = -1$) neither for the quarks ($Q(u) + Q(d) = 1/3$). Therefore the group $SU(2)_L \times U(1)_Y$ is needed to solve this problem, where Y is the hypercharge defined as $Y = 2(Q - I_3)$. These four generators I_\pm , I_3 and Y are associated to four gauge fields $W_\mu^{1,2,3}$ and B_μ .

The strong interaction between coloured quarks is based on the symmetry group $SU(3)_c$ and adds eight generators to the Standard Model. These are the eight gauge fields $G_\mu^{1,\dots,8}$ corresponding to the gluons. The following Lagrangian can be written for these bosons:

$$\mathcal{L}_{gauge} = -\frac{1}{4}B_{\mu\nu}B^{\mu\nu} - \frac{1}{4}W_{\mu\nu}^j W^{j\mu\nu} - \frac{1}{4}G_{\mu\nu}^i G^{i\mu\nu}, \quad (1.4)$$

where the field tensors are defined as:

$$\begin{aligned} B_{\mu\nu} &= \partial_\mu B_\nu - \partial_\nu B_\mu \\ W_{\mu\nu}^j &= \partial_\mu W_\nu^j - \partial_\nu W_\mu^j + g_2 \epsilon^{jkl} W_\mu^k W_\nu^l, & j \in [1, 3] \\ G_{\mu\nu}^i &= \partial_\mu G_\nu^i - \partial_\nu G_\mu^i + g_s f^{ijk} W_\mu^j W_\nu^k, & i \in [1, 8] \end{aligned} \quad (1.5)$$

where f^{ijk} and ϵ^{jkl} are the antisymmetric tensors for the structure constants, respectively, of $SU(3)_c$ and $SU(2)_L$. g_s , g_2 (and g_1) are respectively the coupling constant of $SU(3)_c$, $SU(2)_L$ and $U(1)_Y$.

The non-abelian nature of the $SU(2)_L$ and $SU(3)_c$ groups leads to self-interactions between the gauge fields:

$$\begin{aligned} \text{triple gauge boson couplings : } & ig_i \text{Tr}(\partial_\nu V_\mu - \partial_\mu V_\nu)[V_\mu, V_\nu], \\ \text{quadruple gauge boson couplings : } & \frac{1}{2}g_i^2 \text{Tr}[V_\mu, V_\nu]^2, \end{aligned} \quad (1.6)$$

where $V_\mu \equiv W_\mu$ or G_μ .

The matter fields, ψ , are coupled, with the covariant derivative \mathcal{D}_μ , to the gauge fields. This can be expressed for the quarks as:

$$\mathcal{D}_\mu \psi = \left(\partial_\mu - i \frac{g_s}{2} \lambda_i G_\mu^i - i \frac{g_2}{2} \tau_i A_\mu^i - i \frac{g_1}{2} Y_q B_\mu \right) \psi, \quad (1.7)$$

where τ_i , with $i = 1, 2, 3$, are the non-commuting 2×2 Pauli matrices while λ_i , with $i = 1, \dots, 8$, are the eight 3×3 anti-commuting Gell-Mann matrices. Y_q is the weak hypercharge generator. It leads to unique couplings between the gauge fields V_μ and the fermions:

$$\text{fermion gauge boson couplings : } -g_i \bar{\psi} V_\mu \gamma^\mu \psi. \quad (1.8)$$

But also the matter fields can be classified in function of their charge respectively to the different interactions. Hence there are three chiral generators for the quarks and the leptons. The left-handed fermions are grouped in the weak isodoublets with $I_3 = \pm \frac{1}{2}$ and the right-handed fermions form the weak isosinglets with $I_3 = 0$. The leptons are not affected by the strong interaction, therefore they are singlets in $SU(3)_c$ while the quarks form coloured triplets. The leptons are noted with L_i and e_{R_i} , respectively, for the isodoublets and the isosinglets, where $i = 1, 2, 3$ corresponds to the three kinds of leptons (e, μ, τ). In the same way Q_i are the isodoublets for the quarks while u_{R_i} and d_{R_i} are the isosinglets.

Therefore the Standard Model Lagrangian, without the mass term, is formulated by adding to the first Lagrangian (1.4) the terms related to the fermions, and is given by:

$$\begin{aligned} \mathcal{L}_{SM} = & -\frac{1}{4} B_{\mu\nu} B^{\mu\nu} - \frac{1}{4} W_{\mu\nu}^j W^{j\mu\nu} - \frac{1}{4} G_{\mu\nu}^i G^{i\mu\nu} \\ & + \bar{L}_i i \mathcal{D}_\mu \gamma^\mu L_i + \bar{e}_{R_i} i \mathcal{D}_\mu \gamma^\mu e_{R_i} + \bar{Q}_i i \mathcal{D}_\mu \gamma^\mu Q_i + \bar{u}_{R_i} i \mathcal{D}_\mu \gamma^\mu u_{R_i} + \bar{d}_{R_i} i \mathcal{D}_\mu \gamma^\mu d_{R_i}. \end{aligned} \quad (1.9)$$

1.2.1 Introduction to the Higgs Mechanism

At this point, the electroweak theory is formulated as a $SU(2)_L \times U(1)_Y$ gauge theory with massless bosons and fermions. The Lagrangian of the free massless boson fields is formulated with the composition of the $U(1)_Y$ gauge field B_μ and the three real $SU(2)_L$ gauge fields W_μ^j , $j = 1, 2, 3$:

$$\mathcal{L}_{EW} = -\frac{1}{4} B_{\mu\nu}(x) B^{\mu\nu}(x) - \frac{1}{4} W_{\mu\nu}^j(x) W^{j\mu\nu}(x), \quad (1.10)$$

where $B_{\mu\nu}$ and $W_{\mu\nu}^j$ are the field tensors defined as:

$$\begin{aligned} B_{\mu\nu} &= \partial_\mu B_\nu - \partial_\nu B_\mu, \\ W_{\mu\nu}^j &= \partial_\mu W_\nu^j - \partial_\nu W_\mu^j + g_2 \epsilon^{jkl} W_\mu^k W_\nu^l, \quad j \in [1, 3]. \end{aligned} \quad (1.11)$$

The introduction of the following transformations:

$$\begin{aligned} A_\mu &= \cos \theta_W B_\mu + \sin \theta_W W_\mu^3, \\ Z_\mu &= \sin \theta_W B_\mu - \cos \theta_W W_\mu^3, \\ W_\mu^\pm &= \frac{1}{\sqrt{2}} (W_\mu^1 \mp i W_\mu^2), \end{aligned} \quad (1.12)$$

where the free parameter θ_W is the Weinberg angle, change the Lagrangian (1.10) into:

$$\mathcal{L}_{EW} = -\frac{1}{4}F_{\mu\nu}(x)F^{\mu\nu}(x) - \frac{1}{2}F_{W\mu\nu}^\dagger(x)F_W^{\mu\nu}(x) - \frac{1}{4}F_{Z\mu\nu}(x)F_Z^{\mu\nu}(x). \quad (1.13)$$

$F_{\mu\nu}$ represents the electromagnetic tensor associated to the photon field A_μ . $F_{W\mu\nu}$ and $F_{Z\mu\nu}$ are the tensors related to the electroweak fields W^\pm and Z^0 . In this Lagrangian, the fields W^\pm and Z^0 are still massless, but they can acquire a mass by adding by brute force the terms $m_W^2 W_\mu^\dagger(x)W^\mu(x) + \frac{1}{2}m_Z^2 Z_\mu(x)Z^\mu(x)$ into (1.13). This incorporation of mass terms for gauge bosons and for fermions leads to a breakdown of the local $SU(2)_L \times U(1)_Y$ gauge invariance. This problem causes the theory to be not renormalisable and to be appropriate only at tree level. There are two possibilities, either the masses are given as a fact, or the principle of unbroken or exact gauge symmetry has to be given up. The Higgs-Brout-Englert-Guralnik-Hagen-Kibble mechanism of spontaneous symmetry breaking [11, 12, 13] (or the Higgs Mechanism) is a nice solution to generate the gauge bosons and fermions masses without violating $SU(2) \times U(1)$ gauge invariance. The fundamental idea is to include an extra scalar field which does not vanish into the vacuum. The vacuum is here defined as the state in which all the fields have their lowest possible energy.

1.2.2 The Goldstone Theorem and Spontaneous Symmetry Breaking

Spontaneous Symmetry Breaking (*SSB*) would give masses to the fields W^\pm and Z^0 preserving the $SU(2) \times U(1)$ gauge invariance. This is called the *Goldstone model*.

Consider the simple case of a system with N scalar real fields, ϕ_i , with the Lagrangian:

$$\mathcal{L} = \frac{1}{2}\partial_\mu\phi_i\partial^\mu\phi_i - V(\phi), \quad V(\phi) = \frac{1}{2}\mu^2(\phi_i\phi_i) + \frac{1}{4}\lambda(\phi_i\phi_i)^2. \quad (1.14)$$

\mathcal{L} is invariant under the transformation:

$$\phi_i \rightarrow \phi'_i = R_{ij}\phi_j, \quad (1.15)$$

where R_{ij} are the rotations in $O(N)$. In the case $N = 1$, the reflection symmetry $\phi \rightarrow -\phi$ leaves the Lagrangian invariant since there are only even-powered terms.

The N scalar fields are independent, and in the case of a positive mass term μ^2 , the potential $V(\phi)$ is also positive when the self-coupling term λ is positive (Figure 1.1), therefore the minimum of the potential is obtained for each ϕ_i at $\langle 0|\phi_i|0\rangle \equiv \phi_{i0} = 0$ and \mathcal{L} is simply the Lagrangian for spin-zero particles of mass μ .

In the other interesting case, if μ^2 is negative, the potential $V(\phi)$ has a minimum only when $\partial V/\partial\phi_i = \mu^2\phi_i + \lambda\phi_i^3 = 0$ (Figure 1.2). Indeed:

$$\begin{aligned} \langle 0|\phi_i^2|0\rangle &\equiv \phi_{i0}^2 = 0, \\ &\text{or} \\ \langle 0|\phi_i^2|0\rangle &\equiv \phi_{i0}^2 = -\frac{\mu^2}{\lambda} \equiv v^2. \end{aligned} \quad (1.16)$$

The minimum value $\langle 0|\phi_i|0\rangle \equiv \pm v$ is called the vacuum expectation value (vev) of the scalar field ϕ and differs from $\phi_{i0}^2 = 0$ which is a local maximum. With the expansion around one of

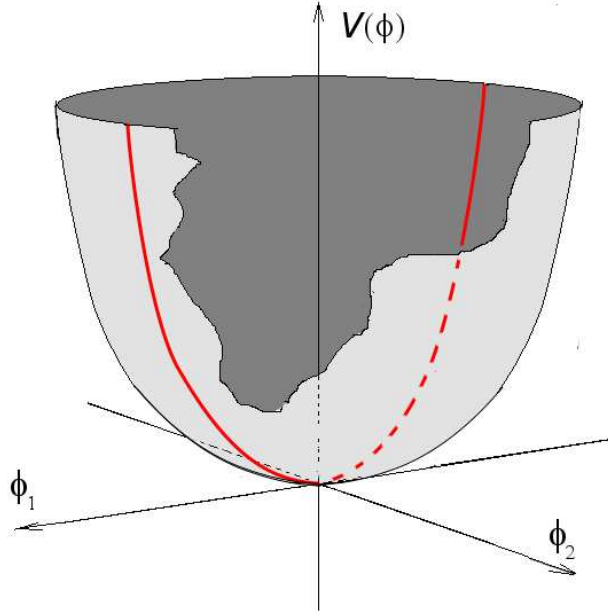


Figure 1.1: Representation of the potential $V(\phi)$ in the case of two real scalar fields and a positive value for μ^2 . The minimum is reached for $|\phi| = 0$

the minima, $\phi_0 = v + \sigma$, and rewriting the fields $\phi_i = \varphi_i$ for $i = 1, \dots, N - 1$, the Lagrangian becomes:

$$\begin{aligned} \mathcal{L} = & \frac{1}{2} \partial_\mu \sigma \partial^\mu \sigma - \frac{1}{2} (-2\mu^2) \sigma^2 - \lambda v \sigma^3 - \frac{\lambda}{4} \sigma^4 \\ & + \frac{1}{2} \partial_\mu \varphi_i \partial^\mu \varphi_i - \frac{\lambda}{4} \lambda \varphi_i^4 - \lambda v \varphi_i \varphi_i \sigma - \frac{\lambda}{2} \varphi_i \varphi_i \sigma^2. \end{aligned} \quad (1.17)$$

One massive σ boson with the mass $m^2 = -2\mu^2$ is present, but also massless bosons (φ_i). An $O(N - 1)$ symmetry among the φ_i fields is still there. In this simple theory of real scalar fields, with the self-interaction terms σ^3 and σ^4 . Since the cubic term σ^3 appears, it breaks the symmetry.

The Goldstone Theorem [14, 15, 16] can be expressed as: There exists one massless scalar (spin-zero) particle, called Goldstone bosons, for each continuous symmetry which is spontaneously broken. The number of these massless bosons is, hence, equal to the number of broken generators. And this number of generators in an $O(N)$ continuous symmetry, is $\frac{1}{2}N(N - 1)$. The residual unbroken symmetry $O(N - 1)$ has $\frac{1}{2}(N - 1)(N - 2)$ generators and $N - 1$ massless Goldstone bosons are created.

This exercise can be made for a complex doublet of scalar fields:

$$\phi = \begin{pmatrix} \phi^+ \\ \phi^0 \end{pmatrix} = \frac{1}{\sqrt{2}} \begin{pmatrix} \phi_1 - i\phi_2 \\ \phi_3 - i\phi_4 \end{pmatrix}, \quad (1.18)$$

where the invariant product is $\phi\phi^\dagger = \frac{1}{2}(\phi_1^2 + \phi_2^2 + \phi_3^2 + \phi_4^2) = \frac{1}{2}\phi_i\phi^i$.

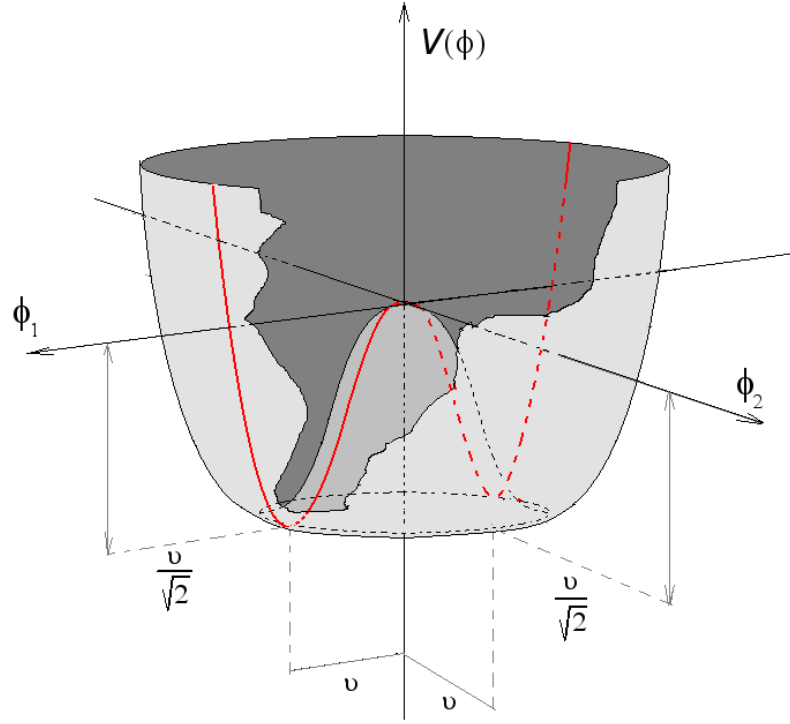


Figure 1.2: Representation of the potential $V(\phi)$ in the case of two real scalar fields and a negative value for μ^2 . A local maximum is reached for $|\phi| = 0$, while the potential gets its minimum for $|\phi| = v$

1.2.3 Higgs Mechanism in an Abelian Theory

The Goldstone model can be extended to create massive vector bosons in a gauge invariant theory. In the case of the abelian $U(1)$ group; the complex scalar field is coupled to itself and to an electromagnetic field A_μ . The covariant derivative $\mathcal{D}_\mu = \partial_\mu + ieA_\mu$ is introduced in the Lagrangian:

$$\mathcal{L} = -\frac{1}{4}F_{\mu\nu}F^{\mu\nu} + \mathcal{D}_\mu\phi^*\mathcal{D}^\mu\phi - V(\phi), \quad (1.19)$$

with the scalar potential $V(\phi) = \mu^2(\phi^*\phi) + \lambda(\phi^*\phi)^2$ and where $F_{\mu\nu} = \partial_\mu A_\nu - \partial_\nu A_\mu$ is the usual electromagnetic tensor associated to the photon, A_μ . The Lagrangian (1.19) is invariant under the local $U(1)$ transformation:

$$\begin{aligned} \phi(x) &\rightarrow \phi'(x) = \phi(x) \cdot e^{i\alpha(x)}, \\ A_\mu(x) &\rightarrow A'_\mu(x) = A_\mu(x) - \frac{1}{q}\partial_\mu\alpha(x), \end{aligned} \quad (1.20)$$

where $\alpha(x)$ is any continuous and differentiable function. For $\mu^2 > 0$, \mathcal{L} is the QED Lagrangian for a charged scalar particle of mass μ and with the ϕ^4 self-interactions. As expected in the Goldstone theorem, for $\mu^2 < 0$, the field $\phi(x)$ gets a vacuum expectation value and the minimum is at:

$$\langle 0|\phi|0\rangle \equiv \phi_0 = \left(-\frac{\mu^2}{2\lambda}\right)^{1/2} \equiv \frac{v}{2}. \quad (1.21)$$

Hence the field $\phi(x)$ can be expanded around the vacuum state:

$$\phi = \frac{1}{\sqrt{2}}(v + \phi_1(x) + i\phi_2(x)) \quad (1.22)$$

and the Lagrangian (1.19) becomes:

$$\begin{aligned} \mathcal{L} &= -\frac{1}{4}F_{\mu\nu}F^{\mu\nu} + (\partial^\mu + ieA^\mu)\phi^*(\partial_\mu - ieA_\mu)\phi - \mu^2(\phi^*\phi) - \lambda(\phi^*\phi)^2 \\ &= -\frac{1}{4}F_{\mu\nu}F^{\mu\nu} + \frac{1}{2}(\partial^\mu\phi_1)^2 + \frac{1}{2}(\partial^\mu\phi_2)^2 - v^2\lambda\phi_1^2 + \frac{1}{2}q^2v^2A_\mu A^\mu - qvA_\mu\partial^\mu\phi_2. \end{aligned} \quad (1.23)$$

The last term describes a photon, or the vector boson field A_μ , which has acquired a mass $m_A = qv = -q\mu^2/\lambda$. The Lagrangian has still one scalar particle ϕ_1 with a mass $m_{\phi_1}^2 = -2\mu^2$ and a massless particle ϕ_2 : a would-be Goldstone boson. The Lagrangian should have four degrees of freedom, two for the complex scalar field ϕ and two for the electromagnetic field A_μ , while the covariant Lagrangian (1.23) has apparently five degrees of freedom, one for ϕ_1 , one for ϕ_2 and three for the massive photon A_μ . Therefore one of the fields should not be physical. The bilinear term $qvA_\mu\partial^\mu\phi_2$ has to be eliminated. Therefore the original field ϕ can be rewritten as:

$$\phi = \frac{1}{\sqrt{2}}(v + \phi_1(x) + i\phi_2(x)) \equiv \frac{1}{\sqrt{2}}(v + \eta(x)) \cdot e^{i\zeta(x)/v}, \quad (1.24)$$

which gives also:

$$A_\mu(x) \rightarrow A'_\mu(x) = A_\mu(x) - \frac{1}{qv}\partial_\mu\zeta(x). \quad (1.25)$$

The bilinear term $A_\mu\partial^\mu\zeta$, and all the other zeta terms, disappear. The photon (two transverse polarisation states, two degrees of freedom) has absorbed the would-be Goldstone boson (one degree of freedom) to become massive (three degrees of freedom). The vector boson has gained a longitudinal mode which is the Goldstone boson. The $U(1)$ gauge symmetry is spontaneously broken. This is the Higgs mechanism that generates masses for gauge bosons.

1.2.4 Higgs Mechanism in the Standard Model

The Higgs mechanism, in the Standard Model, is responsible for the mass generation of the gauge bosons W^\pm and Z^0 , as well as for quarks and leptons. Masses for the three gauge bosons have to be generated while the photon has to be massless and the QED must stay an exact symmetry. Therefore the choice is a complex $SU(2)$ doublet of scalar fields Φ :

$$\Phi = \begin{pmatrix} \phi^+ \\ \phi^0 \end{pmatrix}, \quad Y_\Phi = +1. \quad (1.26)$$

In a full description, the theory has to be invariant under $SU(3)_c$ symmetry which represents the strong interaction between the quarks and which involves eight gluon gauge fields G_μ^α . The Standard Model Lagrangian (1.9) has been defined and if the strong interaction is ignored and the Electroweak interaction is explicitly written, the Lagrangian can be expressed as:

$$\begin{aligned}\mathcal{L}_{SM} = & -\frac{1}{4}B_{\mu\nu}B^{\mu\nu} - \frac{1}{4}W_{\mu\nu}^j W^{j\mu\nu} \\ & + \bar{L}_i \gamma^\mu \left(\partial_\mu - i\frac{g_2}{2}\tau_i W_\mu^i - i\frac{g_1}{2}Y_q B_\mu \right) L_i + \bar{e}_{R_i} \gamma^\mu \left(\partial_\mu - i\frac{g_1}{2}Y_q B_\mu \right) e_{R_i} \\ & + \bar{Q}_i \gamma^\mu \left(\partial_\mu - i\frac{g_2}{2}\tau_i W_\mu^i - i\frac{g_1}{2}Y_q B_\mu \right) Q_i + \bar{u}_{R_i} \gamma^\mu \left(\partial_\mu - i\frac{g_1}{2}Y_q B_\mu \right) u_{R_i} \\ & + \bar{d}_{R_i} \gamma^\mu \left(\partial_\mu - i\frac{g_1}{2}Y_q B_\mu \right) d_{R_i}.\end{aligned}\quad (1.27)$$

To this Lagrangian, the invariant terms of the scalar fields Φ are added:

$$\mathcal{L}_{scalar} = (\mathcal{D}^\mu \Phi^\dagger)(\mathcal{D}_\mu \Phi) - V(\Phi), \quad (1.28)$$

where

$$V(\Phi) = \mu^2(\Phi^\dagger \Phi) + \lambda(\Phi^\dagger \Phi)^2. \quad (1.29)$$

A vacuum expectation value will be developed by the double field Φ for $\mu^2 < 0$. QED must stay an exact symmetry, hence the vev should not be in the charged direction:

$$\langle 0|\Phi|0\rangle \equiv \begin{pmatrix} \langle 0|\phi_+|0\rangle \\ \langle 0|\phi_0|0\rangle \end{pmatrix} = \begin{pmatrix} 0 \\ \frac{v}{\sqrt{2}} \end{pmatrix}, \quad (1.30)$$

where $v = \left(\frac{-\mu^2}{\lambda}\right)^{1/2}$. The field Φ can be rewritten in terms of the four fields $\theta_{1,2,3}(x)$ and $H(x)$ at the first order:

$$\Phi(x) = \begin{pmatrix} \theta_2 + i\theta_1 \\ \frac{1}{\sqrt{2}}(v + H) - i\theta_3 \end{pmatrix} = e^{i\theta_a(x)\tau^a(x)/v} \begin{pmatrix} 0 \\ \frac{1}{\sqrt{2}}(v + H(x)) \end{pmatrix} \quad (1.31)$$

and the unitary gauge can be obtained by the gauge transformation on the field:

$$\Phi(x) \rightarrow e^{-i\theta_a(x)\tau^a(x)/v} \Phi(x) = \frac{1}{\sqrt{2}} \begin{pmatrix} 0 \\ v + H(x) \end{pmatrix}. \quad (1.32)$$

Then the terms $|\mathcal{D}_\mu \Phi|^2$ of the scalar Lagrangian (1.28) can be expanded:

$$\begin{aligned}|\mathcal{D}_\mu \Phi|^2 &= \left| \left(\partial_\mu - i\frac{g_2}{2}\tau_i W_\mu^i - i\frac{g_1}{2}Y_\Phi B_\mu \right) \Phi \right|^2 \\ &= \frac{1}{2} \left| \begin{pmatrix} \partial_\mu - \frac{i}{2}(g_2 W_\mu^3 + g_1 B_\mu) & -\frac{ig_2}{2}(W_\mu^1 - iW_\mu^2) \\ -\frac{ig_2}{2}(W_\mu^1 + iW_\mu^2) & \partial_\mu + \frac{i}{2}(g_2 W_\mu^3 - g_1 B_\mu) \end{pmatrix} \begin{pmatrix} 0 \\ v + H(x) \end{pmatrix} \right|^2 \\ &= \frac{1}{2}(\partial_\mu H)^2 + \frac{1}{8}g_2^2(v + H)^2|W_\mu^1 + iW_\mu^2|^2 + \frac{1}{8}(v + H)^2|g_2 W_\mu^3 - g_1 B_\mu|^2.\end{aligned}\quad (1.33)$$

The new fields W_μ^\pm , Z_μ and A_μ are defined as:

$$\begin{aligned} W_\mu^\pm &= \frac{1}{\sqrt{2}}(W_\mu^1 \mp iW_\mu^2), \\ Z_\mu &= \frac{g_2 W_\mu^3 - g_1 B_\mu}{\sqrt{g_2^2 + g_1^2}}, \\ A_\mu &= \frac{g_2 W_\mu^3 + g_1 B_\mu}{\sqrt{g_2^2 + g_1^2}}. \end{aligned} \quad (1.34)$$

The bilinear terms in the fields W^\pm , Z , and A are:

$$m_W^2 W_\mu^+ W^{-\mu} + \frac{1}{2} m_Z^2 Z_\mu Z^\mu + \frac{1}{2} m_A^2 A_\mu A^\mu. \quad (1.35)$$

In regards of (1.33), the W and Z bosons get now a mass while the photon, A , remains massless:

$$m_W = \frac{1}{2} v g_2, \quad m_Z = \frac{1}{2} v \sqrt{g_1^2 + g_2^2}, \quad m_A = 0 \quad (1.36)$$

The three Goldstone bosons have been absorbed by the W^\pm , Z bosons to form as before their longitudinal mode and to get masses. $U(1)_Q$ remains unbroken, hence the photon, which is its generator, is still massless as wanted. The development of the following Lagrangian:

$$\mathcal{L}_{\text{fermions}} = \bar{L}_i i \mathcal{D}_\mu \gamma^\mu L_i + \bar{e}_{R_i} i \mathcal{D}_\mu \gamma^\mu e_{R_i} + \bar{Q}_i i \mathcal{D}_\mu \gamma^\mu Q_i + \bar{u}_{R_i} i \mathcal{D}_\mu \gamma^\mu u_{R_i} + \bar{d}_{R_i} i \mathcal{D}_\mu \gamma^\mu d_{R_i}, \quad (1.37)$$

with the new fields W_μ^\pm , Z_μ and A_μ , leads to the effective Lagrangian of the theory V-A for the weak interaction and also the effective Lagrangian for the electromagnetic interaction.

1.2.5 Fermion Masses

The fermions, which are still massless, acquire their masses using the same scalar field Φ with the hypercharge $Y_\Phi = 1$, and the isodoublet $\tilde{\Phi} = i\tau_2 \Phi^*$ with the hypercharge $Y_{\tilde{\Phi}} = -1$. The coupling between the scalar field Φ and the left- and right-handed fermions gives the masses to the fermions. The general $SU(2)_L \times U(1)_Y$ invariant Yukawa Lagrangian can be introduced for any fermion family:

$$\mathcal{L} = -\lambda_e \bar{L} \Phi e_R - \lambda_d \bar{Q} \Phi d_R - \lambda_u \bar{Q} \tilde{\Phi} u_R + \text{h.c.} \quad (1.38)$$

In the case of the electron, it gives:

$$\mathcal{L}_{\text{electron}} = -\frac{1}{\sqrt{2}} \lambda_e (\bar{\nu}_e, \bar{e}_L) \begin{pmatrix} 0 \\ v + H \end{pmatrix} e_R + \dots \quad (1.39)$$

$$= -\frac{1}{\sqrt{2}} \lambda_e v \bar{e}_L e_R - \frac{1}{\sqrt{2}} \lambda_e H \bar{e}_L e_R + \dots, \quad (1.40)$$

where the first constant term in front of $\bar{e}_L e_R$ is identified with the electron mass, it gives:

$$m_e = \frac{\lambda_e v}{\sqrt{2}} \quad (1.41)$$

and in the same way the quark masses are given by:

$$m_u = \frac{\lambda_u v}{\sqrt{2}}, \quad m_d = \frac{\lambda_d v}{\sqrt{2}}. \quad (1.42)$$

1.2.6 The Higgs Boson

In the previous subsection, the generation of the boson and fermion masses has been described through the Higgs Mechanism. The parts of the Standard Model Lagrangian which imply the scalar field Φ is now considered (equations 1.28 and 1.7). From the scalar field Φ , v has been absorbed to give the masses to the vector bosons, while H becomes a massive field which is the Higgs particle. Its propagator, $\frac{1}{2}(\partial_\mu H)^2$, is present in equation 1.33, while a mass term and self-interaction terms arise from the scalar potential (1.29):

$$\begin{aligned} V(\Phi) &= \mu^2(\Phi^\dagger \Phi) + \lambda(\Phi^\dagger \Phi)^2 \\ &= \frac{\mu^2}{2}(0, v + H) \begin{pmatrix} 0 \\ v + H \end{pmatrix} + \frac{\lambda}{4} \left| (0, v + H) \begin{pmatrix} 0 \\ v + H \end{pmatrix} \right|^2 \\ &= -\frac{1}{2}\lambda v^2(v + H)^2 + \frac{1}{4}\lambda v^2(v + H)^4 \\ &= \lambda v^2 H^2 + \lambda v H^3 + \frac{\lambda}{4} H^4, \end{aligned} \quad (1.43)$$

where the relation $v^2 = -\mu^2/\lambda$ has been used. Finally the Lagrangian containing the Higgs field H can be written:

$$\mathcal{L}_H = \frac{1}{2}(\partial_\mu H)^2 - \lambda v^2 H^2 - \lambda v H^3 - \frac{\lambda}{4} H^4. \quad (1.44)$$

The Higgs boson appears and its mass can directly be read:

$$m_H^2 = 2\lambda v^2 = -2\mu^2, \quad (1.45)$$

and the couplings for the Higgs self-interaction vertices are given by:

$$g_{HHH} = 3i\frac{m_H^2}{v}, \quad g_{HHHH} = 3i\frac{m_H^2}{v^2}, \quad (1.46)$$

where respectively the factor λv and $\frac{\lambda}{4}$ have been multiplied by a factor $-i$ and also by a factor $n!$ where n is the number of identical particles in the vertex. In the Lagrangian (1.39) and in the covariant terms (1.33), the Higgs boson coupling to the gauge bosons and to the fermions can be derived when the masses of these particles are known or calculated. The second term of 1.39 gives the coupling between the electron and the Higgs boson, hence it can be generalised to the fermions. And in the same way the terms of 1.33 which couple the vector bosons W^\pm and Z to the Higgs bosons can also be derived and calculated with the masses:

$$\begin{aligned}
-\frac{1}{\sqrt{2}}\lambda_f H \bar{f}_L f_R &= -\frac{m_f}{v} H \bar{f}_L f_R \rightarrow g_{Hff} = i\frac{m_f}{v}, \\
m_V^2 \frac{H}{v} V_\mu V^\mu &\rightarrow g_{HVV} = -2i\frac{m_V^2}{v}, \\
m_V^2 \frac{H^2}{v} V_\mu V^\mu &\rightarrow g_{HHVV} = -2i\frac{m_V^2}{v}.
\end{aligned} \tag{1.47}$$

Experimentally, the vacuum expectation value v can be inferred from the mass of the vector bosons W^\pm or with the Fermi constant G_μ calculated from the muon decay:

$$m_{W^\pm} = \frac{1}{2}g_2 v = \left(\frac{\sqrt{2}g^2}{8G_\mu} \right)^{1/2} \Rightarrow v = \frac{1}{(\sqrt{2}G_\mu)^{1/2}} \simeq 246 \text{ GeV}. \tag{1.48}$$

Figure 1.3 summarises all the couplings of the Higgs bosons to the fermions, the vector gauge bosons and to itself. All the couplings are proportional to their respective mass.

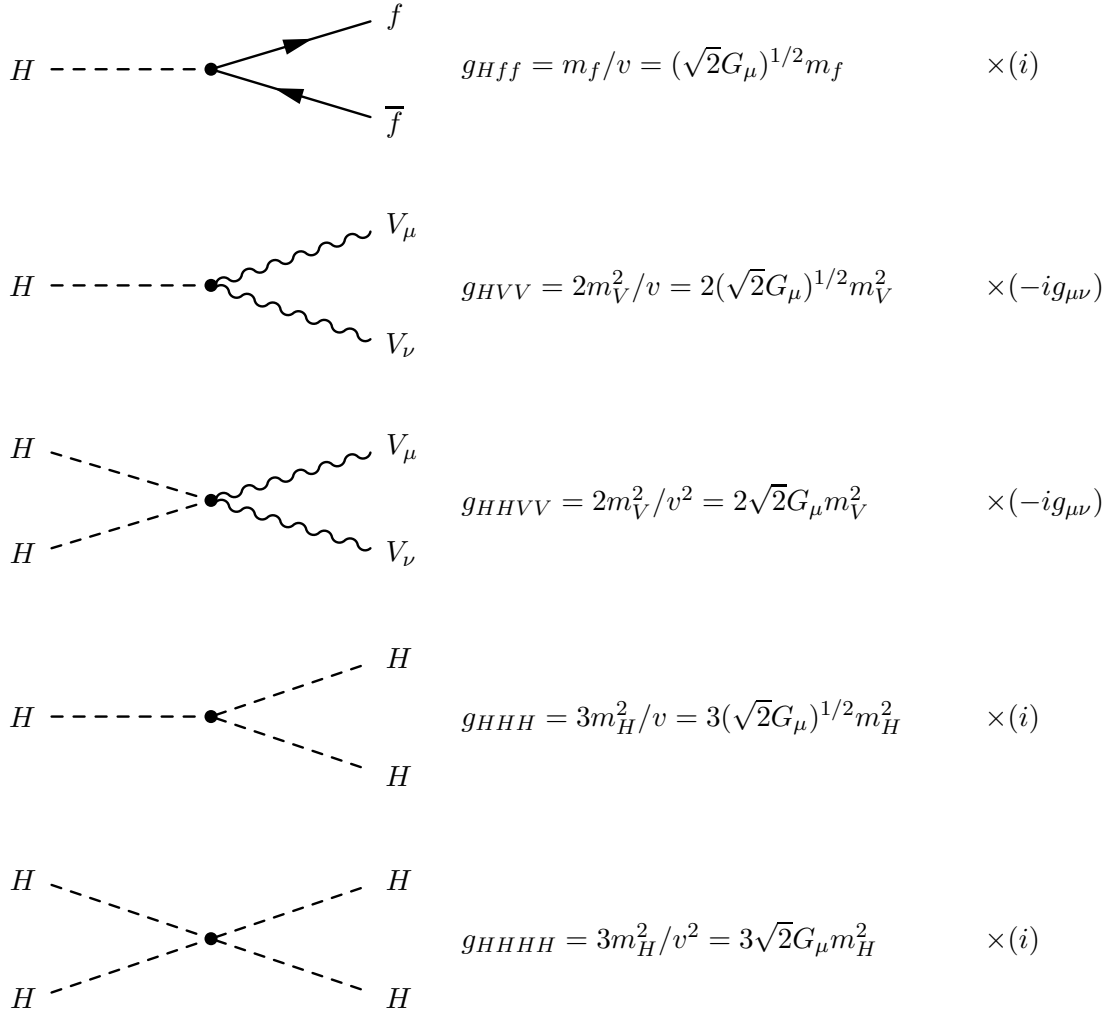


Figure 1.3: Summary of the Higgs boson couplings.

1.2.7 Higgs Production in Hadron Colliders

It has been seen that the Higgs boson couplings depend on the mass of the particles that are coupled to it (Figure 1.3), which means that the Higgs boson couples in preference to the vector bosons W^\pm and Z^0 , and to the top and bottom quarks. Therefore, in hadron collider, the Higgs production is achieved via the processes listed in Figure 1.4.

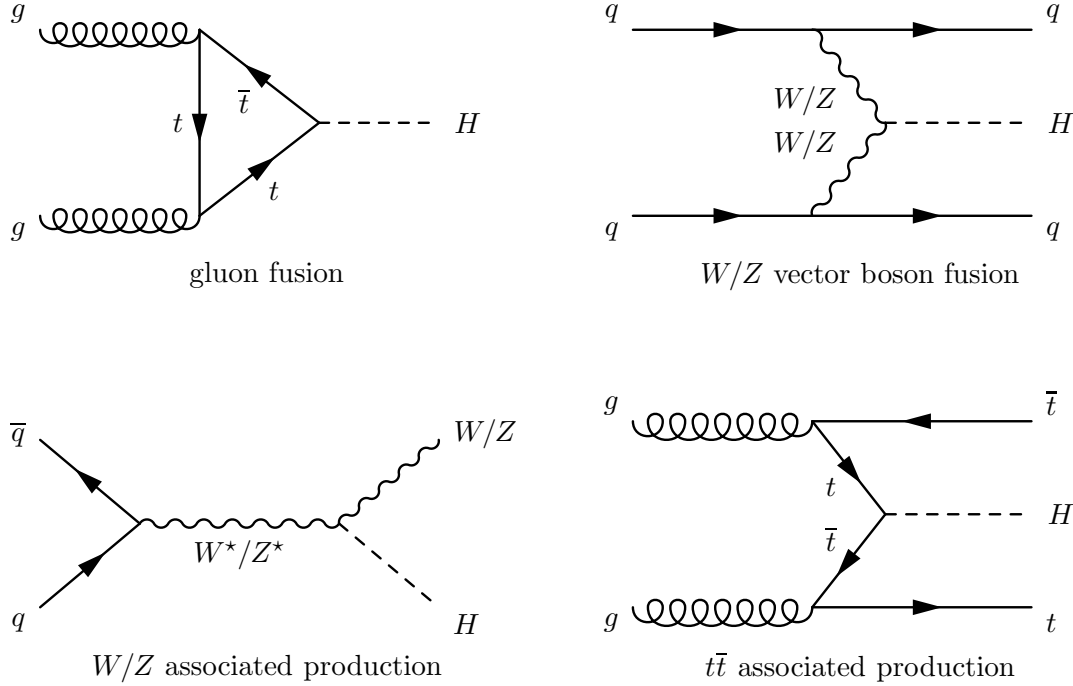


Figure 1.4: The dominant Standard Model Higgs boson production mode in a hadron collider.

The predominant process is the gluon fusion $gg \rightarrow H$. The gluons melt into a quark loop. The loop is dominated by the top quark due to his large mass in comparison to the other quarks and the fact that the coupling between fermion and Higgs grows with the mass of the fermion. The cross section of the gluon fusion at the LHC nominal energy is presented in Figure 1.5 as a function of the Higgs mass.

The second mechanism is the vector boson fusion: $qq \rightarrow qqVV \rightarrow qqH$ ($V = W^\pm, Z^0$), where the two incoming quarks emit two vector bosons (W^+W^- or Z^0) which annihilate to create a Higgs boson. This process has almost the same cross section as the gluon fusion for a Higgs mass higher than $\sim 1000 \text{ GeV}/c^2$.

The two last dominant production modes are associated production with a vector boson W/Z and associated production with a $t\bar{t}$ quark pair. In the first process, an off-shell vector boson $W^{\pm*}/Z^{0*}$ is created by the annihilation of a pair $qq/q\bar{q} \rightarrow V^* \rightarrow VH$, with $V = W^\pm, Z^0$. The off-shell vector boson is de-excited by the emission of a Higgs boson. In the $t\bar{t}$ associated production ($gg \rightarrow t\bar{t}t\bar{t} \rightarrow t\bar{t}H$), each gluon creates a $t\bar{t}$ pair, and the annihilation of a t with the \bar{t} from the other side creates the Higgs boson particle. The mechanism with the top quark dominates the other quark processes. The cross sections of Higgs associated productions are much lower than the two other mechanisms seen before (Figure 1.5). But in the case of a light Higgs mass, processes give a clear signature, especially in the case of W/Z associated production

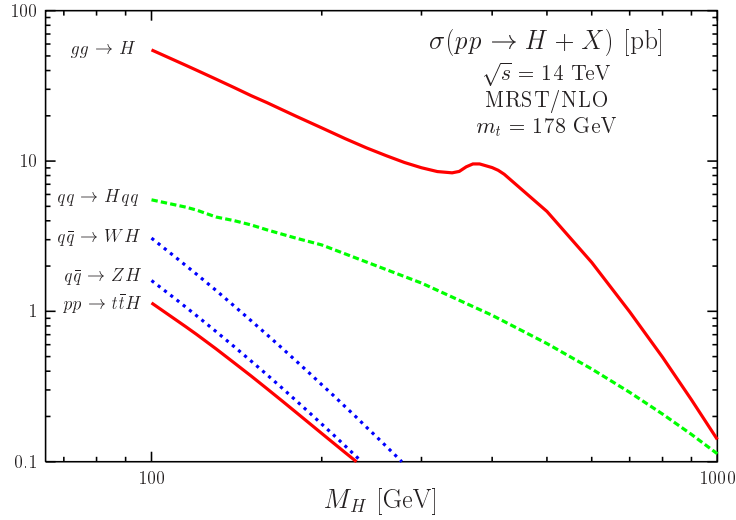


Figure 1.5: Cross sections of the dominate Standard Model Higgs boson production mode at LHC with $\sqrt{s} = 14$ TeV

when the vector boson decays leptonically. It appears that in the large majority of cases at least one lepton is isolated with a large transverse momentum in the final state.

1.2.8 Higgs Decays

With a fixed Higgs mass, all the couplings of the Higgs boson to all the particles of the Standard Model are known. The Higgs decay width Γ is directly related to these coupling factors. The values for g_{HVV} and g_{Hff} are proportional to the masses of the particles involved, the Higgs boson will decay in most of cases to heavy particles such as W^\pm , Z^0 , quarks t and b , τ^- and μ^- . Nevertheless there are final states with pair of photons or gluons, produced through heavy particle loops. The partial decay widths at the first order are presented in this subsection.

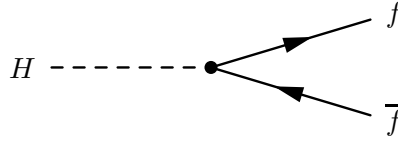
Fermionic Decays

In the Born approximation, the partial width of the Higgs decaying into two fermions is given by:

$$\Gamma_{Born}(H \rightarrow f\bar{f}) = \frac{G_F N_C}{4\sqrt{2}\pi} m_H m_f^2 \beta_f^3 \quad (1.49)$$

where $\beta_f = \sqrt{1 - 4m_f^2/m_H^2}$ and N_C is the colour factor ($N_C = 3$ or 1 , respectively for the quarks or the leptons). Γ is strongly suppressed for $m_H < 2m_f$ because the β term is not defined under this limit. This means that a decay $H \rightarrow t\bar{t}$ is not expected below $m_H = 350$ GeV/ c^2 . This also leads to the conclusion that largest contributions to leptonic decay of Higgs ($m_H < 350$ GeV/ c^2) are through the $b\bar{b}$, $\tau^-\tau^+$, $c\bar{c}$, $s\bar{s}$ and $\mu^-\mu^+$ ordered with respect to their relative couplings to the Higgs boson.

For the quark decay channels, QCD corrections, due to higher order process, have been taken into account for the calculation of the partial width. These corrections could be important for the light quarks channels.

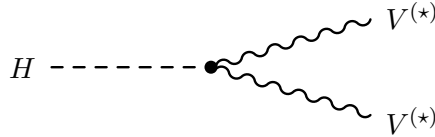
Figure 1.6: Feynman diagram of $H \rightarrow f\bar{f}$

Vector Boson Decays

The first approximation of the partial width of the Higgs decaying into real pairs of gauge bosons ($VV = W^+W^-$ or Z^0Z^0) is given by:

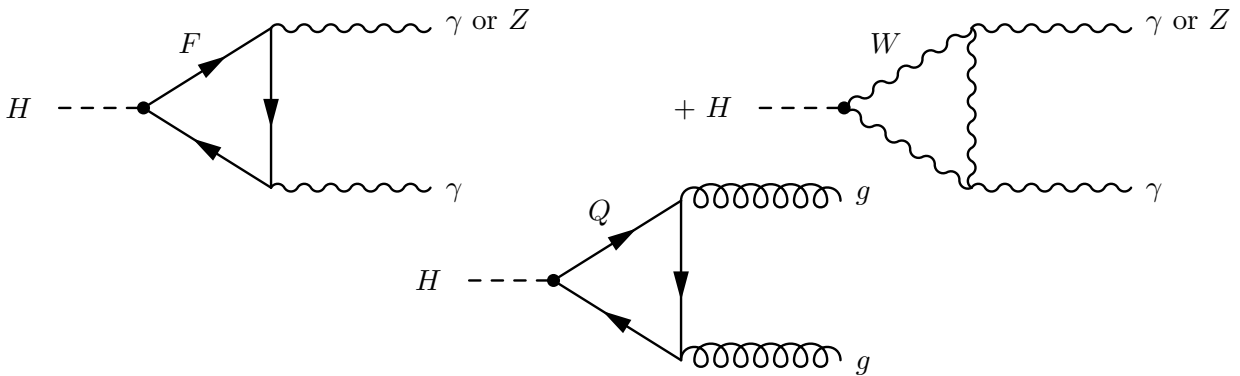
$$\Gamma(H \rightarrow VV) = \frac{G_F m_H^3}{16\sqrt{2}\pi} \delta_V \sqrt{1 - 4x_V} (1 - 4x_V + 12x_V^2) \quad (1.50)$$

where $x_V = m_V^2/m_H^2$ and $\delta_V = \delta_{Z,W} = 1, 2$

Figure 1.7: Feynman diagram of $H \rightarrow VV, VV^*$ or V^*V^*

The terms in m_H^3 imply that for $m_V^2 > m_H^2$, the Higgs decay into vector boson dominates the fermionic decays. These channels are almost suppressed for light Higgs but because the vector boson could be off-shell (virtual gauge bosons), the branching ratio is not vanishing.

Loop-induced Decays into $\gamma\gamma$, γZ^0 and gg

Figure 1.8: Feynman diagram of $H \rightarrow \gamma\gamma, \gamma Z^0$ or gg

The Higgs boson does not couple to massless particles, therefore these decay modes are induced by heavy particles (W^\pm or heavy fermions). For example, in the high-order QCD correction for the quark-loop calculation, the partial width of the Higgs decaying into two photons is:

$$\Gamma(H \rightarrow \gamma\gamma) = \frac{G_F \alpha^2 m_H^3}{128 \sqrt{2} \pi^3} \cdot \left| \sum_i N_C e_i^2 F_i \right|^2, \quad (1.51)$$

where N_C is the number of active flavours, and F_i is a function of the form factor for the fermions and the gauge bosons, W^\pm , in which the terms m_f^2/m_H^2 or m_W^2/m_H^2 are involved. The complicated partial width calculation can be approximated for Higgs mass $m_H \ll 160 \text{ GeV}/c^2$ to:

$$\Gamma(H \rightarrow \gamma\gamma) = \frac{G_F \alpha^2 m_H^3}{128 \sqrt{2} \pi^3} \cdot \left(\frac{4}{3} N_C e_t^2 - 7 \right)^2. \quad (1.52)$$

The value of $\Gamma(H \rightarrow \gamma\gamma)$ is always lower ($\sim 0.3\%$) for the Higgs mass region $[80, 160] \text{ GeV}/c^2$, but this channel has the advantage of a very clear signature with the two back-to-back photon in the final state. The partial width $\Gamma(H \rightarrow \gamma Z^0)$ is not discussed here.

The first order calculation of the partial width $\Gamma(H \rightarrow gg)$ is:

$$\Gamma(H \rightarrow gg) = \frac{G_F \alpha_s^2 m_H^3}{36 \sqrt{2} \pi^3} \cdot \left| \sum_q F_q \right|^2, \quad (1.53)$$

where F_q is also a function of the form factor for the quarks in which the term m_q^2/m_H^2 is involved. This calculation can be approximated for Higgs mass $m_H \ll 160 \text{ GeV}/c^2$ to:

$$\Gamma(H \rightarrow gg) = \frac{G_F \alpha_s^2 m_H^3}{36 \sqrt{2} \pi^3} \cdot \left(1 + \left(\frac{95}{4} - \frac{7N_F}{6} \right) \frac{\alpha_S}{\pi} \right). \quad (1.54)$$

Even if the branching ratio is about 40 times larger than that of the two photon decay, this channel is less interesting due to the less clean signature (jets in the final states coming from the decay but also from the hadronic collision). This partial width is significantly increased ($\sim 65\%$) when QCD corrections taking into account the ggg and $gg\bar{q}$ final states are applied.

Branching Ratios and Total Decay Width

The global picture of the branching ratios (Figure 1.9 (left)) can be divided into three ranges. The light Higgs mass region ($m_H < 130 \text{ GeV}/c^2$) is dominated by the fermionic decays in which the decay $H \rightarrow b\bar{b}$ predominates with a branching ratio between 50% and 75%. This mode gets a reduced cross section of $\sigma_{\text{red}} = \sigma[pp \rightarrow H(+X) \rightarrow b\bar{b}(+X)] \approx 20 \text{ pb}$ while the QCD background has a cross section of $\sigma[pp \rightarrow b\bar{b}(+X)] \approx 500 \mu\text{b}$. The rare photonic decay reaches its maximum ($\sim 0.2\%$) for a Higgs mass around $120 \text{ GeV}/c^2$, but has a clear signature. The decays into two gauge bosons in the light region is not negligible, due to the possibility to have one or two virtual vector bosons. Therefore, the sum of branching ratios of these modes is about 30% for $m_H < 130 \text{ GeV}/c^2$.

In the intermediate mass region ($130 \text{ GeV}/c^2 < m_H < 180 \text{ GeV}/c^2$), the vector boson decays are strongly dominant, while the $b\bar{b}$ part is reduced to less than a percent. The W^+W^- decay is predominant between its mass threshold production, when the energy is sufficient to create two W^\pm vector bosons, and the Z^0Z^0 mass threshold (i.e. $2m_{W^\pm} < m_H < 2m_{Z^0}$). The partial width for this modes gets up to 95%.

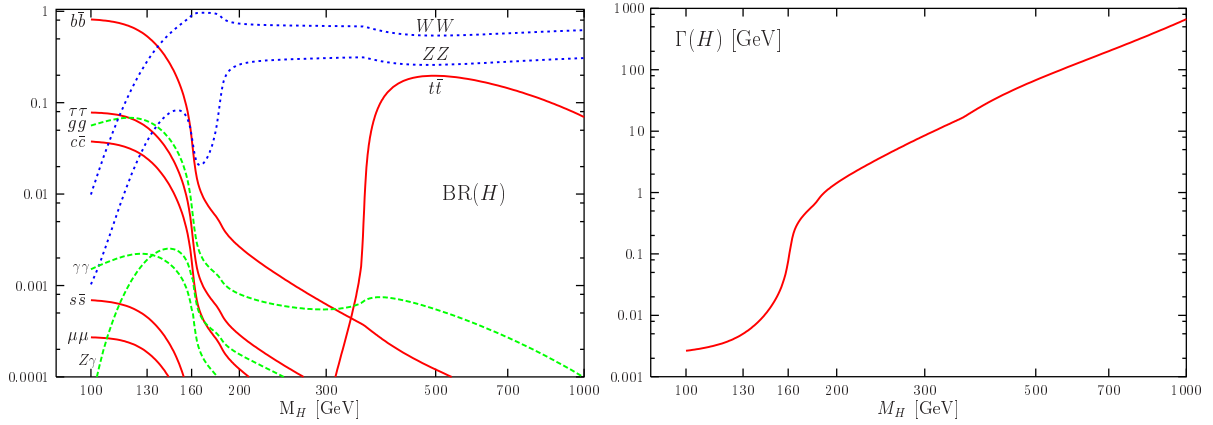


Figure 1.9: Branching ratios of the Higgs decay mode ($BR(H \rightarrow X)$) as a function of its mass (left). The total decay width of the Higgs boson as a function of its mass (right).

Finally, the heavy Higgs mass range ($m_H > 180 \text{ GeV}/c^2$) is also strongly dominated by the vector boson decays (with $\sim 70\%$ of W^+W^- and 30% of Z^0Z^0). This is the case until a Higgs mass of $\sim 400 \text{ GeV}/c^2$, where the decay into a $t\bar{t}$ pair begins to contribute significantly. For a Higgs mass of $\sim 500 \text{ GeV}/c^2$, the ratios are $\sim 55\%$ for W^+W^- , 25% for Z^0Z^0 and 20% for $t\bar{t}$.

The total width of the Higgs decay as a function of its mass is also represented in Figure 1.9 (right). The main contribution to a Higgs mass below $130 \text{ GeV}/c^2$ is the $b\bar{b}$ channel and the Higgs boson total width is very narrow $\Gamma_H < 10 \text{ MeV}$. The total width quickly becomes wider, when the two vector bosons (real or virtual) channels are kinematically available, reaching $\sim 1 \text{ GeV}$. The width is dominated by the $t\bar{t}$ channel above a Higgs mass of $\sim 400 \text{ GeV}/c^2$ and is larger than about 10 GeV . In this high Higgs mass range, its width becomes comparable to its mass due to the longitudinal contributions in the decays $H \rightarrow W^+W^-, Z^0Z^0$.

1.2.9 Constraints on the Higgs Mass

It has been shown that the Higgs boson mass is given by:

$$m_H = v\sqrt{2\lambda} = \sqrt{-2\mu^2}. \quad (1.55)$$

This mass cannot be predicted due to the lack of information. The parameter λ is the last unknown parameter of the Standard Model. It has been shown that all the couplings are fixed by the particle masses which have been determined experimentally. Therefore, the determination of the Higgs mass has been constrained by theories and experiments (direct or indirect searches).

Theoretical Constraints on the Higgs Mass

The theoretical constraints on the Higgs mass are the following:

- *Violation of unitarity:* The renormalisation of the quantum field theories guarantees that the calculation could be solved in a perturbative theory. This means that for a fixed energy range, all the terms stay bound. Some divergences could appear at much higher energies than the Fermi scale, as for the scattering process $W^+W^- \rightarrow W^+W^-$, which could lead to cross sections increasing with the energy. In this case the divergence is due to the longitudinal component of the charged vector boson. Therefore the upper bound to guarantee the unitarity in [17] is:

$$m_H \lesssim 870 \text{ GeV}. \quad (1.56)$$

- *Triviality bound:* The triviality bound is based on the fact that the Higgs self-interaction coupling constants should be upper-bounded. When the energy is much higher than the weak scale, the quadratic coupling g_{HHHH} grows and could become infinite. The energy at which the coupling becomes infinite, called the Landau pole, is:

$$\Lambda_C = v \exp \left(\frac{4\pi^2 v^2}{m_H^2} \right). \quad (1.57)$$

Hence, to have a theory that remains perturbative and renormalisable, the energy scale (in which the SM is valid) must be lower than the energy cut-off Λ_C

- *Stability bound:* The stability of the electroweak vacuum is guaranteed by the existence of a minimal value of the potential $V(\Phi)$. The consideration of processes of higher order, such as a top quark loop contribution, could lead to a non-physical value of $\lambda < 0$ (equation 1.29).

The triviality and stability bounds are summarised and combined in Figure 1.10 [18]. It shows that the electroweak theory is valid for any Higgs mass, constrained on these two concepts, up to the energy of the Landau pole of $\Lambda_C \sim 1 \text{ TeV}$. The Higgs mass is significantly constrained when Λ_C reaches the Grand Unification Theory (GUT) scale ($\Lambda_C = \Lambda_{GUT} \sim 10^{16} \text{ GeV}$). In this case the Higgs mass has to be between 130 and 180 GeV/c^2 .

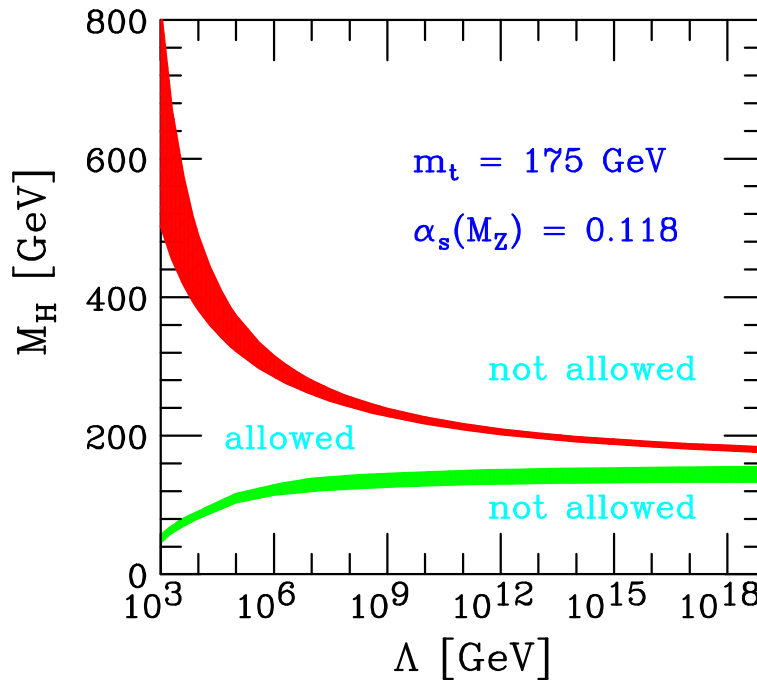


Figure 1.10: Upper limit (Triviality) and lower limit (Stability) on the Higgs mass as a function of the Landau pole Λ_C energy (energy cut-off).

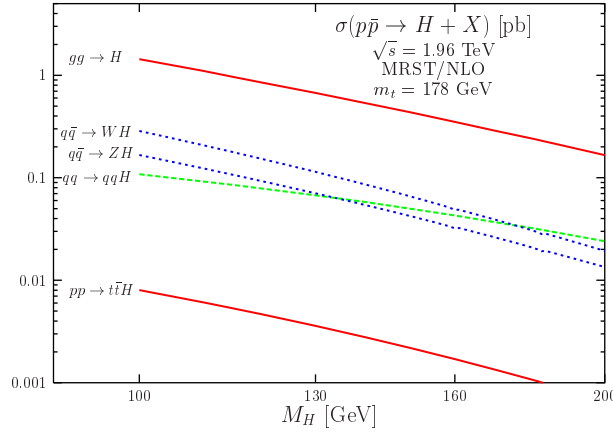


Figure 1.11: The Higgs production cross section for an energy of $\sqrt{s} = 1.96$ GeV at hadron colliders.

Experimental Constraints on the Higgs Mass

On the other hand, the experimental limits on the Higgs mass are based on the results of the LEP and SLD electronic collider experiments, and of the Tevatron hadronic collider.

- Direct Searches at LEP-II:

The dominant Higgs production mechanism at the LEP-II energy is Higgs-strahlung which is a Higgs produced in association with a vector boson Z^0 : $e^-e^+ \rightarrow Z^{0*} \rightarrow HZ^0$.

The Higgs boson was searched in four different final state topologies:

- Final states with four jets: $H \rightarrow b\bar{b}$ and $Z^0 \rightarrow q\bar{q}$,
- Final states with τ leptons: $H \rightarrow \tau^-\tau^+$ and $Z^0 \rightarrow q\bar{q}$, or $H \rightarrow b\bar{b}$ and $Z^0 \rightarrow \tau^-\tau^+$,
- Final states with missing energy: $H \rightarrow b\bar{b}$ and $Z^0 \rightarrow \nu\bar{\nu}$,
- Leptonic final states : $H \rightarrow b\bar{b}$ and $Z^0 \rightarrow e^-e^+$ or $\mu^-\mu^+$.

The main backgrounds are: $e^-e^+ \rightarrow Z^{0*} \rightarrow q\bar{q}\ell^+\ell^-$ which has a production cross section of 100 pb, final states in $Z^0\gamma$ (~ 10 pb), final states in W^+W^- (~ 20 pb) and Z^0Z^0 (~ 10 pb). The sum of the cross section of these modes is higher than that of Higgs production.

The combined results of the four experiments based at the LEP accelerator have not shown any significant excess, which could be explained by Higgs production above the expected background [19], but they have excluded a Higgs mass below 114.4 GeV/ c^2 at 95% CL.

- Direct Searches at Tevatron:

The dominant Higgs production mechanism at the Tevatron accelerator are gluon fusion $gg \rightarrow H$ and the vector boson associated production $W^\pm H$ or $Z^0 H$. The Higgs production cross section at the RUN-II Tevatron energy of $\sqrt{s} = 1.96$ GeV is presented in Figure 1.11. For a Higgs mass $m_H < 135$ GeV/ c^2 , the searches are based on associated production with the following final states:

- $q\bar{q} \rightarrow W^\pm H \rightarrow \ell\nu b\bar{b}$,
- $q\bar{q} \rightarrow Z^0 H \rightarrow \nu\bar{\nu} b\bar{b}$: characterised by a missing transverse energy and two b -jets,

- $q\bar{q} \rightarrow Z^0 H \rightarrow \ell^+ \ell^- b\bar{b}$: this channel has less background but also a lower branching ratio.

For a heavier Higgs ($m_H > 135 \text{ GeV}/c^2$), direct production with gluon fusion is more efficient and the most sensitive decay channel is:

- $gg \rightarrow H \rightarrow W^+ W^-$, with the leptonic decay of the vector bosons.

For intermediate masses it is possible to use the channel:

- $q\bar{q} \rightarrow W^\pm H \rightarrow W^\pm W^+ W^-$.

Finally, other channels have been used to increase the general sensitivity, such as: $H \rightarrow \gamma\gamma$, $W^\pm H \rightarrow \tau\nu b\bar{b}$, $VH \rightarrow \tau\tau b\bar{b}/\tau\tau jj$, $VH \rightarrow b\bar{b}jj$ and $t\bar{t}H \rightarrow t\bar{t}b\bar{b}$.

The combined CDF and DØ results, published on November 16, 2009 [20], on direct searches for a SM Higgs boson based on $2.0 - 4.8 \text{ fb}^{-1}$ of data analysed at CDF, and $2.1 - 5.4 \text{ fb}^{-1}$ at DØ, sets the 95% C.L. upper limits on Higgs boson production at a factor of 2.70 (0.94) times the SM cross section for a Higgs boson mass of $m_H = 115(165) \text{ GeV}/c^2$ (Figure 1.12). The corresponding median upper limits expected in the absence of Higgs boson production are 1.78 (0.89). The collaboration of the two experiments also sets the exclusion mass range at 95% C.L. for a SM Higgs mass in the interval $163 < m_H < 166 \text{ GeV}/c^2$, with an expected exclusion of the range $159 < m_H < 168 \text{ GeV}/c^2$ (Figure 1.13).

- Indirect Searches:

Several parameters of the Standard Model are affected by the Higgs Mass. With these parameters, all the observables of the Standard Model can be calculated and compared to

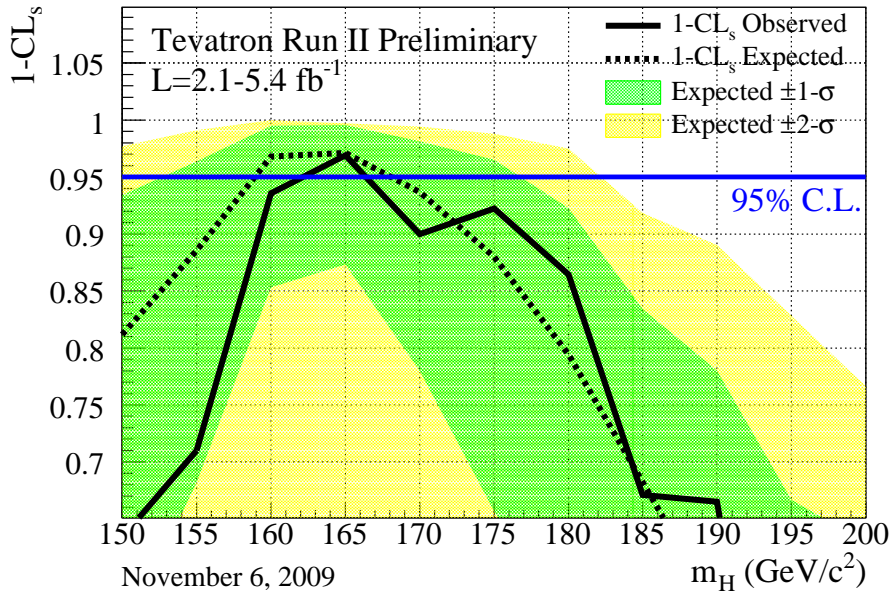


Figure 1.12: $1 - CL_s$ distribution as a function of the Higgs Mass in the combined analyses of CDF and DØ [20]

the experimental results. The experiments at LEP-II and at SLC, followed by the measurements on the vector boson W^\pm and on the top quark at CDF and DØ, have reached a considerable level of precision which permits testing of all the predictions, especially the radiative corrections. The radiative correction on the vector boson system takes into account the QCD corrections for the final quark states, the QED corrections on the radiative photon on the initial and final states and the Electroweak radiative corrections on the gauge boson propagator, or on its decay vertex. The Higgs couplings take part in the ElectroWeak radiative corrections on the W^\pm or Z^0 propagator (Figure 1.14). The comparison of these predicted corrections to the high precision measurements constrains indirectly the Higgs mass.

The dependency of the Higgs mass with respect to the W^\pm and t masses is relatively important (Figure 1.15). The dependency on the hadronic contribution of $\alpha_{\text{had}}(m_Z^2)$ is also high (represented by $\Delta\alpha_{\text{had}}$ in Figure 1.16).

Supposing that the Standard Model is valid, the LEP Electroweak Working Group [20, 21] compiled all the experimental results from the different experiments to adjust the Higgs mass. Figure 1.16 shows $\Delta\chi^2 = \chi^2 - \chi_{\text{min}}^2$ versus the Higgs mass. The value for the Higgs

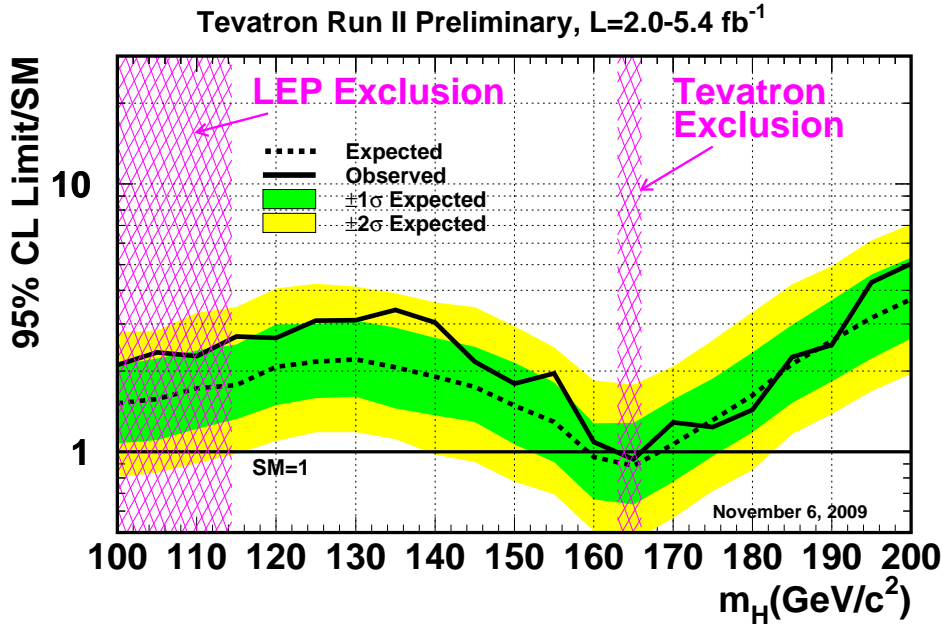


Figure 1.13: Observed and expected (median, for the background-only hypothesis) 95% C.L. upper limits on the ratios to the SM cross section, as functions of the Higgs boson mass for the combined CDF and DØ analyses. The limits are expressed as a multiple of the SM prediction for test masses (every 5 GeV/c^2) for which both experiments have performed dedicated searches in different channels. The points are joined by straight lines for better readability. The bands indicate the 68% and 95% probability regions where the limits can fluctuate, in the absence of signal. The limits displayed in this figure are obtained with the Bayesian calculation [20].

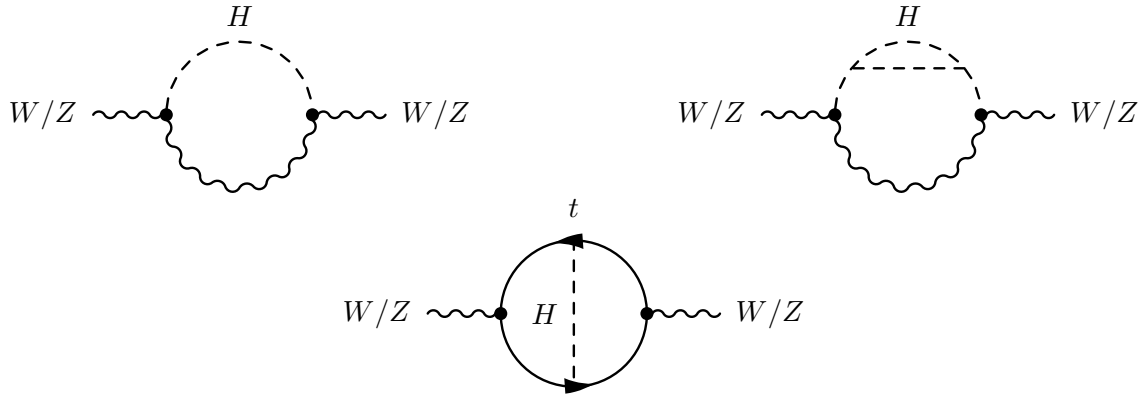


Figure 1.14: Higgs bosons contribution to the Electroweak radiative corrections

mass, which corresponds to the minimal $\Delta\chi^2$, is:

$$m_H = 87^{+35}_{-26} \text{ GeV}/c^2 \quad (1.58)$$

where the errors are for 68% C.L. This value is tied to the measure of the top mass (and its uncertainty). The upper limit obtained at 95% C.L. is $m_H < 157 \text{ GeV}/c^2$ (including theoretical and experimental uncertainties) which is less affected by the dependency on m_t . This limit grows to $m_H < 191 \text{ GeV}/c^2$ at 95% C.L. when the direct searches at LEP-II are included. Due to a statistical reason, the 95% C.L. are also pushed to the right.

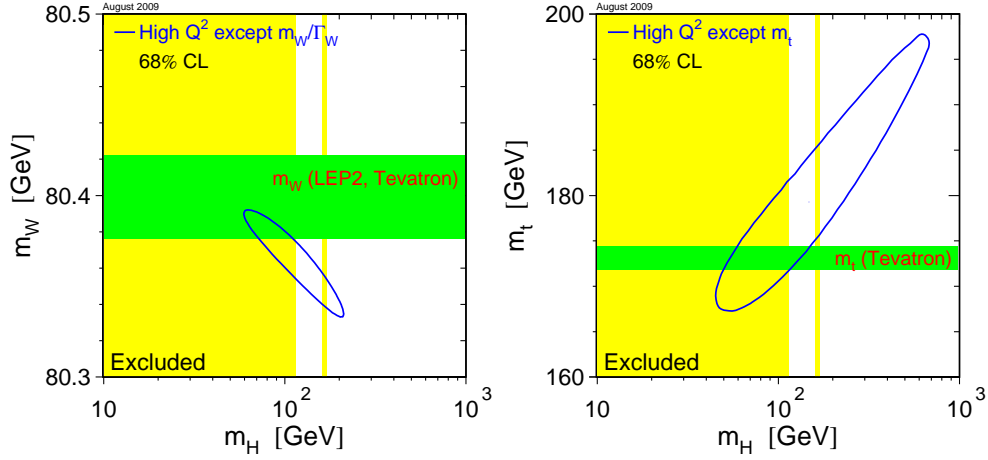


Figure 1.15: The 68% C.L. contour in m_W (left) (or m_t (right)) and m_H for the fit to all data except the direct measurement of m_W (or m_t), indicated by the shaded horizontal band of ± 1 sigma width. The vertical bands show the 95% C.L. exclusion limit on m_H from the direct searches at LEP-II (up to 114 GeV/c²) and the Tevatron (from 159 GeV/c² to 168 GeV/c²) [20].

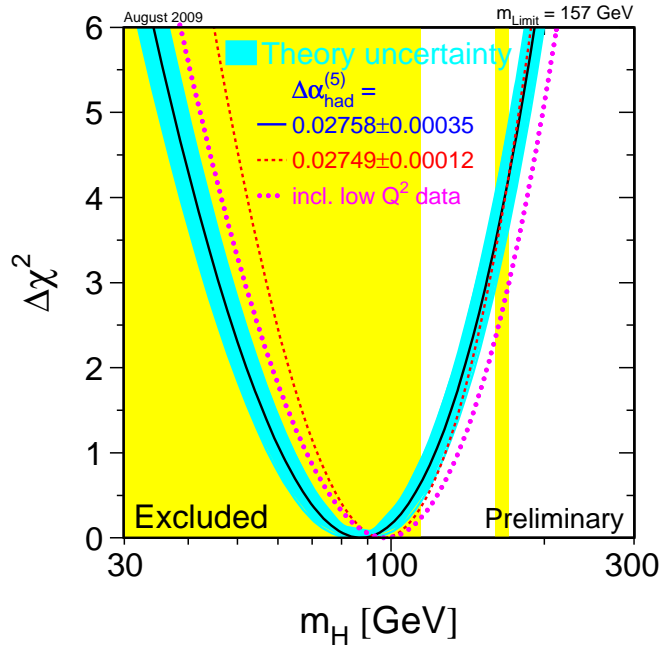


Figure 1.16: $\Delta\chi^2 = \chi^2 - \chi_{min}^2$ vs. m_H curve. The line is the result of the fit using all electroweak data from the LEP, SLD, CDF and DØ experiments [22], while the vertical bands show the 95% C.L. exclusion limit on m_H from the direct searches at LEP-II (up to 114 GeV/c²) and the Tevatron (from 159 GeV/c² to 168 GeV/c²) [20].

2

CERN and the LHC



CERN, the European Organisation for Nuclear Research, is one of the worlds largest centre for scientific research the studies are on the fundamental physics, finding out what the Universe is made of and how it works. Founded in 1954, the CERN Laboratory sits on the Franco-Swiss border near Geneva. It was one of Europes first joint ventures and 20 member states contains to it. In 2009 the most powerful accelerator has begun its commissioning and with it, the new experiments have started to record collisions.

2.1 The European Organisation for Nuclear Research CERN

CERN is the European Organisation for Nuclear Research. The name is derived from the french acronym for Conseil Européen pour la Recherche Nucléaire, or European Council for Nuclear Research. The Organisation officially came into being in 1954, when at that time, pure physics research concentrated on understanding the inside of the atom, hence the word “nuclear”.

Our actual understanding of matter goes much deeper than the nucleus, and CERN’s main area of research is particle physics. Therefore CERN is commonly referred to as the European Laboratory for Particle Physics.

In the convention that CERN established in 1954, CERN’s main missions are stated:

The Organisation shall provide for collaboration among European States in nuclear research of a pure scientific and fundamental character (...). The Organisation shall have no concern with work for military requirements and the results of its experimental and theoretical work shall be published or otherwise made generally available.

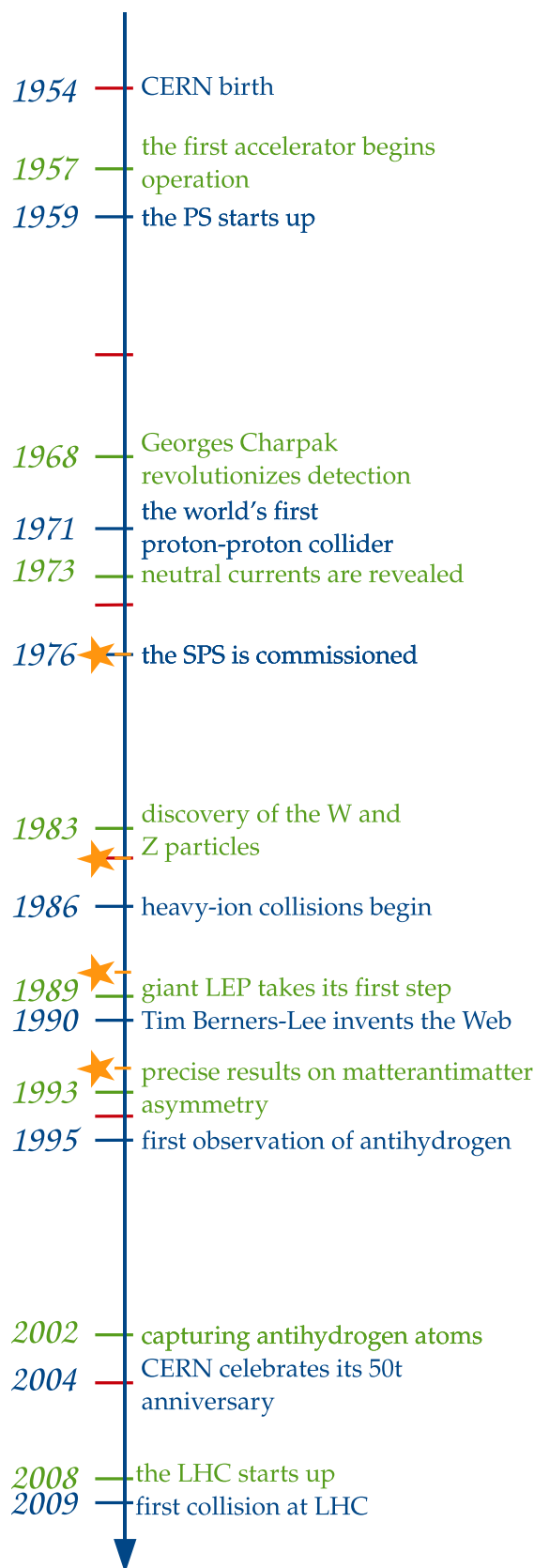


Figure 2.1: CERN History highlights, yellow ★ are the Nobel Prizes

CERN is driven by an international community, it was formed with 12 member states, but now CERN is run by 20 European Member States and non-European countries are also involved in different ways. CERN employs around 2'500 people, scientific and technical staff. 8'000 visiting researchers, which represent half of the world's particle physicists, are also working with the CERN facilities. These scientists represent a large community of 85 different nationalities and coming from 580 universities.

CERN's greatest achievements (the highlights are presented in figure 2.1) are the construction of great colliders such as: the first proton-proton collider, the *Intersecting Storage Rings* (ISR) commissioned in 1971; the first proton-antiproton collider, *Super Proton Synchrotron* (SPS) that lead to the discovery of the W^\pm and Z^0 bosons; the *Large Electron Positron* (LEP) collider takes its first step in 1989; and finally the *Large Hadron Collider* era started in 2008. All these colliders have guided the research and great discoveries made at CERN such as the neutral current in the weak interaction. But also in 1989-90, Tim Berners-Lee, a scientist at CERN, invented the World Wide Web which was developed to the demand for automatic information sharing between scientists working in different universities and institutes all over the world.

During the history of CERN, several Nobel Prizes in physics have been awarded to scientists working at the facilities (the received dates are represented by the yellow ★ in figure 2.1).

In 1976, the Large ElectronPositron Collider (LEP) experiment L3 spokesman Sam Ting, with Burt Richter, received the Nobel “for their pioneering work in the discovery of a heavy elementary particle of a new kind”. The charmonium ($c\bar{c}$) particle J/ψ was discovered two years before, but not at CERN.

In 1984, just one year after the discovery of the W^\pm and Z bosons, Carlo Rubbia and Simon Van de Meer received the Prizes for “their decisive contributions to the large project which led to the discovery of the field particles W and Z , communicators of the weak interaction”. The experimental results confirmed the unification of weak and electromagnetic forces, the elec-

troweak theory of the Standard Model.

Jack Steinberger received the Nobel in 1988 with Leon Lederman and Mel Schwartz, “*for the neutrino beam method and the demonstration of the doublet structure of the leptons through the discovery of the muon neutrino*”. It was at this time at the head of the ALEPH experiment, but the discovery that led to the Nobel Prize was made in 1962 at the US Brookhaven National Laboratory and showed that there was more than one type of neutrino.

And finally, Georges Charpak, a CERN physicist since 1959, received the Nobel Prizes the 1992 Nobel Prize of physics for “*his invention and development of particle detectors, in particular the multiwire proportional chamber, a breakthrough in the technique for exploring the innermost parts of matter*”. Charpak invented in 1968 the multiwire proportional chamber.

It can also be noted that the first Director-General, Felix Bloch, was awarded the 1952 Nobel prize with Edward Mills Purcell, “*for their development of new methods for nuclear magnetic precision measurements and discoveries in connection therewith*”.

2.2 The LHC Machine

The Large Hadron Collider (LHC) at CERN is the most power tool for particle physics studies. The LHC project was approved by the CERN Council in December 1994 and decided to replace the LEP machine. It was decided to install the LHC in the existing 26.659 km tunnel houses the LEP ring between 1989 and 2001. The tunnel has eight straight sections and eight arcs and lies about 100 m below the surface of earth on a plane inclined at 1.4%.

The aim of the LHC and its experiments (section 2.3) is to test or reveal the physics beyond the Standard Model. In order to achieve theses tests, it was decided that the LHC machine would accelerate protons to a centre of mass collision energies of 14 TeV.

The nominal number of events (collisions) that the LHC machine generates per second is given by:

$$N_{\text{event}} = \mathcal{L} \cdot \sigma_{\text{event}}, \quad (2.1)$$

where σ_{event} is the cross section of the event studied and \mathcal{L} the luminosity which depends only on the machine parameter and is given by:

$$\mathcal{L} = \frac{N_b^2 n_b f_{\text{rev}}}{F} [\text{cm}^{-2} \text{s}^{-1}], \quad (2.2)$$

where N_b is the number of particles per bunch, n_b the number of bunches per beam, f_{rev} the revolution frequency and F is a factor which includes all the geometrical and beams parameters.

The ATLAS and CMS experiments (see section 2.3) are designed to run with a high luminosity peak of $\mathcal{L}_{\text{LHC}} = 10^{34} \text{cm}^{-2} \text{s}^{-1}$, while the LHCb experiment (see section 2.3) will have a nominal luminosity of $\mathcal{L}_{\text{LHCb}} = 2 \cdot 10^{32} \text{cm}^{-2} \text{s}^{-1}$ which gives predominantly a single interaction per bunch crossing.

The high beam energy and intensity required for a peak luminosity of $\mathcal{L}_{\text{LHC}} = 10^{34} \text{cm}^{-2} \text{s}^{-1}$ has guided the choice of a proton-proton (pp) collider. The easiest configuration of a proton-anti-proton ($p\bar{p}$) collider with common vacuum and magnet systems for both circulating beams was excluded, because the production of anti-proton could not be sufficient to achieve the goal, the LHC collides pp . Two counter-rotating proton beams require opposite magnetic dipole fields in both ring. Therefore the LHC machine is designed with separated magnet fields and vacuum chamber in the main portion of the rings (figure 2.2).

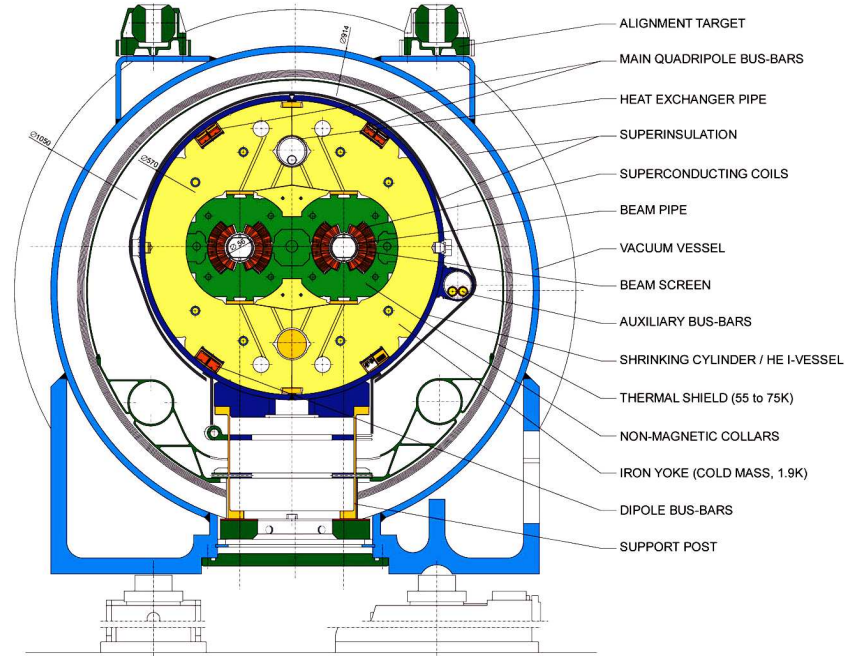


Figure 2.2: Cross-section of a LHC superconducting cryodipole [23, 24].

This high peak luminosity is reached through an important number of bunches per beam, $n_b = 2808$, a high rate of revolution per second $f_{\text{rev}} = 11245$ Hz, and finally a large number of protons per bunch $N_b = 1.1 \times 10^{11}$. The frequency combined to the number of bunch gives a minimal distance of about ~ 7 m between bunches, and the time between two bunch crossing is 25 ns. The compilation of all these value give the high luminosity and, a bunch crossing of 40 MHz and a colliding rate of about 600 MHz.

2.2.1 Accelerator and Energy

The LHC is the last step of a chain of accelerators (figure 2.3) which brings the protons up to a kinetic energy of 7 TeV. The protons are produced at 100 keV by an ion source, and they get a first acceleration by the *LINEar ACcelerator 2* (LINAC 2) up to an energy of 50 MeV. They are injected in the *PSBooster* which is a small synchrotron that raises the energy to 1 GeV. The protons are then boosted in the *Proton Synchrotron* (PS) to 26 GeV before they enter a third accelerator, the *Super Proton Synchrotron* (SPS), which accelerates the protons to 450 GeV. At this step the proton beam is separated in two parts to be injected in a counter-rotating configuration in the LHC. The energy of 7 TeV per proton is reached in the LHC itself.

The peak energy depends strongly on the fields applied in the dipole to bend the trajectory of the proton. In order to keep a beam of 7 TeV protons along the circular portion of the LHC accelerator, the use of superconducting dipoles (figures 2.2) must supply a magnetic field of 8.3 T. This is only feasible using superconducting electromagnets. The magnets used need to be cooled down to a temperature of 1.9 K.

The total beam current of 0.584 A corresponds to a stored energy in the beams of about 362 MJ, while the energy stored in the superconducting magnet is approximately of 600 MJ. Hence the total amount of energy, which is almost reaching the level of the GJ, has to be safely absorbed at the end of each run or in an emergency situation.

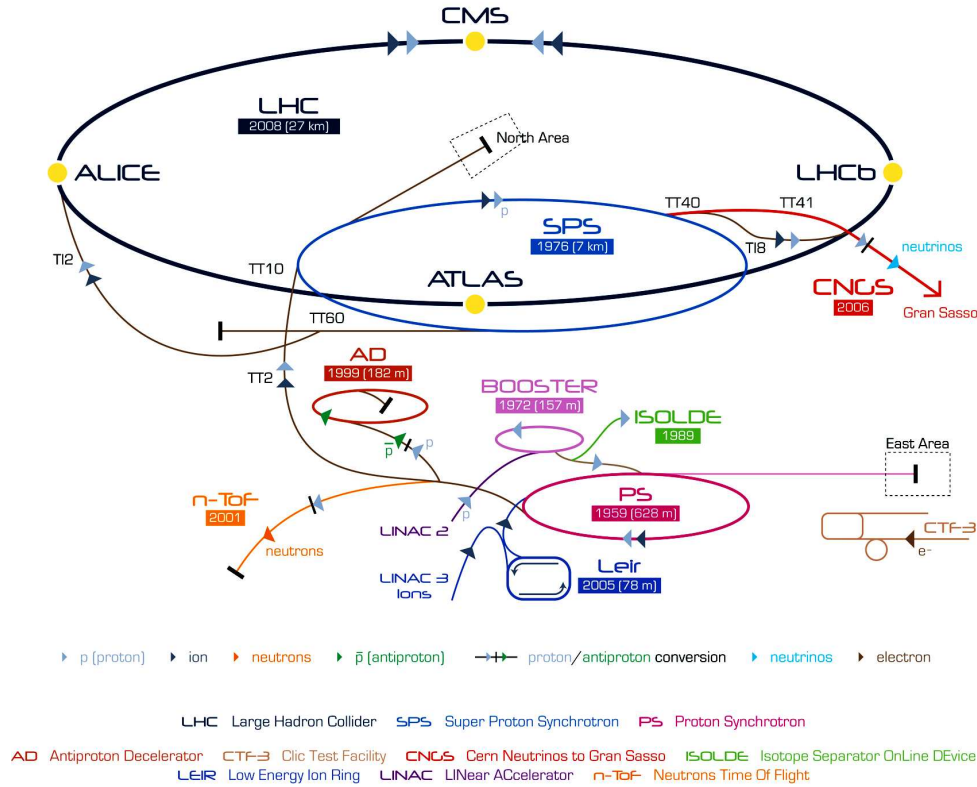


Figure 2.3: The CERN accelerator complex (not to scale) [23, 25].

Almost the same chain is used to accelerate heavy lead ions Pb^{82} to an energy of 574 TeV which corresponds to a centre of mass energy of 2.76 TeV/nucleon in $Pb - Pb$ collisions.

The two rings cross at 4 point on the tunnel, where the detectors are located.

2.3 The Experiments on the LHC

Four huge detectors (ALICE, ATLAS, CMS, LHCb) and two smaller experiments in size and staff (LHCf, TOTEM) are placed in four places on the LHC ring where the beams cross. The detectors are briefly described below:

ALICE [26]: A Large Ion Collider Experiment which is dedicated to the study of quark-gluon plasma (QGP), the state of the matter rising in heavy ions collision at high energy. One of the big challenges that the ALICE collaboration faces is the high multiplicity from the $Pb - Pb$ collisions. The figure 2.4 is a schematic view of the ALICE detector (left) and a example of simulated event $Pb - Pb$ (right).

ATLAS [27]: A Toroidal LH**C** Apparatus System is a general purpose experiment which aims to test the Standard Model at the TeV scale and to search for the Higgs boson and physics beyond the Standard Model. Figure 2.5 (left) represents ATLAS which is the biggest 4π detector built (a diameter of 25m for a length of 44m) on the LHC. It has a specific magnetic field achieves with the enormous toroidal magnets. A Higgs event within the detector is shown on the right side of the figure 2.5.

CMS [28]: The Compact Muon Solenoid detector has the same research prospect than the ATLAS experiment. CMS is built with a strong superconducting magnetic field of 4 T to collect the maximum energy from the particles. The detector contains 12'500 tonnes of material. The CMS apparatus is presented in figure 2.6 on the left with a Higgs boson event on the right.

LHCb [29]: The Large Hadron Collider beauty experiment, dedicated to the b -hadron sector, aims to study CP-violation processes and rare decays. It is a single arm forward spectrometer and is detailed in Chapter 3.

LHCf [30]: The Large Hadron Collider forward experiment is the smallest of all the LHC experiments. Its aim is to study the particles generated in the “forward” region of collisions, to verify hadronic models at very high energy for the understanding of ultra-high energetic cosmic rays. It consists of two small detectors, 140 m on either side of the ATLAS intersection point.

TOTEM [31]: The TOTEM experiment will measure the total pp cross section and study elastic scattering and diffractive dissociation at the LHC. TOTEM also aims to measure the luminosity at the CMS interaction point where it is based (figure 2.7). It covers the very forward region in the pseudo-rapidity range.

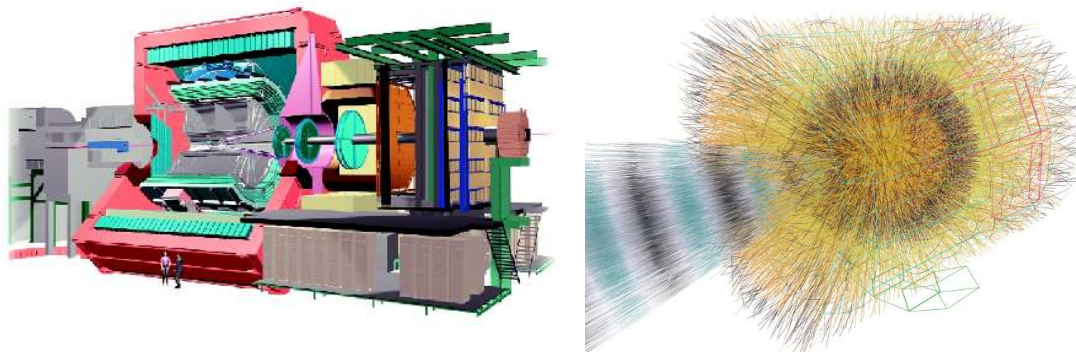


Figure 2.4: ALICE apparatus (left), simulated event ($Pb - Pb$) collision where the lines represented the particles emitted

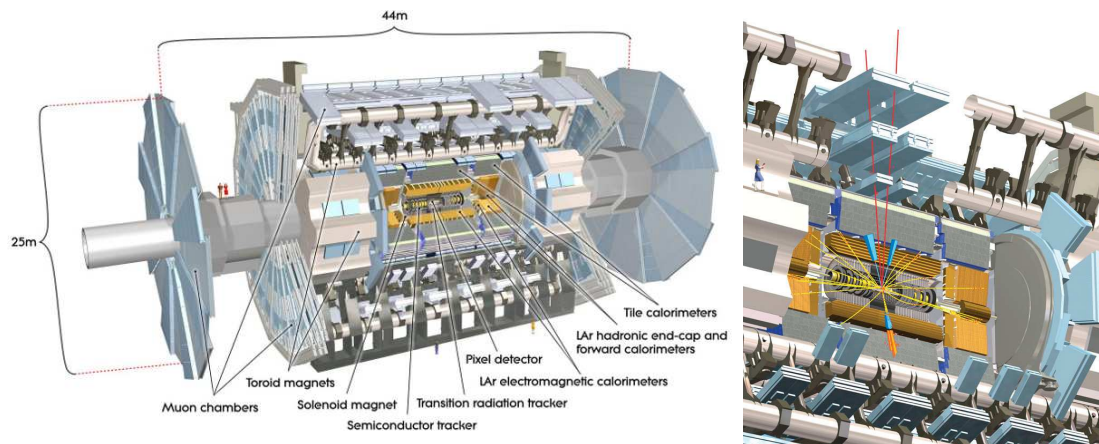


Figure 2.5: ATLAS apparatus (left), Higgs simulated event within the ATLAS detector (right)

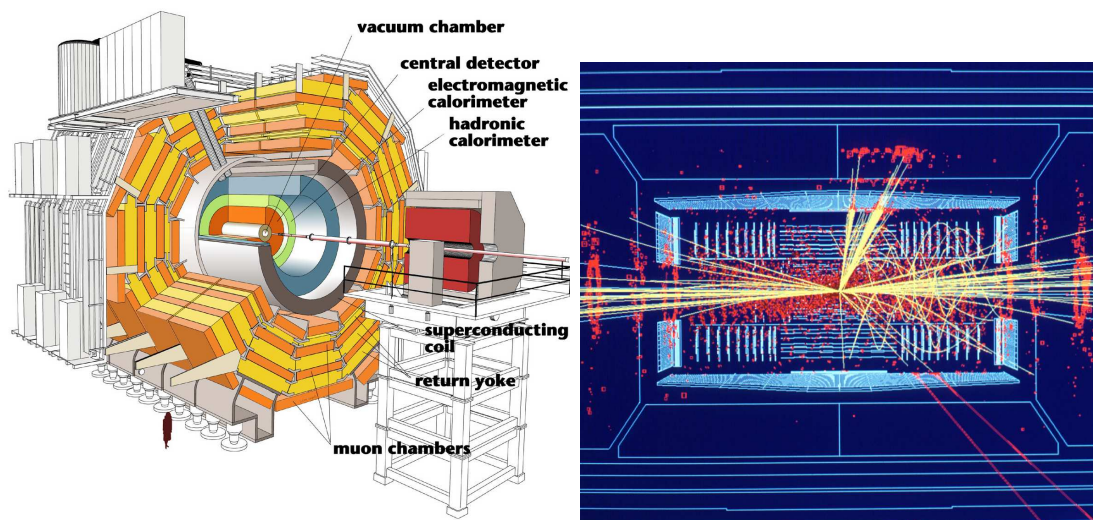


Figure 2.6: CMS apparatus (left), Higgs simulated event within the CMS detector (right)

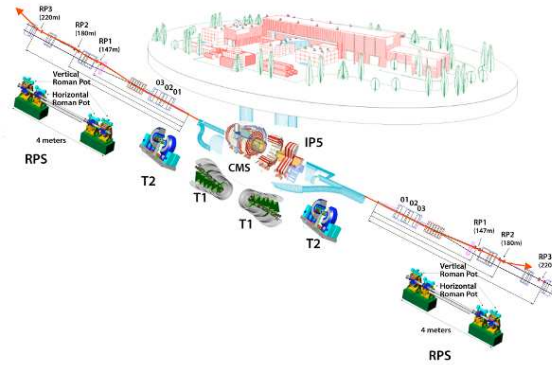


Figure 2.7: TOTEM apparatus

2.4 Computing Solutions

At full operational intensity, the LHC will produce roughly 15 Petabytes of data annually, which thousands of scientists around the world will access and analyse.

To store and analyse this huge amount of data, the use of several thousand computers is needed. The Worldwide LHC Computing Grid (WLCG) [32, 33] is a global collaboration linking grid infrastructures and computer centres worldwide that allows the distribution, storage and analysis of this immense amounts of data generated by the Large Hadron Collider.

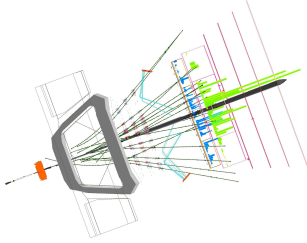
Today, the WLCG combines the computing resources of more than 100,000 processors from over 170 sites in 34 countries, producing a massive distributed computing infrastructure that provides physicists around the world with near real-time access to LHC data and the power to process it.



Figure 2.8: LHC Computing Grid Globe [34]

3

The LHCb Experiment



The Large Hadron Collider beauty experiment, LHCb, is one of the four main experiments based at CERN. It is dedicated to the b -hadron sector and aims to study CP-violation processes and rare decays. Hence LHCb has been built as a single arm forward spectrometer.

3.1 Generalities on the LHCb Detector

The LHCb experiment is installed at point 8 on the LHC accelerator (figure 2.3). It takes the place of the DELPHI detector of the LEP. The LHCb detector [29] is a single arm forward spectrometer (figure 3.1) the design was guided by two main aspects:

- the b -hadrons are produced in a large majority very narrow to the beam direction.
- a compromise between the available space in the cavern, the cost of the detector and its efficiency to detect b -hadrons.

The production of b quarks in a proton-proton collision is only available through the strong interaction. The partons, involved in the inelastic scattering of the proton-proton interaction, exchange a great part of momentum. Since the momentum exchanged increases with the centre of mass energy, the $b\bar{b}$ pairs are boosted in the direction of the most energetic parton which follows the direction of the beam. Therefore the b -hadrons coming from the $b\bar{b}$ pairs are produced in a large majority in the same cone in a forward or backward direction. The figure 3.2 shows the angular correlation between the b -hadron and the \bar{b} -hadron which are produced.

In order to simplify the research in the LHCb's analysis, matching the reconstructed b decay to the primary vertex in which it was created is required. At the nominal luminosity peak of $10^{34} \text{ cm}^{-2}\text{s}^{-1}$ the number of interactions per bunch crossing is ~ 25 . This is not useful for the LHCb experiment. Therefore the beams are slightly less focused before they reach the LHCb interaction point. As a consequence, the luminosity is adjusted to have a nominal interaction number per bunch crossing of about 1, this gives the LHCb luminosity of $\mathcal{L}_{\text{LHCb}} = 2 \times 10^{32} \text{ cm}^{-2}\text{s}^{-1}$.

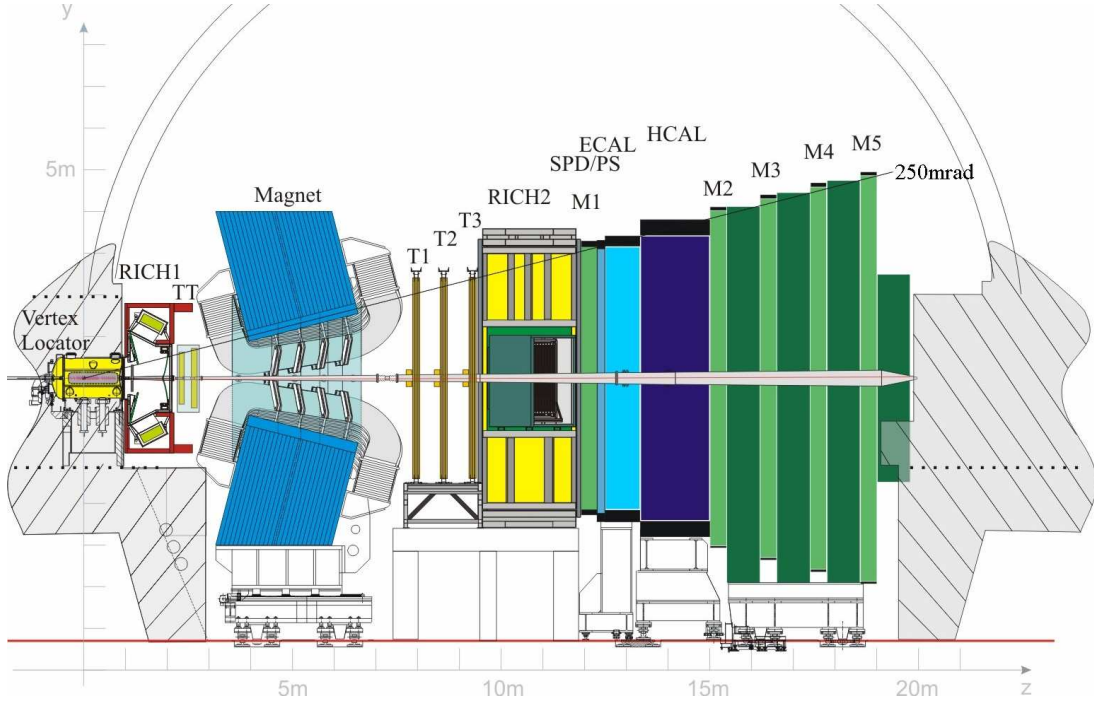


Figure 3.1: View the LHCb detector

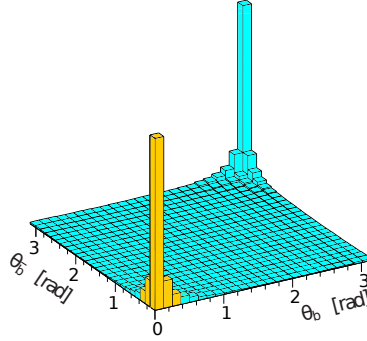
Figure 3.2: Correlation of the polar angle of the b -hadron and the \bar{b} -hadron calculated by the PYTHIA event generator. The yellow area indicates the LHCb acceptance sector.

Figure 3.3 shows the probabilities to have 0, 1, 2, 3 or 4 interaction per bunch crossing as a function of the luminosity.

The integrated luminosity over a nominal year, 10^7 seconds, at LHCb is of $\mathcal{L}_{\text{int}} = 10^7 \cdot \mathcal{L}_{\text{LHCb}} = 2 \text{ fb}^{-1}$.

The production cross section of $b\bar{b}$ in a pp collision at $\sqrt{s} = 14 \text{ TeV}$ is predicted to be between $500 \mu\text{b}$ and $1000 \mu\text{b}$ (figure 3.4). Consequently the LHCb experiment expects 10^{12} $b\bar{b}$ pairs per year, since this number is given by:

$$N_{b\bar{b}} = \mathcal{L}_{\text{int}} \times \sigma_{b\bar{b}}$$

The $b\bar{b}$ pairs will then hadronise into b -hadrons in the following ratio :39.9 % of charged B , 39.9 % of neutral B^0 , 11 % of neutral B_s^0 and b -baryons for 9.2 % [1].

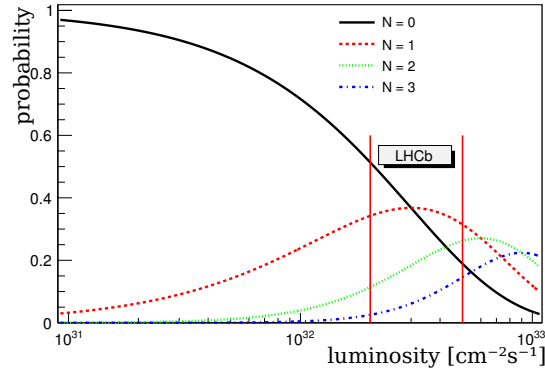


Figure 3.3: Probability to observe N interactions per bunch crossing as a function of luminosity. The LHCb luminosity region shows a probability of about one interaction.

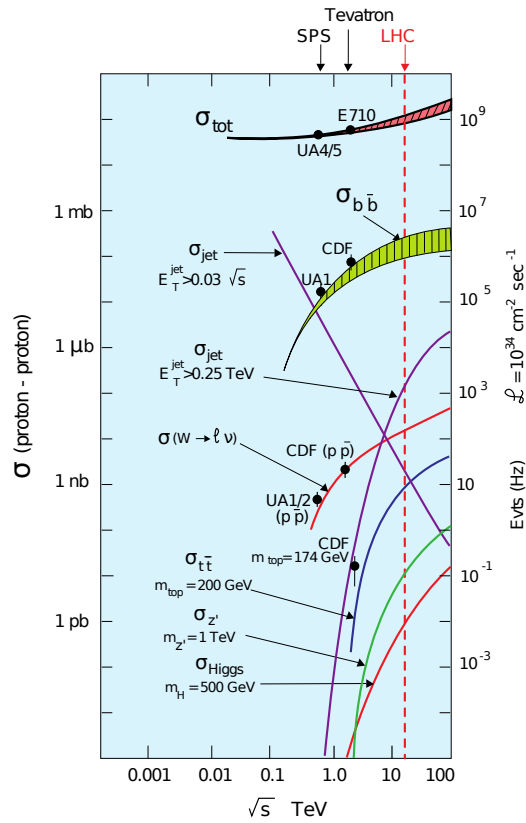


Figure 3.4: Production cross sections as a function of the centre of mass energy of proton-proton collisions. The left axis displays the inelastic cross section while the right axis displays the number of expected events for a luminosity of $10^{34} \text{ cm}^{-2} \text{ s}^{-1}$. The $b\bar{b}$ cross section has value between $500 \mu\text{b}$ and $1000 \mu\text{b}$ for the LHC centre of mass energy $\sqrt{s} = 14 \text{ TeV}$.

3.2 LHCb layout

The general layout of the LHCb detector is presented in the figure 3.1. A right-handed coordinate system is defined with its origin at the nominal interaction point, which is at one side of the detector, z axis along the beam axis, while the x and y are respectively the horizontal and vertical coordinates in the beam axis transverse plane. The detector is about 20 m long (z -axis), 12 m wide in the horizontal direction (x -axis) and 10 m high (y -axis). It has a forward angular coverage from about ± 15 mrad to ± 300 mrad. In terms of pseudo-rapidity ($\eta = -\ln \tan(\frac{\theta}{2})$) the acceptance is:

$$1.9 < \eta < 4.9 \quad (3.1)$$

The chosen design leads to an excellent spatial and proper time resolution, an admirable particle identification system, with a good separation between hadrons (π/K) and between leptons (e/μ).

The LHCb detector is composed of six sub-detectors which are grouped in three inter-depend systems: the Tracking System, the Particle Identification (PID) System and the Trigger System. The LHCb sub-detectors are:

- The Tracking System:
 - the **V**ertex **L**ocator (VeLo) [35].
 - the **T**racker **T**uricensis (TT) [36].
 - the three tracking stations (T1, T2 and T3), each is composed of a central **I**nnner Tracker station (IT) [37] surrounded by an **O**uter **T**racker station (OT) [38].
 - the Magnet [39].
- The Particle Identification System:
 - the two **R**ing and **I**maging **Č**erenkov counter (RICH1 and RICH2) [40].
 - the Calorimeters, the **S**cintillating **P**ad **D**etector and the **P**re-**S**hower detector (SPD/PS), the **E**lectromagnetic **C**ALorimeter (ECAL) and the **H**adronic **C**ALorimeter (HCAL) [41].
 - the **M**uon System (M1, M2, M3, M4 and M5) [42].

The Trigger system [43] is composed of some of these sub-detector. The pile-up system is dedicated exclusively to triggering.

The beam pipe (figure 3.5) is designed to minimise its contribution to the material budget in the acceptance since the LHCb experiment is focused in the high pseudo-rapidity region, where the particle density is high. The number of secondary particles depends on the amount and the kind of material seen by incident primary particles. The first 12 m is composed of Beryllium. This material has a relatively long radiation length which reduces the amount of secondary interactions and it is resistant enough for the vacuum in the region of the LHCb detector. The last meters of the beam pipe are made of stainless steel.

3.3 The Tracking System

CP-violation and rare decay studies require good knowledge of b -mesons life time. It is therefore important that the LHCb detector can precisely measure the distance of flight and the momentum of particles, since they both contribute to the life time calculation. The tracking system (see figure 3.6) is dedicated to this purpose. Therefore it reconstructs the trajectories of

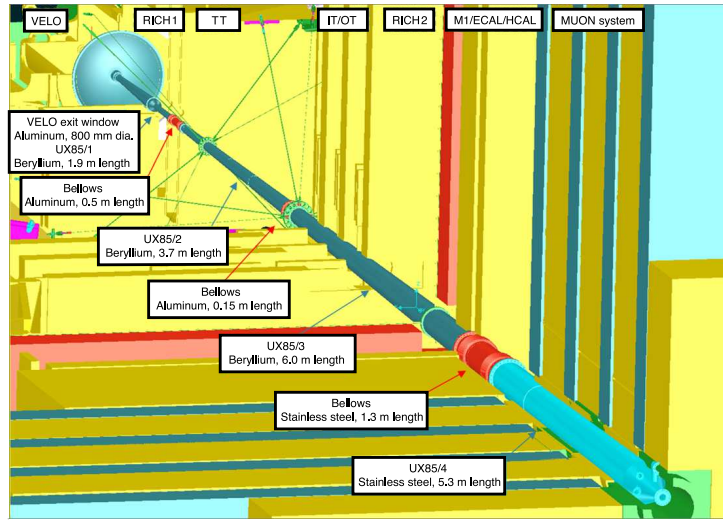


Figure 3.5: The beam pipe layout through LHCb.

charged particles that pass through the LHCb detector. The ratio of the electric charge and the momentum of these particles ($q/|p|$) can be computed from the curvature of the tracks induced by the magnetic field. To achieve the goal of the LHCb physics program [44], it is important that the detector provides an excellent momentum resolution of about $\delta p/p \simeq 0.4\%$.

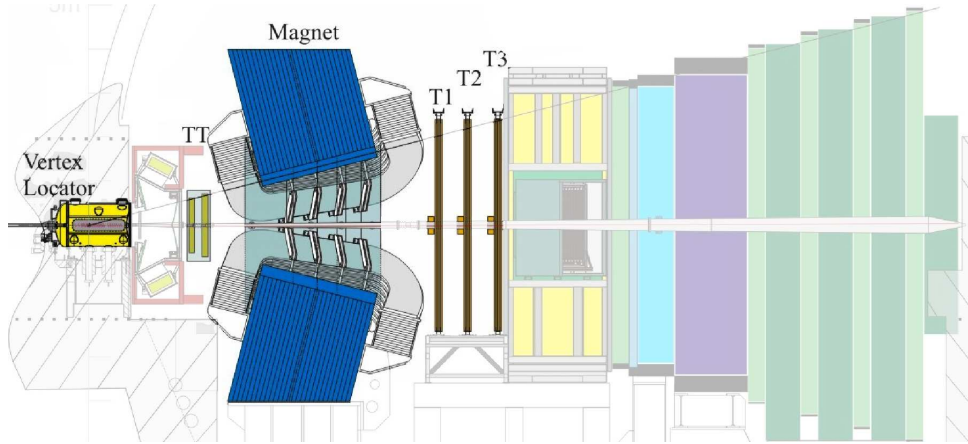


Figure 3.6: The Tracking System of the LHCb detector.

3.3.1 Vertex Locator

The Vertex Locator is a solid-state detector which provides very precise measurement of the location of primary vertex and secondary vertices of b -hadrons (or c -hadrons). The typical length covered by b -hadrons coming from the primary vertex is a few centimetres (the proper time is $\tau_B \sim 1.5 \cdot 10^{-12}$ s, the Lorentz boost $\gamma \sim 10 - 100$ and the distance of flight is $d_B = \gamma c \tau_B \simeq 458.7 \mu\text{m}$).

The majority of b -hadrons decay inside the VeLo. In a secondary vertex, the b -hadron daughter tracks converge to a point displaced from the primary vertex. Therefore a precise track reconstruction in this region is needed to separate vertices. The VeLo is also used in the

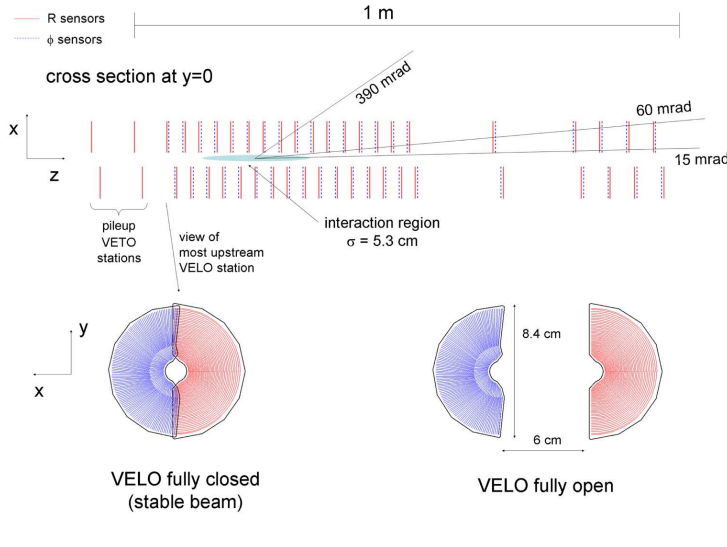


Figure 3.7: (left) cross section in the (x, z) plane of the VeLo silicon sensor (top) in the fully closed position. The r (red) and ϕ (blue) sensor are displayed below.

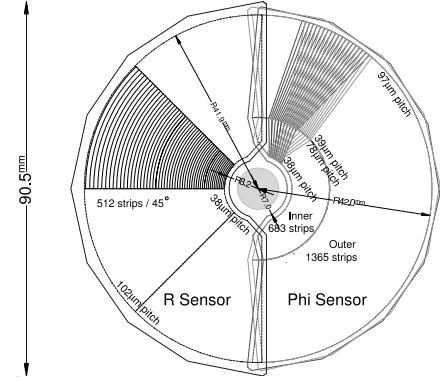


Figure 3.8: r and ϕ sensors geometry.

high level trigger (section 3.5) to tag b decay by selecting particles with large impact parameters significance with respect to the primary vertex.

The VeLo layout has been optimised to minimise the amount of material in the acceptance region while providing a good geometrical coverage. It has been decided to use silicon strip technology to build the sensors of the VeLo. The layout is presented in the figure 3.7. The VeLo is made of a series of 21 stations arranged along the z -axis. Each station is composed of two modules providing r and ϕ coordinates of the trajectory of the charged particles. When closed, the sensors are placed at 8 mm from the beam axis. This distance is smaller than the aperture required by the LHC during the injection, therefore the modules are retractable to a distance of 30 mm. Before the interaction point, four r -modules are used by the Level-0 Trigger as Pile-Up Veto system.

The VeLo modules are composed of one r -sensors and one ϕ -sensors that are made of silicon short strips, shown in figure 3.8. The r -sensors have concentric semi-circles (4×512 strips) centred on the nominal LHC beam position. The strips have a minimum pitch of $32 \mu\text{m}$ in the inner region increasing linearly to $101.6 \mu\text{m}$ at the outer radius. The ϕ -sensors have quasi-radial strips. There are two regions: the inner region which has 683 strip with a pitch from $38 \mu\text{m}$ to $78.3 \mu\text{m}$, and the outer region with 1365 strips and a pitch from $39.3 \mu\text{m}$ to $97 \mu\text{m}$.

The track definition within the LHCb acceptance ($1.9 < \eta < 4.9$) request at least hits in three modules and are reconstructed with the polar coordinates collected in these modules. The spatial resolution on the primary vertex depends on the number of tracks but is on average of about $42 \mu\text{m}$ on the z -axis direction and $10 \mu\text{m}$ in the transverse plane.

3.3.2 Dipole Magnet

The charged particle path is bent in a magnetic field, and the momentum of the particle can be determined from its curvature in the field. For that reason, the LHCb dipole magnet (figures 3.6) is used for measurement of the momentum of charged particles. The dipole magnet is located close to the interaction point to maximise the global LHCb acceptance which is limited to the

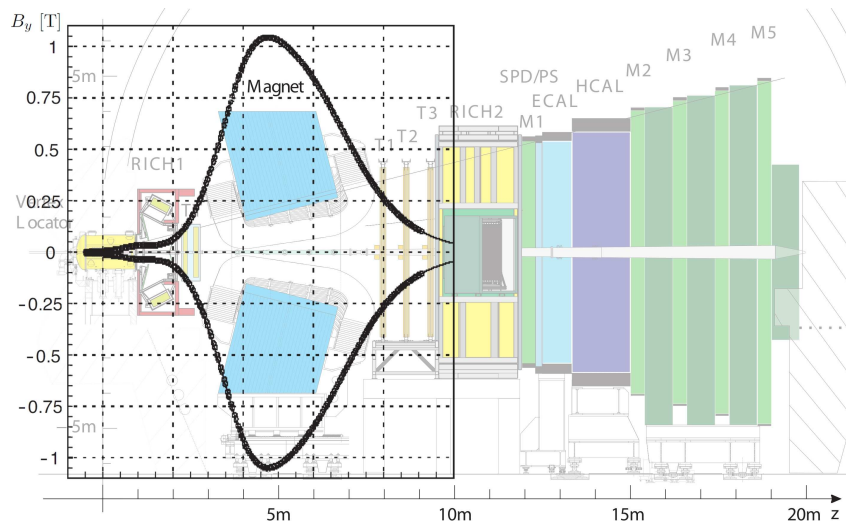


Figure 3.9: Magnetic field along the z -axis, both polarities are shown (taken from [45]).

dipole opening.

The main contribution of field is on the y -axis. The integrated field value is about $\int B dl \sim 4 \text{ Tm}$. The magnetic field can be easily inverted in order to minimise the systematic errors from the left-right detector asymmetries. The fields strength for both polarities along the z -axis are shown in the figure 3.9.

A warm magnet was preferred to a superconducting one which would also have been too expensive. The dipole consists of two trapezoidal coils made of 25 tons of laminated low carbon steel bent at 45° on the two transverse sides. The magnet is surrounded by an iron yoke of 1500 tons.

3.3.3 Silicon Trackers

The silicon trackers consist of two different sub-detectors, the Tracker Turicensis (TT) located just before the magnet, and the Inner Tracker (IT) is located at the centre of the three tracking stations (T1, T2 and T3) after the magnet. The TT, T1, T2 and T3 stations are highlighted in figure 3.6. Both TT and IT use silicon microstrip sensors with a strip pitch of about $\sim 200 \mu\text{m}$.

Tracker Turicensis

The Tracker Turicensis station is made of with four rectangular layers covering the complete LHCb angular acceptance. The layers are composed of silicon-strip modules which represent more than 140k readout channels. The layers are arranged in a (x-u-v-x) design where the strips of the x layers are vertical while the u and v layers have respectively strips with an angle of -5 and $+5$ degrees with respect to the vertical. In order to have a stereo measurement of charged particle tracks, the layers are disposed by pairs, (x-u) and (v-x), separated by 27 cm along the beam axis. (Figure 3.10) A layer is composed of modules (Figure 3.11). Each module consists of a row of seven silicon-strip sensors with a stack of two or three readout sectors. A sensor is $500 \mu\text{m}$ thick of 9.64 cm wide and 9.44 cm long, it carries 512 readout strips with a pitch of $183 \mu\text{m}$.

The maximal strip occupancy is $\sim 3.5\%$ in the region close to the beam pipe. The TT has a spatial hit resolution of about $50 \mu\text{m}$.

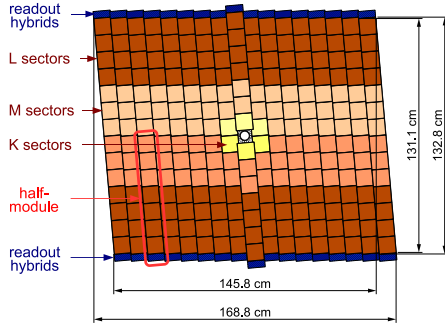


Figure 3.10: Layout of the third TT layer.

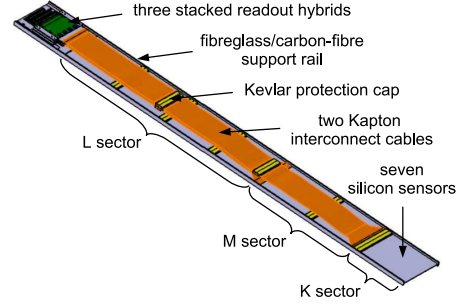


Figure 3.11: View of a TT module.

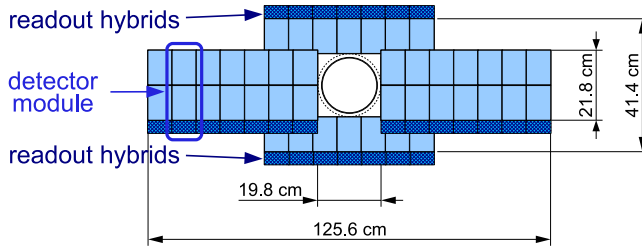


Figure 3.12: Layout of an IT station.

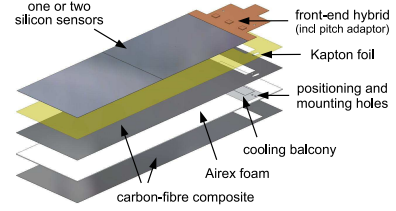


Figure 3.13: View of a IT module.

Inner Tracker

The Inner Tracker is composed of three stations that are located after the magnet at the centre of each Tracking stations (T1, T2 and T3). The IT stations are close to the beam pipe where the particle flux density is the highest. They are composed of four boxes each surrounding the beam pipe (figure 3.12). Each box contains four layers of seven silicon-strip modules. The layers are placed in the same (x-u-v-x) configuration with tilt angles of 0, -5, +5 and 0 degrees respectively to the y -axis.

The silicon-strip sensors are 11 cm long and 7.6 cm wide. To ensure the maximum signal-to-noise ratio the thickness of the sensors has been chosen to minimise the amount of material. The modules of the left and right layers are made of two 410 μm thick sensors while the modules of the top and bottom layers have only one 320 μm thick sensor. All sensors possess 384 silicon strips with a strip pitch of 198 μm . The Inner Tracker has a spatial resolution of about 57 μm .

A complete description of the construction of the Inner Tracker detector boxes can be found in reference [45].

The IT has been aligned with a precision better than 20 μm at the module level using a software procedure described in Ref. [46].

3.3.4 Outer Tracker

The Outer Tracker (OT) is a drift-time detector, for the tracking of charged particles and the measurement of their momentum in the outer region of the LHCb detector. The Outer Tracker is composed of three stations located in T1, T2 and T3 and surrounding the IT stations (figure 3.14). Hence, it covers all the LHCb acceptance not covered by the IT in the Tracking Stations. The resolution is about 200 μm .

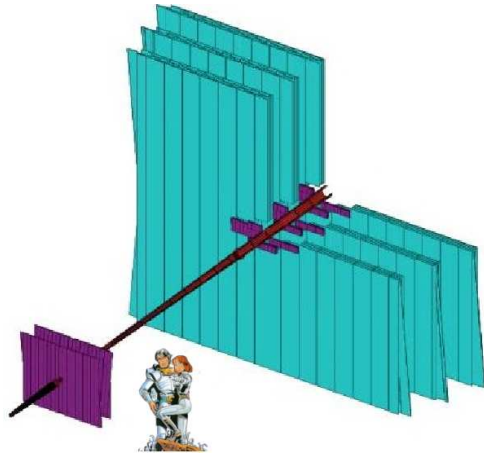


Figure 3.14: Layout of the 3 trackers, where the OT, in blue, surround the IT.

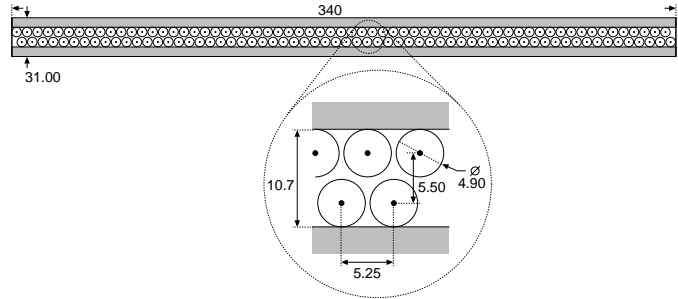


Figure 3.15: Cross section of a straw-tube module of the OT.

3.3.5 Track Reconstruction and Performances

The track reconstruction software combines the hits in the VeLo, the TT, the IT and the OT sub-detectors to compute the particle trajectories and momentum. The algorithm aims to reconstruct all the tracks in the event that have sufficient hits in the sub-detectors.

Depending on their trajectories inside the detector, the charged tracks are classified according to the following scheme, illustrated in figure 3.16:

Long tracks : traverse the whole Tracking System, from the VeLo to the Tracking Stations. They are the most useful tracks for b -hadrons decay studies, since they have the most precise momentum determination.

Upstream tracks : detection limited to VeLo and TT stations. They have generally a lower momentum than the long tracks, which bent them outside the spectrometer acceptance before the tracking stations. The upstream tracks have a momentum resolution of about 10-20 %, but they are needed to filter the background in the RICH1 particle identification algorithm. They are also useful for flavour tagging or for b -hadron decay reconstruction.

Downstream tracks : traverse only the TT and the Tracking stations. They are, in the majority of cases, decay products of K_S^0 or Λ that decay outside the LHCb geometrical acceptance.

VeLo tracks : with hits only in the VeLo. They have a large angle in the forward direction or fly in the backward direction. They are used to increase the Primary Vertex reconstruction fitting resolution.

T tracks : are only measured in the Tracking stations. They often come from secondary interaction in the materials, but as the upstream tracks for the RICH1, they are useful for the RICH2 pattern recognition algorithm.

Track reconstruction starts with search of *seeds* in the VeLo and Tracking stations region where the magnetic field is low (see figure 3.9). The hits found in the VeLo region, called *VeLo track seeds*, should be almost aligned. The same is valid for the Tracking stations where these

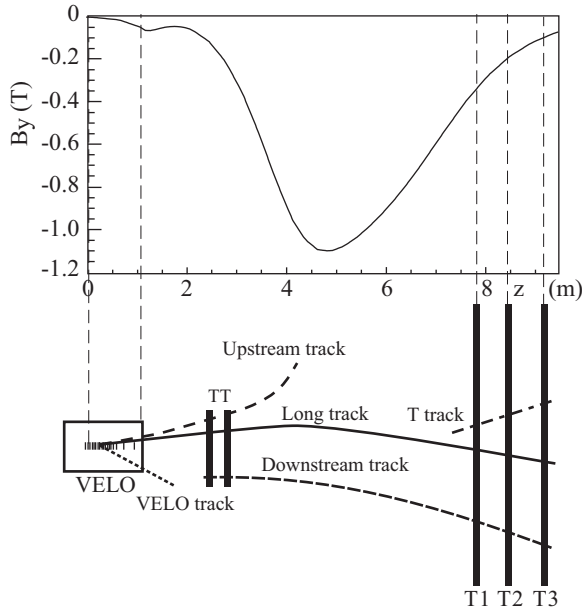


Figure 3.16: Characterisation of the different tracks according to their topology in a schematic LHCb detector. The main B -field is also plotted.

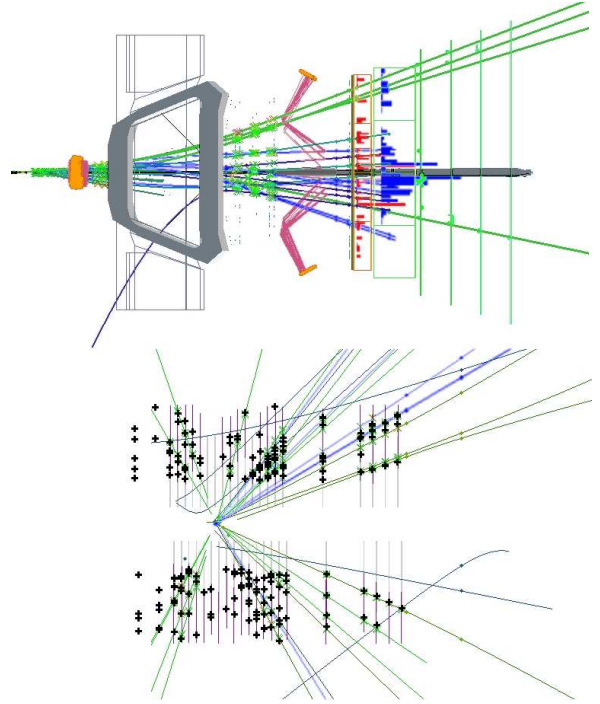


Figure 3.17: Display of reconstructed tracks within the LHCb detector (top), it is an event record on the 11/12/2009 during the first collisions. The reconstruction has shown a nice primary vertices (bottom) and at least three long tracks.

segments are called *T track seeds*. These track seeds are refitted in order to take into account the multiple scattering and the dE/dx energy loss. The algorithm then tries to associate hits in the other tracking subsystems to form track candidates. Depending on the quality of the fit, number of hits, etc., they are classified in the different categories previously described.

The performances of the tracking algorithm is evaluated in terms of reconstruction efficiency (fraction of possible reconstructible tracks successfully reconstructed) and ghost rate which is the fraction of the tracks reconstructed with hits that do not correspond to a single particle. The ghost rate can only be determined in MONTE-CARLO (MC) simulations, where a track is defined to be successfully reconstructed when it has at least 70 % of its associated hits coming from the same single MC particle.

On a MC sample of $B^0 \rightarrow J/\psi K_S^0$ [29] where decays on average of 72 tracks are successfully reconstructed per event, the pattern recognition algorithm finds 26 long tracks, 11 upstream tracks, 4 downstream tracks, 26 VeLo tracks and finally 5 T tracks.

The efficiency for long tracks reconstruction with a momentum bigger than 10 GeV/c is about 94 % and in the case of b -hadron decays this efficiency is about 95-96 %. The ghost fraction is less than 9 %, and most of the “wrong” tracks have a low reconstructed transverse momentum. The long track momentum resolutions is plotted on the figure 3.18 (left) and shows that the tracks with a low momentum have a resolution of $\delta p/p \simeq 0.35$ %, while the high momentum tracks have $\delta p/p \simeq 0.55$ %.

Figure 3.18 shows the resolution which can be parametrised by $\sigma_{IP}(\mu m) = 14 + 35/p_T$, where the transverse momentum p_T is in GeV.

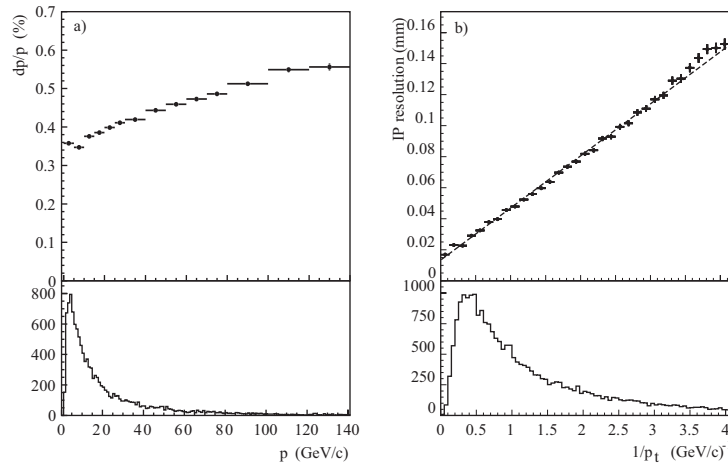


Figure 3.18: Track momentum resolutions as a function of their momentum (left) and impact parameter resolution as a function of $1/p_T$ (right).

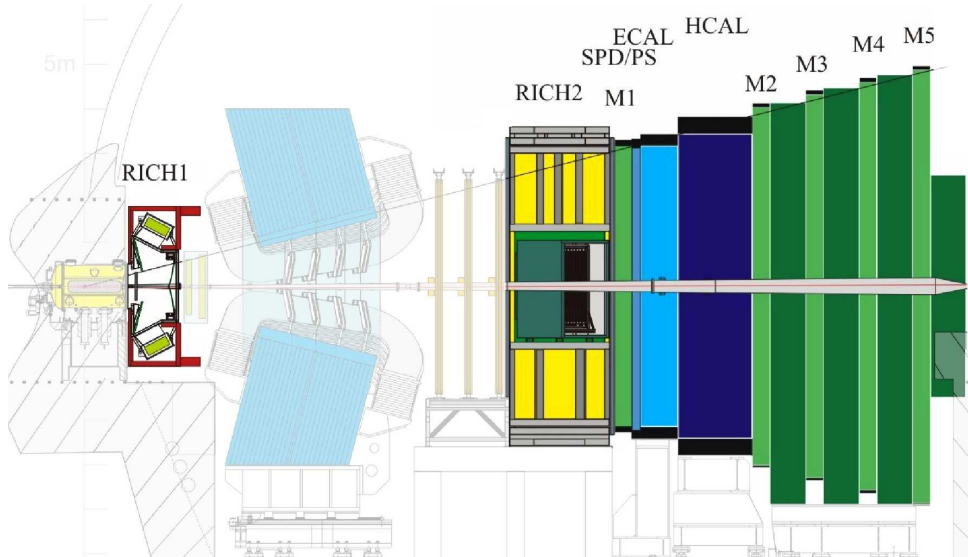


Figure 3.19: The Particle Identification System of the LHCb detector.

3.4 The Particle Identification Systems and Calorimetry

In order to reconstruct and tag b -hadrons, with the best efficiency and accuracy, the LHCb experiment needs excellent Particle Identification (PID) Systems.

For that purpose the particle identification collects information from (figure 3.19): two Ring Imaging Čerenkov counter detectors (RICH1 and RICH2), a calorimeter system composed of the pad/preshower calorimeter (SPD/PS), the electromagnetic calorimeter (ECAL) and the hadronic calorimeter (HCAL), and finally the muon chambers (M1-M5).

3.4.1 Ring Imaging Čerenkov Detectors

It is important in b -hadron physics to have an excellent separation between charged kaons and charged pions. Hence the LHCb experiment uses two Ring Imaging Čerenkov Detectors (RICH), these detectors use the Čerenkov effect to distinguish these two mesons. When a charged particle

flies through a medium with a speed βc greater than the speed of light c/n in that medium, where n is the refractive index of the medium, the particle emits electromagnetic radiation. This effect has been rigorously characterised by the Russian Čerenkov who won the Nobel Prize for in 1958. The Čerenkov photons are emitted within a cone whose aperture angle θ is given by:

$$\cos \theta = \frac{c}{n \cdot v} = \frac{1}{\beta \cdot n} \quad , \text{ with } \beta = \frac{v}{c} \quad (3.2)$$

The use of two Ring Imaging Čerenkov detectors with different mediums provides a full coverage of the momentum spectrum.

The first RICH detector (RICH1) is located at the end of the VeLo, before the magnet and the TT stations. It is optimised for the low momentum, from 1 GeV/c to 60 GeV/c. RICH1 covers the full LHCb acceptance and contains C_4F_{10} ($n = 1.0014$) gas radiator and aerogel ($n = 1.03$).

The second RICH detector (RICH2) is located between the Tracking station and the SPD/PD calorimeter, it does not cover the full LHCb acceptance but only the inner part of the detector (from ± 15 mrad to ± 120 mrad for the bending plane and ± 100 for the non-bending plane). RICH2 is designed to separate charged particles with a momentum between ~ 15 GeV/c and 100 GeV/c. It uses CF_4 as radiator, that have a tunable factor n between 1.01 and 1.10.

In both RICH detectors, the Čerenkov light is captured by pixelated Hybrid Photon Detectors (HPD) after reflections on mirrors. The 196 HPDs of RICH1 and the 288 HPDs of RICH2 are isolated outside magnetic field and have 1'024 pixel each. On average, a charged particle with $n\beta > 1$ produces 6.7 Čerenkov photon in the aerogel, 30.3 in the C_4F_{10} and 21.9 in the CF_4 .

Figure 3.20 shows the first real Čerenkov light rings observed during the first collision runs.

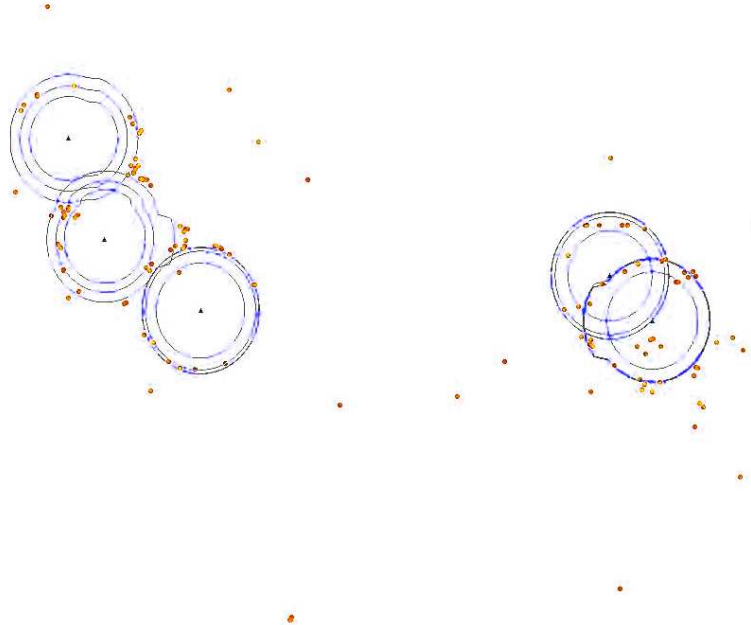


Figure 3.20: The first real Čerenkov light rings observed. The circles show possible position of measured points for different kinds of particles traversing the detector. The measured points clearly choose one possibility for every circle and in this way allow to identify particles.

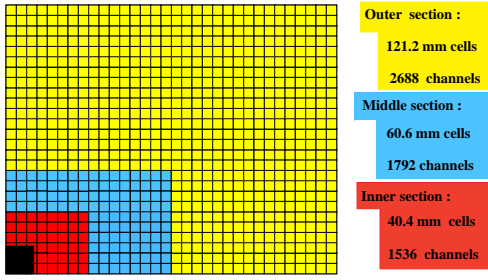


Figure 3.21: Transverse segmentation of the SPD/PS and ECAL.

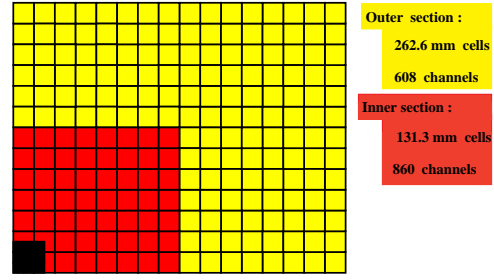


Figure 3.22: Transverse segmentation of the HCAL.

3.4.2 Calorimeters

The Calorimeter system is used for the particle identification of electrons, photons and hadrons and also for their energy measurement and position. This specification allows a good reconstruction of the π^0 and the photons. It also selects and gives fast raw information, within $4 \mu s$ after the interaction, about hadron, electron and photon candidates with a certain amount of transverse energy for the Level-0 Trigger.

The Calorimeter system is composed of the pad/preshower detectors (SPD/PS), the electromagnetic calorimeter (ECAL) and the hadronic calorimeter (HCAL) (see figure 3.19).

For the separation of the electromagnetic and hadronic particles, the longitudinal profile of the electromagnetic showers is an excellent factor of discrimination. Therefore the Pre Shower (PS) is located in front of the ECAL just after a layer of lead absorber. To have a good identification of charged particles, the Scintillating Pad Detector (SPD) is located just before the layer of lead. Finally the HCAL is located after the ECAL to evaluate the energy of the hadronic particle candidates.

All the calorimeters are based on the same basic concept, scintillating light is transmitted to PhotoMultipliers (PMT) by wavelength-shifting (WLS) fibres. In order to have a constant transverse energy (E_T) measurement over the whole detector acceptance, the photomultiplier gains are tuned as a function of the distance of the cell to the beam pipe.

The SPD/PS, ECAL and HCAL have variable lateral segmentation (shown in figure 3.21 and 3.22), in order to have an almost constant cell occupancy since the hit density varies by two order of magnitude as a function of the distance to the z -axis. The segmentation is approximately projective in the direction of the interaction point to get a fast evaluation of the trigger candidates.

The Pad/Preshower Calorimeter (SPD/PS) consist of a 15 mm lead layer converter $2.5X_0$ thick which is sandwiched between the cell layers of SPD and the PS. In total, the SPD/PS has 12'032 detection channels which cover the two planes. The SPD is used to separate photons from electrons which release part of their energy when they go through the lead layer into a electromagnetic shower. This separation e^\pm/γ is also used in the first trigger stage to reject the high- E_T π^0 background. Photons with a energy between 20 and 50 GeV have a misidentification probability of about 0.8 %. The distinction between charged pions and electrons also uses the electromagnetic shower dispersion of the electrons. For electrons with a momentum of 10 GeV/c, 20 GeV/c and 50 GeV/c, the SPD/PS has a pion rejection factor of respectively 91 %, 92 % and 97 % while the electron retention is respectively 99.6 %, 99.6 % and 99.7 % .

The Electromagnetic Calorimeter (ECAL) has been designed to contain the whole elec-

tromagnetic shower of the high energy incoming photons. The ECAL has a total thickness of $25X_0$. Electromagnetic showers are initiated in the lead absorber sandwiched between the SPD and the PS. The energy resolution is given by:

$$\sigma_E/E = 10\%/\sqrt{E} \oplus 1\% \quad , E \text{ in GeV}$$

where the first term is the statistical fluctuation of the shower while the second comes from the systematic uncertainties of the calibration. The ECAL has been designed for b -hadron physics therefore the maximum transverse energy per cell has been limited by the possible gain applied to the PMT and is optimised for a transverse energy $0 < E_T < 10 \text{ GeV}/c$. Measures of E_T beyond this value are saturated. This fact deteriorates the measurement of high energetic electrons.. Its consequence on the Higgs reconstruction and selection will be discussed later (section 4.4.3) where the identification of high- p_T electrons is important to detect Z^0 or W^\pm in the event.

The Hadronic Calorimeter (HCAL) its aim is mainly for trigger and particle identification. Therefore it has only a thickness of $5.6X_0$ which would not contain the full hadronic shower. It gives only a estimation of the hadron energy with a limited resolution:

$$\sigma_E/E = 80\%/\sqrt{E} \oplus 10\% \quad , E \text{ in GeV}$$

3.4.3 Muon system

Muons coming from semi-leptonic b -meson decays provide the tag of the initial flavour of the second neutral B meson. Muons are also involved in some rare decays, such as $B_s^0 \rightarrow \mu^- \mu^+$ [45], which could hint new physics beyond the standard model.

The muon system provides fast information for the high- p_T muon trigger for the Level 0 Trigger and the muon identification. In the case of Higgs studies, muons are important to identify W^\pm and Z^0 .

Since the muons have a long life time $\tau_\mu \simeq 2.2\mu\text{s}$, which gives a $c\tau_\mu$ of about 659 m, and a low interaction probability, they fly through the whole detector. Muon chambers are installed at the end of the detector (shown on figure 3.19), all the other possible charged particle should be filtered. The chambers are made of multi-wire proportional chambers (MWPC) and their planes are perpendicular to the beam axis. The stations M2 to M5 are interleaved with 80

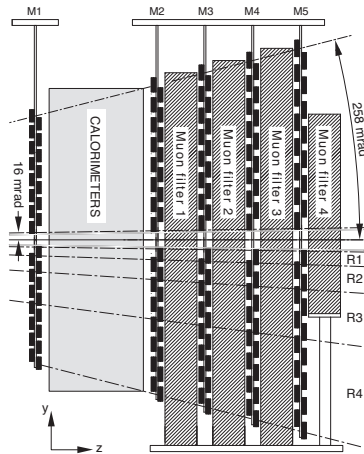


Figure 3.23: Schematic side view of the muon chambers location.

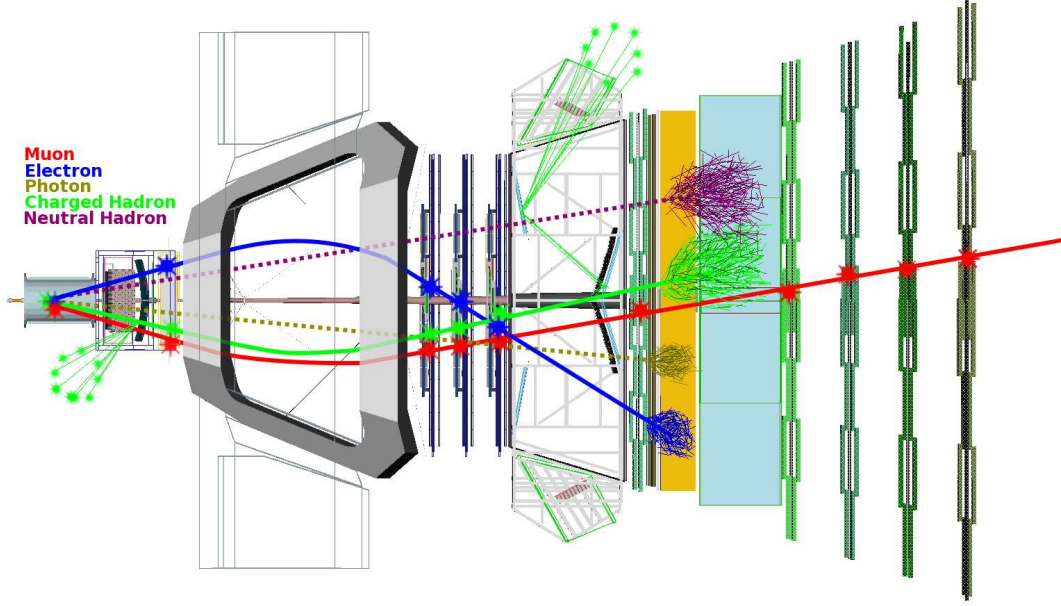


Figure 3.24: Schematic view of the different particle signatures in the LHCb detector. The hits in the tracking system are highlighted, the Čerenkov rings are shown for the charged hadron and the different showers are also displayed.

cm thick iron absorbers which should select only the penetrating muons. The muons should have a momentum bigger than 6 GeV/c in order to fly through the 5 stations (including the calorimeters).

The M1 station is placed before the calorimeter to improve a fast decision on the p_T measurement for the Level-0 Trigger. The muon trigger consists of a stand-alone muon track reconstruction with aligned hits in all the station and a p_T measurement. Based on the three first stations, this requirements lead to a fast track direction definition (< 25 ns) with a designed efficiency greater than 95 % while the momentum resolution for the trigger is less than 20 %. M4 and M5 are grandly used only for the identification of very penetrating particles.

3.4.4 Particle Identification Performances

Charged particle (e, μ, π, K, p) identification uses the information coming from the two Čerenkov detectors, the three calorimeters and the muon systems. Neutral particles (γ, π^0) are identified with the help the electromagnetic calorimeter.

All these particles have different signature in the LHCb detector, illustrated in the figure 3.24, which is the key point of PID determination.

Hadron Identification : The identification with the RICHes is done through a maximum likelihood approach that compares the hit pixels in the RICH HPD to the expected rings from the reconstructed tracks under a given particle hypothesis (e, μ, π, K, p) and gives as an output the best PID hypothesis for each track.

The kaon identification with momentum between 2 and 100 GeV/c has on average efficiency of $\sigma(K \rightarrow K) \sim 95\%$, while the pion misidentification is $\sigma(\pi \rightarrow K) \sim 5\%$.

Muon Identification : Muon identification is done by the search of hits in the muon chambers close to the extrapolation of the track trajectories with a transverse momentum $p_T > 3 \text{ GeV/c}$. A track is considered as muon if:

- for $3 \text{ GeV/c} < p_T < 6 \text{ GeV/c}$, hits in M2 and M3,
- for $6 \text{ GeV/c} < p_T < 10 \text{ GeV/c}$, hits in M2, M3 and M4 or M5,
- for $p_T > 10 \text{ GeV/c}$, hits in M2, M3, M4 and M5.

In a sample of $B^0 \rightarrow J/\psi K_S^0$ event, it has been found out that $\sigma(\mu \rightarrow \mu) \sim 94\%$ for a misidentification rate of $\sigma(\pi \rightarrow \mu) \sim 3\%$. While the combination of the information with the RICHes ones gives $\sigma(\mu \rightarrow \mu) \sim 93\%$ and $\sigma(\pi \rightarrow \mu) \sim 1\%$.

Electron Identification : The electron identification is mainly based on matching a track momentum to the corresponding energy of charged cluster in the ECAL. To minimise the emission of bremsstrahlung photons which could change the energy deposit in the ECAL, the amount of material has also been minimised.

In the same sample of $B^0 \rightarrow J/\psi K_S^0$, the efficiency is $\sigma(e \rightarrow e) \sim 95\%$ while the misidentification rate is $\sigma(\pi \rightarrow e) \sim 0.7\%$.

The saturation of the ECAL's cells for the high- p_T electrons ($p_T > 10 \text{ GeV}$) would make the identification considerably difficult.

Electron identification is improved through matching clusters in the PS and ECAL along the extrapolated tracks.

Photon Identification : Cluster without an associated track are associated with photon. The photons coming from a conversion in the material after the Tracking Stations are identified from the number of hits in the SPD.

The efficiency of the unconverted photon identification in a $B^0 \rightarrow K^* \gamma$ sample is $\sigma(\gamma \rightarrow \gamma) \sim 90\%$ and the converted photon rate is $\sigma(\gamma \rightarrow \gamma) \sim 0\%$.

π^0 : These π^0 are referred to “merged π^0 ”.

The figure 3.25 shows the reconstruction of $\pi^0 \rightarrow \gamma\gamma$ with the real data of the 23rd November 2009 runs. It illustrates how well the ECAL works even with the first raw data available at the LHC.

Log-Likelihood Difference : For each type of charged particle, the different particle identification detector contributions are combined into a log-likelihood difference (DLL) between a given PID hypothesis and the pion hypothesis. The DLL for a particle type a is given by:

$$\text{DLL}_a = \Delta \ln \mathcal{L}_{a\pi} = \ln \mathcal{L}_a - \ln \mathcal{L}_\pi = \ln \left[\frac{\mathcal{L}_a}{\mathcal{L}_\pi} \right] \quad (3.3)$$

where \mathcal{L}_a combines in a likelihood the information of the various sub detector used for the identification. The DLL between two particle hypotheses a and b is then given by:

$$\Delta \ln \mathcal{L}_{ab} = \Delta \ln \mathcal{L}_{a\pi} - \Delta \ln \mathcal{L}_{b\pi} = \ln \left[\frac{\mathcal{L}_a}{\mathcal{L}_b} \right] \quad (3.4)$$

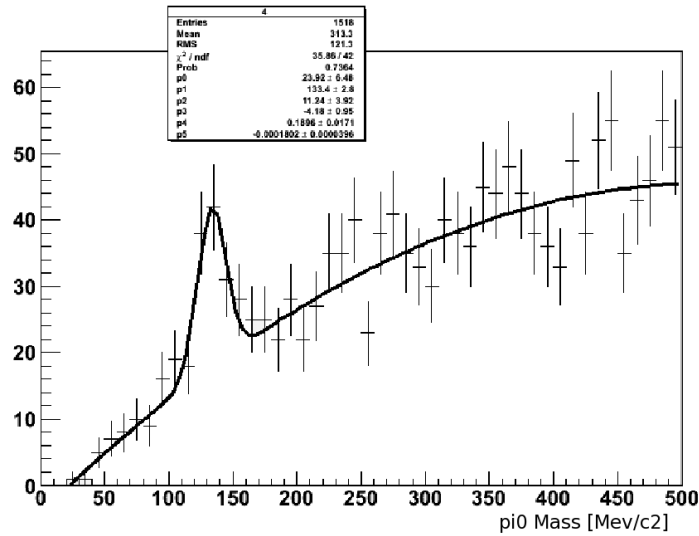


Figure 3.25: The nearly perfect π^0 reconstruction on the real data taken from the 23rd November runs, measured in the ECAL.

3.5 The Trigger System

The number of interactions per bunch crossing is dominated by single interaction due to the relatively low LHCb luminosity of $2 \times 10^{32} \text{ cm}^{-2}\text{s}^{-1}$ (section 3.1). The expected rate of pp collision is about 10 MHz including 15 kHz of events containing at least one b -hadron with its decay daughters in the LHCb acceptance.

The 10 MHz has then to be reduced by a factor of 5'000 in order to be able to store the event for the offline analysis. To achieve this 2 kHz rate, two trigger levels [43] are applied, the Level-0 Trigger (L0) and the High Level Trigger (HLT). The HLT is subdivided into two sub-systems (HLT1 and HLT2), the schematic layout is illustrated in figure 3.26. The triggering criteria must keep the largest fraction of good events, keeping the background as low as possible.

3.5.1 Level-0 Trigger

The first trigger level (Level-0) is designed to reduce the rate to 1 MHz which is the maximum readout frequency of the Data Acquisition Cards (TELL1). It is implemented using custom made electronics and running synchronously with the 40 MHz bunch crossing frequency. The B meson decay products are usually particles with a large transverse momentum, p_T , and transverse energy, E_T . Therefore the Level-0 decision is based on:

- the reconstruction of the highest E_T hadron, electron and photon cluster in the Calorimeters,
- the reconstruction of the highest p_T muons,
- the numbers of tracks based on the SPD hits, the total energy observed in the calorimeters,
- the number of primary vertex estimated by the pile-up system in the VeLo.

The L0 Calorimeter Trigger looks for high E_T electron, photon, neutral pion or hadron candidates. It forms clusters by summing the E_T of 2×2 cells and selects the highest E_T clusters. Then the information from the SPD/PS, ECAL and HCAL tags the clusters as

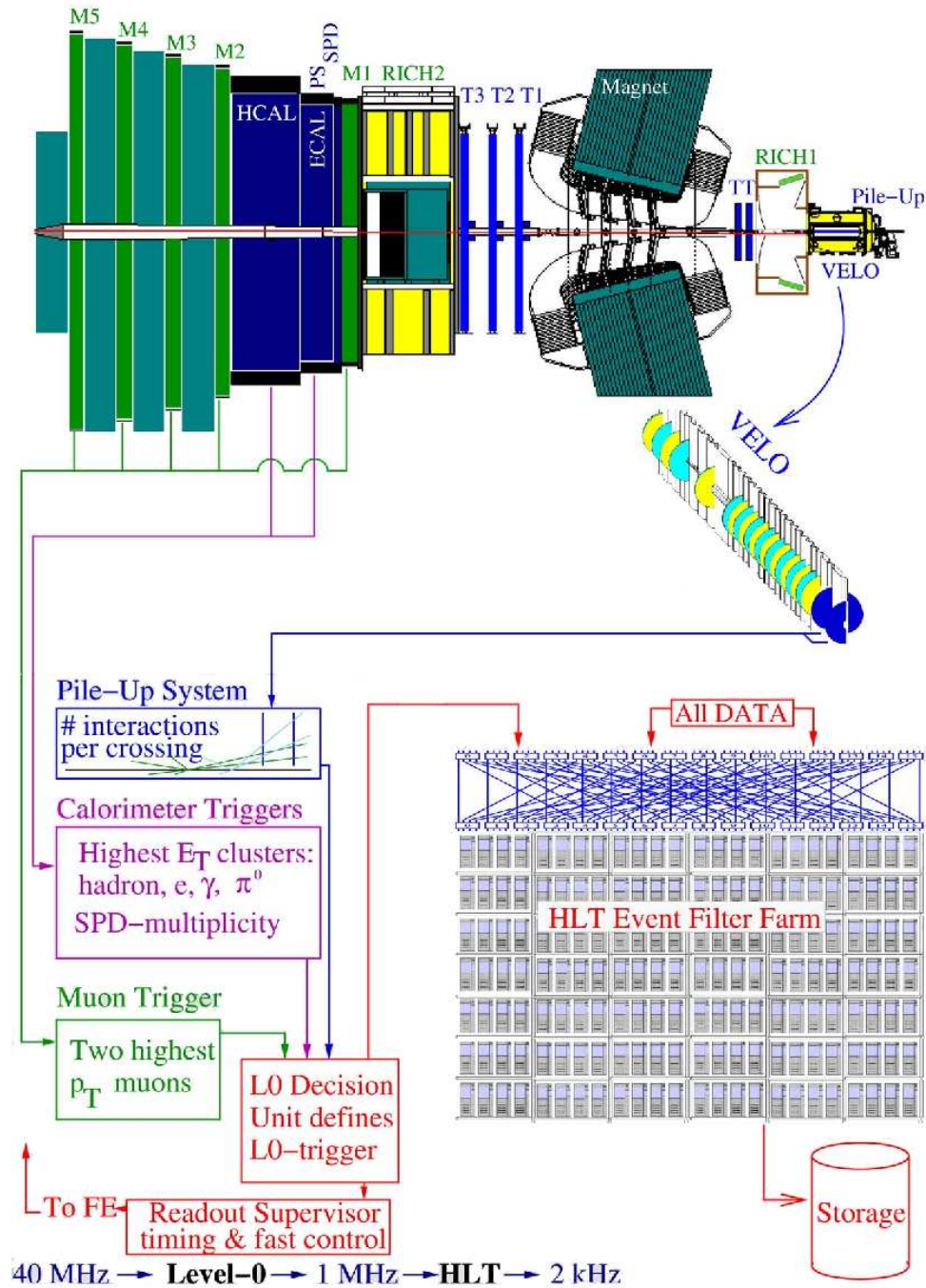


Figure 3.26: Overview of the layout of the LHCb Trigger system.

electron, photon or hadron. Besides the total E_T in the HCAL is used to reject crossings without any visible interaction and to reject events triggered by halo muons. Finally the numbers of hit cells of the SPD is used to evaluate the charged track multiplicity.

The L0 Muon Trigger uses a fast stand-alone reconstruction of muon tracks with a $\sigma_{p_T} \sim 20\%$. A track is found if hits in the five muon chambers can form a straight line pointing to the interaction region. Then in each quadrant of the muon detector, the two highest- p_T muons are selected for the decision.

The Pile-Up System is designed to distinguish between the single interactions from multiple ones. Four r -sensors, similar to the ones used in the VeLo, are located before the interaction region to measure the radial position of the backward tracks. The information of the Pile-Up system contains the positions of the primary vertices and also the backward charged track multiplicity.

The Level-0 Decision Unit ((L0 DU) collects all the information of the previous systems in an OR-ed logical and makes a final decision. The L0 DU should release its decision in the $4\mu\text{s}$ after a collision, this corresponds to the buffer width implemented in the front-end read-out chips. Furthermore, the time-of-flight of the particle, plus the cable delays, plus the electronics delay already corresponds to $2\mu\text{s}$, therefore the L0 system has only $2\mu\text{s}$ to deliver a decision.

3.5.2 HLT

The HLT is performed in a CPU farm of almost 2'000 computing nodes running a C++ application. However, the frequency of the incoming events from the Level-0 Trigger and the computing power limitation of the HLT farm do not allow the use of the full event data information to reject uninteresting events.

The HLT is divided in two stages, the first stage (HLT1) aims to confirm the Level-0 decision by adding Tracking information. HLT1 performs partial reconstruction of the particle including the transverse momentum, p_T , and impact parameters of tracks. The $\sim 30\text{ kHz}$ selected by HLT1 are passed to HLT2. The HLT2 input rate is sufficiently low to perform a simple reconstruction of full tracks in the CPU farm dedicated to this trigger. These tracks with loose cuts, on their transverse momenta and impact parameters, are used to form composite particles (K^* , ϕ , D^0 , D_s and J/ψ).

The HLT2 stage is based on inclusive or exclusive triggers that aims to reduce the output rate of the events that are stored. The inclusive trigger selects partial B decays, while the exclusive triggers select specific decays to cover the LHCb physics analyses. The bandwidth of each exclusive or inclusive trigger is adjustable in order to optimise the physics analysis efficiencies.

3.6 Online System

The aim of the Online System [43, 47, 48] is to perform the transfer of the data from the front-end electronics to the storage system. This includes the storage of the detector conditions and configurations, the monitoring of the LHCb internal parameters and the external parameters such as the temperature or pressure. It also ensures the synchronisation of each detector channel with the LHC clock.

The Online System can be divided into three different subsystems, illustrated in figure 3.28: the Data Acquisition System (DAQ), the Timing and Fast Control system (TFC) and the Experiment Control System (ECS).

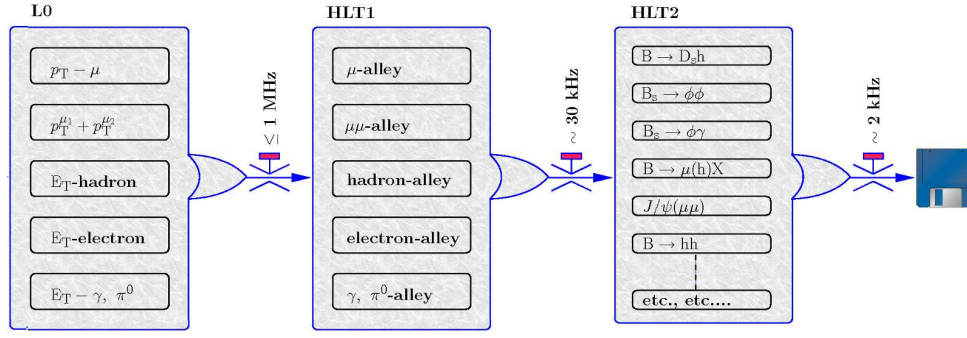


Figure 3.27: Flow diagram of the different trigger sequences.

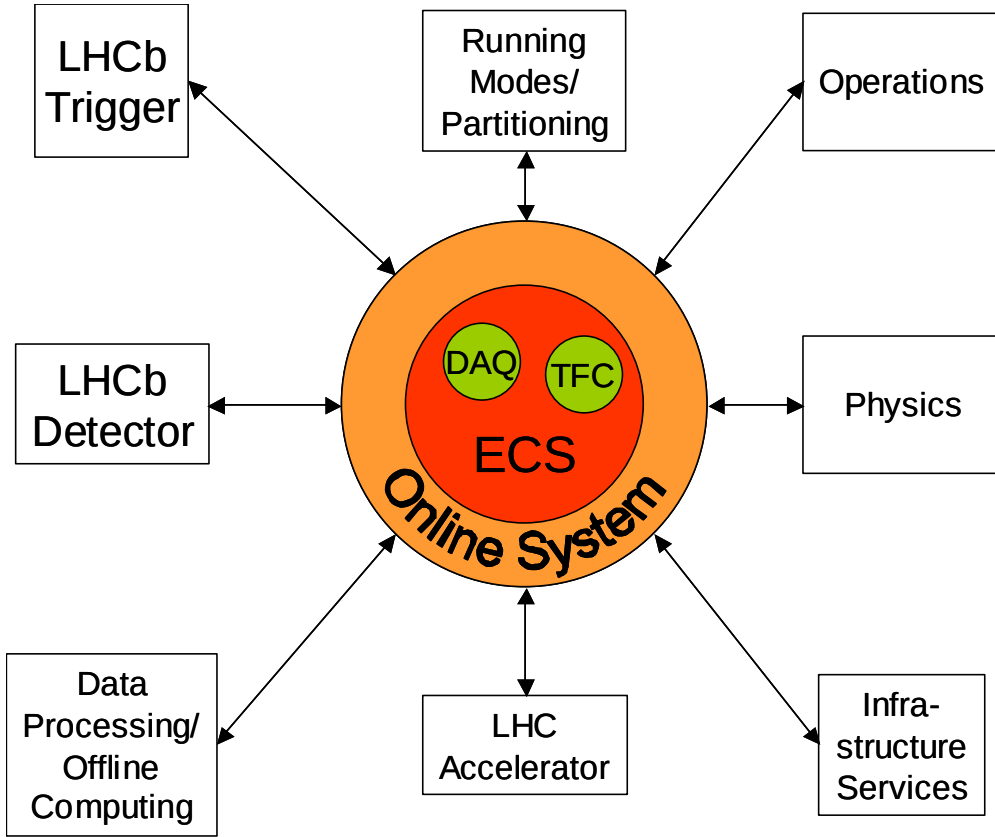


Figure 3.28: Online system architecture.

3.6.1 Data Acquisition System

The goal of the Data Acquisition System (DAQ) is to transport the data belonging to a certain bunch crossing that has been accepted by the Level-0 Trigger to a storage system. The L0 decision is sent to the *Readout Supervisor* (the ODIN cards). A signal is sent to the Front-End (FE) electronics which are based near the detector. As soon as the FE receives the decision the buffered data is transferred to the TELL1 [49, 50] boards placed outside the irradiated area, via optical or analog links. The TELL1 boards are fully explained in the section 5.1.

All the subdetector DAQ systems use the TELL1 board, aside from the RICHes which use the UKL1 boards. Both boards use *Field Programmable Gate Arrays* (FPGA) technology and are

designed to use simple protocols, a small numbers of components and able to react to changing system parameters. This features has allowed all the subdetectors to have specific algorithms implemented on FPGA of their dedicated TELL1. The data are cleaned, compressed and packed before being sent via Gigabit-Ethernet links to the Event Builder which reassembles the data on all the subdetectors for single event.

3.6.2 Timing and Fast Control

The Timing and Fast Control (TFC) system control all the online system, from the front-end electronics to the online HLT processing farm, by distributing the LHC beam-synchronous clock, the L0 trigger and synchronous resets and the fast commands. All the signals are sent by the Readout Supervisor, ODIN, which decides the destination node of the data. Special triggering patterns are transmitted for calibration runs.

3.6.3 Experiment Control System

The Experiment Control System (ECS), which is explained in more detail in the Chapter 5, ensures the control and monitoring of the entire LHCb detector. This implies not only the subsystem already presented, but also the cooling systems, the gas flow, the high and low voltages, the Trigger, TFC and the DAQ. The LHCb ECS system is based on the PVSS-II [51, 52, 53] which is a commercial *Supervisory Control And Data Acquisition* (SCADA) tool providing a large panel of possibilities in the control such as the management of database, the communication in distributive systems, graphical tools and alarms systems.

The LHCb ECS is built on a hierarchical and distributed system which allows the control of the whole detector from the top level, but also to release a sub group, such as a detector, or the HLT farm in order to be able to test these system in a stand-alone mode.

The commands flow down the hierarchy whereas the alarms goes up to the top node. These command and error flows are managed by using a Finite State Machine package based on SMI++ [54, 55] that allows creating complex logic needed, as is the implementation of elaborate sequencing or the automatic error recovery.

3.7 Computing and Resources

3.7.1 LHCb Computing Model

All the data coming from the CERN experiments are treated and distributed on the Worldwide LHC Computing Grid (WLCG) (see section 2.4 for a short introduction) [56]. On the WLCG three kind of computer cluster can be distinguished as a function of their significance, the Tiers 0, 1 and 2 (shown on figure 3.29).

The raw data selected with the trigger systems, real or simulated, coming from the experiment are transferred to the CERN Tier-0 for further processing and archiving. The next step is the reconstruction of the real physical particle (track + pid) data from the raw information such as the hits or the calorimeter cluster energies. The output data is saved in a new format, called the *Data Summary Tape* (DST), containing only enough information to allow pre-selection algorithm. Therefore these DST are called the *reduced DST* (rDST). The data flow from the detector to the rDST is in quasi-real time.

The rDST are analysed in order to produce selections of events for further physical analysis. During this sequence, known as the *stripping*, the rDST information are used to reconstruct the particle four momentum vectors, to locate the primary and secondary vertices, etc. Each

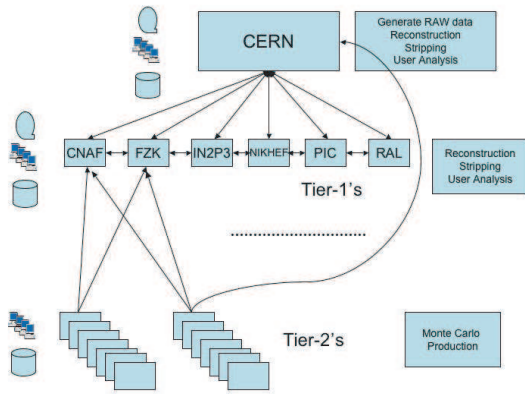


Figure 3.29: Schematic LHCb computing model.

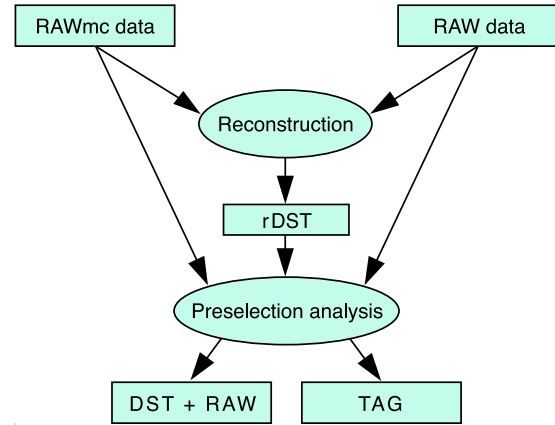


Figure 3.30: LHCb computing logical data-flow model.

physics channel of interest has its own algorithm, and whenever an event passes the selection criteria, a full reconstruction of the events is done. The output is a (*full*) DST containing all the possible information needed for analysis of the event. An event tag collection is also created for faster reference to selected events. The data-flow model is shown in figure 3.30. The data are re-processed several times a year with the improvement of the reconstruction, alignment and pre-selection software.

The LHCb computing model is based on the multi-tier model which gives more flexibility to the data analysis. As seen before, the CERN computer centre works as a Tier-0 that collects the data and transmits them in a quasi-real time to the six Tier-1 centres affiliated with LHCb, CNAF (Italy), FZK (Germany), IN2P3 (France), NIKHEF (The Netherlands), PIC (Spain) and RAL (United Kingdom). In addition, CERN also works as a Tier-1 centre.

The Tier-1 centres are responsible for the production-processing phases. The real data are stored entirely at CERN and another copy is sent to one or several Tier-1. Since the production of the rDST and DST is done at these computer centres, the analysis are generally distributed to the Tier-1 centres as well.

The large number of Tier-2 centres work in parallel with the system to produce MONTE-CARLO data to prepare selection algorithms, better reconstruction tools, etc. Large Tier-2 centres could in principle also run analysis.

3.7.2 LHCb Software

The LHCb experiment software is based on the GAUDI [57] architecture which provides an Object Oriented framework for all the LHCb software. It has a large flexibility which allows the LHCb software chain from the MONTE-CARLO generation to data analysis to use the same tools. The main subsystems are briefly described.

GAUSS : The validation of a physics analysis or a reconstruction scheme have to be validated using MONTE-CARLO simulation. For that purpose the LHCb collaboration uses its own software, called GAUSS [58], to simulate all the physical aspects of a pp collision in the LHCb detector. The first step is the generation of physics events at the interaction point. The software uses the PYTHIA program [59] to produce the collision, the generated particles and their corresponding momentum four-vectors. The produced particles are then decayed with PYTHIA or through a LHCb tuned EVTGEN package [60] (for the b -physics dedicated

physics). The second phase is the detector interaction which is done with GEANT4 [61]. GEANT4 is used to transport the particles through the detector. A full description of the detector geometry and materials is stored in a database.

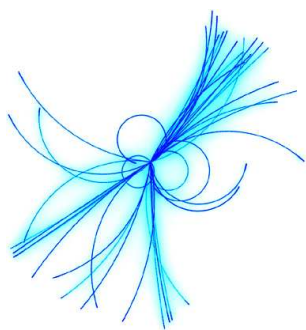
BOOLE : BOOLE [62] performs digitisation of the energy depositions. The L0 Triggers is also simulated. The digitisation takes into account the spill-over which is the interference from the previous or the next pp event. At this point the output raw MONTE CARLO data mimic the real data and can be reconstructed with the same program.

BRUNEL : The reconstruction of real or MONTE-CARLO events is done by BRUNEL [63] (see section 3.3). The output is saved in DSTs (explained in section 3.7.1) that are then used in the analysis programs.

DAVINCI : The analysis program and selection tools are contained in DAVINCI [64]. The particle identification (section 3.4) which gives the mass to the particles, is included in this program, as well as functions for vertex fitting and other algorithms for the end-users.

4

Direct Search for Standard Model-Like Higgs Boson



The capability of the LHCb detector to distinguish displaced vertices with respect to the interaction point is necessary to study CP violation in the B -meson system. This feature leads to the idea of using the LHCb detector in order to study the light Higgs sector decaying into a b -quark pair. The high-resolution Vertex Locator, situated around the interaction point at LHCb, is ergo the advantage that LHCb has in comparison to the other experiments to identify $H \rightarrow b\bar{b}$ decay.

Light Higgs decay predominantly into a b -quark pair. The LHCb detector is limited in its solid angle acceptance and its low instantaneous luminosity, but these limitations do not affect the study of CP-violation in the B -meson sector, one of LHCb's main purpose. In order to study this phenomenon, it is necessary to locate the decay vertices of the b -hadrons and therefore the precise Vertex Locator is imperative. The VeLo plays one of the most important roles in the LHCb experiment, allows to distinguish vertices with a good spatial resolution and to measure time of flight. Higgs decay studies at LHCb are therefore based on its capability to detect displaced vertices.

Historically, the idea to use the LHCb detector to study Higgs events at LHC has begun with the PhD thesis of Charles Currat [65] in 2001. His work pioneered a setup for the simulation and the analysis of Higgs events and *hard jets* in the LHCb detector. The studies were carried out in the framework of SICB, the ancestor of the present full simulation program. The studies showed that the accessible channels at LHCb are $HW^\pm \rightarrow b\bar{b} + \ell^\pm (\bar{\nu}_\ell^-)$ and $HZ^0 \rightarrow b\bar{b} + \ell^+\ell^-$. His results demonstrated that the LHCb detector design allows to efficiently identify, reconstruct and trigger the b -jets coming from the Higgs. He designed a “fast simulation” which included the relevant detector effects (such as the acceptance) which was used in particular to simulate the huge amount of $b\bar{b}$ background. This work set the base for the b -jet analysis within LHCb. Laurent Locatelli [66], in 2007, continued the analysis to assess the feasibility to discover a Higgs boson with intermediate mass at LHCb. This second study concentrated on pure four-vector level information from the generator. Two different jet reconstruction algorithms have been used

and tested, the cone algorithm (Section 4.3.1) and the K_T algorithm (Section 4.3.2). In parallel to the reconstruction of the Higgs events, several important background channels were studied ($t\bar{t} \rightarrow bW^+ \bar{b}W^-$, $Z^0W^\pm \rightarrow b\bar{b} + \ell^\pm \bar{\nu}_\ell$, $Z^0Z^0 \rightarrow b\bar{b} + \ell^+\ell^-$, $W^\pm + 2b$, $\gamma^*/Z^0 + 2b$ and generic $b\bar{b}$). The aim was to find and exploit discriminating variables which behave differently for Higgs signal and background sources. In particular, a neural network technique has been used to discriminate the signal from background events. This second study has obtained, with the improvement of the neural network, a significance $S/\sqrt{B} = 0.59$ for an integrated luminosity of $\int \mathcal{L} = 2 \text{ fb}^{-1}$ which is in agreement to the first significance calculated by Charles Currat ($S/\sqrt{B} \sim 0.7$). A third analysis was performed on this Higgs channel by Victor Coco [67]. A full and complete simulation of the events was performed within the new LHCb software framework. This study is a similar analysis to the one presented here. The main difference is the reconstruction algorithm. The K_T algorithm was used in Coco's analysis, whereas a combination of the cone algorithm and a seed finder are used in the present study. Coco's study concludes with a significance of $S/\sqrt{B} \sim 0.34$ for a Higgs mass $m_H = 120 \text{ GeV}/c^2$ and an integrated luminosity of $\int \mathcal{L} = 2 \text{ fb}^{-1}$.

4.1 Phenomenology and Topology

In order to understand the phenomenology and the underlying topology of the Higgs events, it is important to introduce some aspects of QCD and in particular the definition of jets. Since the *Deep Inelastic Scattering* (DIS) experiments have revealed the existence of an internal structure in nucleons, a *parton model* has been developed. Subsequently, the parton theoretical model has been developed to explain this structure. The partons can be identified with the elementary particles currently known as quarks. The fruitless searches for free quarks, which hint at the concept of quark confinement, point towards the existence of “string” forces, while the scaling from DIS to electromagnetic scattering computation at low-order calls for weakly-bound partons. The perturbative QCD and asymptotic freedom models take into account both of these features.

4.1.1 QCD, Asymptotic Freedom and Confinement

The quarks and gluons carry a charge of colour that leads to interaction between them (qq , gg or qg). Furthermore, the coupling constant of the strong interaction, α_s , is affected by loop corrections. The constant α_s depends on the measurement energy μ^2 and since QCD should be renormalisable, it should not be influenced by the renormalisation scale. This leads to the essential feature of QCD, known as asymptotic freedom [68, 69], which stipulates that the strong interaction coupling decreases at short distances. This fact was first discovered in the early 1970s by David Politzer and by Frank Wilczek and David Gross who received the Nobel Prize for this discovery in 2004.

Asymptotic freedom determines that the renormalised QCD coupling is small only at high energy. The running coupling constant α_s is determined by the renormalisation group equation [70]:

$$\mu^2 \frac{\partial \alpha_s}{\partial \mu^2} = \beta(\alpha_s) \quad (4.1)$$

The QCD β -function¹ gets the following perturbative expansion:

$$\begin{aligned}\beta(\alpha_s) &= -b\alpha_s^2(1 + b'\alpha_s + b''\alpha_s + O(\alpha_s^3)), \\ b &= \frac{33 - 2n_f}{12\pi}, \\ b' &= \frac{153 - 19n_f}{2\pi(33 - n_f)}, \\ b'' &= \frac{77139 - 15099n_f + 325n_f^2}{288\pi^2(33 - n_f)},\end{aligned}\tag{4.2}$$

where n_f is the number of quarks with a mass less than the energy scale μ . The b term corresponds to the one-loop contributions, while b' is the two-loop and b'' the three-loop contributions. The leading term of the β -function, $-(11/4\pi) \cdot \alpha_s^2$, can be understood as a polarisation of gluon loops that creates an anti-screening effect on the colour charge in the QCD vacuum which increases the colour charge. The second term, $(n_f/6\pi) \cdot \alpha_s^2$, corresponds to one or several colourless quark-antiquark loops which screen the colour charge.

The renormalisation introduces a second mass term, Λ , that can be a parameter of arbitrary dimension which corresponds to the mass scale at which the subtractions removing the ultraviolet divergences are performed. The result is that the running coupling $\alpha_s(\mu^2)$ depends on the choice of the Λ parameter, which is usually defined as:

$$\ln \frac{\mu^2}{\Lambda^2} = - \int_{\alpha_s(\mu^2)}^{\infty} \frac{dx}{\beta x}.\tag{4.3}$$

If the β -function terms are neglected above $n = 0$, and if $\alpha_s(\mu^2)$ and $\alpha_s(\Lambda^2)$ are in the perturbative region the series, then the leading order terms of the β -function as a function of the Λ parameter can be truncated to:

$$\alpha_s(\mu^2) = \frac{1}{\alpha_s(\Lambda^2) \cdot \left(\frac{33-2n_f}{12\pi}\right) \cdot \ln\left(\frac{\mu^2}{\Lambda^2}\right)}.\tag{4.4}$$

This illustrates asymptotic freedom and the confinement property: $\alpha_s \rightarrow 0$ when $\mu \rightarrow \infty$ and strong couplings occur at $\mu \sim \Lambda$ (or $\mu \rightarrow 0$). This statement is true if the number of quark flavours, n_f , satisfies: $n_f < \frac{33}{2}$. In other words, the non-Abelian gauge bosons produce a dominating anti-screening effect that leads to the effect of confinement. So the coupling constant grows at large distances, while asymptotic freedom occurs at short.

The strong coupling is experimentally observed for different energy scales. Recent measurements are shown in Figure 4.1. The Z^0 boson mass is usually used as reference for energy scale, Λ , of the Z^0 boson mass: $\alpha_s(m_{Z^0}) \simeq 0.1176 \pm 0.0002$.

4.1.2 Hadronisation, Parton Shower and Jets in QCD

Quark confinement dominates at low energy; consequently, quarks form colourless hadrons such as mesons ($q\bar{q}$). When a quark-antiquark pair is produced in a hard process, the available

¹The β -function can also be written as the following series:

$$\begin{aligned}\mu^2 \frac{\partial \alpha_s}{\partial \mu^2} &= \beta(\alpha_s) = -\alpha_s \sum_{n=0}^{\infty} \beta_n \left(\frac{\alpha_s}{4\pi}\right)^{(n+1)} \\ \beta_0 &= 11 - \frac{2}{3}n_f, \beta_1 = 102 - \frac{38}{3}n_f, \beta_2 = \frac{2857}{2} - \frac{5033}{18}n_f + \frac{325}{27}n_f^2, \dots\end{aligned}$$

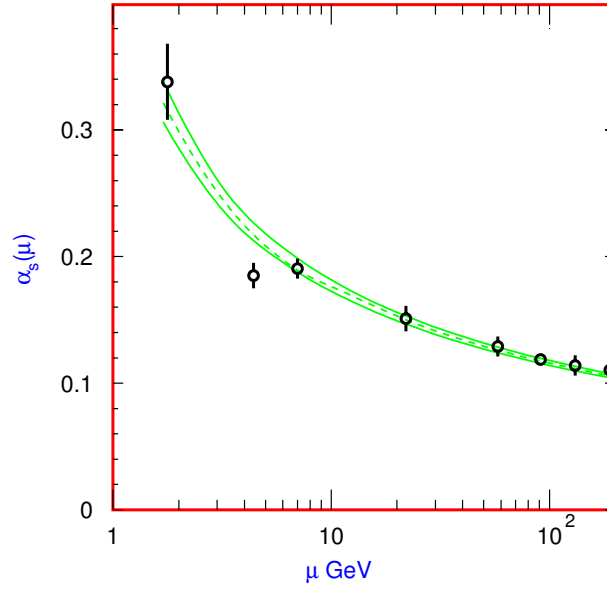


Figure 4.1: Measurements of $\alpha_s(\mu)$ in function of the energy μ where they are measured. The lines show the central values and the $\pm 1\sigma$ limits (from [1]).

kinematic energy can separate the two colour particles. When the distance between two quarks increases, the strong coupling due to the colour charges grows as a side effect of the confinement. The process can be illustrated as if the quarks were glued together with colour flux strings. When the distance grows between the colour particles, the flux is constant but the local energy density of the string increases until the production of quark-antiquark or gluon pairs from the QCD vacuum is energetically favoured. This phenomenon continues between the new pairs until the energy density in the colour flux strings is sufficient to create new pairs from the QCD vacuum. The created pairs are subsequently confined into colourless hadrons. Figure 4.2 illustrates the hadronisation.

Hadronisation is a long distance process, implying small transfers of momentum, therefore the energy flux at the hadron level is collinear to the energy flux of the outgoing quarks. Consequently, the resulting hadrons form a collimated **jet** that carries the momentum of the original parton. Another source of jets are the energetic quarks that can emit *hard*-gluons. This perturbative effect, called a *parton shower*, produces sets of gluons that subsequently hadronise.

In order to reconstruction quark-antiquark pairs decaying from the Higgs boson, it is necessary to be able to reconstruct the hadronic jets which come from the leading b quarks.

4.1.3 Signal $HW^\pm/Z^0 \rightarrow b\bar{b} + \ell$

The Feynman diagram, shown in Figure 4.3, illustrates the process of $HW^\pm/Z^0 \rightarrow b\bar{b} + \ell$.

In this study, the Higgs boson is assumed to have a mass between 115 GeV/c² and 140 GeV/c². Within this mass range, the dominant decay proceeds through a $b\bar{b}$ pair with a branching ratio between 50% and 75% (see Section 1.2.8 and Figure 1.9).

The motivation behind the focus of this study on this particular channel is related to the LHCb detector specifications. Indeed, it is dedicated to b -hadron physics and has a high efficiency to find secondary vertices coming from a b -hadron decay. The LHCb limited acceptance ($1.8 < \eta < 4.9$), the resolution of the electromagnetic calorimeter and the limited luminosity prevent classical direct Higgs searches such as $H \rightarrow \gamma\gamma$ or channels with large missing energy ($H \rightarrow$

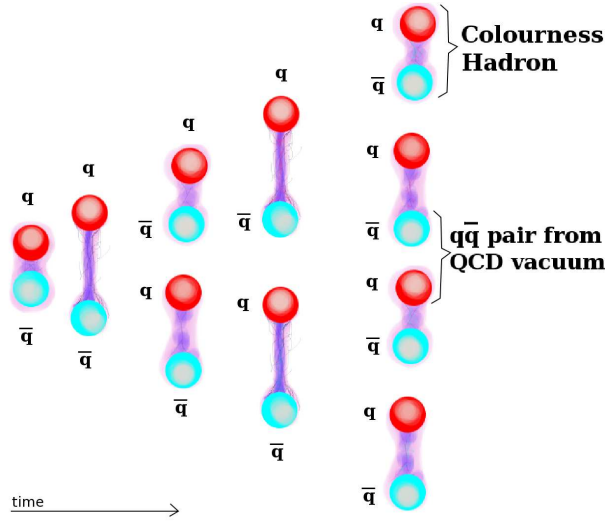


Figure 4.2: Illustration of the hadronisation of a colour flux string with creation of $q\bar{q}$ pairs from the QCD vacuum.

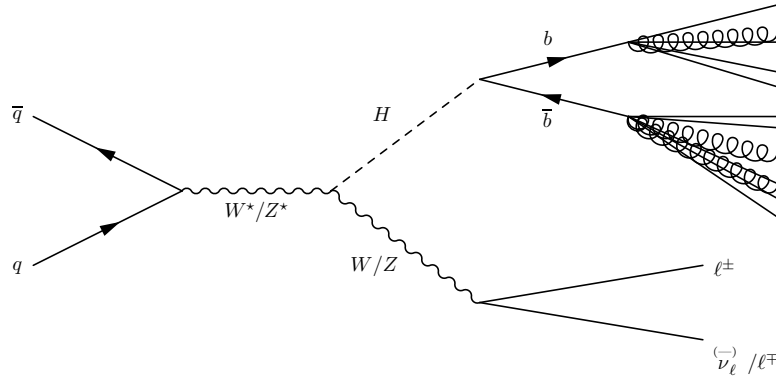


Figure 4.3: Feynman diagram of the signal event $HW^\pm/Z^0 \rightarrow b\bar{b} + \ell$

W^+W^-). The LHCb vertexing capabilities and b -tagging efficiency are extremely relevant to the reconstruction of the b -quark pair channel.

In $H \rightarrow b\bar{b}$, the two b -quarks are produced back to back in the Higgs boson rest frame. Each of the b -quarks initiates a parton shower which hadronises into colourless hadrons, one of which containing the leading b -quark. The parton shower then propagates forming a jet. Such jets are called b -jets. Two b -jets are therefore required to identify $H \rightarrow b\bar{b}$ decays.

While a large fraction ($\sim 30\%$) of the Standard Model Higgs bosons are produced within the LHCb acceptance, the fraction of the events where both the b -jet and \bar{b} -jet are within the acceptance is unfortunately below $\sim 30\%$ [65]. Figure 4.4 shows the pseudorapidity distributions for the Higgs and its decay products.

The signal event $H \rightarrow b\bar{b}$ produces jets that have to be extracted from a large QCD background. By focusing on the Higgs boson produced with associated gauge bosons (W^\pm/Z^0), a clear trigger signature can be defined. The leptonic decays of the vector bosons predominantly create isolated charged leptons. Hence a high p_T charged lepton is required in this analysis to reject the QCD backgrounds.

Finally, at the LHC nominal centre-of-mass energy and assuming a Higgs bosons of $m_H = 120 \text{ GeV}/c^2$, the cross sections of the associated production channels $q\bar{q} \rightarrow HW^\pm$ and $q\bar{q} \rightarrow HZ^0$

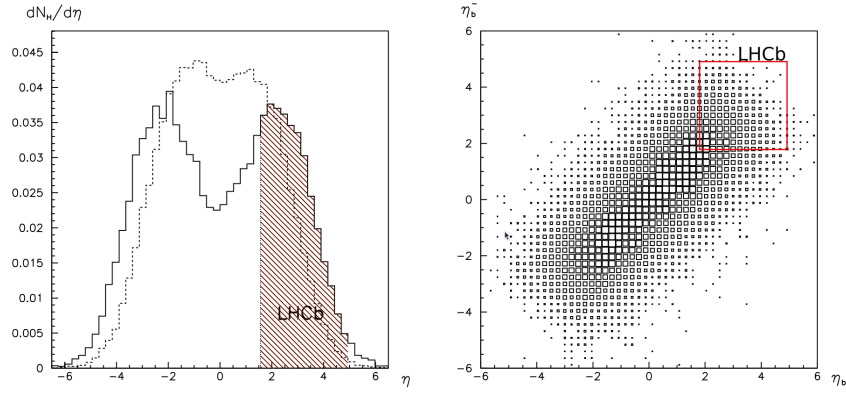


Figure 4.4: Pseudorapidity distribution (left) of the Higgs particle (solid line) and the final states particle from this decay (dashed line). Pseudorapidity of the b quark versus the \bar{b} quark (right) from the Higgs decay (from [65]).

are $\sigma(q\bar{q} \rightarrow HW^\pm) = 1.65 \text{ pb}$ and $\sigma(q\bar{q} \rightarrow HZ^0) = 0.89 \text{ pb}$ respectively [71]. Figure 4.5 shows predictions for those cross section including QCD corrections.

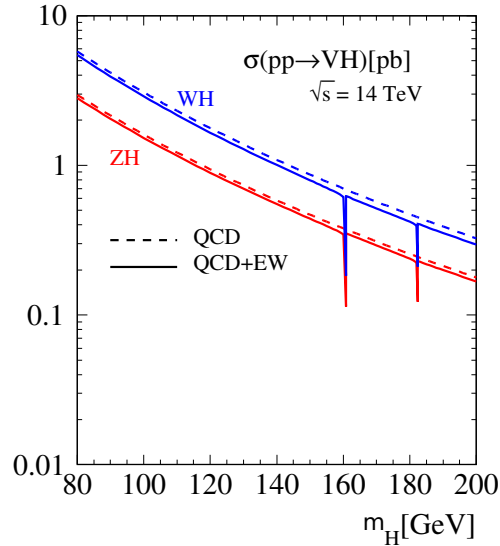


Figure 4.5: Cross section prediction for HW^\pm and HZ^0 at the LHC including NNLO QCD and EW corrections (using CTEQ6) (from [71]).

The branching ratio of the Higgs boson decaying into a $b\bar{b}$ quark pair is calculated for the same Higgs mass to be:

$$\text{BR}(H \rightarrow b\bar{b}) \simeq 67.2\%. \quad (4.5)$$

The branching fractions of the decay of the W^\pm and Z^0 vector bosons into final states composed of either of the two lightest charged leptons (e^\pm, μ^\pm) and its associated lepton are:

$$\begin{aligned} \text{BR}(W^\pm \rightarrow \ell^\pm \bar{\nu}_\ell) &= 21.32\%, \\ \text{BR}(Z^0 \rightarrow \ell^+ \ell^-) &= 6.74\%. \end{aligned} \quad (4.6)$$

The combination of these values gives reduced cross sections of:

$$\sigma(q\bar{q} \rightarrow HW^\pm \rightarrow b\bar{b} + \ell^\pm \bar{\nu}_\ell) = 0.237 \text{ pb}, \quad (4.7)$$

$$\sigma(q\bar{q} \rightarrow HZ^0 \rightarrow b\bar{b} + \ell^+ \ell^-) = 0.040 \text{ pb}. \quad (4.8)$$

4.1.4 Background: $t\bar{t}$, $Z^0 Z^0$, $W^\pm Z^0$, $Z^0 + b\text{-jets}$, $W^\pm + b\text{-jets}$, ...

The most problematic background events are those characterised by two b -jets and an isolated charged lepton in the final state which mimic signal events. In addition, light quark jets (u , d , c) have been studied because of the large production rate.

The following background processes have been considered:

- $t\bar{t} \rightarrow bW^+ \bar{b}W^-$:

The $t\bar{t}$ background is the most dangerous to deal with in a mass window around a Higgs mass of 120 GeV/c² when at least one of the W has a leptonic decay. It is produced in the hard process $q\bar{q} \rightarrow g \rightarrow t\bar{t}$ and the top quarks then decay to bottom quarks through the decay $t\bar{t} \rightarrow bW^+ \bar{b}W^-$ in the large majority of cases (99.83%). The cross section of $t\bar{t}$ production at the LHC is 560 pb at the leading order and 860 pb at NLO. Therefore the reduced cross section $\sigma(q\bar{q} \rightarrow g \rightarrow t\bar{t} \rightarrow bW^+ \bar{b}W^- \rightarrow b\bar{b} + \ell^\pm + X) = 119.4 \text{ pb}$ (183.4 pb for NLO). Unfortunately the typical missing energy of this decay cannot be determined in the LHCb detector as well as in 4π detectors. The worst case is when the two gauge bosons decay in leptonic final states, as illustrated in Figure 4.6.

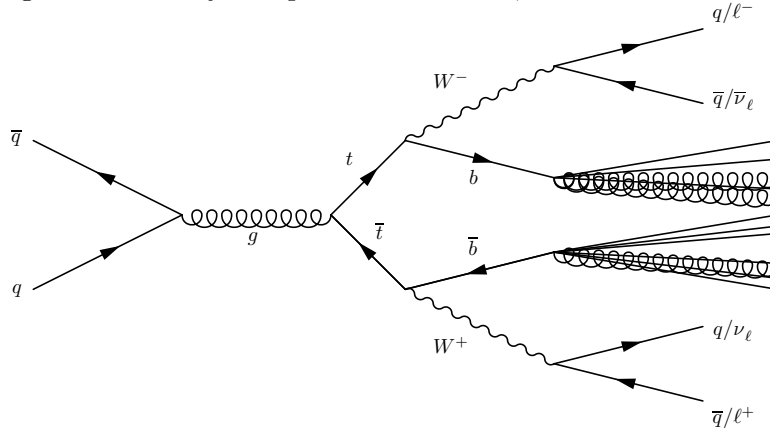


Figure 4.6: Feynman diagram of the background event $t\bar{t} \rightarrow bW^+ \bar{b}W^-$ producing two b -jets.

- $Z^0 V \rightarrow b\bar{b} + \ell$, where $V = Z^0$ or W^\pm :

These decays are irreducible with respect to the signal $HW^\pm/Z^0 \rightarrow b\bar{b} + \ell$. They produce the same kind of signal but with a smaller dijet mass in these cases. The other difference is the scalar or vectorial nature of the emitted boson of the offshell vector bosons. A statistical separation may be possible based on an angular analysis of VV and VH . These events have respectively a cross section of $\sigma(Z^0 W^\pm \rightarrow b\bar{b} + \ell) = 0.863 \text{ pb}$ and $\sigma(Z^0 Z^0 \rightarrow b\bar{b} + \ell) = 0.77 \text{ pb}$.

- $b\bar{b}$:

The $b\bar{b}$ background has a large cross section $\sigma_{b\bar{b}} = 0.698 \text{ mb}$ and is produced in hard QCD interactions, such as the gluon fusion or $q\bar{q}$ annihilation. The presence of an isolated high- p_T lepton is rare.

- $W^\pm + b$ -jets and $\gamma^*/Z^0 + b$ -jets:

The final states mimic those of signal events. $W^\pm + b$ -jets arise when a W^\pm is produced in association with a gluon decaying into $b\bar{b}$, while $\gamma^*/Z^0 + b$ -jets comes from the $b\bar{b}$ background where one of the b -quarks emits a γ^*/Z^0 . The expected number of these events decreases exponentially with the dijet mass, therefore only the tail of the distribution remains.

- Additional sources of background:

There are some additional background channels that have yet not been studied such as: light jets with a misidentified muon, $W^\pm/Z^0 +$ light jets and $W^\pm/Z^0 (\rightarrow \tau (\rightarrow e \text{ or } \mu)) +$ jets. However, these are small sources of background in comparison to the other channels.

4.2 Generation of the Monte-Carlo Higgs and $t\bar{t}$ Events, and Single Quark Jets

MONTE-CARLO events have been generated through the LHCb simulation and digitisation software chain: GAUSS, BOOLE and BRUNEL as explained in Section 3.7.2.

Three versions of MC simulations have been used, labelled “10 TeV - lumi2”, “14 TeV - lumi2” and “14 TeV - lumi5”. The differences between those versions lies in the beam energies and the instantaneous luminosity: lumi2 represent the instantaneous luminosity that leads to a integrated luminosity on one year of 2fb^{-1} , while lumi5 is for 5fb^{-1} . All the event type of each version of the simulation have pass the whole LHCb software chain: GAUSS, BOOLE and BRUNEL. The event generator is PYTHIA 6.325.2 with the usual LHCb parameters and by changing the centre-of-mass energy and the instantaneous luminosity. In order to produce signal and background events in a efficient way, an external algorithm has been written that selects the most interesting events. To produce Higgs or $t\bar{t}$ from pp collisions, only the relevant Pythia subprocesses are switched on. In addition, only specific channels are enabled ($W \rightarrow \ell\nu, \dots$). The options used for the signal and the main background sources are summarised in Table 4.1.

The events created by Pythia then go through a special selection which retains only the events inside the LHCb detector acceptance. The Higgs events are requested to have a least one charged high- p_T lepton which decays from a gauge boson and within an enlarged LHCb acceptance ($\eta > 1.6$ and $p_T > 10 \text{ GeV}/c$). The only cut on the b -quarks is that they are required to fly in the forward region ($p_z > 0$). The cuts on all the background event types are strictly identical to ensure a global consistency between the samples.

All the cuts and cross sections of the generated events are summarised in the Table 4.2, together with the expected number of events for a nominal year and the simulated numbers of events.

In order to study the selection scheme on the jets, a tool called “jetgun”, which simulates single quark-jets within the LHCb experiment, has been developed. This kind of event is artificial: the jetgun places a quark of chosen flavor in the particle list of the Pythia generator setup for independent fragmentation. These jets have all been simulated in the “14 TeV - lumi2” configuration for all quarks and antiquarks, except for t and \bar{t} , with a flat distribution of original momentum between $20 \text{ GeV}/c$ and $3000 \text{ GeV}/c$ and flat azimuthal distributions spraying the whole detector acceptance. The simulation produced 10'000 of each species of quark or antiquark, but in order not to exceed too much the expected range of b quarks from Higgs, the analysis have been limited to jets with the generated quark momenta $P < 2000 \text{ GeV}/c$ and $P_t < 150 \text{ GeV}/c$.

		Production		Decay		Option
		MSUB	Description	MDME	Description	
signal	H events	24	$f_i \bar{f}_i \rightarrow H Z^0$	128	$Z^0 \rightarrow e^- e^+$	MSTP(7) = 6 $Q_k = t$
				130	$Z^0 \rightarrow \mu^- \mu^+$	
				160	$H \rightarrow b\bar{b}$	
		26	$f_i \bar{f}_i \rightarrow H W^\pm$	152	$W^\pm \rightarrow e^\pm \overset{(-)}{\nu}_e$	
				153	$W^\pm \rightarrow \mu^\pm \overset{(-)}{\nu}_\mu$	
background	$t\bar{t}$ events	81	$f_i \bar{f}_i \rightarrow Q_k \bar{Q}_k$		free to decay	MSTP(7) = 6 $Q_k = t$
		82	$gg \rightarrow Q_k \bar{Q}_k$			
	$Z^0 V$ events	22	$f_i \bar{f}_i \rightarrow Z^0 Z^0$	128	$Z^0 \rightarrow e^- e^+$	
				130	$Z^0 \rightarrow \mu^- \mu^+$	
				124	$Z^0 \rightarrow b\bar{b}$	
		23	$f_i \bar{f}_j \rightarrow Z^0 W^\pm$	152	$W^\pm \rightarrow e^\pm \overset{(-)}{\nu}_e$	
				153	$W^\pm \rightarrow \mu^\pm \overset{(-)}{\nu}_\mu$	

Table 4.1: Pythia options to create signal events and the main background sources.

Energy	Process	σ [pb]	$\sigma_{\text{red}}^{\text{MC09}}$ [pb]	$N_{\text{evts}}^{2\text{fb}^{-1}}$	$N_{\text{sim}}^{\text{lumi2}}$	$N_{\text{sim}}^{\text{lumi5}}$
10 TeV	$H Z^0 \rightarrow b\bar{b} + \ell^+ \ell^-$	0.02	0.145	0.028	56	224.8 k
	$H W^\pm \rightarrow b\bar{b} + \ell^\pm \overset{(-)}{\nu}_\ell$	0.125				
	$t\bar{t} \rightarrow b W^+ \bar{b} W^-$	240		10.5	21 k	922.4 k
	$Z^0 Z^0 \rightarrow b\bar{b} + \ell^+ \ell^-$	0.56		0.05	100	104.8 k
	$Z^0 W^\pm \rightarrow b\bar{b} + \ell^\pm \overset{(-)}{\nu}_\ell$	0.56		0.11	202	348 k
	$\gamma^*/Z^0 + 2b$	$4.5 \cdot 10^3$		29	58 k	132.8 k
	$W^\pm + 2b$	$5 \cdot 10^4$		32	64 k	122.6 k
	$b\bar{b}$	$69.8 \cdot 10^8$	–	–	3 M	
14 TeV	$H Z^0 \rightarrow b\bar{b} + \ell^+ \ell^-$	0.033	0.228	0.051	103	70.9 k
	$H W^\pm \rightarrow b\bar{b} + \ell^\pm \overset{(-)}{\nu}_\ell$	0.195				
	$t\bar{t} \rightarrow b W^+ \bar{b} W^-$	550		27	53.9 k	33.9 k
	$Z^0 Z^0 \rightarrow b\bar{b} + \ell^+ \ell^-$	0.85		0.08	160	38.1 k
	$Z^0 W^\pm \rightarrow b\bar{b} + \ell^\pm \overset{(-)}{\nu}_\ell$	0.86		0.15	300	23.2 k
	$\gamma^*/Z^0 + 2b$	$7.5 \cdot 10^3$		50	100 k	26.9 k
	$W^\pm + 2b$	$8 \cdot 10^4$		60	120 k	30.2 k

 Table 4.2: Reduced cross section (before and after generation cut) and number of expected events for signal and background per 2fb^{-1} .

ℓ stands for electron or muon. σ_{red} uses the generator cuts: the b with $p_Z > 0$ and $\eta_\ell > 1.6$.

4.3 Jet Algorithms and Beauty Tagging

Jets of particles are produced by the hadronisation of hard quarks and gluons (see section 4.1.2). Several algorithms are available for the identification of jets and for the determination of the associated four-momenta. Two algorithms are considered:

- the “cone algorithm” which integrates the energy deposited inside a cone of given radius R_{\max} defined in the $\eta - \phi$ space. The axis of the cone (the “seed”) must be provided by some *a priori* knowledge of the jet direction. In the case of b -jets this direction is obtained from the position of the secondary vertices found in the decay chain of the b -hadron (see subsection 4.3.1).
- the “ k_T algorithm” which looks for the nearest tracks in the $\eta - \phi$ space (see subsection 4.3.2).

The b -jet seed finder presented here is inspired from the one described in [65]. The study is MONTE-CARLO based. This analysis uses events of 120 GeV/ c^2 Higgs produced in association with a Z^0 or W^\pm , generated by Pythia and fully simulated, assuming a single interaction per event. The event selection requires a prompt and isolated lepton from W^\pm or Z^0 .

The events produced by the “jetgun” have been used in order to optimise the seed finder algorithm.

The seed algorithm must tag the b -jet with the optimal efficiency and purity and provide the direction for the cone algorithm which will result in the best jet momentum resolution.

In the present study, at the level of single events a comparison of the seed found with the MC truth can follow 3 possibilities: the comparison can be done with the direction of:

1. The b quark just after Higgs decay,
2. The b quark after parton shower (in the string),
3. The corresponding b hadron.

Nevertheless the difference in direction is normally not very large, of the order of 1° degree, as shown in figure 4.7 for the b -jets from Higgs decay. As expected, the hadron direction is very close to the b quark leading the string. Deviations are expected to be large in case of hard gluon emission, i. e. for events with more than 2 b -jets, in which case a poor energy estimate is unavoidable.

4.3.1 The VV Seed Finder Algorithm

The goal of VV Seed Finder is to identify jets which can be associated to the hadronization of b quarks (the “VV” name is to indicate the jets that the algorithm is designed to find). It consists in identifying all displaced vertices in the event, therefore all possible 2-tracks vertices are formed, and grouped in subsets of similar direction with respect to the primary vertex (V^0). Each set is then used to infer an average vector which is taken to be the seed. In this section only the events with an unique interaction per bunch crossing are considered, so there is no ambiguity in the definition of V^0 . But the algorithm has been adapted for the case of several V^0 . In these cases, only the V^0 with the biggest sum of transverse momentum of tracks is kept and all the non-associated tracks are deleted.

The procedure VV is subdivided in 7 phases.

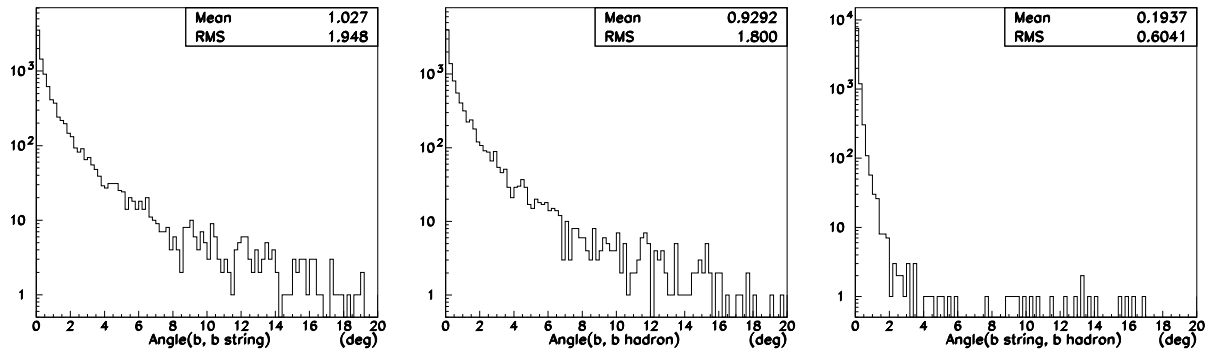


Figure 4.7: Left: angle from the b quark from Higgs to the b quark before hadronization. Middle: angle from the b quark from Higgs to the b hadron. Right: angle from the b quark before hadronization to the b hadron.

Phase 1, tracks selection

Tracks are selected with $p_T > p_T^{\min}$. “Ghosts” (spurious tracks) are filter from the set. The plots for the transverse momenta are given in figure 4.8.

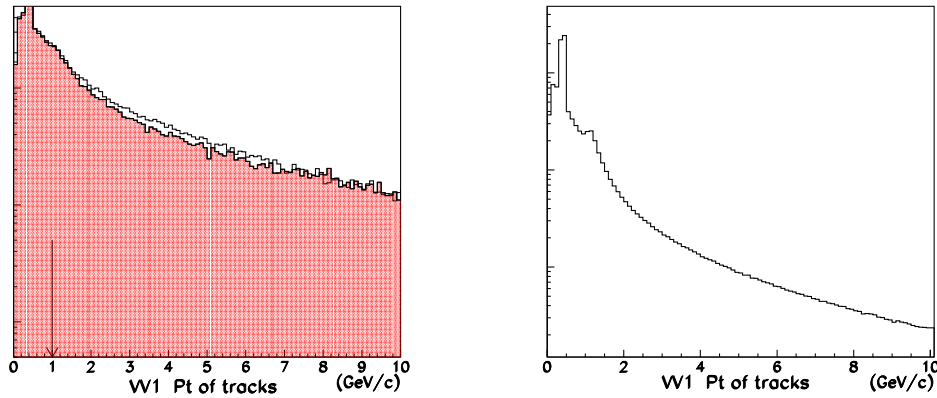


Figure 4.8: p_T of tracks. Left: events from the jetgun for b (black) and u quarks (in red, filled), right: from Higgs decay

The arrow indicates the typical cut $p_T^{\min} = 1$ GeV/c. The results for b -jetgun data is on the left, and from u jets (in red, filled). The two plots are normalised to the same area. On the right the plot from Higgs decays.

After p_T selection, the Impact Parameters (IP) to V^0 is calculated for each track (for jetgun data, V^0 is the generated origin of the quark, smeared to reproduce the expected V^0 resolution). IP and its significance $IPS \equiv IP/\sigma(IP)$ are shown in figure 4.9. Tacks are selected with $IP > IP_{\min} = 0.1\text{mm}$, and $IP/\sigma(IP) > IP_{sig}^{\min} = 3$.

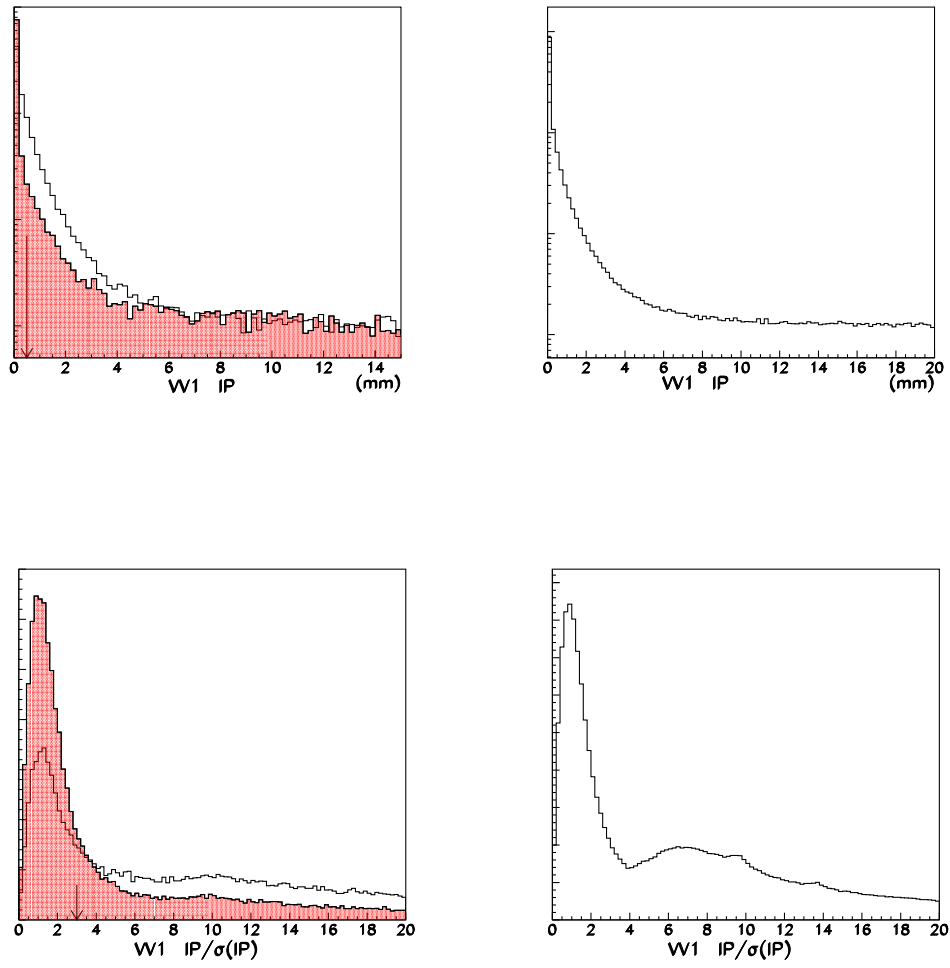


Figure 4.9: Top: IP of tracks. Bottom: IP significance, $IP/\sigma(IP)$

Phase 2, K^0 rejection

In order to reduce the K^0 background, the pairs of tracks fulfilling the following criteria are discarded: invariant mass compatible with the K^0 mass within 10 MeV/c² and Distance of Closest Approach (DCA) of the two tracks less than 0.5 mm.

The statistics of the number of tracks selected at this stage is shown in figure 4.10. Given the fact that the Higgs data contains at least two b -jets plus the underlying event, it is normal to have more tracks than with single b -jets.

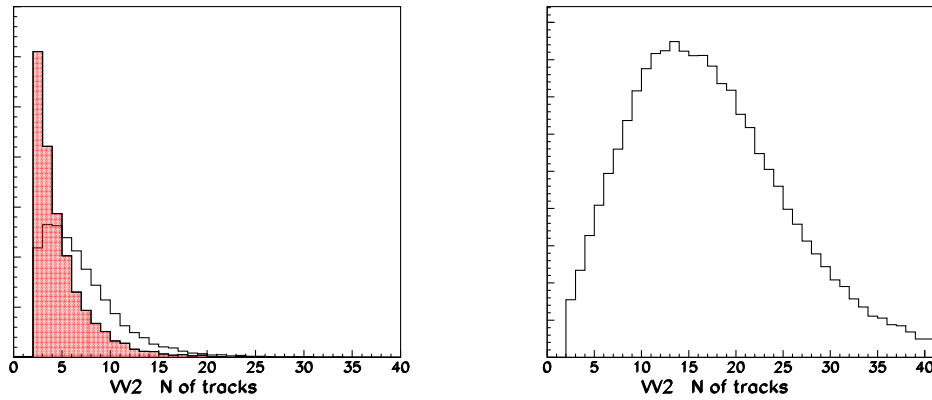


Figure 4.10: Number of tracks selected after Phase 2

Phase 3, Search of Displaced Vertices

Figure 4.11 shows the DCA distributions for the track-pairs. Track-pairs with $DCA < DCA_{\max} = 0.5$ mm are selected and used to form a candidate secondary vertex V^i . V^i is discarded if found upstream: it requires $V_z^i > V_z^0$. Moreover V^i are requested to have at least a minimal distance $d = |V^i - V^0|$ from the primary vertex $d > d_{\min} = 1.5$ mm, while the maximum is limited to the interesting decay region: $d < d_{\max} = 200$ mm. Similarly in the transverse plane where the radial distance is computed $r = |V^i - V^0|_t$, and required to satisfied: $r_{\min} < r < r_{\max}$, $r_{\min} = 0.1$ mm, $r_{\max} = 50$ mm.

The distance of flight is presented in figure 4.12, while the statistics of the number of V^i is shown in figure 4.13.

Phase 4, Construction of *Protojets*

A cone is defined in the $\eta - \phi$ plane in the direction (η_i, ϕ_i) with the following radius R :

$$R = \sqrt{(\eta_i - \eta)^2 + (\phi_i - \phi)^2} \quad (4.9)$$

The cone algorithm for each V^i constructs a “protojet” around the direction from the primary vertex to V^i , with a $\eta - \phi$ aperture $R_{\max} = 0.15$. The statistics of the number of protojets is shown in figure 4.14.

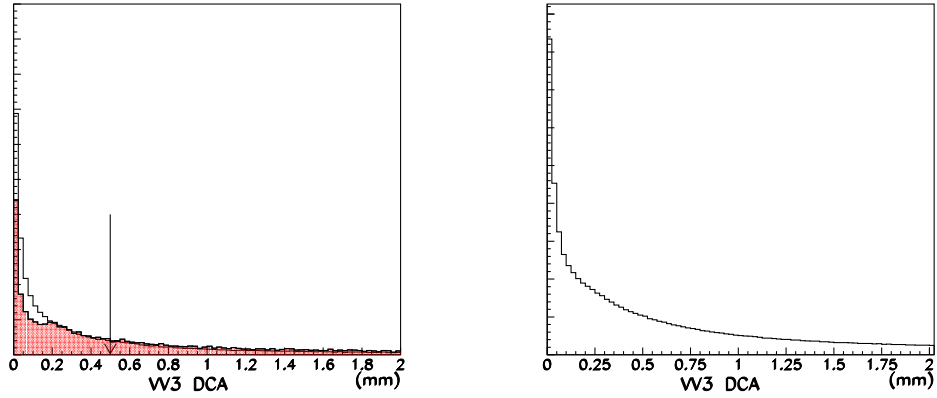
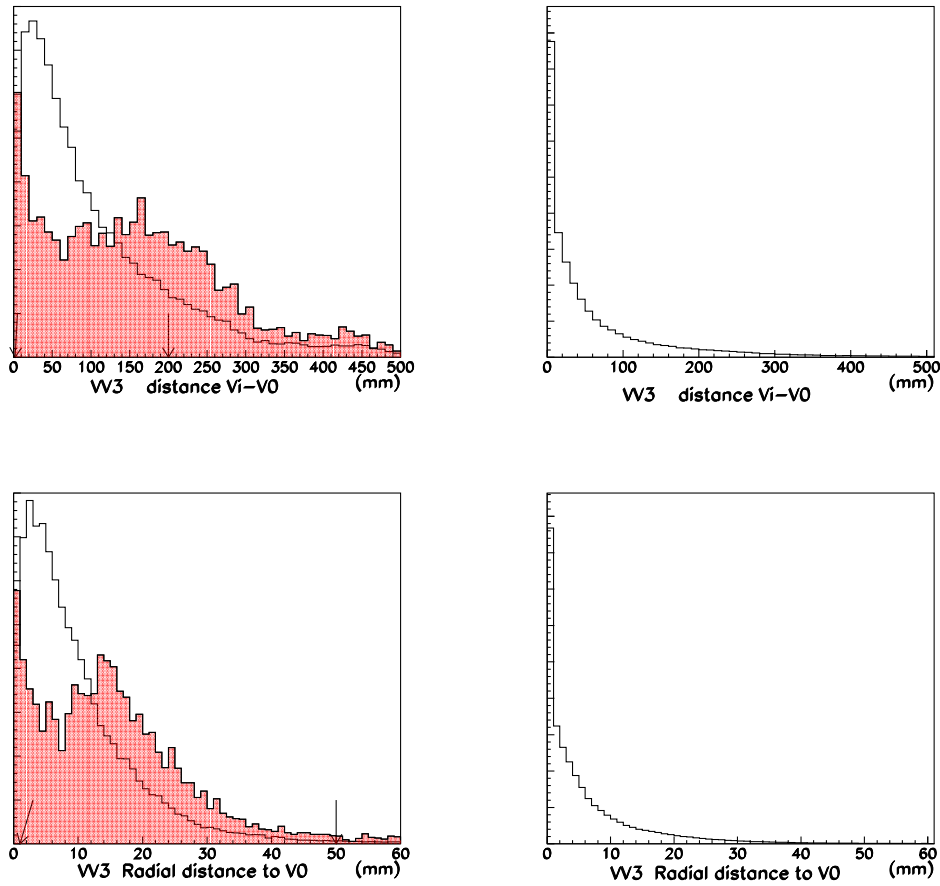


Figure 4.11: DCA of couples

Figure 4.12: Top: distance of flight $d = |V^i - V^0|$ in 3D, bottom: projected on the transverse plane $r = |(V^i - V^0)_t|$

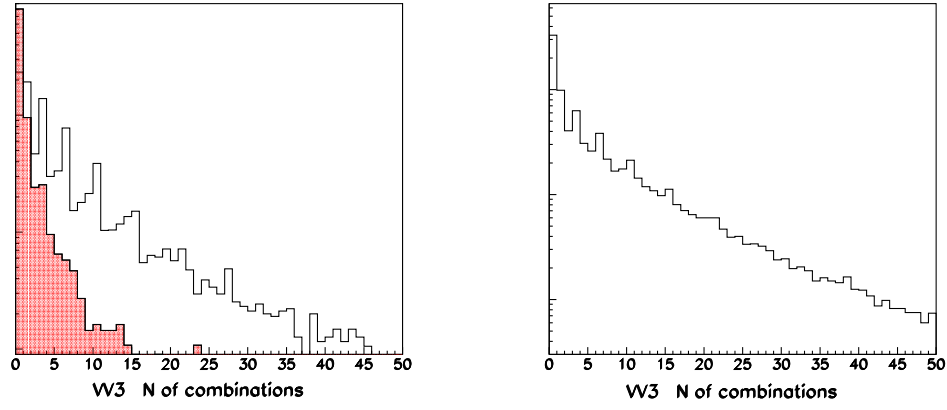


Figure 4.13: Number of selected track-pair combinations that make a valid V^i after Phase 3

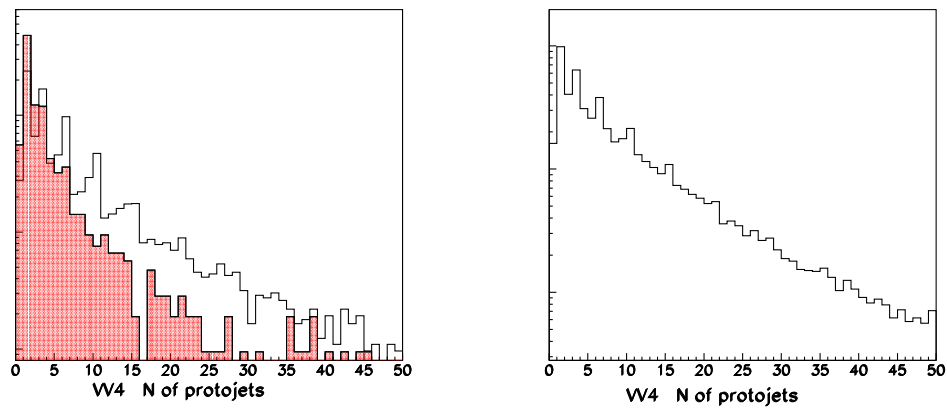


Figure 4.14: Number of protojets after Phase 4

Phase 5, Protojets Reduction

All the protojets are scanned by pairs and merged (i, j) when the $\eta - \phi$ distance is less than $\Delta R_{proto}^{\max} = 0.45$.

$$\Delta R = \sqrt{(\eta_i - \eta_j)^2 + (\phi_i - \phi_j)^2} \quad (4.10)$$

This value of ΔR_{proto}^{\max} was chosen because the cone radius for jet calculation is usually larger than 0.5. The procedure is done iteratively: the two closest protojets are merged, and the procedure continues until all the protojets have a distance larger than ΔR_{proto}^{\max} . The statistics of the number of protojets after grouping is shown in figure 4.15.

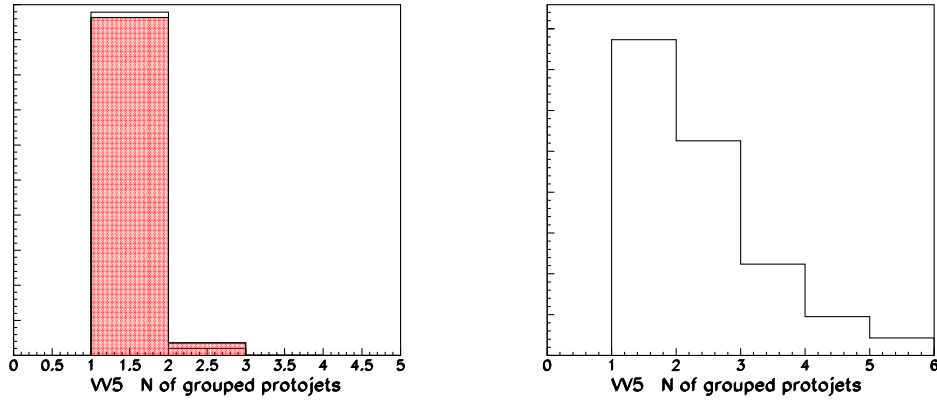


Figure 4.15: Final number of protojets after grouping in Phase 5

Phase 6, Seeds Selection

The direction of the protojet are recomputed with same R_{\max} as in Phase 4. Only the protojets that have when $p_T > p_{T_{seed}}^{\min} = 8 \text{ GeV}/c$ are kept, see figure 4.16. The protojets surviving are the “seed” candidates \mathbf{p}^i . The number of seeds per event that will be transferred to Phase 7 is shown in figure 4.17. It must be understood that already about 30% of b -jets have been lost at this stage, by the previous selection criteria. Note that in this histogram the first bin corresponding to zero seeds only represents the fraction discarded by the $p_T > p_{T_{seed}}^{\min}$ cut.

Phase 7, Seed Ordering

To this final phase the seeds are ordered in function of the number of V^i they contains. For seeds with the same number of V^i they are ordered in term of decreasing p_T . The best seeds are expected to have a large number of V^i in the associated jet. Figure 4.18 shows that there is some difference between the number of V^i produced by b -jets and what is found in the u jets which have survived.

Tests

From the b jetgun events and the set of cuts and parameter as indicated, the efficiency for finding at least one seed is about 68 %. The events were generated with flat quark momentum

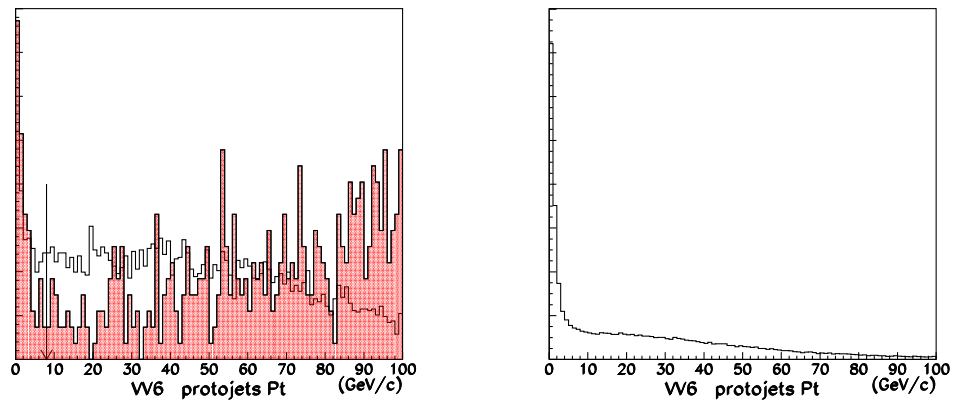
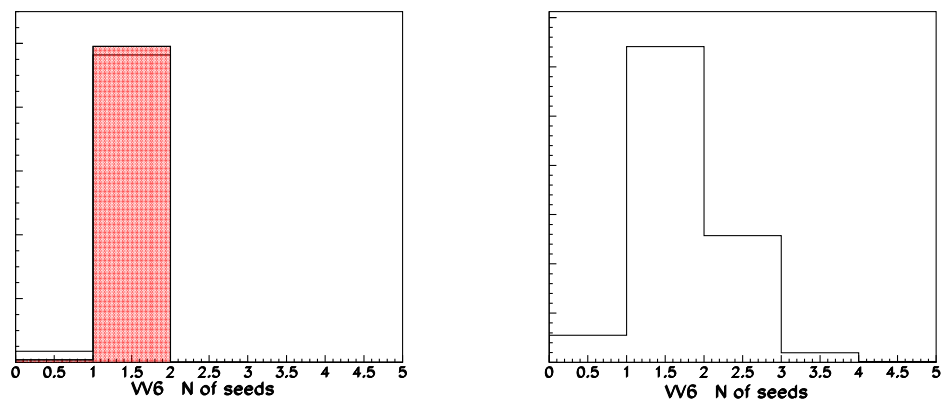
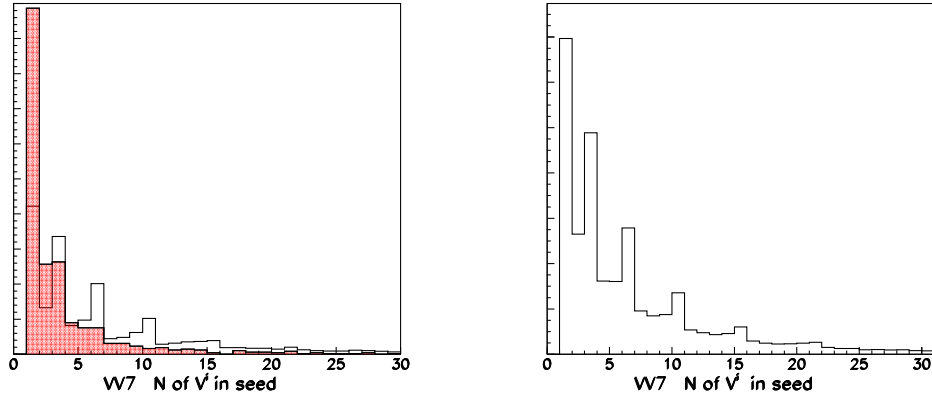
Figure 4.16: Protojets p_T distribution

Figure 4.17: Number of seeds per event after Phase 6

Figure 4.18: Number of V^i in each seed

and azimuthal angle distributions. The events have also been computed with weights function of the quark p and p_T to match the two-dimensional spectrum of b quarks produced from Higgs decay. If these weights are used in the calculation of the number of seeds, the efficiency to find the jet in b -jetgun data increase to 74%.

The selection have been tested on the Higgs events, selected to have two b quarks in the acceptance pseudorapidity window of $[1.9, 4.8]$. The distribution of number of seeds found in Higgs events is shown in the figure 4.19, together with the dijet reconstructed mass. 48% of the events have at least two seeds found, while 3% of events have more than two seeds. The extra seed number is controlled by the cone radius R_{\max} . A binomial distribution has been fitted, assuming two b quarks in the acceptance, plus a Poisson function to describe the source of extra seeds. The fitted binomial probability is $p = 0.66$, while the Poissonian component has $\mu = 0.08$. So the efficiency to find one seed is 66 %, which can be compared to the 74 % obtained with single jets. This deviation might come from the presence of an underlying event, or from the fragmentation model.

The angular separation of the seeds from the generated b quark is shown in figure 4.20. Its distribution is very close to the four-vector results of the first two histograms of figure 4.7 which show the separation between the b -quark, the b -string and the b -hadron. On the right figure the distance in $\eta - \phi$ space is given, with an average of 0.14.

The figure 4.21 displays the pseudorapidity distribution of all the b quarks, and for the events in which VV Seed Finder did not find seeds. For this analysis the pseudorapidity cut on the generated b quarks has been released. The difficult region is seen to be for $\eta < 2$ and a drop of efficiency at high η is observed.

In order to better understand the efficiency, the analysis has been restricted to an inner acceptance region requiring the b quarks to fall in the pseudorapidity window $[2.3, 3.5]$. With this restriction, the distribution of number of seeds found is shown in figure 4.22, left. The fraction of events with at least two seed is now approximately 56%, and 4% of the events have extra seeds. The fitted binomial average is $p = 0.74$.

As an alternative, during Phase 2 the possibility exists to search for triplets, instead of pairs of tracks compatible with a common vertex. Without any change in the parameters, and always with the restriction to the inner part of the detector, the fitted binomial average is $p = 0.58$, see figure 4.22, right.

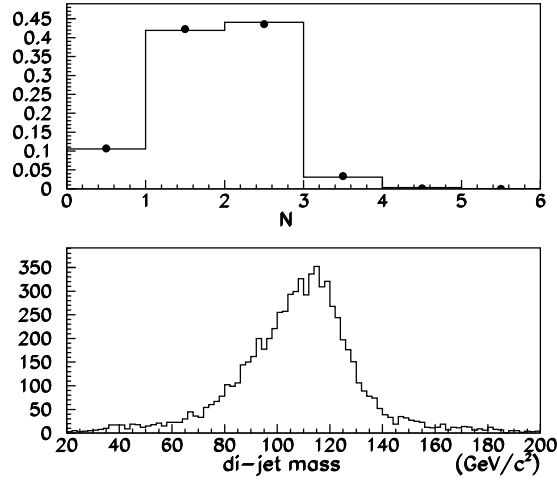


Figure 4.19: Top: distribution of the number of seeds found in Higgs events, the histogram normalised to 1 and the dots are the result of the fit described in the text. Bottom: the dijet mass reconstructed from the seeds and using the procedure described in section 4.3.3

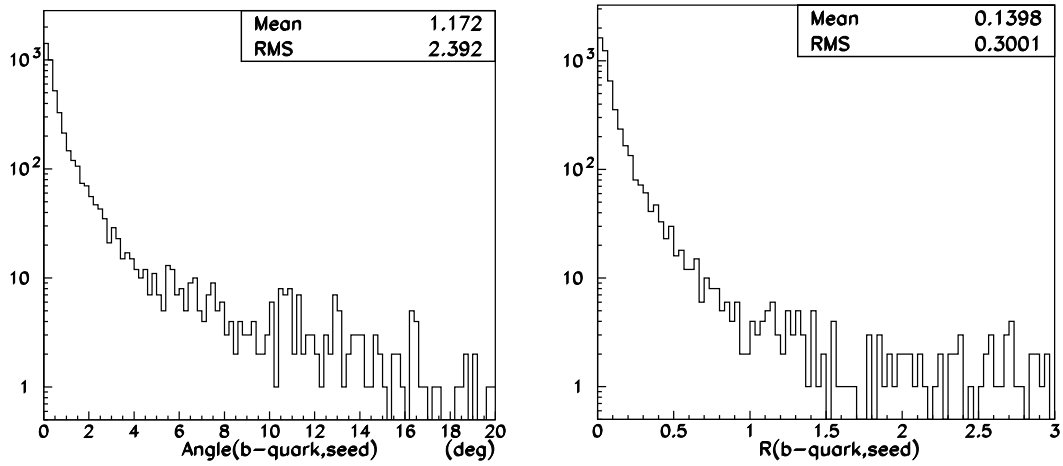


Figure 4.20: Left: angle between seed and b quark, right: distance in $\eta - \phi$ space

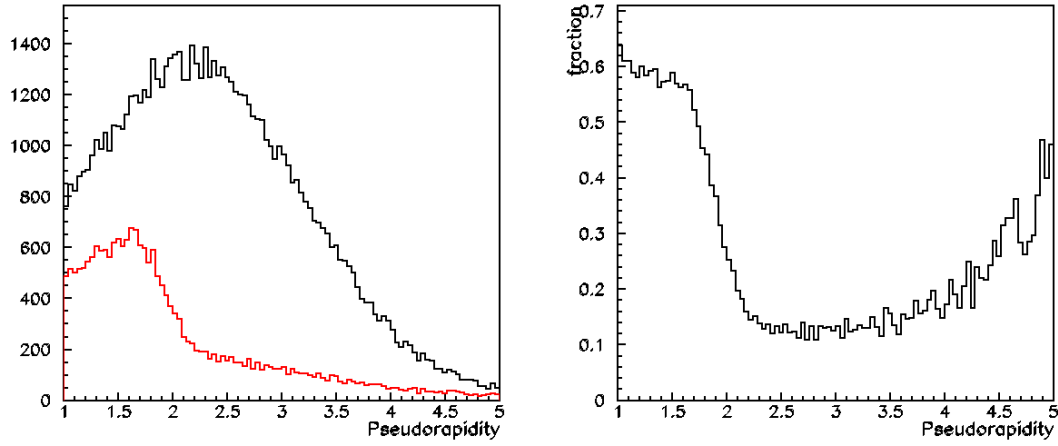


Figure 4.21: Left: Pseudorapidity of the generated b quarks. In red the pseudorapidity of the two b quarks for events with zero seed found. The fraction of events with zero seeds is shown on the right plot as function of pseudorapidity

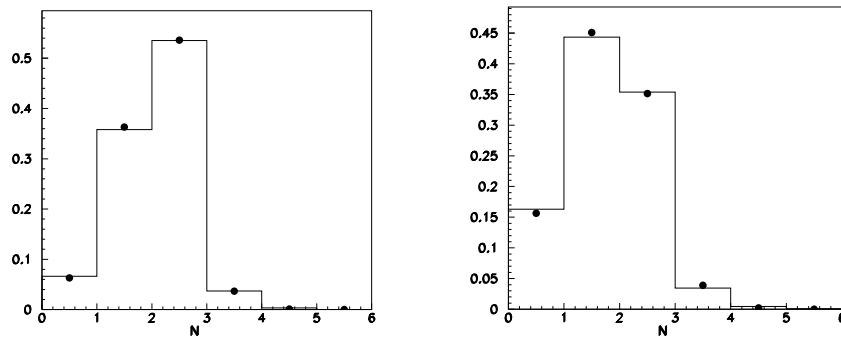


Figure 4.22: Number of seeds distribution in Higgs events, for b quarks in the inner part of the detector, $\eta = [2.3, 3.5]$. The histogram is normalised to 1. The dots are the result of a fit, see text. On the left the result using doublets of tracks, on the right using triplets

A further test was done by selecting “visible” Higgs events: as before the two b quarks are required to be in the inner rapidity region, and in addition the dijet invariant mass from MC truth is asked to be inside a $70 - 160 \text{ GeV}/c^2$ window (the seeds for the cone jet calculation with the MC four-vectors are given by the b quark direction, the particles outside acceptance and neutrinos are discarded). After this tight selection no significant change is observed in the number of seeds found. Figure 4.23 shows the seed number distribution, and the reconstructed dijet invariant mass obtained, the fitted value of p is 0.75.

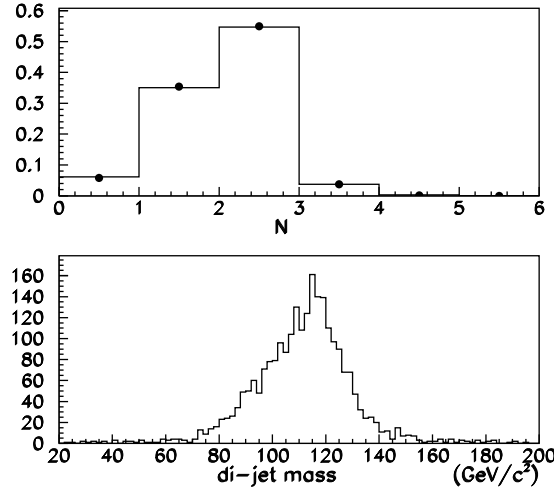


Figure 4.23: Top: N of seeds distribution after selection of the MC truth dijet mass value in $70-160 \text{ GeV}/c^2$. Bottom: reconstructed dijet mass

Light flavor (u , d and s) discrimination was assessed with the help of jetgun data. For an efficiency to b quarks of 68 %, the charm rejection is about 72 %, and lighter quarks rejection at the level of 90 %. These results have been obtained with quarks generated with flat momentum and azimuthal distributions. Re-weighting all the distributions as a function of p and p_T in order to match the distribution of the decay products of the Higgs, taking the same weights for all the flavors, the b acceptance is 0.74, as seen before, with no change for the other flavors. These results remain stable if the study is restricted to the inner detector region.

The choice of the VV Seed Finder parameters was inspired by previous studies, mainly discussed in [65]. The optimisation should be done by a scan over some ranges, the physical variables of interest plotted as a function of the parameter value. Examples are given in figures 4.24 and 4.25, where the variables shown are the p - and n -values fitted to the distributions of the number of seeds found. The analysis was performed with the same conditions as before, with an isolated lepton, and two b in the inner part of the detector. The choice of R_{max} lower than about 0.2 reduces the number of spurious seeds to a very small fraction, while the efficiency stays close to 75%. All the other plots have been obtained with $R_{\text{max}} = 0.15$. Another criterion is to improve the b -jet detection efficiency versus other flavors rejection, see figures 4.26 and 4.27. Here the jetgun data are used, with quarks in the inner part of the detector, and the results weighted to match p and p_T of the b quarks distribution from Higgs. It shows that a choice of the min IP significance of 40 gives 30 % efficiency and a 97 % rejection for c and u .

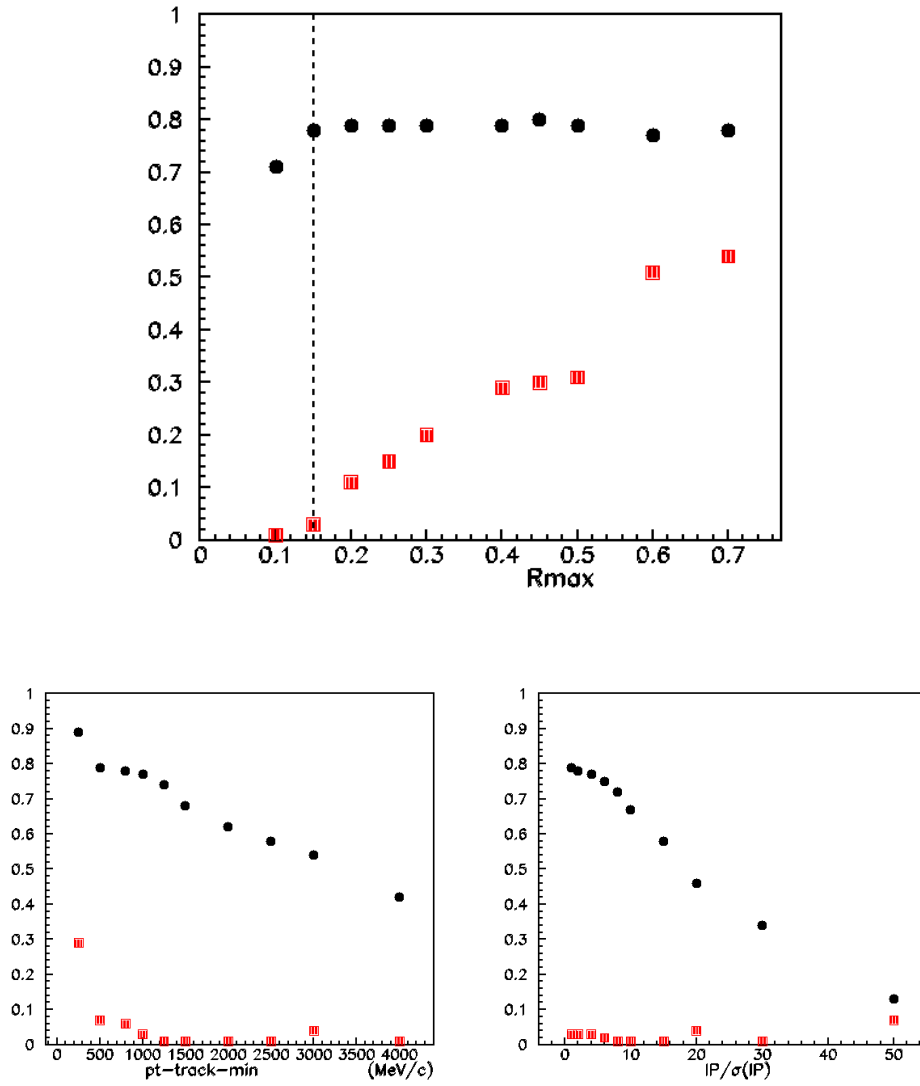


Figure 4.24: Fitted values of p (black dots) and n (red squares) as a function of various VV parameters. The top plot is for R_{\max} with the selected value shown by a dashed line. The other figures are, from top left to bottom right: tracks $p_{t\text{-min}}$, $IP_{\text{sig-min}}$.

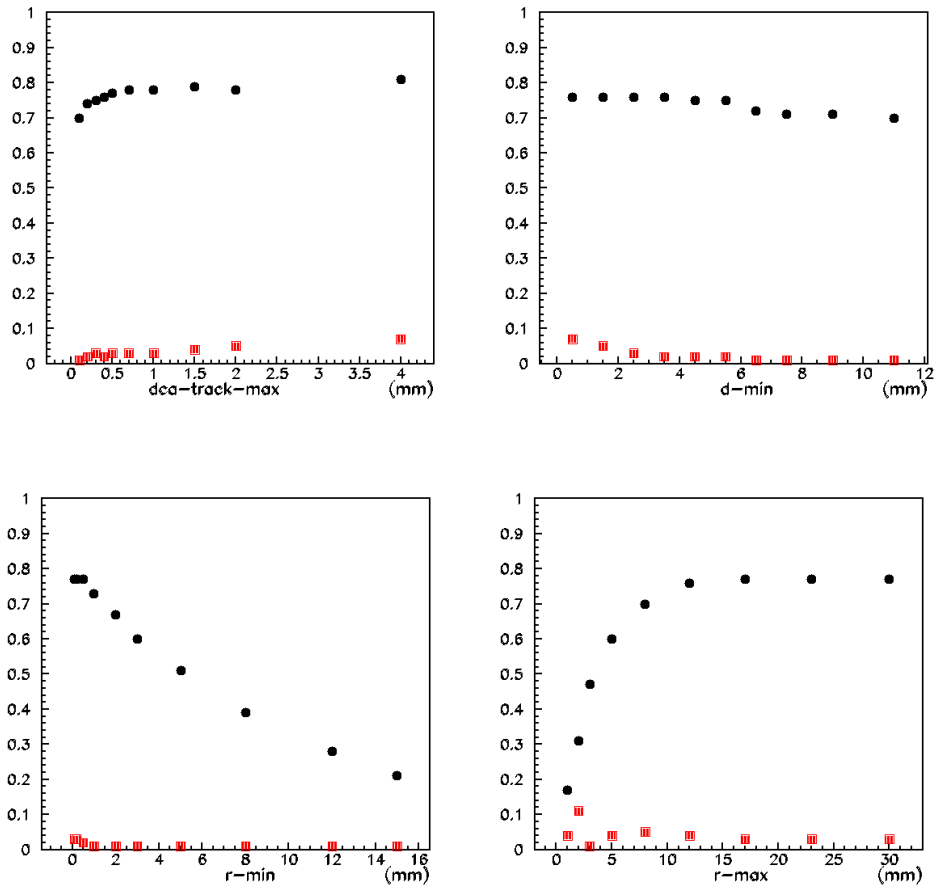


Figure 4.25: Fitted values of p (black dots) and n (red squares) as a function of various VV parameters. The figures are, from top left to bottom right: DCA_{\max} , d_{\min} , r_{\min} , and r_{\max}

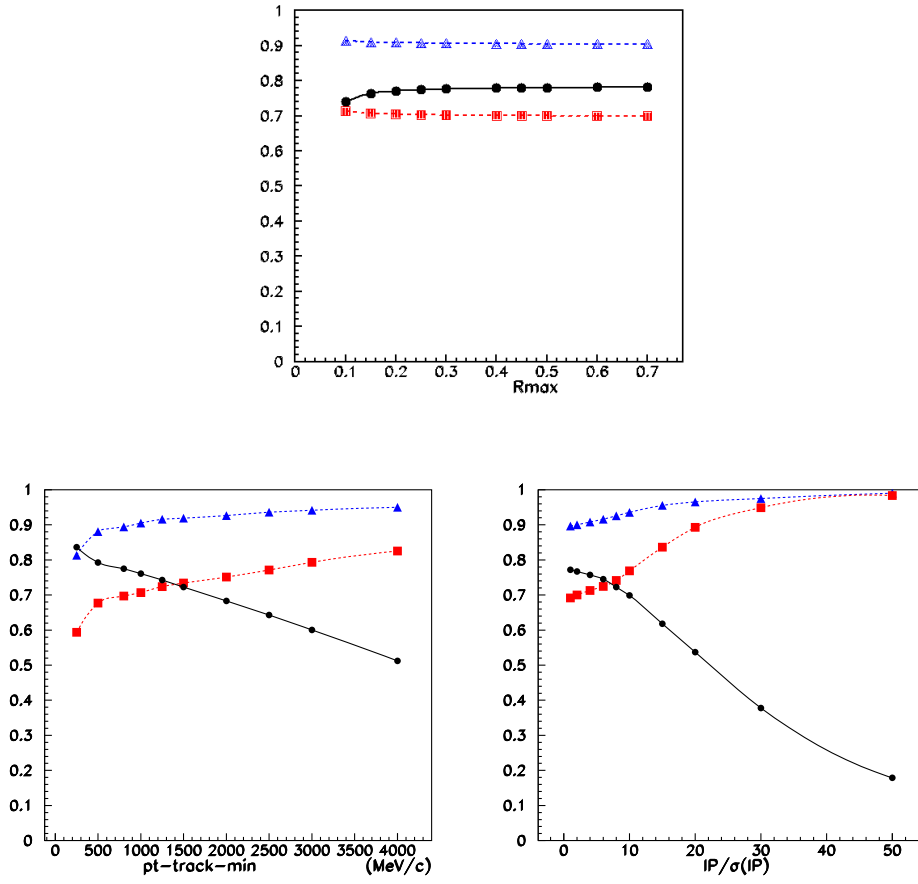


Figure 4.26: Selection yield for b -jets (dots) , and rejected fraction for c (squares) , and u (triangles), as a function of various VV parameters already presented in figure 4.24

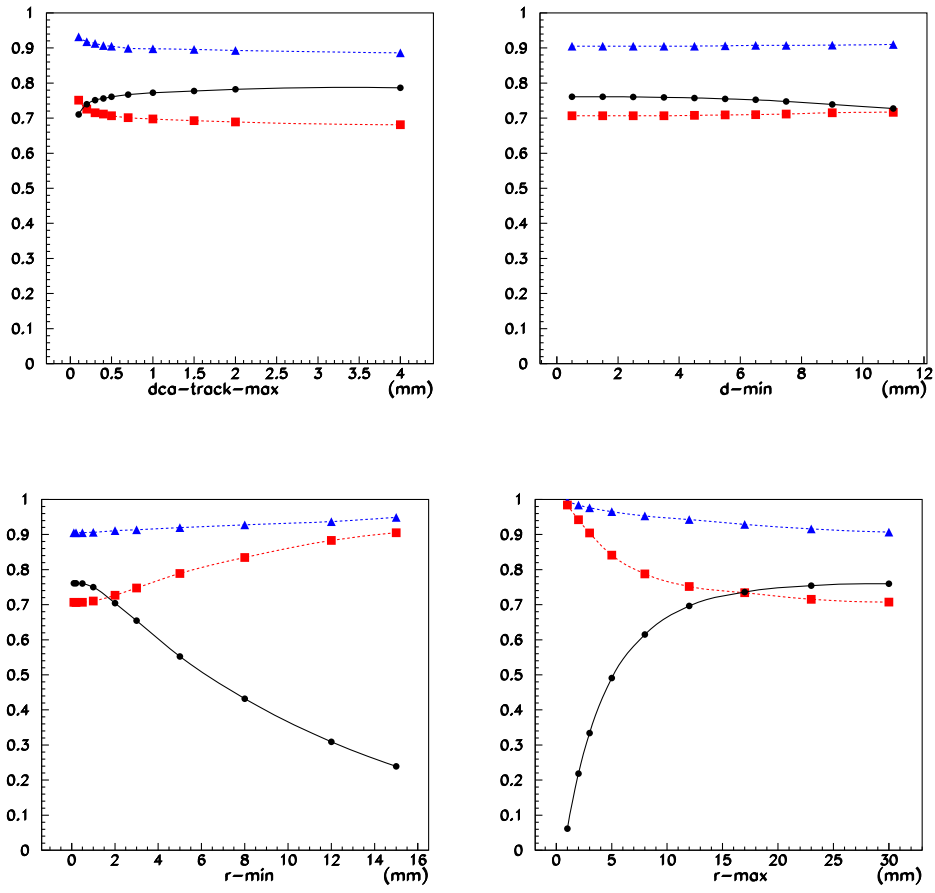


Figure 4.27: Selection yield for b -jets (dots) , and rejected fraction for c (squares) , and u (triangles), as a function of various VV parameters already presented in figure 4.24

Conclusion

The typical efficiency of VV Seed Finder to discover b -jets is of 70 %, while the rejection of jets initiated by c quarks is of about 70%, and 90 % for lighter quarks. For a reduced b efficiency of 30 % the other quarks are rejected in 97 % of cases. Enhanced flavour discrimination criteria could be addressed in further studies.

The angular precision to find the original b quark direction is about 1 degree, compatible with four-vector (generator level) predictions.

The parameters with their default values are also shown in the table 4.3.1 (except $d_{\min} = 2$. mm instead of 1.5).

Keyword	default value	name	meaning
General			
FilterPart	true		discard particles loaded twice
JetConeID	10098		PID of the seeds
VVNJetsMin	1		minimal n of seeds needed (to speed up calculation)
Phase 1			
VVPtTrackMin	1000 [MeV/c]	$P_{t-\min}$	p_T min for track selection
VVIPmin	0.1 [mm]	IP_{\min}	IP min for track selection
VVSignif	3.0	$IP_{\text{sig}-\min}$	IP significance min for track selection
Phase 2			
VVDMK0	10 [GeV/c ²]		window for K^0 rejection
VVDtrakMaxK0	0.5 [mm]		dca max for pions to form a K^0
Phase 3			
VVtriplets	0		use triplets of tracks when true, else doublets
VVDtrakMax	0.5 [mm]	DCA_{\max}	dca max for track doublets (triplets) to form a vertex V^i
VVChi2min	0		min χ^2 in vertex calculation
VVChi2max	1000		max χ^2
VVTseedVtxMin	2.0 [mm]	d_{\min}	minimal distance d to accept V^i
VVTseedVtxMax	200 [mm]	d_{\max}	maximal distance d
VVDRmin	0.1 [mm]	r_{\min}	minimal radial distance r to accept V^i
VVDRmax	50. [mm]	r_{\max}	maximal radial distance r
Phase 4			
VVRParameter	0.15	R_{\max}	radius in $\eta - \phi$ for “protojet” calculation
Phase 5			
VVDeltaRSeeds	0.45	$\Delta R_{\text{proto}}^{\max}$	min distance between couples of protojets, else merge
Phase 6			
VVPtSeedsMin	8000 [MeV/c]	$p_{T_{\text{seed}}}^{\min}$	min p_T of the seed

4.3.2 K_T Algorithm

A second algorithm is used to create jets in this analysis, the K_T algorithm which is an iterative clustering algorithm. The K_T jet finder combines the nearest particles in the (η, ϕ) . This recombination can be seen as the inverse reconstruction of the hadronisation process. The use of the transverse momentum p_T of the particle ensures that the invariance of K_T algorithm under boosts along the beam axis. The algorithm merges the particles into a protojet when they have nearly parallel momenta and then the operation is iterated. This jets reconstruction is performed in three steps:

1. For each particle, i , in the event, the algorithm defines a distance to the beam axis:

$$d_i = p_{T_i}^2$$

and for each possible pair $(i - j)$ of particle (or protojet) defines the following pseudo-distance:

$$d_{ij} = \min(p_{T_i}^2, p_{T_j}^2) \frac{\Delta R_{ij}^2}{R^2}$$

where $\Delta R_{ij}^2 = (\eta_i - \eta_j)^2 + (\phi_i - \phi_j)^2$ is the distance in the (η, ϕ) plan, and R^2 is the parameter which defines the characteristic size of the jets.

2. Search of the minimum between all the associated d_{ij} and d_i . If $d_{ij} < d_i$ the protojet i and j are combined together into a new protojet k by adding their Lorentz Vector. i and j are then erased from the list of protojets. If $d_i < d_{ij}$, i is considered to be a jet
3. Go back to the first step with the new list of protojets and continue this procedure until no more protojet are left.

Inside each jets, all the particles have distance smaller than R in the $\eta - \phi$ plane to each others, while the jets are separated with a distance bigger than R in the $\eta - \phi$ plane. This is comparable to the cone algorithm presented in the section 4.3.1. The K_T algorithm has been tested and compared to the other available algorithms, like the cone one associated to a seed finder, in the previous works [65, 66, 67]. It has to be mentioned that for a long time the disadvantage of this method was the execution time which was proportional to N^3 , where N is the number of particles in the event. This was due to the large number of iteration between the pair of protojets and particles. Some recent progress in the implementation of this algorithm (and some others) increases performance to $N \ln N$ which is also the kind of execution time of a cone algorithm [72, 73].

When only a jet is formed by the VV Seed Finder algorithm in the event, the K_T algorithm has been used to create a second set of jets in the analysed events. The K_T jets are termed “untagged” to differentiate them from the ones created with the seed finder (“tagged”).

4.3.3 Optimisation of b -jet Energy Measurement in LHCb

In order to precisely reconstruct the Higgs invariant mass, the two b -jets have to be measured with the best four-momentum resolution. The present section aims at obtaining the best b -jets energy resolution. The absolute calibration of the jets will be determined experimentally from hadronic Z^0 decays. This point is not considered here.

As it has been presented in the previous sections (4.3.1 and 4.3.2), several algorithms are available for the identification of jets and for the determination of the associated four-momenta. The jet energy measurement at LHCb has already been discussed in references [65, 66, 67]. The algorithm performance in terms of dijet invariant mass resolution is shown in figure 4.28, where the two b -jets are produced by the decay of an Higgs boson, with a mass of 120 GeV/c². The cone algorithm is used. The rise of the curve for R_{\max} larger than 0.5 is due to the increasing pollution from the “underlying event” (UE) particles. In the following, the default value will be $R_{\max} = 0.5$, close to the optimal resolution for Higgs events.

The energy flow in the cone delimited by R_{\max} is obtained from the tracking and calorimeters data, which suffer of several problems, specific to LHCb: in particular the LHCb detector acceptance is limited to a forward window of about [15, 300] mrad, and the calorimeter spectroscopic channels saturate for a transverse energy deposited above ~ 10 GeV/c.

In this implementation a jet cone algorithm collects around the seeds the information from all the sub-detectors (except RICHes) to compute the energy. This procedure requires some *ad hoc* weighting of each contribution and a global calibration, as explained at the end of this section.

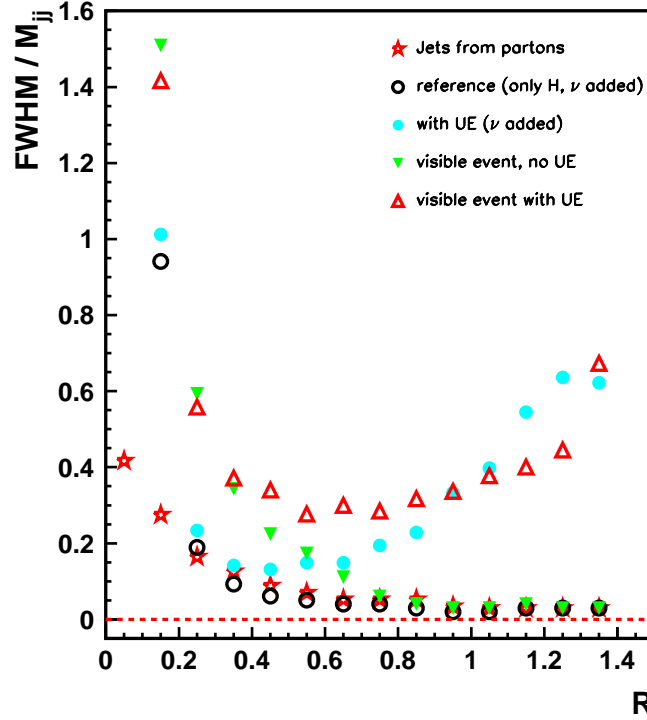


Figure 4.28: The Full Width at Half Maximum (FWHM) (normalised to the central value) of the dijet invariant mass distributions versus the resolution parameter R_{\max} . The stars represent the resolution when the two jets are computed using the partonic shower from the Higgs decay. At the other extreme, the open triangles show the resolution when stable particles are considered, neutrinos discarded, and the “underlying event” (UE) included. Three other situations are also presented: pure Higgs event, no UE, with neutrinos detected; Higgs plus UE, also with neutrinos detected; pure Higgs, no UE, neutrinos undetected (data from [67])

The energy deposited in each calorimeter cell is used to construct a pseudo-particle (zero mass) four-momentum pointing from the primary vertex to the centre of the cell, and size corresponding to the energy deposited. The pseudo-particle is discarded if falling outside the R_{\max} window. A “raw” jet four-momentum, p_{raw} (energy E_{raw}), is computed from the (unweighted) ECAL, HCAL, and muons four-momenta in the cone.

The DC06 Higgs events (see table 4.2) have been used in this study (only the study for an UE correction, presented at the end of this section, was limited at the generator level). Besides Higgs events, “jetgun” events have also been used.

Some plots obtained with the b -jetgun are shown in figure 4.29. They present the energies collected in the $R_{\max} = 0.5$ cone by the tracker, ECAL and HCAL, and E_{raw} in function of the HEP b quark energy.

The scatter plots shows that saturation affects the energy resolution starting from $E_b \sim 1$ TeV. Moreover the momenta from the magnetic spectrometer are also quite dispersed beyond 0.5–1 TeV. It can already be guessed that corrections η and energy dependent are needed in the procedure, justified by the observation that the probability of saturation grows with E_b and decreases with η .

What are the criteria for the algorithm optimisation ?

The final goal is to transform the raw detector information into a quantity suitable for

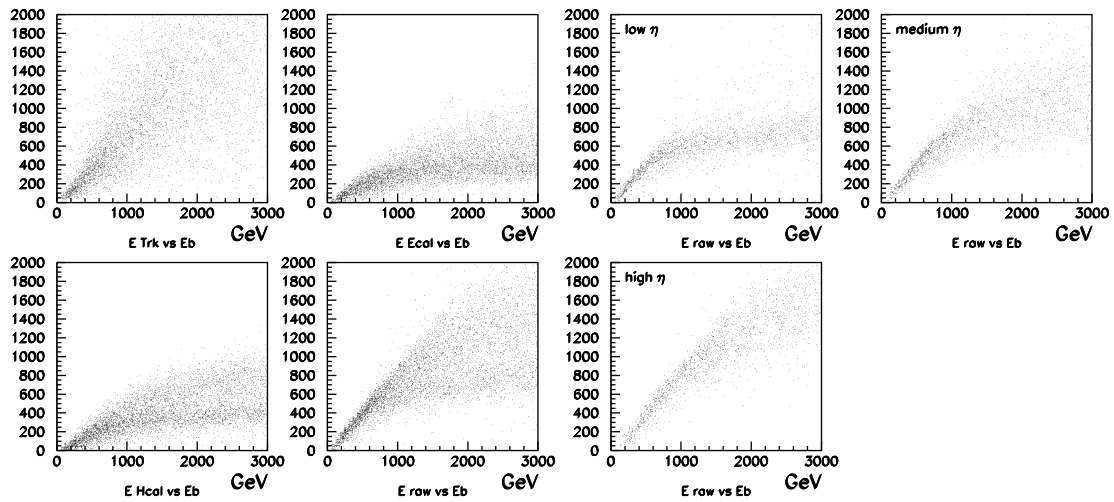


Figure 4.29: Left 4 scatter plots: energy in the cone measured by the tracker, ECAL, HCAL, and also the “raw” value $E_{\text{raw}} = \text{ECAL} + \text{HCAL} + \text{muons}$, vs the energy E_b of the quark. Right: E_{raw} vs E_b , for 3 pseudorapidity ranges: low: $\eta < 2.4$, medium: $2.4 < \eta < 2.8$, and high: $\eta > 2.8$

physics. Three different points of view of this problem have been considered.

1. In the most conservative approach the algorithm aims at reconstructing precisely the “visible” energy flow in the cone delimited by R_{max} :
in practice the energy of reference is inferred from the particle four-momenta known from MONTE-CARLO truth, the neutrinos are discarded and also all particles with trajectories outside the detector acceptance.
2. In a more involved approach, the acceptance cut is dropped:
then the algorithm is designed to correct also for the energy lost outside the detector.

In other words, the choice is given to setup the procedure to reproduce as precisely as possible the visible energy only, or to obtain the best approximation of the total energy flow in a cone which can partially lie outside the acceptance. The second option is the default one. Because the VV seed finder is considered, for seeds falling very close to the detector limits, the energy outside the acceptance is never more than $\sim 40\%$ of the total.

3. The third more radical approach is to ask the algorithm to guess the partonic energy. In the case of $H \rightarrow b\bar{b}$ the goal being to reconstruct the two b-quark four-momenta, in addition to detector effects the algorithm is required to correct for possible hard gluon emission, neutrinos, the presence of particles from the underlying event, etc...

The Neural Network

Given the complexity of the task, a Neural Network technique has been chosen to explore the different possibilities (for comparison, other simpler algorithms have also been tested, see next section 4.3.3).

The aim is to setup a general procedure to be called from the analysis code (DaVinci), individually for each jet. The variables are collected from long tracks and calorimeters as already explained. The following 17 variables are computed from the set of four-momenta constructed

from tracking, including muons, and from the channels hits in the PS, SPD, ECAL, and HCAL subdetectors (the names given in the following are the names of variables used in the code):

- 6 energies from tracking and calorimeters: ETRK, EPRS, ESPD, ECAL, HCAL, EMUS
- 6 masses: MTRK, MPRS, MSPD, MCAL, MCAL, MMUS. The goal of these “invariant masses” is an attempt to parametrise the energy spread inside the cone
- the pseudorapidity of p_{raw} : ETA
- 2 numbers to define the granularity of the region hit in the calorimeters: by extrapolating p_{raw} to the ECAL and HCAL surfaces, EPOS = 0, 0.5, and 1, respectively for inner, middle, and outer ECAL, and HPOS = 0, 1 for inner, outer HCAL
- 2 numbers to measure of the energy in the saturated calorimeter cells: for each cell in the cone found at saturation, the saturation value increments a parameter ESAT for ECAL, and HSAT for HCAL.

An example of these variables is shown in figure 4.30 (from b -jet candidates found in 120 GeV/c² Higgs events). To better feed the NN, the variables are regularised in the approximate interval [0,1], see figure 4.31. The same treatment is reserved to the variable to be guessed, E_{mc} , also shown in the two figures.

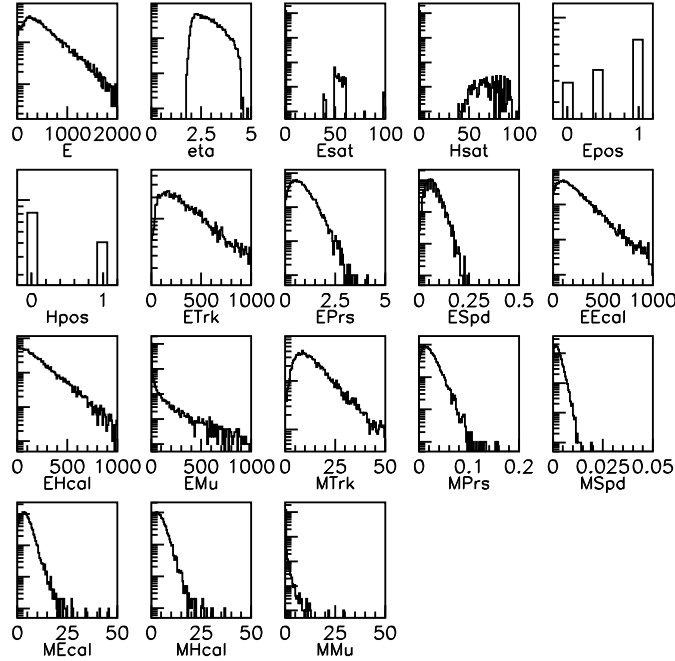


Figure 4.30: Variables considered for feeding the neural-network, the first plot labelled with E is the energy considered for training, i.e. the value E_{mc} wished at the NN output

The NN was setup with 17 inputs, two hidden layers of 18 and 12 neurons, 1 output neurons. Train and tests are done on sets of the order of 10k events.

The NN was first studied on the b -jet events from the jetgun, with energies ranging up to 3 TeV. The underlying event and the hard gluon radiation are not considered in this case. In figure 4.32 the plot the distribution of $R = (E_{\text{mc}} - E_{\text{nn}})/E_{\text{mc}}$. This distribution must be centred

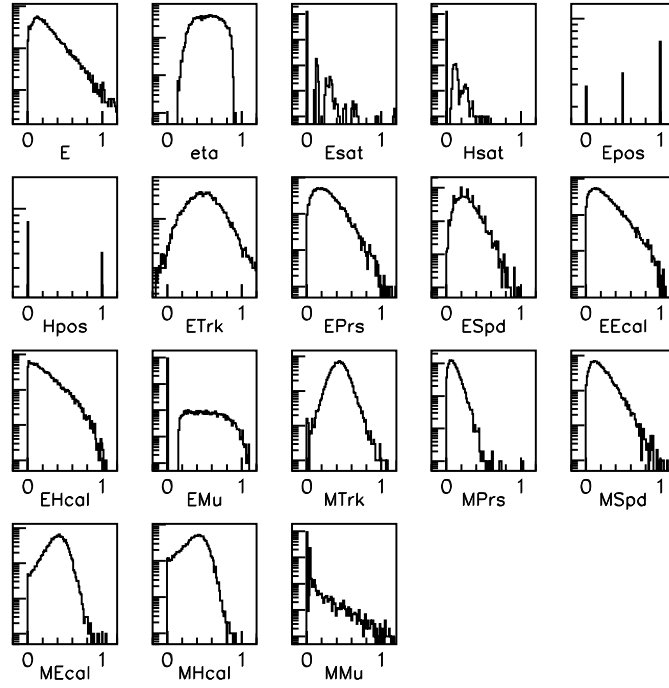


Figure 4.31: Like figure 4.30, after “regularisation”, to better fit the preferred NN input range

on zero, when the rms is providing the average energy resolution. E_{mc} was chosen following the three options discussed above, in increasing order of difficulty:

1. E_{mc} is the visible energy in the acceptance,
2. Similarly but gathered without acceptance cuts (default),
3. $E_{mc} = E_b$, the b quark energy.

As can be expected, a degradation of the resolution can be observed for the more demanding setup: the rms values are 0.2276, 0.2281, and 0.2476, for the 3 options. The bottom right scatter plot shows the profile from the scatter plot, E_{mc} versus E_{nn} . The 45° slope shows that the NN is behaving well, each slice in E_{nn} giving the correct E_{mc} on average.

On the other hand, from the E_{nn} vs E_{mc} (or R vs E_{mc}) plots, the response of the detector deteriorates after ~ 1.5 TeV. The effect is mainly due to calorimetric saturation as can be seen from the large dispersion at low η visible in the R vs η scatter plot. Considering the default option (no. 2 above) a rms of ~ 0.30 is observed in the region $\eta < 2.4$ and ~ 0.20 at large η . An attempt was done to split the sample in two regions of low and high η , and process them independently, but no improvement was observed compared to the previous results, which indicates that the NN handles this dependency in a correct way.

Another study was performed as a function of the input energy range. The NN trained with b -jets up to 3 TeV overestimates the energy in the lower 2/3 of the range. The average of the R distribution is found to be -0.12 in the 0-2 TeV region. To try to adjust the response under 2 TeV (this is the region of interest for Higgs searches), the NN training was limited to $E_b < 2$ TeV, see figure 4.33. In that case the R -distribution is well-centred, with a width of 0.19 but the response is distorted after 1.8 TeV. In general, one can observe that it is better to include in the training set events with energies $\sim 10\%$ higher than the desired range to obtain a more uniform energy response.

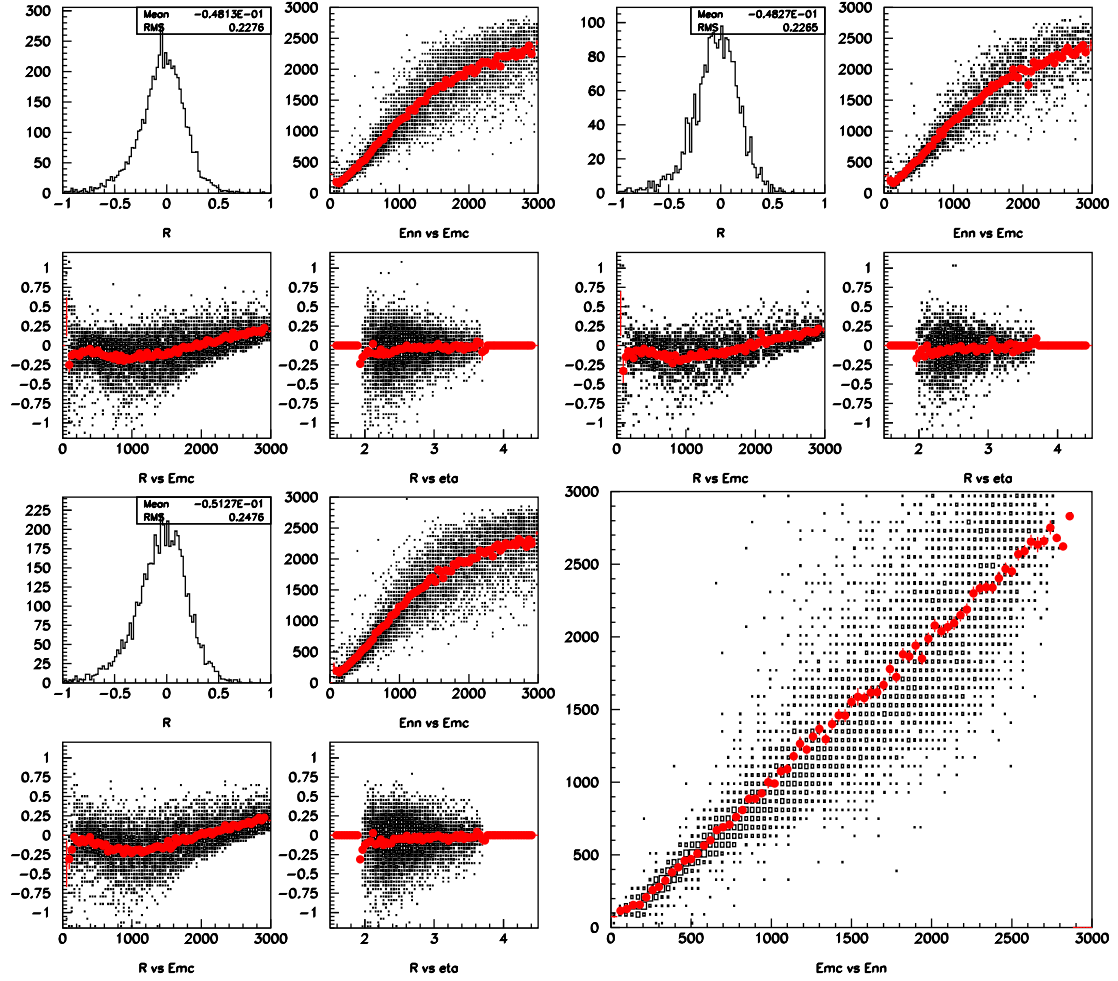


Figure 4.32: Performance plots for the NN. Each group of four gives the distribution of $R = (E_{mc} - E_{nn})/E_{mc}$, and the scatter plot (in red) with the profile of E_{nn} vs E_{mc} , R vs E_{mc} , and R vs η . The three different groups correspond to E_{mc} chosen as the visible energy, the visible energy but without acceptance cuts, and the b quark energy used to generate the events respectively. The bottom right scatter plot is E_{mc} vs E_{nn} , showing a profile at 45 degrees.

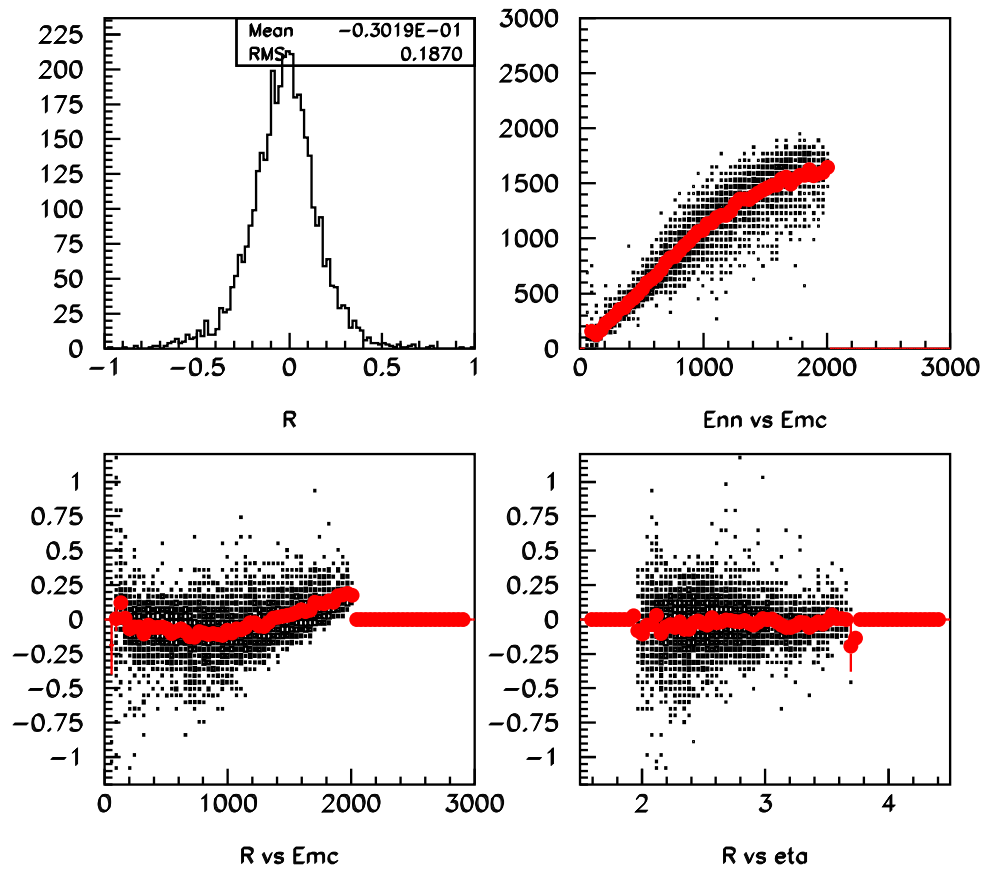


Figure 4.33: Performance of a NN trained with energies up to 2 TeV

Other variables have also been studied, mainly to reduce the saturation effect:

- the multiplicity of tracks, and the number of hits in the calorimeter inside the cone ,
- the energy deposited around the jet cone: inside a region from R_{\max} to $R_{\max} + 0.3$ or $R_{\max} + 0.5$.

By inspection of scatter plots, no useful correlation with the true energy was found. Inserted into an extended NN these variables were found ineffective, and were discarded.

Other non NN procedures

For comparison other simpler algorithms have been tested. It consists of fitting the profile of E_{mc} vs E_{raw} by a polynomial, subsequently used to correct E_{raw} (it is shown in figure 4.34 on the left group of 4 plots). Also shown in the figure (four right plots) the result from a similar procedure but assuming $E_{\text{raw}} = E_{\text{TRK}} + E_{\text{CAL}} + 0.7 \cdot H_{\text{CAL}}$ (as suggested in [65]). In both cases the resolution is worse that with the NN.

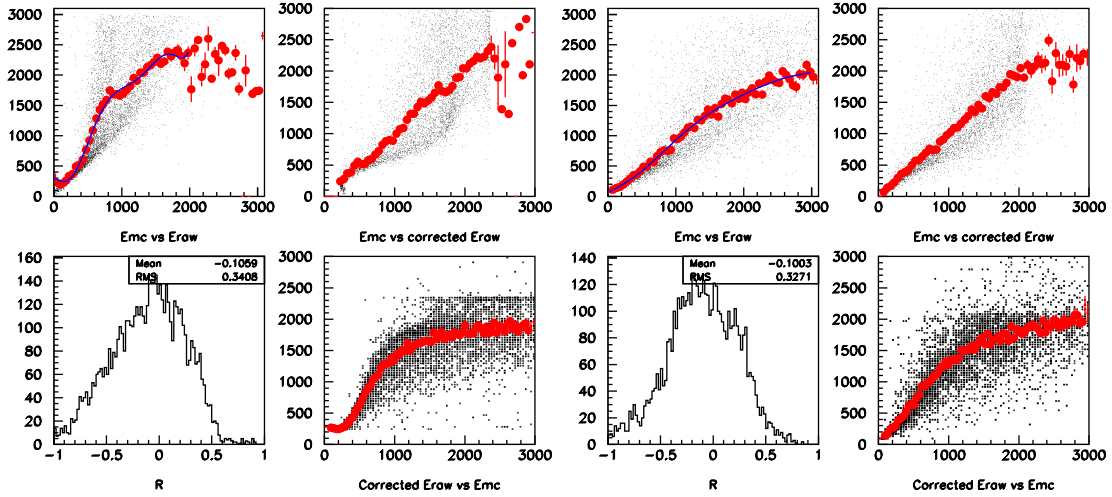


Figure 4.34: Four plots at the left: simple energy correction starting from the raw energy E_{raw} . The profile of E_{mc} vs E_{raw} (top left figure) is fitted with a polynomial of degree 7 (blue line), used to correct E_{raw} (top right). R parameter and corrected E_{raw} vs E_{mc} are shown at the bottom. Four plots at the right: idem, but $E_{\text{raw}} = E_{\text{TRK}} + E_{\text{CAL}} + 0.7 \cdot H_{\text{CAL}}$.

Neural Networking the Higgs events

The procedure has been tested in the context of an analysis for the search of Higgs in associated production with Z^0 or W^\pm . Several thousands of fully simulated events in the DC06 configuration were produced with Higgs mass of 90, 110, 120, 130, and 140 GeV/c^2 . The event selection requires a prompt and isolated lepton from the W^\pm or Z^0 , and two b -jets. The VV Seed Finder has been used to find the b -jets and events are rejected if less than two seeds are found. For each seed, p_{raw} is computed with $R_{\max} = 0.5$, and the two jets which give the largest dijet invariant mass are chosen, but with an upper limit of 250 GeV/c^2 . The events are discarded if E_{raw} of one of the two jets is less than 100 GeV . After these cuts the b -jets of the surviving events were divided in two sets of 10-20k jets each, one set was used for training, and the other for testing

the NN. The NN was setup as seen in the previous section 4.3.3, but with a larger number of hidden nodes (17 input nodes, two hidden layers of 30 nodes, and 1 output).

The four left plots of figure 4.35 result from the NN trained to guess the visible energy, while for the right plots E_b has been defined as the b quark energy before parton shower. The choice was to train on a mixture of 90 and 120 GeV/ c^2 events, this makes the NN response more linear. As seen with the b -jetgun events, the NN has a much easier task when E_{raw} is used, giving a single jet rms of 0.22, and 0.25 when E_b is used. The same figures shows that the NN response is linear with E_{mc} . A distortion is also observed for $E_{\text{mc}} < 200$ GeV. The minimal E_{nn} value is around 100-150 GeV and does not extrapolate to zero: the NN is using an E_{mc} average value when E_{raw} is too small, and no additional information is available to guess the right E_{mc} . This can also be seen from the E_{mc} vs E_{raw} scatter plot of figure 4.36: the profile has also an intercept at around $E_{\text{mc}} = 200$ GeV. This threshold is responsible for the curvature in the R vs E_{mc} scatter plot at small E_{mc} . Finally, no large distortions are present at the acceptance limits of the detector, as can be deduced from the flat pseudorapidity plot: it is remarkable that this is not the case when the number of train cycles, or “histories”, is too low.

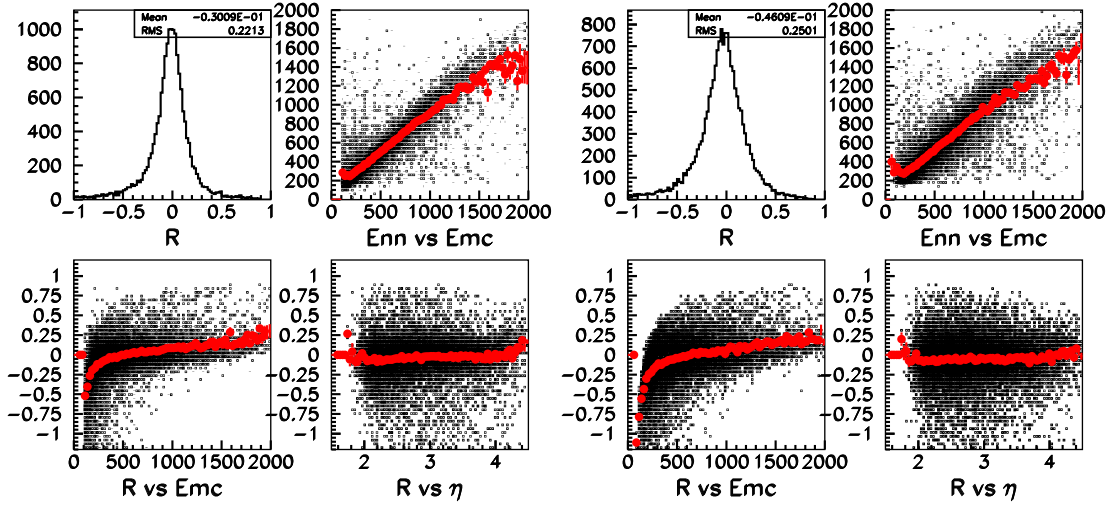


Figure 4.35: The four left plots are results for the NN trained assuming the visible energy as training parameter, at the right assuming the b quark energy E_b . For each group, the top left plot: $R = (E_{\text{mc}} - E_{\text{nn}})/E_{\text{mc}}$, top right: E vs E_{nn} , bottom left: R vs E_{nn} , bottom right: R vs η . The red dots are the scatter plot profiles.

The number of train histories was chosen to minimise the rms width of the R -distribution ($R = (E_{\text{mc}} - E_{\text{nn}})/E_{\text{mc}}$). An example of such optimisation procedure is shown in figure 4.37. It can be seen that the optimum is around 400–500 histories, for a train set of about 10'000 jets.

The four-momenta of the two jets are subsequently combined to obtain the Higgs mass estimate. The plots of figure 4.38 are the mass distributions, obtained from the two p_{raw} four-momenta, and also after NN. A Gaussian fit is shown superimposed. The energy of the peak is shifted by the NN action from 82 to 107 GeV/ c^2 , closer to the 120 GeV/ c^2 generated. The performance has been computed graphically by taking the Full Width at Half Maximum (FWHM) of the peak. Defining the relative resolution $r = \text{FWHM}/M_{\text{jj}}$, where M_{jj} is the centre of the peak, An improvement on the mass peak for the Higgs event of 120 GeV/ c^2 can be measured from $r=44.5/82=54\%$ to $r=41/107=38\%$, before and after NN respectively.

The behaviour of the setup is summarised in table 4.3 and figure 4.39, for Higgs masses of

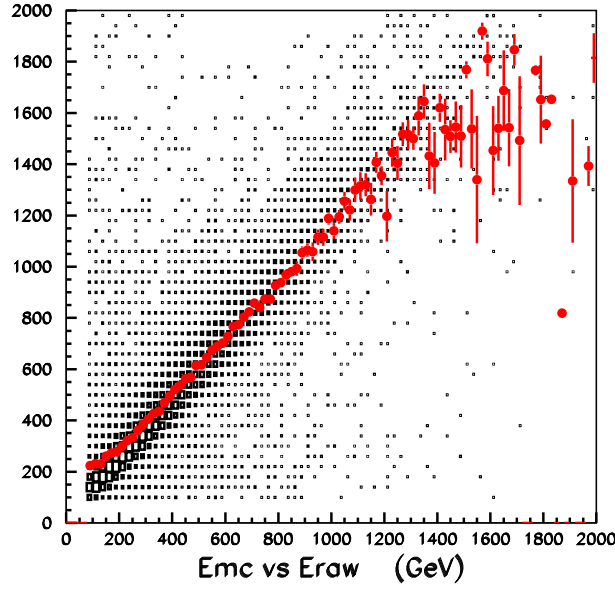


Figure 4.36: E_{mc} vs E_{raw} for jets from Higgs with a mass of $120 \text{ GeV}/c^2$

M	E_{raw}	FWHM	E_{nn}	FWHM	$E_{nn} (E_b)$	FWHM
90	61.5	36.5	84.3	34.2	99.7	29.2
110	75.2	38.2	99.1	36.5	113.9	36.5
120	82.0	44.5	107.1	41.0	120.8	42.2
130	91.1	45.6	115.1	44.4	126.5	39.9
140	97.3	50.0	121.9	47.9	133.9	45.6

Table 4.3: Dijet masses obtained for 5 generated mass values indicated in the first column. Columns 2 and 3 are the results from E_{raw} , while in column 4 and 5 the NN corrected jet energies have been used. The last two columns correspond to the NN trained to guess the b quark energy. Units are GeV/c^2

90, 110, 120, 140 GeV/c^2 . The bottom series of points in the figure is the raw response, from the p_{raw} four-momenta. The two other series are the results after NN, assuming visible energy (points in the middle), and E_b (at the top). One can notice that the response of the NN trained to reconstruct E_b , gives a mass value closer to the diagonal, but the response has slope less than 1.

As a final test, the procedure has been re-evaluated for different values of R_{max} . The plot of figure 4.40 shows that after NN is applied the dijet mass resolution is only slowly dependent on R_{max} , and that the value of 0.5 is optimal.

Discussion on the Neural Network

As seen before, the relative resolution FWHM/M_{jj} for a $120 \text{ GeV}/c^2$ Higgs is 38% after NN, to be compared with 54% for raw energies.

In the context of Higgs analysis the irreducible background comes from $Z^0 Z^0$ and $W^\pm Z^0$ events: these events have the same topology as Higgs in associated production. The separation

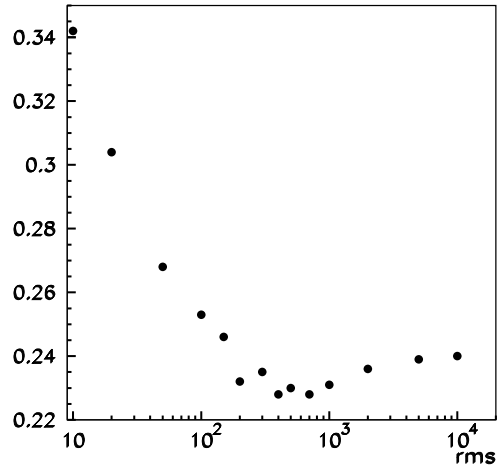


Figure 4.37: Single jet resolution (rms of the R distribution) vs number of train histories

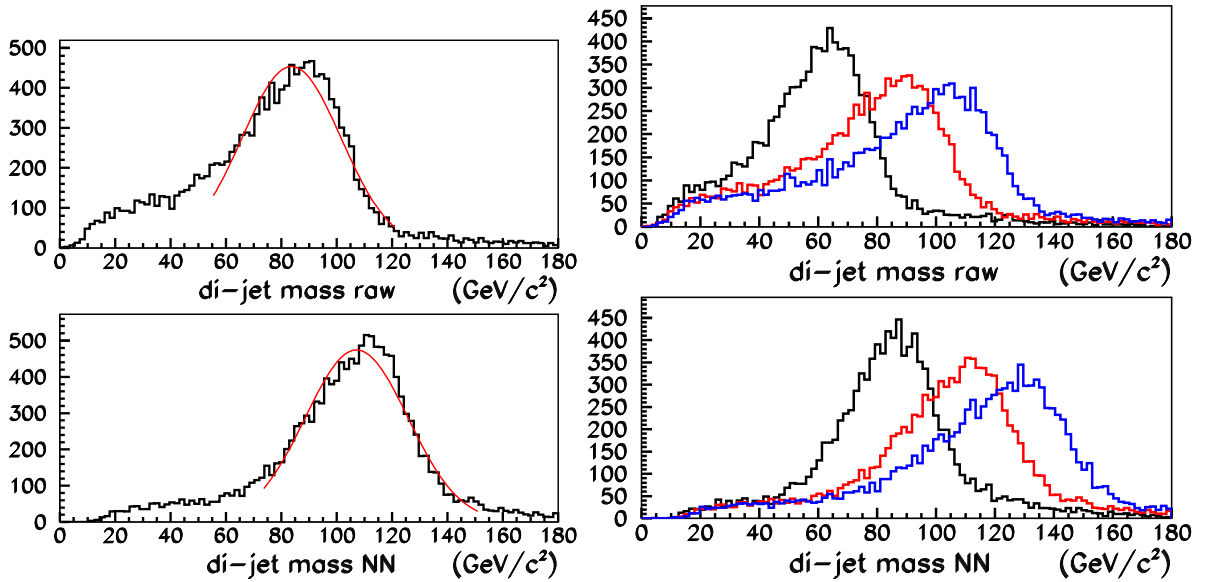


Figure 4.38: Left: dijet invariant mass for a generated Higgs mass of $120 \text{ GeV}/c^2$. The top plot is the raw result, the bottom after NN. The result of a Gaussian fit is also shown. Right: similarly, for three generated energies of 90, 120, and $140 \text{ GeV}/c^2$, before (top) and after (bottom) the NN procedure.

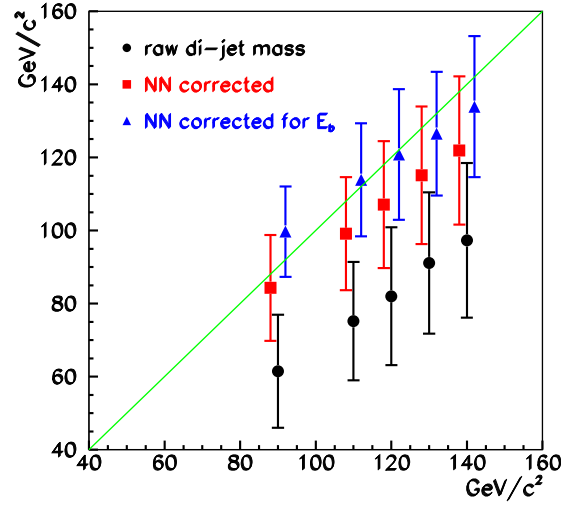


Figure 4.39: Reconstructed Higgs dijet invariant mass as a function of the generated mass value. The dots shows the values obtained from the two p_{raw} four-momenta. The squares and triangles are obtained after NN correction, with the NN trained to guess the visible energy and E_b , respectively. The points and error bars represents the centre of the peak and $\sigma = \text{FWHM}/2.36$

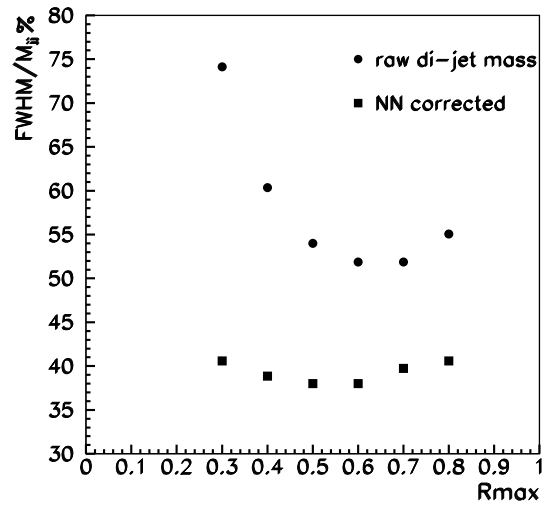


Figure 4.40: Dijet mass relative resolution for 6 values of R_{max} . The generated Higgs mass is $120 \text{ GeV}/c^2$

of a 90 GeV/c² particle ($\sim Z$) from a 120 GeV/c² one can be inferred from the results of table 4.3:

$$s = (m_{120} - m_{90}) / \sqrt{\sigma_{120}^2 + \sigma_{90}^2} \quad (4.11)$$

where m_x is the reconstructed mass for a generated mass x , and $\sigma_x = FWHM_x/2.36$. An increase has been obtained from $s = 0.84$ for raw dijet masses, to $s = 1.01$ after NN processing (0.97 for NN trained to find E_b). The result is less good as one could hope from the “local” improvement of the resolution at 120 GeV/c²: the problem can be understood from figure 4.39 where it can be noticed that the NN corrected (red) point for 90 GeV/c² mass has been pushed closer to the diagonal than the other four points.

Sources of Systematic Error

Multiple sources of systematic error can be identified. Firstly, the momentum measurement errors of all the particles used in the reconstruction should be considered. The momenta are mainly used to compute the b -jet energy. Secondly, the calorimetric energy measurement has an effect. To be less dependent on the momentum measurement and the particle reconstruction, the b -jets energy is computed using the raw calorimeter energy, hence the estimation of the errors might be important. The saturation of the ECAL is also an important point. All the particles with a transverse momentum larger than 10 GeV/c cannot be well reconstructed due to the saturation of the calorimeter cells. PID error is assumed to have a negligible contribution, the track momentum and the energy deposited in the calorimeter are more important than the type of particle involved. It can be noted that the final estimation of the systematic errors is complicated by the use of this NN.

A Try on the Correction for the Underlying Event

The UE is generated by the hadronization of the spectator partons. In addition, in the case of multiple beam interactions, the product of other p-p collisions can overlap, giving rise to a second contribution. This second contribution is not addressed here and deserves separate treatment. The effect of UE has already been shown in figure 4.28. The rise after $R_{\max} \approx 0.5$ is clearly seen and the comparison with the resolution obtained from pure Higgs decay particles, shows that the degradation is due to the particles from the UE. An attempt to correct for this effect was presented in [67].

In the present study, the problem was addressed at a pure four-vector level. This point is crucial to dissociate from detector effects, which can mask correlations or create artificial ones. The MC events considered are Higgs ($m_H = 120$ GeV/c²) produced in association with a Z^0 or W^\pm . The bosons are tagged by an isolated lepton with a $p_T > 10$ GeV/c. The detector is simulated only by its acceptance, from 15 to 300 mrad.

The plots of figure 4.41 gives the dijet invariant mass for 4 values of R_{\max} . The seed of the cone is given by the direction of the hadron carrying a b quark. The black histograms are calculated using particles coming from the Higgs decay only, while the red histograms includes all the visible particles in acceptance, and neutrinos discarded.

Again, it can be seen that the UE contributes significantly only for $R_{\max} > 0.5$. One can also see from the black curves, that there is a potential improvement in mass resolution for $R_{\max} = 0.8$ compared to $R_{\max} = 0.5$. It is clear that advantage can be taken of this only if a way can be found to correct for the UE.

A correction to the jet energy can be written as $E_{\text{cor}} = E_{\text{cone}} - \delta$, where E_{cone} is the jet energy estimated by the cone algorithm ($R_{\max} = 0.8$ is chosen), and δ is the contribution from UE particles in the same cone area. The aim is to estimate δ value for each event: a set of

variables has been investigated to see if they carry the wished information. A Neural Network has also been used to the tests.

The initial jet four-momentum p_j is calculated with $R_{\max}=0.8$, using all visible particles, and the energy of p_j is indicated by E_j . Two b -jets (p_j^1 and p_j^2) are coming from the Higgs decay, therefore the procedure is done independently for the two jets. Seven variables are calculated with the following procedure:

- A new four-vector p_L is computed, with same direction as p_j , but with a larger cone aperture $R_{\max}=1.0$. Δp_L is defined as $\Delta p = p_L - p_j$, with energy ΔE_L , and $M_L = |\Delta p|$.
- The sum of all the visible particle energies four vector of the event p_E is computed, the four-momenta of the two jets are subtracted and also the four-momentum of the tagging lepton (or the two leptons from a Z^0). The energy, and the invariant mass from the resulting four-vector are ΔE_E and M_E .
- Three “pseudo-jets” are computed by choosing three cone directions which have the same pseudorapidity as p_j . Two of the “pseudo-jets” have a ϕ angle chosen in such a way that the two cones are adjacent to the p_j one. The third has opposed azimuthal angle than p_j . The energies integrated in the cones are E_1 , E_2 and E_3 .

The variables tested are $\Delta E_L/E$, M_L , $\Delta E_E/E$, M_E , E_1 , E_2 , and E_3 shown in figure 4.42, before and after regularisation. The same is done for the variable to optimise, which was defined to be $X = (E - U)/E$, where U is the jet energy computed from pure Higgs decays (no UE). The original and transformed distributions for X are shown in figure 4.43.

Unfortunately, no evident correlation exists between X and any of the chosen variables. The normalised variables are combined into a 7 inputs NN (2 hidden layers with 7 nodes each, 1 output). The training is performed on about 7000 events. The test on a similar amount of data is performed for each Higgs event to correct the energy of the two jets, p_j^1 and p_j^2 . Figure 4.44 shows the dijet mass plots obtained before and after calculation, in red and blue respectively. For reference, the black curve shows the dijet mass obtained discarding the UE background particles.

The FWHM resolutions before and after correction are almost identical (33% and 32%). The improvement (if any) is marginal, and therefore the procedure was abandoned in this study.

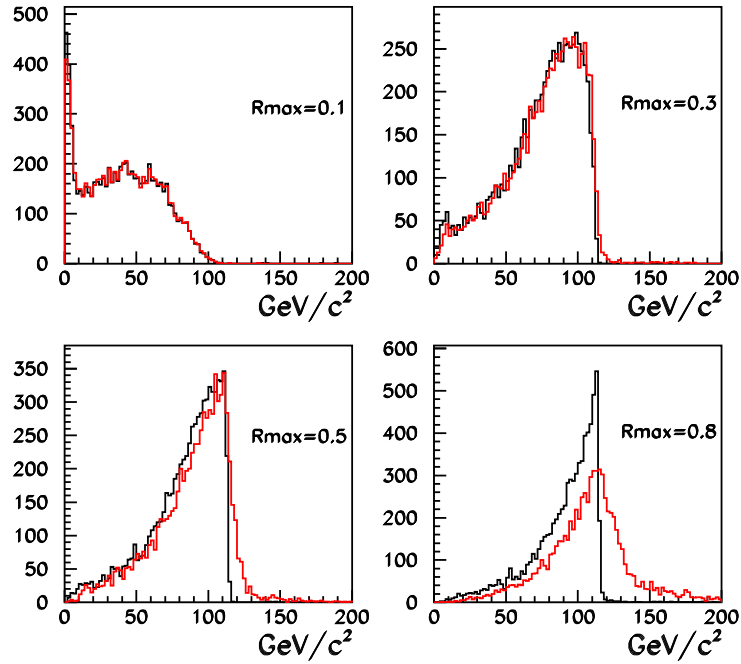


Figure 4.41: Dijet invariant mass distributions for 4 values of R_{\max} . For the histograms in red all the visible particles are used in the calculation, while UE particles are discarded for the calculation of the black histograms

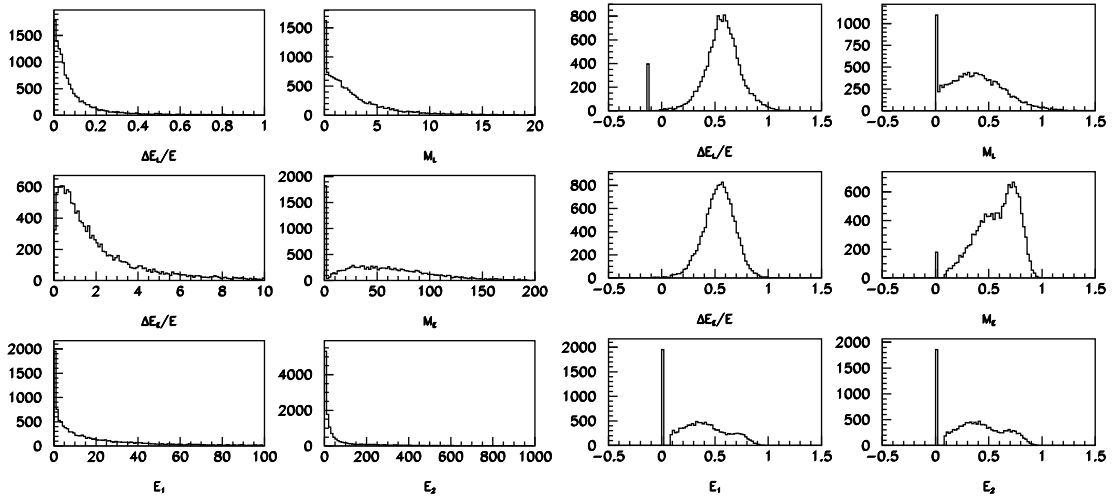


Figure 4.42: Two first columns: six of the seven variables considered for feeding the neural-network. Two last columns: as before but after "regularisation", to better fit the preferred NN input range

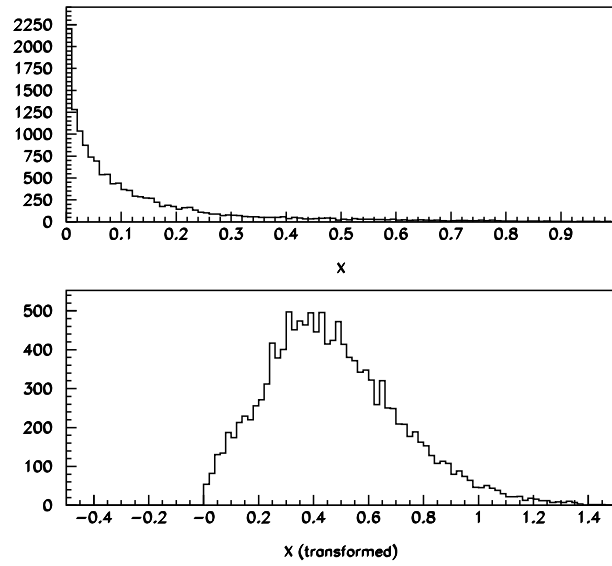


Figure 4.43: $X=(E-U)/E$ is used to measure the UE contribution, to be subtracted. The bottom plot is after regularisation

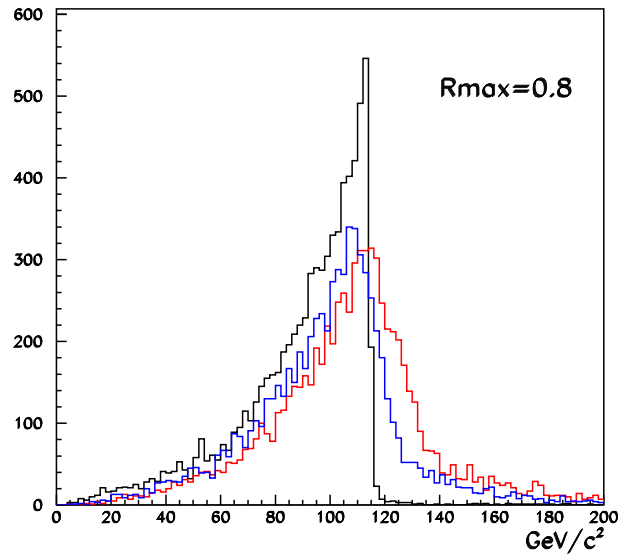


Figure 4.44: Dijet mass obtained before and after NN, in red and blue respectively. In black the dijet mass obtained discarding UE particles (the ideal case)

4.4 Lepton Selection

The search focuses on a Higgs boson which is produced in association with a gauge boson decaying leptonically: $HW^\pm \rightarrow b\bar{b} + \ell^\pm (\bar{\nu}_\ell^-)$ and $HZ^0 \rightarrow b\bar{b} + \ell^+\ell^-$. The hard leptons produced through the decay of the gauge boson are quite often isolated from the other particles in the event, especially from the b -jets, and are predicted to have a high transverse momentum. Moreover, the gauge boson does not fly but decays directly, hence its daughters are required to be prompt with respect to the primary vertex. This event selection therefore requires an isolated and prompt lepton.

4.4.1 Lepton Generator Level Studies

A study is performed on the four-vector particles generated by Pythia. Only the stable particles are retained. Two sets of leptons are distinguished: the leptons associated to the gauge boson and those without association. The leptons which have the gauge boson as one of their ancestors are called associated leptons.

At the four-vector level, the isolation of the lepton can be assessed by summing the four-vectors of all the particles within a cone around the lepton direction and comparing the result to the lepton energy. For a cone radius of $R = 0.4$ in the $\eta - \phi$ plane, the following ratio is defined:

$$\frac{E_{\text{lep}}^{\text{cone}}}{E_{\text{lep}}} = \frac{\sum_{\text{particles}}^{\text{cone}} E_i}{E_{\text{lepton}}}, \quad (4.12)$$

where E_i are the energies of the particles in the cone. It is found that cutting on this variable rejects most of the QCD background, as shown in Figure 4.45. The cut value has been chosen to keep only the events with at least one isolated lepton which have a ratio $E_{\text{lep}}^{\text{cone}}/E_{\text{lept}} < 130\%$, this cut is represented by the vertical line in the plot.

A cut on the transverse momentum of the lepton is also useful as can be seen from the normalised plots of the p_T distributions shown in Figure 4.46. Figure 4.47 shows the normalised correlation plots of $E_{\text{lep}}^{\text{cone}}/E_{\text{lep}}$ vs p_T . The generation was performed with a cut on the transverse momentum of one lepton at 10 GeV/c, but the stable associated lepton was allowed to have a p_T smaller than the generation cut. The other leptons are the remaining leptons of the Higgs events that are not associated to the gauge boson, and are found in the low- p_T region. The leptons from the $b\bar{b}$ events have the lowest transverse momenta, and are rejected by this cut. Therefore the lepton is requested to have at least 7 GeV/c.

Selection efficiencies are reported in Table 4.4.

	$p_T > 7 \text{ GeV/c}$	$\Delta E < 130\%$	$p_T \text{ \& } \Delta E$
associated leptons	99.7%	92.3%	92.0%
non-associated leptons	10.7%	8.2%	0.1%
$b\bar{b}$ event leptons	$12.8 \cdot 10^{-5}$	18.6%	$2.95 \cdot 10^{-5}$

Table 4.4: Lepton cut efficiencies at the four-vector level.

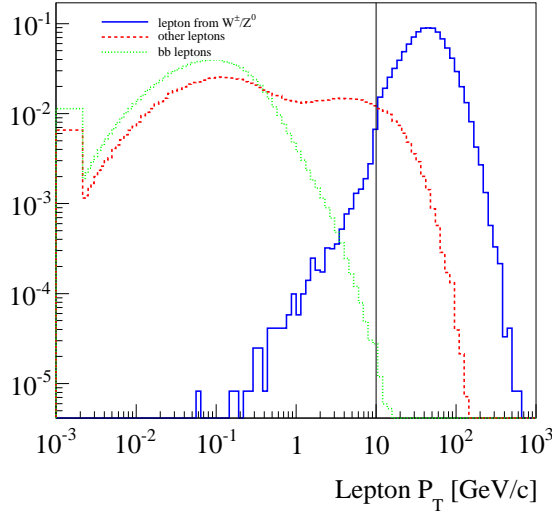


Figure 4.45: The solid blue line shows leptons decaying from an associated gauge boson, the dashed red line is the remaining leptons. The green dots represent leptons from the $b\bar{b}$ events.

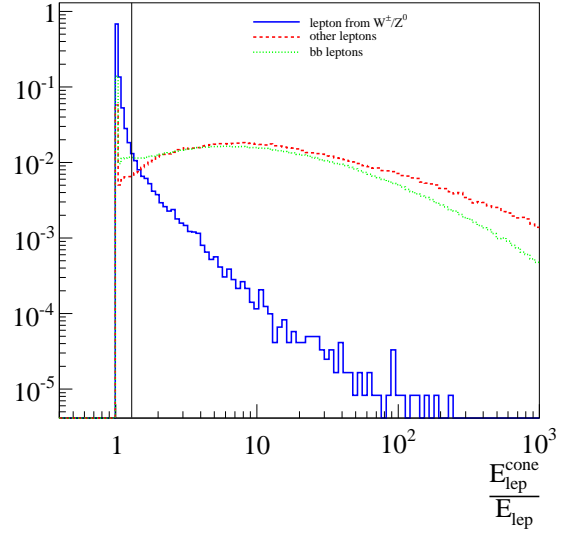


Figure 4.46: ΔE of the stable leptons at the four-vector level of the Higgs events and $b\bar{b}$ events. The solid blue line shows leptons decaying from an associated gauge boson, the dashed red line is the remaining leptons, while the green dots show leptons from the $b\bar{b}$ events.

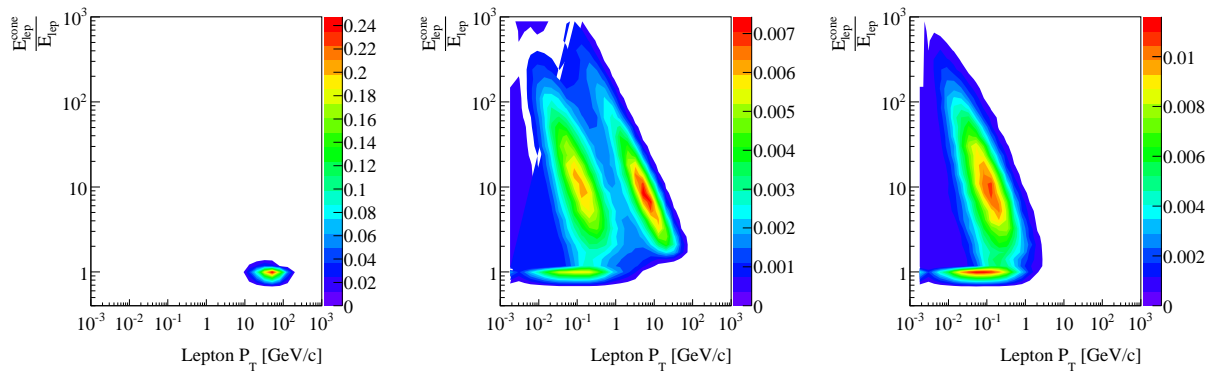


Figure 4.47: ΔE vs p_T for the associated leptons (left), the remaining leptons (middle) of the $HW^\pm/Z^0 \rightarrow b\bar{b} + \ell$ events, and leptons of the $b\bar{b}$ events (right). The excess at p_T ranging between 3 and 20 GeV/c visible in the middle plot consists of leptons which have the Higgs as ancestor.

4.4.2 Full Simulation

In the fully-simulated events, the muons are requested to have a particle identification likelihood ratio (DLL) (see Section 3.4.4) of:

$$\ln \left[\frac{\mathcal{L}(\mu)}{\mathcal{L}(\pi)} \right] > -3.0, \quad (4.13)$$

giving a high purity sample.

The combined likelihood for electrons uses information from the calorimeters. The electrons are required to have a likelihood ratio:

$$\ln \left[\frac{\mathcal{L}(e)}{\mathcal{L}(\pi)} \right] > 0.0. \quad (4.14)$$

As seen before, leptons are required to have a transverse momentum (p_T) larger than 7 GeV/c (Figure 4.45).

Only tracks with an impact parameter, IP , with respect to the primary vertex smaller than 0.1 mm are selected for both electrons and muons. These tracks are required to have a significance of the impact parameter $IP/\sigma_{IP} < 2.6$ to ensure that the lepton comes from primary vertex, V^0 .

Finally, a high p_T lepton from Higgs events is in general isolated from the other particles. The computation of a pseudo jet ($R = 0.4$) around the lepton direction is performed. In order not to depend on the reconstruction, these jets use the raw energy of the calorimeters and muons in their cone (not the reconstructed particles). The local amount of energy within the cone in the $\eta - \phi$ plane should not exceed 130% of the lepton energy itself:

$$F = \frac{\sum_{\text{hits}}^{\text{cone}} E_{\text{CALO}} + \sum_{\text{particles}}^{\text{cone}} E_{\mu}}{E_{\text{lepton}}} < 1.3. \quad (4.15)$$

The cut efficiencies are reported in Table 4.5.

	$p_T > 7 \text{ GeV/c}$	$IP < 0.1 \text{ mm}$	$IP/\sigma_{IP} < 2.6$	All	All + $F < 1.3$
$HW^{\pm}/Z^0 \rightarrow b\bar{b} + \ell$	74.2%	90.4%	92.6%	68.1%	60.7%
$t\bar{t} \rightarrow bW^+ \bar{b}W^-$	67.37%	89.1%	92.3%	62.1%	53.0%
$Z^0 Z^0 \rightarrow b\bar{b} + \ell^+ \ell^-$	80.0%	92.6%	94.6%	75.6%	65.0%
$Z^0 W^{\pm} \rightarrow b\bar{b} + \ell^{\pm} \nu_{\ell}^{(-)}$	77.7%	91.4%	93.3%	72.4%	63.3%
$\gamma^*/Z^0 + 2b$	74.2%	88.7%	92.1%	70.7%	63.5%
$W^{\pm} + 2b$	75.6%	90.2%	93.0%	72.0%	64.2%
$b\bar{b}$	$4.27 \cdot 10^{-4}$	33.0%	48.8%	$2.27 \cdot 10^{-4}$	$1.22 \cdot 10^{-4}$

Table 4.5: Lepton cut efficiencies for full simulated events.

4.4.3 High- p_T Electrons

High- p_T electrons have to be carefully checked. The ECAL is not tuned for very high- p_T particles and its cells saturate around a transverse energy value of 10 GeV/c. This saturation causes problems to evaluate the energy of the electrons. A Neural Network for the jet-energy optimisation is used to partially recover from this issue.

This effect is due to the gain applied to ECAL channels. In principle, a change in the gain could be applied to improve the energy measurement of high- p_T electrons. Muons do not suffer from this problem, because their momentum is only measured with the tracking stations.

Figure 4.48 shows the saturation of the electromagnetic calorimeter. Electrons were fired into the detector using the particle gun simulator. They were produced with a flat energy distribution up to 600 GeV and fired in the external region of the detector to have a p_T between 7 GeV/c and 100 GeV/c. The saturation of the ECAL decreases the identification of the electrons. Table 4.6 gives a summary of the electron identification efficiency as a function of the p_T cut.

In order not to depend on the high- p_T lepton cut requirement, the cut is lowered to $p_T > 7$ GeV/c.

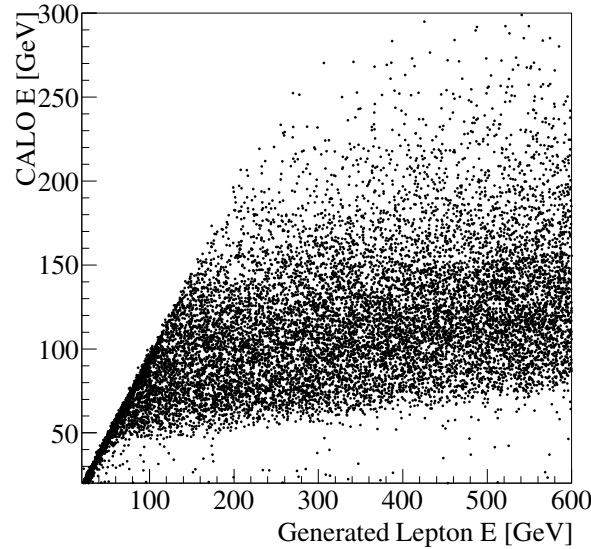


Figure 4.48: Saturation of the ECAL cells for high- p_T electron ($7 \text{ GeV/c} > p_T < 100 \text{ GeV/c}$), the visible energy in the ECAL suffers because of the saturation.

	$7 \text{ GeV/c} > p_T$	$> 10 \text{ GeV/c} > p_T$	$> 20 \text{ GeV/c} > p_T$	$> 30 \text{ GeV/c} > p_T$
Rec & $\sigma_E < 5\%$	57.0%	44.9%	31.2%	29.5%
Rec & $\sigma_E < 10\%$	62.6%	55.1%	41.5%	38.2%

Table 4.6: Reconstruction and identification efficiencies as a function of the four-vector level electron p_T .

4.5 Higgs Selection

In this section, a method to select Higgs events is proposed.

First, two sets of jets are created using the tools previously described: the *tagged* jets produced by the VV Seed Finder algorithm (Section 4.3.1), and the *untagged* jets created by the K_T algorithm (Section 4.3.2).

All the jets are passed through the energy optimisation neural network tool (see Section 4.3.3) in order to improve the energy resolution. The choice was made to use the neural network setup to optimise the energy measurement taking as reference the visible energy (correction for detector effects only). The algorithm computes the energy and raw calorimeters information within a cone (the R -parameter was set at 0.45) around the jet direction. In practice all the jets are used as seeds for the algorithm.

Next, the selection of the isolated and prompt leptons is performed. Finally, an event selection is performed using the global event information, the jets and the selected leptons.

1. Global Event Information

Events containing a Higgs are expected to have a large transverse energy. In order to reduce the QCD background the sum of raw transverse energies of the event should be larger than 20 GeV/c:

$$\sum_{\text{CALO hits}} E_T + \sum_{\text{muons}} p_T > 20 \text{ GeV/c}, \quad (4.16)$$

where $\sum_{\text{hits}}^{\text{CALO}} E_T$ is the sum of the transverse energy deposited in the different cells of all calorimeters (PS/SPD, ECAL and HCAL) with respect to the primary vertex. The reconstructed muons transverse energies are also added.

	$E_T^{4v} > 20 \text{ GeV/c}$	$E_T^{\text{rec}} > 20 \text{ GeV/c}$
HW^\pm/Z^0	96.5 %	96.5 %
$t\bar{t}$	97.1 %	96.2 %
$Z^0 Z^0$	97.5 %	97.0 %
$Z^0 W^\pm$	97.0 %	96.9 %
$\gamma^*/Z^0 + 2b$	94.2 %	94.4 %
$W^\pm + 2b$	97.2 %	96.0 %
$b\bar{b}$	15.3 %	20.2 %

Table 4.7: Fraction of events selected after the cut the global transverse energy (at the four-vector level and in the full simulation).

2. b -Jets Selection

Cuts are used to discard the soft jets that are unlikely to be associated to b -quarks. Each b -jet candidate of both sets has to pass some kinematic cuts.

In order to determine these cuts, the four-vector level information have been studied. Figure 4.51 shows the transverse momentum and the invariant mass of the jets for each kind of

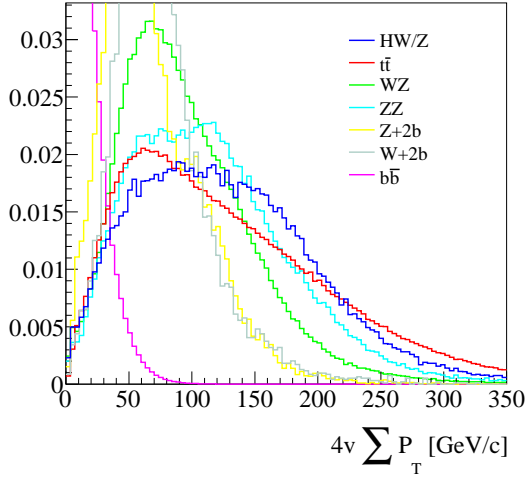


Figure 4.49: Sum of the p_T of all the stable and visible particles in the LHCb acceptance at the four-vector level, in each channel.

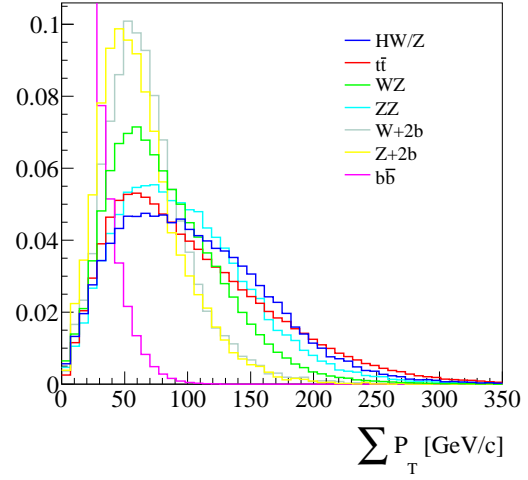


Figure 4.50: Sum of the E_T of the calorimeters and p_T of the reconstructed muons in the full simulation for all the channels.

events. In this four-vector analysis, jets are built within a cone ($R = 0.45$) around the direction of the b -hadrons using only stable particles in PYTHIA falling in the LHCb acceptance. Table 4.8 presents the fraction of the events that pass the cuts. HW^\pm/Z^0 has the largest probability to have at least one jet (71 %) within the LHCb detector, and 27 % probability to have two jets.

	no Jet in Acc	1 Jet in Acc	2 Jets in Acc	2J+ P_T cut	2J+ P_T + m cuts
HW^\pm/Z^0	28.8 %	42.8 %	27.6 %	25.1 %	23.9 %
$t\bar{t}$	52.8 %	37.3 %	9.4 %	8.0 %	7.6 %
Z^0Z^0	32.4 %	35.6 %	31.2 %	26.7 %	24.7 %
Z^0W^\pm	44.5 %	32.5 %	22.5 %	18.9 %	17.4 %
γ^*/Z^0+2b	29.9 %	58.3 %	11.5 %	1.7 %	1.4 %
$W^\pm+2b$	34.1 %	28.0 %	37.5 %	6.3 %	5.1 %
$b\bar{b}$	99.7 %	$1.6 \cdot 10^{-3}$	$1.2 \cdot 10^{-3}$	$2.3 \cdot 10^{-5}$	$1.4 \cdot 10^{-5}$

Table 4.8: Cut efficiencies and numbers of jets within the LHCb acceptance. This study is performed at the four-vector level using stable particles, with a centre-of-mass energy of $\sqrt{s} = 10$ TeV.

Figure 4.52 illustrates the p_T and the invariant mass of the reconstructed jets for all the channels in the case of the VV Seed Finder algorithm only on the left and right-hand sides respectively. The $b\bar{b}$ events present softer jets. The VV Seed Finder algorithm requires at least two charged particles with a $p_T > 1$ GeV/c (see section 4.3.1) to create a displaced vertex. As an effect of this requirement, a large part of the soft jets is already discarded. The effect is seen on the distributions that do not have any value below a transverse momentum of 10 GeV/c.

The criteria to select the jets are:

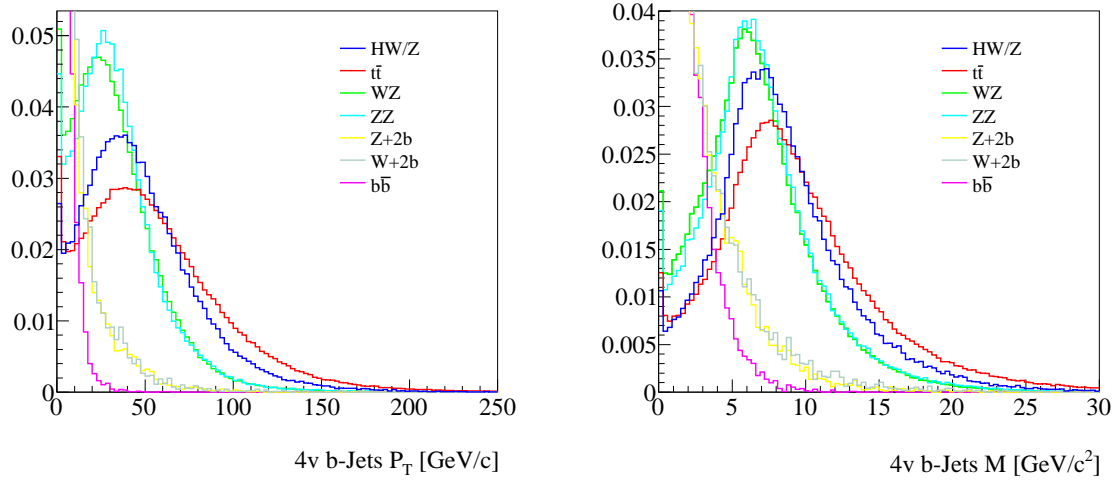


Figure 4.51: Transverse momentum, p_T (left) and invariant mass, m_{jets} (right), of the four-vector level jets.

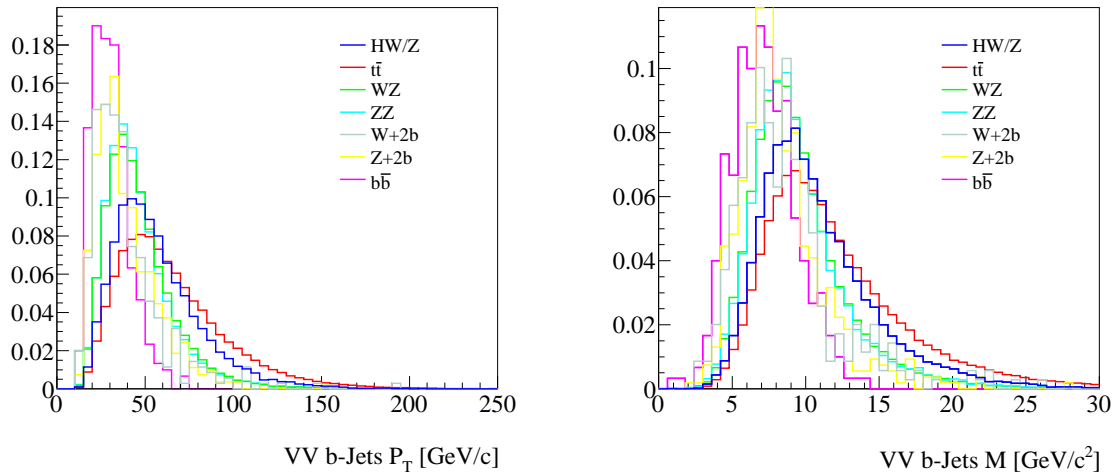


Figure 4.52: Transverse momentum, p_T (left) and invariant mass, m_{jets} (right), of the VV Seed jets.

- a transverse momentum p_T of at least 8 GeV/c;
- the invariant mass of the jet should exceed 3 GeV/c².

The selected jets are ranked in decreasing order according to the number of protojets (or particles) combined to form them in each set separately (*tagged* or *untagged*). If two jets have the same number of merged protojets (or particles), they are sorted as a function of transverse momentum p_T .

Table 4.9 summarises the fraction of jets selected by these cuts on fully simulated events. The two VV jets have a 7 % efficiency, preserving more the HW^\pm/Z^0 events compared to the $t\bar{t}$ background in particular. The reconstruction of K_T jets does not try to tag the b -hadrons, therefore it creates many more jets per event and the fraction of selected events increases for all the channels. In the “single tagged” dijets, the signal efficiency is multiplied by a factor of ~ 5 , but the $t\bar{t}$ background is increased by about 10 times.

	$(N_{jet}^{VV} = 1)$	$(N_{jet}^{VV} \geq 2)$	“double tagged” dijet	at least one of both jets	“single tagged” dijet
HW^\pm/Z^0	31.7 %	7.6 %	7.2 %	38.9 %	38.8 %
$t\bar{t}$	21.7 %	2.5 %	2.5 %	24.3 %	24.2 %
$Z^0 Z^0$	26.5 %	6.6 %	6.6 %	33.1 %	32.8 %
$Z^0 W^\pm$	20.8 %	4.5 %	4.4 %	25.2 %	25.1 %
$\gamma^*/Z^0 + 2b$	4.9 %	$7.6 \cdot 10^{-4}$	$7.6 \cdot 10^{-4}$	4.8 %	4.7 %
$W^\pm + 2b$	6.0 %	$3.4 \cdot 10^{-3}$	$3.4 \cdot 10^{-3}$	6.2 %	6.0 %
$b\bar{b}$	$1.7 \cdot 10^{-4}$	$2.00 \cdot 10^{-6}$	$2.00 \cdot 10^{-6}$	$1.59 \cdot 10^{-4}$	$1.56 \cdot 10^{-4}$

Table 4.9: Selection efficiencies in the full simulated events, with two tagged jets (double tagged) or a mixture of tagged and untagged jets (single tagged). Cuts are made on p_T and the jets invariant mass.

3. Selection of the Best b -Jet + b -Jet + Lepton Combination

The final selection consists in the choice of the best combination of two b -jets and one prompt and isolated lepton.

Figures 4.53 to 4.56 present the event topology cuts at four-vector level as well as for full simulated events. In both cases, it can be observed that the b -jets are well separated in the $\eta - \phi$ plane and that the distributions are similar. This shows that the VV Seed Finder algorithm works efficiently.

First, the dijets created with *tagged* jets are considered. All possible combinations $b\text{-jet}_{VV}(j_1) + b\text{-jet}_{VV}(j_2) + \text{lepton}(l)$ are tested with the following topological cuts:

- a minimal distance between the two jets in the (η, ϕ) plane: $\Delta R(j_1, j_2) > 0.65$;
- a minimal distance between the lepton and the two jets: $\Delta R(j_{1,2}, l) > 0.7$.

In addition two thresholds are applied on the:

- jet sum energies: $E_{j_1} + E_{j_2} > 40$ GeV;
- and on the sum of the transverse momenta: $p_T^{j_1} + p_T^{j_2} > 20$ GeV/c.

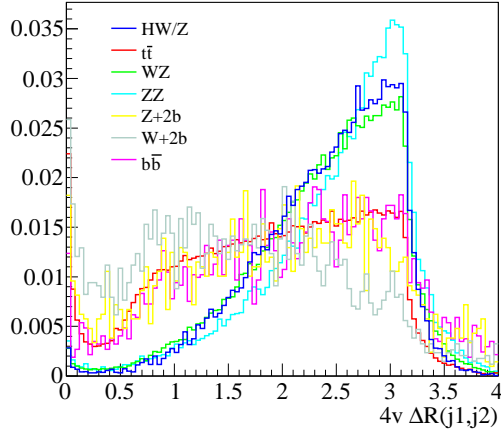


Figure 4.53: Separation between the two four-vector level jets in the $\eta - \phi$ plane.

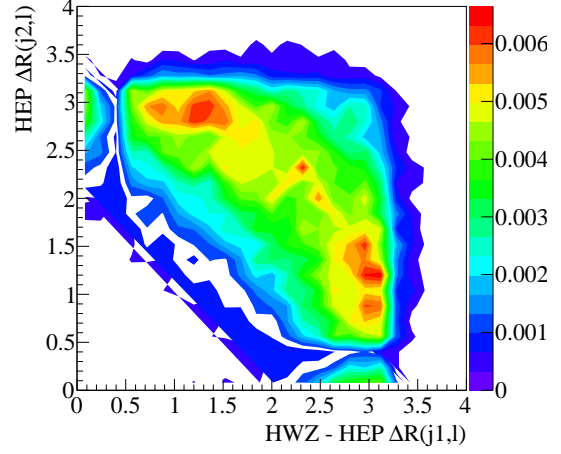


Figure 4.54: Separation between the two four-vector level jets and the lepton in the $\eta - \phi$ plane for the signal HW^\pm/Z^0 .

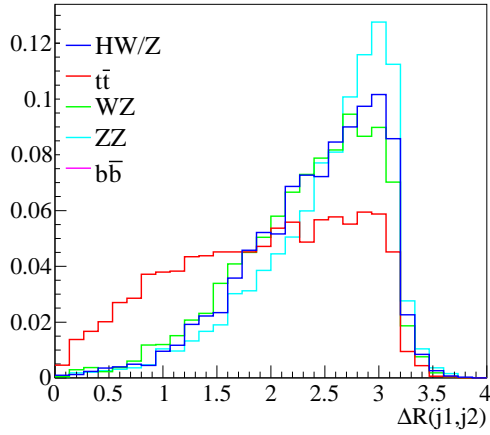


Figure 4.55: Separation between the reconstructed VV Seed jets in the $\eta - \phi$ plane for fully simulated events.

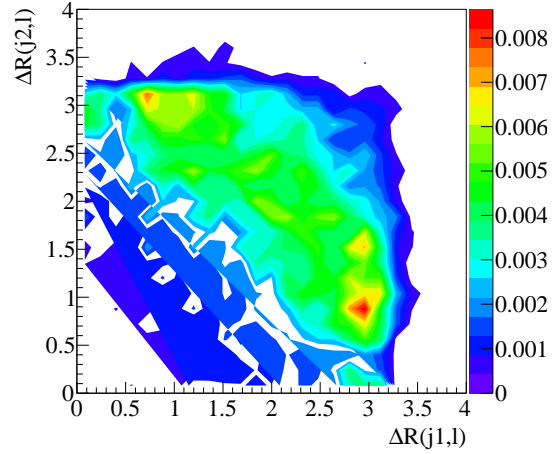


Figure 4.56: Separation between the two reconstructed VV Seed jets and the selected lepton in the $\eta - \phi$ plane for the signal HW^\pm/Z^0 . The ranking of the jets by transverse momentum changes the distribution.

If any triplet is found, the event is selected as a Higgs event candidate, and the two jets and the lepton are saved with all the available information (kinematics parameters, jets topology, etc). If there are still multiple dijet possibilities, the dijet with the highest invariant mass is chosen.

In case that no candidate passes the selection, *untagged* jets (b -jet $_{K_T}$) are considered and are tested with *tagged* jets and the selected leptons. The events which fulfil the criteria discussed above are saved as Higgs event candidates.

Table 4.10 shows the final selection efficiency for double tagged dijet. At the centre-of-mass energy of 10 TeV, the creation of a double tagged dijet is the most stringent criterion in all the channels, but the $HW^\pm/Z^0 \rightarrow b\bar{b} + \ell$ decay remains the most probable. Almost all the $b\bar{b}$ events have been discarded by the successive selection criteria, and a large fraction of the $t\bar{t}$ and $Z^0 X$ events have also been rejected.

	global evt cut	ℓ	2VV jets	& ΔR & $\sum E_T^{\text{jets}}$ & $\sum P_T^{\text{jets}}$	
HW^\pm/Z^0	96.5 %	60.7 %	7.2 %		4.1 %
$t\bar{t}$	96.2 %	53.0 %	2.5 %		1.1 %
$Z^0 Z^0$	97.0 %	65.0 %	4.6 %		3.7 %
$Z^0 W^\pm$	96.9 %	63.3 %	4.4 %		2.3 %
γ^*/Z^0+2b	97.0 %	65.0 %	4.6 %		0.8 %
$W^\pm+2b$	96.9 %	63.3 %	4.4 %		1.6 %
$b\bar{b}$	35.3 %	$1.22 \cdot 10^{-4}$	$2.0 \cdot 10^{-6}$		$3.7 \cdot 10^{-7}$

Table 4.10: Summary of the selection efficiency for all channels with only one primary vertex.

4.5.1 Dijet Mass Distribution

Figure 4.57 shows the normalised dijet mass distributions after the selection procedure and the jet energy optimisation algorithm (Section 4.3.3). The plots are normalised to unity.

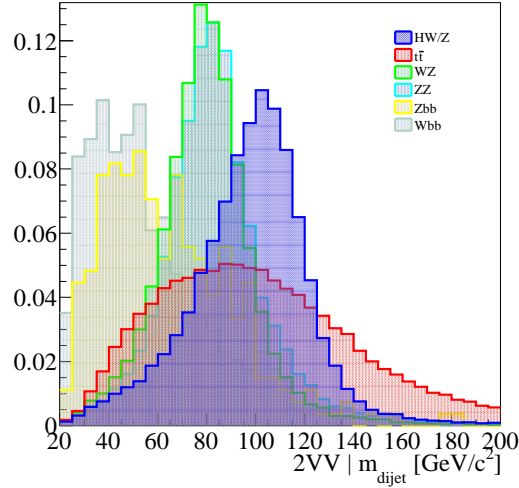


Figure 4.57: Normalised dijet invariant mass distributions with only 2 VV Seed jets.

Figure 4.58 shows the expectations for dijets built with two VV seeds normalised to one $\text{year}_{\text{LHCb}}$ (2 fb^{-1}) assuming $\sqrt{s} = 10 \text{ TeV}$, while figure 4.59 shows single tagged events (HW^{\pm}/Z^0 , Z^0Z^0 and Z^0W^{\pm} distributions are represented scaled up by a factor ten).

Raw significances calculated for $\int \mathcal{L} dt = 2 \text{ fb}^{-1}$ and 10 fb^{-1} , and $\sqrt{s} = 10 \text{ TeV}$, are given in Table 4.12. The expected number of events are given in Table 4.11. The situation with $\sqrt{s} = 14 \text{ TeV}$ will be discussed later. Both number of expected events and the significances obtained so far are low. Thus, additional criteria are needed in order to improve the selection and the efficiencies (see section 4.6.1).

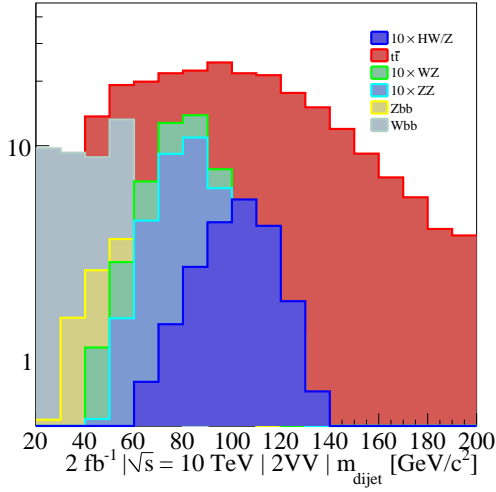


Figure 4.58: Expected dijet invariant mass distributions with only 2 VV Seed jets for 2 fb^{-1} at $\sqrt{s} = 10 \text{ TeV}$.

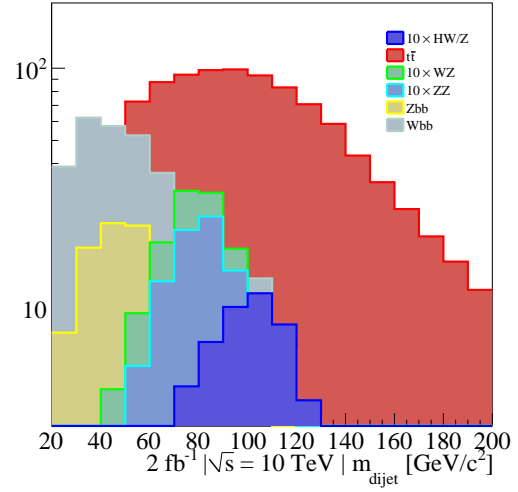


Figure 4.59: Expected dijet invariant mass distributions with 2 VV Seed jets or 1 VV + 1 K_T for 2 fb^{-1} at $\sqrt{s} = 10 \text{ TeV}$.

	σ [pb]	σ_{red} [pb]	N_{evts}	N_{sel} $80 < m_{\text{dijet}}^{\text{VV}} < 130$	N_{sel} $80 < m_{\text{dijet}}^{\text{VV or VK}_T} < 130$
HW^\pm/Z^0	0.145	0.028	56	1.8	4.1
$t\bar{t}$	240	10.5	21 k	106.9	441.3
$Z^0 Z^0$	0.56	0.05	100	2.1	4.9
$Z^0 W^\pm$	0.56	0.11	202	2.4	5.7
$\gamma^*/Z^0 + 2b$	4500	29	58 k	6.6	52.0
$W^\pm + 2b$	50000	32	64 k	3.1	32.4

Table 4.11: Total cross section and expected number of reconstructed events for the signal and the various background per year_{LHCb} ($\int \mathcal{L} dt = 2 \text{ fb}^{-1}$) and for a centre-of-mass energy of $\sqrt{s} = 10 \text{ TeV}$.

Nb years	$\int \mathcal{L} \text{ fb}^{-1}$	Type of dijets	S/\sqrt{B}
1	2	double tagged	$1.8/\sqrt{106.9 + 2.1 + 2.4 + 6.6 + 3.1} = 0.17$
		single or double tagged	$4.1/\sqrt{441.3 + 4.9 + 5.7 + 52.0 + 32.4} = 0.18$
5	10	double tagged	$9/\sqrt{605.5} = 0.37$
		single or double tagged	$20.5/\sqrt{2681.5} = 0.40$

Table 4.12: Raw significance for two integrated luminosity scenarios, at $\sqrt{s} = 10 \text{ TeV}$ with year_{LHCb}, and scaled up to five years.

4.5.2 Higgs Selection Efficiency and Purity

The performance of a selection procedure can be assessed through the calculation of the “efficiency” and “purity” values. For this study the fully simulated dijet mass is compared to the “ideal” invariant mass which can be inferred using jets determined on full-MC but using the b -hadron direction from the Monte-Carlo truth (b -hadron_{4v}). The following numbers are computed:

- $N_{\text{dijet}}^{\text{rec}}$ is the number of selected events with a reconstructed dijet mass between 80 GeV/c² and 130 GeV/c²,
- $N_{\text{dijet}}^{\text{MC}}$ is the number of events with dijet mass computed using the b -hadron_{4v} between 80 GeV/c² and 130 GeV/c²,
- N_{good} is the number of event, with reconstructed dijet mass between 80 GeV/c² and 130 GeV/c² in agreement with the four-vector level.

Figure 4.60 illustrates idea: the red square represents N_{good} , the vertical slice, labelled “Efficiency”, contains $N_{\text{dijet}}^{\text{MC}}$ events, while the horizontal slice, labelled “Purity”, contains $N_{\text{dijet}}^{\text{rec}}$ events.

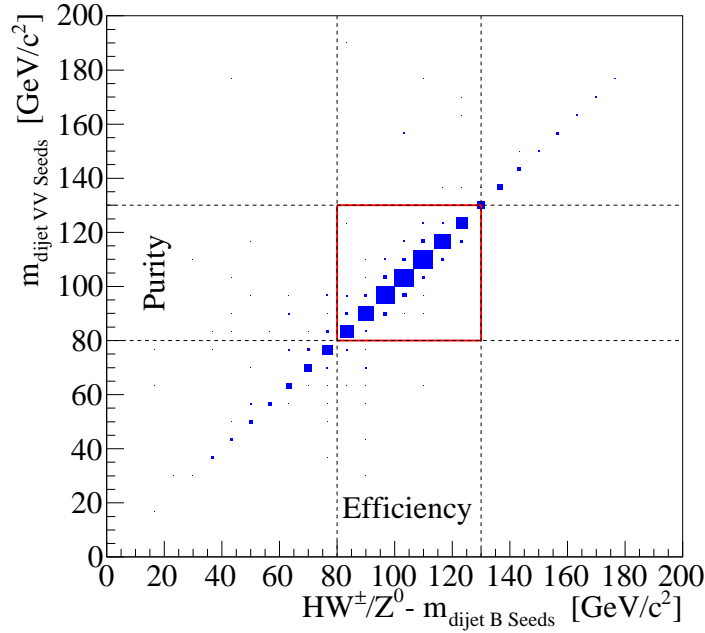


Figure 4.60: Comparison between the dijet mass reconstructed from tagged jets and using a seed from the MC-truth. The selection window is [80, 130] GeV/c² for the Higgs events $HW^{\pm}/Z^0 \rightarrow b\bar{b} + \ell$.

“Purity” and “Efficiency” ratios are defined as follows: “purity” = $N_{\text{good}}/N_{\text{dijet}}^{\text{rec}}$ and “efficiency” = $N_{\text{good}}/N_{\text{dijet}}^{\text{MC}}$. For the final selection, the “purity” defines the number of events that have been reconstructed in the correct mass range, while the “efficiency” is the number of reconstructed events compared to the ideal case, from the knowledge of the four-vector level truth. Table 4.13 shows the “purity” and “efficiency” figures for the “double” and “double+single” tagged dijet. The “purity” decreases in the second case because of K_T jets produced by underlying particles in

the events. The "efficiency" is also lower, due to the fact that the total number of reconstructed events increases more than the good reconstructed single tagged dijet in the sensitive region.

	Dijet type	"Efficiency"	"Purity"
$HW^\pm/Z^0 \rightarrow b\bar{b} + \ell$	double tagged dijet	98.8 %	95.7 %
	single or double tagged dijet	96.6 %	88.5 %

Table 4.13: "Efficiency" and "Purity" of the $HW^\pm/Z^0 \rightarrow b\bar{b} + \ell$ selection.

4.6 Background Studies

4.6.1 $t\bar{t}$ Rejection

As discussed in Section 4.5, in LHCb the most significant background for the channel $HW^\pm/Z^0 \rightarrow b\bar{b} + \ell$ is the production of $t\bar{t}$ pairs. The $t\bar{t}$ pairs give two b -jets and also two vector bosons (W^- and W^+). When at least one of the two bosons W^\pm decays leptonically, this channel mimics the signal events.

The number of $t\bar{t} \rightarrow bW^+ \bar{b}W^-$ events that pass the selection leads to a number of events in the interesting dijet mass region as seen above (Table 4.11) almost two orders of magnitude larger than the signal HW^\pm/Z^0 . In order to discriminate the signal from the background and to increase the significance S/\sqrt{B} , several observables were considered to be combined into a Neural Network ($\text{NN}_{t\bar{t}}$).

The final choice of discriminant variables has been driven by the previous research on the Higgs in LHCb [66, 67].

Kinematical Variables: For the two b -jets (j_1, j_2), the transverse momenta, $p_T^{j_{1,2}}$, the energies $E_{j_{1,2}}$, invariant masses $m_{j_{1,2}}$ and pseudorapidities $\eta_{j_{1,2}}$ are considered. For the lepton, the momentum, p_ℓ , the transverse momentum, p_T^ℓ , and the energy, E_ℓ , are considered.

A pseudo-particle is formed adding the four momenta of the two b -jets and the lepton. Its transverse momentum, $p_T^{j_1+j_2+\ell}$, represents a fundamental component of hard processes such as HW^\pm/Z^0 , whereas $t\bar{t}$ pair events contain at least an additional lepton. Figures 4.61 and 4.62 show all the variables for the HW^\pm/Z^0 (line) and $t\bar{t}$ (dashed line) channels, for events with a reconstructed dijet mass between 80 GeV/c^2 and 130 GeV/c^2 .

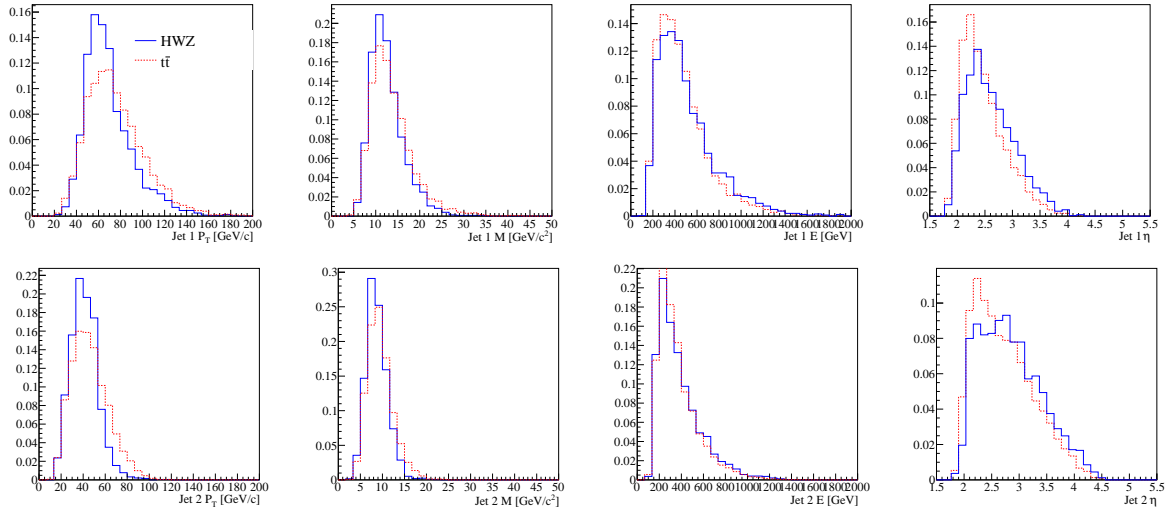


Figure 4.61: The transverse momentum, p_T , the invariant mass, m , the energy, E and the pseudorapidity, η , distributions of the jet (1) with the highest p_T are shown on the first row for the signal HW^\pm/Z^0 (blue) and the background $t\bar{t}$ (dashed red). The same distributions for the second jet are depicted in the second row.

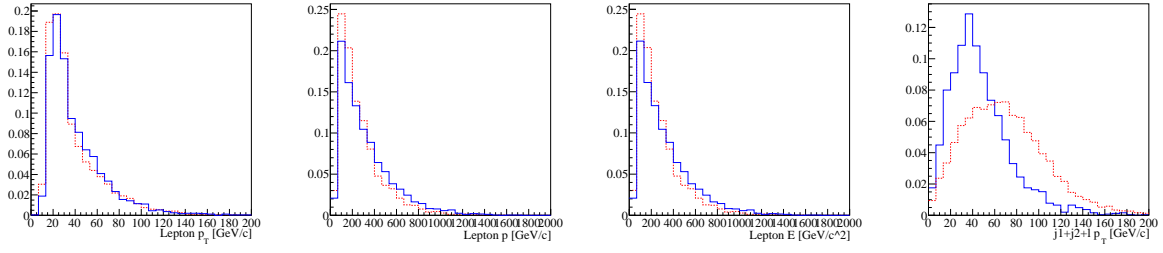


Figure 4.62: The transverse momentum, p_T , the momentum, p and the energy, E distributions of the selected lepton for the signal HW^\pm/Z^0 (blue) and the background $t\bar{t}$ (dashed red). The plot on the right shows $p_T^{j_1+j_2+\ell}$.

Global Event Pattern Variables: The total visible energy of the event, E_{evt} , its invariant mass, m_{evt} , and the sum of the transverse momenta of the event, $p_T^{\text{evt}} = \sum |p_T|$, are used in the Neural Network. All these values are built from the calorimeters raw information and from the reconstructed muons. Each hit in one of the calorimeters forms a massless particle coming from the primary vertex. The summation of their respective four-momentum gives the total energy of the event and the pseudo-invariant mass, while the total transverse momentum is the scalar summation of the transverse momenta. The pseudo-invariant mass and p_T^{evt} provide an information on the spread of the particles in the detector volume. Finally, the pseudo invariant mass of the event in which the lepton four-momentum has been removed, $m_{\text{evt}-\ell}$ is also included.

All these distributions, for a reconstructed dijet with a mass between 80 GeV/c^2 and 130 GeV/c^2 are illustrated in Figure 4.63.

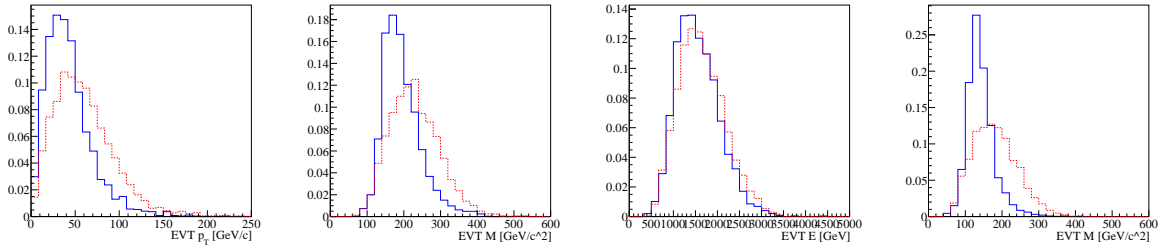


Figure 4.63: The transverse momentum, p_T , the invariant mass, m , the energy, E and $m_{\text{evt}-\ell}$ distributions of all visible events for the signal HW^\pm/Z^0 (blue) and the $t\bar{t}$ background (dashed red).

Topological Variables: The distances between each b -jet and the selected lepton, $\Delta R(j_{1,2}, \ell)$, are kept for the Neural Network. HW^\pm/Z^0 and Z^0W^\pm or Z^0Z^0 differ in the nature of the boson which decays into the $b\bar{b}$ pair. The Higgs boson is scalar while the Z^0 is a vector boson. When a vector boson decays into a $b\bar{b}$ pair an asymmetry appears between the b -jets pseudorapidities η_b and $\eta_{\bar{b}}$. This effect can in principal be used to reduce the “irreducible” background Z^0W^\pm and Z^0Z^0 . Therefore the dijet polar angle $\theta_{\text{dijet}}^{V^*}$ in the primary off-shell gauge boson $V^* = W^\pm$ or Z^{0*} rest-frame is computed. An event is said to be Z^0 -associated if a pair of opposite charge leptons, μ or e , can be found with an invariant mass in the range 76 GeV/c^2 to 106 GeV/c^2 . In this case the primary “off-shell” boson is reconstructed with the dijet and the dilepton four-momentum vectors. The

non Z^0 -associated events in which no Z^0 can be reconstructed, not only represent the events that have a W^\pm but also the events in which one lepton is not detected. The reconstruction of the primary off-shell gauge boson is experimentally not possible due to the missing information (either a neutrino or a lepton is missing). The primary “off-shell” gauge bosons can approximately be reconstructed assuming that it was emitted with a negligible transverse momentum. This gives a (second-degree) equation which leads to two solutions for the polar angle, $\theta_{\text{dijet}}^{V^*}$ and $\theta_{\text{dijet}}^{V^*}$. Both are kept as NN input variables, since it is not possible to distinguish between them (even if one is non-physical). For the Z^0 -associated events, $\theta_{\text{dijet}}^{V^*}$ is saved twice in $\theta_{\text{dijet}}^{V^*}$ and $\theta_{\text{dijet}}^{V^*}$.

Finally, the polar angle of the b -jet with the largest transverse momentum, and the lepton in the dijet rest-frame are also used. Figure 4.64 shows the distributions for these variables for the signal and the $t\bar{t}$ background, for a reconstructed dijet with a mass between 80 GeV/ c^2 and 130 GeV/ c^2 .

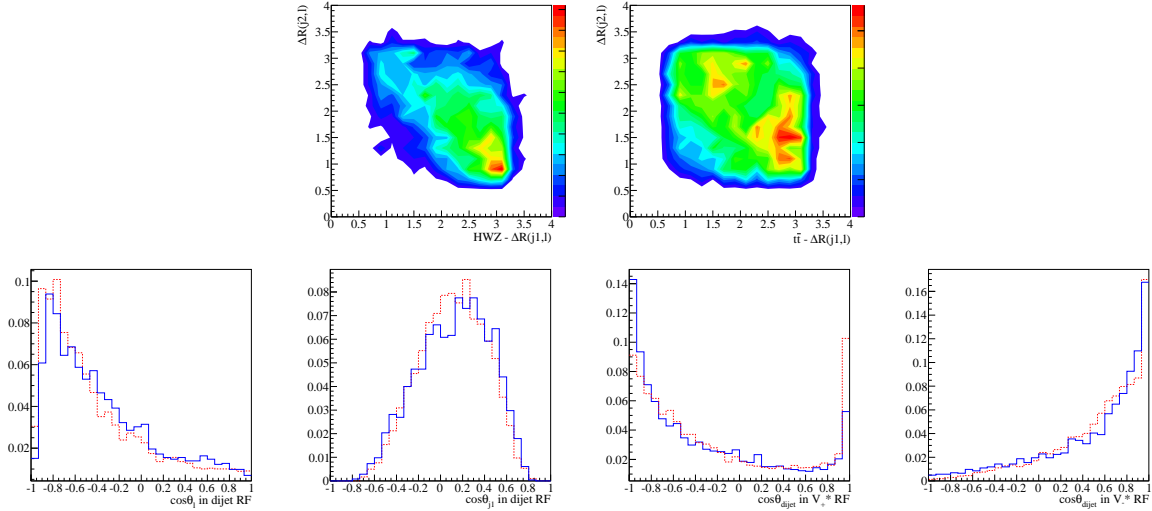


Figure 4.64: The first row represents $\Delta R(j_1, \ell)$ vs $\Delta R(j_2, \ell)$ for the HW^\pm/Z^0 signal on the left and for the $t\bar{t}$ background on the right. The second row shows the cosine of the polar angle of: ℓ in the dijet rest-frame (RF), j_1 in the dijet RF and the two possibilities for the dijet in the reconstructed V^* RF for the signal HW^\pm/Z^0 (blue line) and the background $t\bar{t}$ (dashed red line).

All the variables entering in the Neural Network are grouped together in Table 4.14. Figures 4.61 to 4.63 illustrate how similar the signal and the background distribution are for each variable taken separately.

The NN is trained using the *Toolkit for Multivariate Data Analysis with ROOT* (TMVA) [74]. The Multilayer Perceptron (MLP) Neural Network has been chosen to discriminate between signal over background. It uses the Broyden-Fletcher-Goldfarb-Shannon (BFGS) method for the training and the neuron activation function is a sigmoid. Two hidden layers with respectively 27 and 25 cells are used (see Figure 4.65), while the answer is given by only one neuron. The input variables, x_i^1 , are transformed in order to be in the range $[0, 1]$. Each cell i of the layer k is connected to all cells of the next layer, $k + 1$, with a weight $w_{i \rightarrow j}^k$. The value of the cell j in

variable	description
m_{j_1}	b -jet 1 invariant mass
E_{j_1}	b -jet 1 energy
$p_T^{j_1}$	b -jet 1 transverse momentum
η_{j_1}	b -jet 1 pseudorapidity
m_{j_2}	b -jet 2 invariant mass
E_{j_2}	b -jet 2 energy
$p_T^{j_2}$	b -jet 2 transverse momentum
η_{j_2}	b -jet 2 pseudorapidity
$ \vec{p}_\ell $	selected lepton momentum
p_T^ℓ	selected lepton transverse momentum
E_ℓ	selected lepton energy
$p_T^{j_1+j_2+\ell}$	(b -jet 1 + b -jet 2 + selected lepton) transverse momentum
p_T^{evt}	sum of the transverse momenta in the event
E_{evt}	total visible event energy
m_{evt}	total visible event invariant mass
$m_{\text{evt}-\ell}$	total visible event invariant mass without the selected lepton
$\Delta R(j_1, \ell)$	separation in the $\eta - \phi$ plane between b -jet 1 and the selected lepton
$\Delta R(j_2, \ell)$	separation in the $\eta - \phi$ plane between b -jet 2 and the selected lepton
$\cos(\theta_\ell^{\text{dijet}})$	cosine of the selected lepton polar angle in the dijet rest-frame
$\cos(\theta_{j_1}^{\text{dijet}})$	cosine of the highest- p_T b -jet polar angle in the dijet rest-frame
$\cos(\theta_{\text{dijet}}^{V^*})$	cosine of the dijet polar angle in the primary off-shell gauge boson V^* rest-frame (1 st solution)
$\cos(\theta_{\text{dijet}}^{V^*_-})$	cosine of the dijet polar angle in the primary off-shell gauge boson V^* rest-frame (2 nd solution)

Table 4.14: Discriminating variables used as input for the Neural Network. b -jet 1 is the jet with the highest p_T . For Z^0 - associated: $\theta_{\text{dijet}}^{V^*_-} = \theta_{\text{dijet}}^{V^*_+} = \theta_{\text{dijet}}^{V^*}$.

the new layer ($k + 1$) is calculated with:

$$x_i^{k+1} = F \left(w_{0 \rightarrow j}^k + \sum_i w_{i \rightarrow j}^k \cdot x_i^k \right), \quad \text{with } F(t) = \frac{1}{1 + e^{-t}}. \quad (4.17)$$

$F(t)$ is the sigmoid function and $w_{0 \rightarrow j}^k$ is the weight of the “bias neuron” to the x_j^{k+1} cell. The weights, $w_{i \rightarrow j}^k$, are calculated by minimising the difference between the network response and the desired value. The same procedure is applied to the next layer. Table 4.15 presents the main parameters of the Neural Network used for the $t\bar{t}$ rejection.

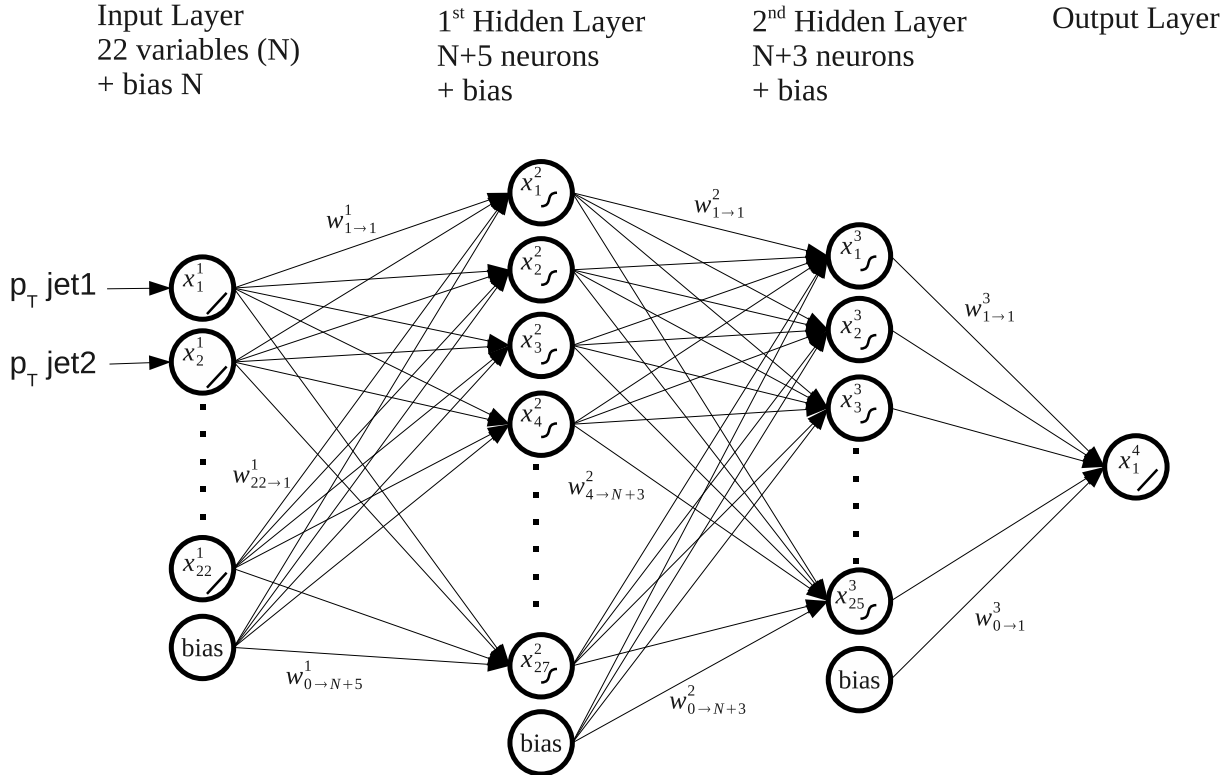


Figure 4.65: Illustration of the Multilayer Perceptron with one input layer containing 22 neurons, two hidden layers (with 27 and 25 neurons) and one output cell that gives the Neural Network response. The “bias neurons” are fixed at 1.

variable	value
Number of training cycle	600
Hidden layer architecture	$N + 5(+1)$, $N + 3(+1)$
Neuron activation function type	sigmoid
Training method	BFGS
Learning rate	0.02
Decay rate	0.01

Table 4.15: Main parameters of the Neural Network for the $t\bar{t}$ rejection.

The Neural Network has been trained on events having a dijet mass in the range of interest, between 80 GeV/c² and 130 GeV/c². Single- and double-tagged events have been used. Figure 4.66 shows the Neural Network output value, NN_{out} , for the signal HW^\pm/Z^0 and the background $t\bar{t}$. NN_{out} should peak at a value of one for signal-like event and at zero for the background. The irreducible background channels, Z^0Z^0 and Z^0W^\pm , are still mimicking the HW^\pm/Z^0 events. The choice of the cut value maximises the significance ratio S/\sqrt{B} . Figure 4.67 shows the significance as a function of the cut on NN_{out} in the case of a scenario with $\sqrt{s} = 10$ TeV and for $\int \mathcal{L} dt = 2 \text{ fb}^{-1}$. The maximum is reached for $NN_{\text{out}} = 0.48$. This cut gives a significance of 0.27, with 2.6 expected HW^\pm/Z^0 signal events, 85.4 $t\bar{t}$ events, and 3.0 events, 2.4 events for the Z^0W^\pm and Z^0Z^0 respectively. Table 4.16 shows the final results with the cut on the NN response at 0.48.

	σ [pb]	σ_{red} [pb]	N_{evts}	N_{sel} $80 < m_{\text{dijet}} < 130$	$NN_{\text{out}} > 0.48$
HW^\pm/Z^0	0.145	0.028	56	4.1	2.9
$t\bar{t}$	240	10.5	21'000	441.3	100.1
Z^0Z^0	0.56	0.05	100	4.9	3.7
Z^0W^\pm	0.56	0.11	202	5.7	4.0
$\gamma^*/Z^0 + 2b$	4500	29	58'000	52.0	37.9
$W^\pm + 2b$	50000	32	64'000	32.4	24.6

Table 4.16: Summary of the cross section and numbers of expected reconstructed events for the signal and the backgrounds per year_{LHCb} and for a centre-of-mass energy of $\sqrt{s} = 10$ TeV.

The number of $t\bar{t}$ events is almost one order of magnitude below the previous selection after the cut on the Neural Network response. The “irreducible” background, that are Z^0Z^0 and Z^0W^\pm , have almost the same reduction factor $\sim 60\%$ as the signal.

A second NN has been trained on the same variables to remove the $Z^0 \rightarrow b\bar{b}$ without any significant improvement. Finally a third NN was trained on all the considered background species simultaneously without any improvement.

The final significance is given for the integrated luminosities: 2 fb^{-1} and scaled up to 10 fb^{-1} . Table 4.17 shows this significance, and figures 4.68 and 4.69 show the dijet mass distributions for the signal and the background channels. The detail of the signal region, from 80 GeV/c² to 130 GeV/c², is shown on the plot at the right.

Nb years	$\int \mathcal{L} [\text{fb}^{-1}]$	S/\sqrt{B}
1	2	$2.9/\sqrt{100.1 + 3.7 + 4.0 + 37.9 + 24.6} = 0.22$
5	10	$14.5/\sqrt{851.5} = 0.50$

Table 4.17: Raw significance calculation, with $\sqrt{s} = 10$ TeV, for two integrated luminosity scenarios.

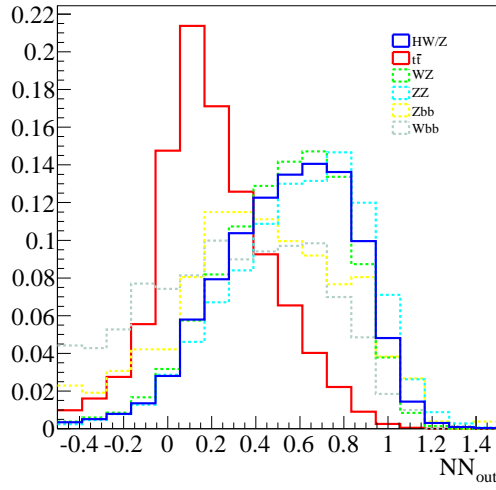


Figure 4.66: Output variable of the Neural Network, NN_{out} , used to discriminate the $t\bar{t}$ background from the signal.

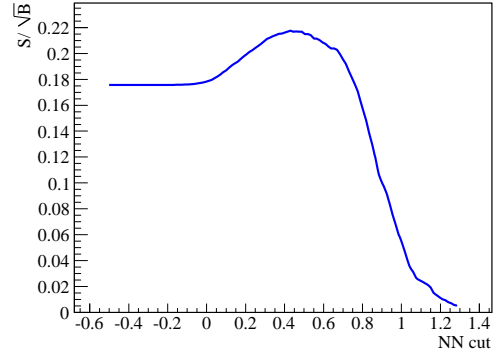


Figure 4.67: Significance ratio, S/\sqrt{B} , as a function of the cut on NN_{out} in the sensitive mass range and for 2 fb^{-1} .

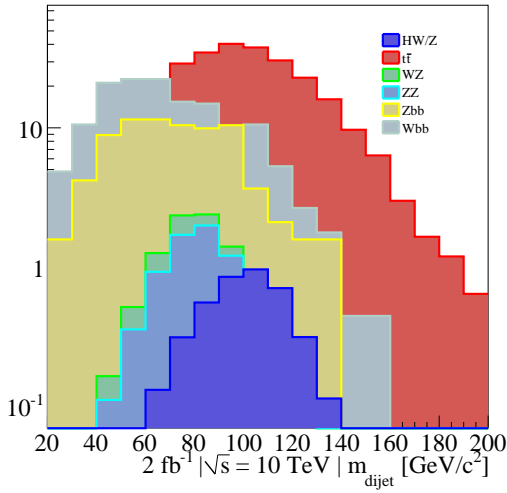


Figure 4.68: Logarithmic scale dijet mass distribution for the candidates passing the cut $NN_{out} > 0.48$ for the signal HW^\pm/Z^0 and for various background sources. Stacked histograms.

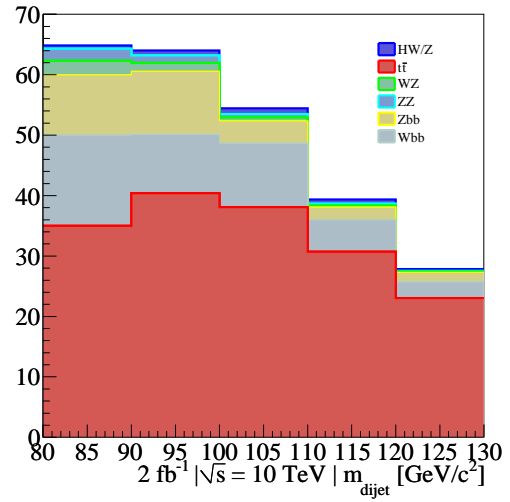


Figure 4.69: Dijet mass distribution for the candidates passing the cut $NN_{out} > 0.48$ for the signal HW^\pm/Z^0 and for various background sources in the sensitive mass range. Stacked histograms.

4.6.2 Z^0 Selection

Reconstruction with Isolated Leptons

When multiple high- p_T prompt leptons are selected, considering or not the isolation criterion, a dilepton invariant mass m_{dilepton} can be reconstructed. The invariant mass is calculated for the momentum of the jet built around each lepton, for leptons identified as a lepton-antilepton pair. The plots 4.70 and 4.71 show the invariant mass, when at least one of the lepton passes the ΔE cut, for the $HW^\pm/Z^0 \rightarrow b\bar{b} + \ell$ and $Z^0Z^0 \rightarrow b\bar{b} + \ell^+\ell^-$ events. The dimuon, plain blue line, pairs show a peak at m_{Z^0} when the two muons pass the ΔE criterion, while the dielectron suffer from the saturation of the ECAL for the high- p_T , and therefore shows a plateau which extends up to m_{Z^0} .

Table 4.18 shows the expected number of dimuon events within a mass window of $m_{Z^0} \pm 5 \text{ GeV}/c^2$ per year_{LHCb} in the event type analysed.

	selection	σ_{red} [pb]	$N_{\text{evt}}^{\text{year}_{\text{LHCb}}}$
$HW^\pm/Z^0 \rightarrow b\bar{b} + \ell$	$2.39 \cdot 10^{-3}$	0.028	0.25
$t\bar{t} \rightarrow bW^+ \bar{b}W^-$	$1.73 \cdot 10^{-5}$	10.5	0.88
$Z^0Z^0 \rightarrow b\bar{b} + \ell^+\ell^-$	$7.89 \cdot 10^{-3}$	0.05	1.14
$Z^0W^\pm \rightarrow b\bar{b} + \ell^\pm \ell^\pm \nu_\ell^{(-)}$	0	0.11	0

Table 4.18: Expected number of dimuon events per year_{LHCb}.

The expected events in the dimuon peak within a mass window of $m_{Z^0} \pm 5 \text{ GeV}/c^2$ could

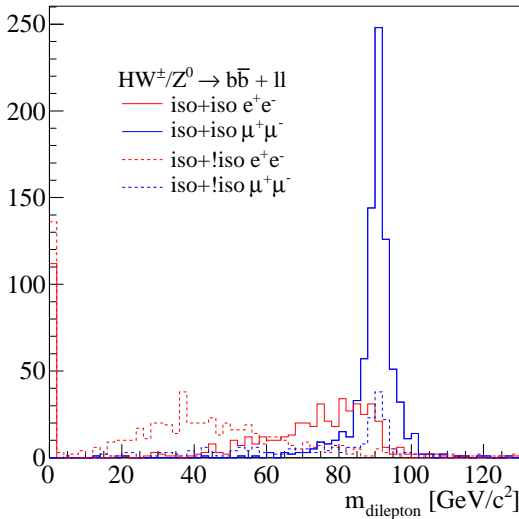


Figure 4.70: Dilepton invariant mass, for high- p_T prompt leptons ($HW^\pm/Z^0 \rightarrow b\bar{b} + \ell$). The isolation cut (ΔE) is applied at least on one lepton.

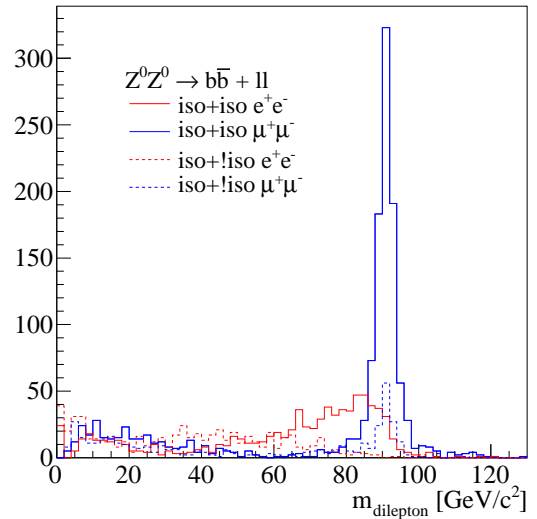


Figure 4.71: Dilepton invariant mass, for high- p_T prompt leptons ($Z^0Z^0 \rightarrow b\bar{b} + \ell^+\ell^-$). The isolation cut (ΔE) is applied at least on one lepton.

be evaluated for $HW^\pm/Z^0 \rightarrow b\bar{b} + \ell$ and $Z^0Z^0 \rightarrow b\bar{b} + \ell^+\ell^-$ which are now “signal”, while $t\bar{t} \rightarrow bW^+ \bar{b}W^-$ and $Z^0W^\pm \rightarrow b\bar{b} + \ell^\pm \overset{(-)}{\nu}_\ell$ are the background. For the events at the centre-of-mass of 10 TeV, one event is expected.

Reconstruction with b -Jets

The selection criteria of b -jets seen above can be directly applied to select Z^0Z^0 and Z^0W^\pm events which contains a Z^0 that decays into a $b\bar{b}$ pair. In the case of search for SM-like Higgs, this kind of events is background. It is important to study the Z^0 channels that can be used as control and calibration channels.

The analysis is therefore applied to $Z^0W^\pm \rightarrow b\bar{b} + \ell^\pm \overset{(-)}{\nu}_\ell$ and $Z^0Z^0 \rightarrow b\bar{b} + \ell^+\ell^-$ decays. The results have been shown above (section 4.5). The raw selection reconstructs dijets with a mass that peaks around m_{Z^0} (see figure 4.57) for both channels. Table 4.19 gives the expected number of events for $\int \mathcal{L}dt = 2 \text{ fb}^{-1}$ with the raw selection.

For this kind of decay, Z^0Z^0 and Z^0W^\pm are signals and $t\bar{t}$ (and HW^\pm/Z^0 is neglected) is the background. In the case of the usage of the two set of jets: $S/\sqrt{B} = 0.62$ in a mass window from 56 GeV/c² to 111 GeV/c² and an integrated luminosity of 2 fb⁻¹.

The analysis can be checked by requesting associated Z^0 reconstructed in the dimuon channel with $m_{\text{dimuon}} = m_{Z^0} \pm 5 \text{ GeV}/c^2$, as shown in section 4.6.2. On the same events, and with the K_T jets enabled, less than one event is expected in the $t\bar{t}$ decay (0.33), almost one event for the signal Z^0Z^0 (0.93) and none in the Z^0W^\pm channel (0.13 event in the HW^\pm/Z^0 decay). This strong requirement gives a unique signal event in the Z^0Z^0 channel.

Figure 4.72 shows the expected number of events normalised to one year ($\int \mathcal{L}dt = 2 \text{ fb}^{-1}$) at $\sqrt{s} = 10 \text{ TeV}$, with the associated selection decay $Z^0 \rightarrow \mu^-\mu^+$.

In Table 4.20 purity and efficiency are assessed for Z^0Z^0 and Z^0W^\pm events and the corresponding plots are shown in figure 4.73.

	N_{sel} $56 < m_{\text{dijet}}^{\text{VV}} < 111$	N_{sel} $56 < m_{\text{dijet}}^{\text{VV or VK}_T} < 111$
Z^0Z^0	2.8	7.1
Z^0W^\pm	3.8	9.8
$t\bar{t}$	166	732

Table 4.19: Cross section and expected number of reconstructed events for the signal and the backgrounds per year_{LHCb}.

	Dijet type	Efficiency	Purity
$Z^0 Z^0 \rightarrow b\bar{b} + \ell^+ \ell^-$	double tagged	99.1 %	95.8 %
	single or double tagged	96.8 %	86.4 %
$Z^0 W^\pm \rightarrow b\bar{b} + \ell^\pm \bar{\nu}_\ell$	double tagged	99.2 %	96.1 %
	single or double tagged	97.6 %	87.6 %

Table 4.20: Efficiency and Purity of the $Z^0 Z^0 \rightarrow b\bar{b} + \ell^+ \ell^-$ and $Z^0 W^\pm \rightarrow b\bar{b} + \ell^\pm \bar{\nu}_\ell$ selections.

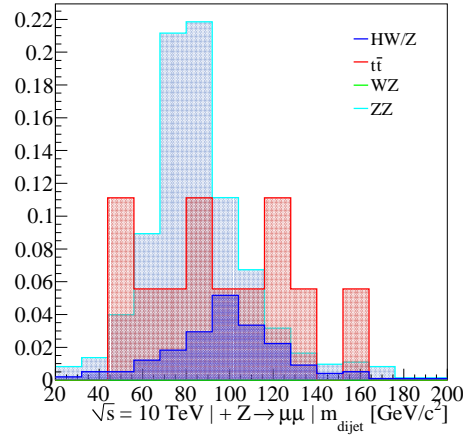


Figure 4.72: Invariant mass distributions of dijets with an associated reconstructed second Z^0 in the dimuon channel.

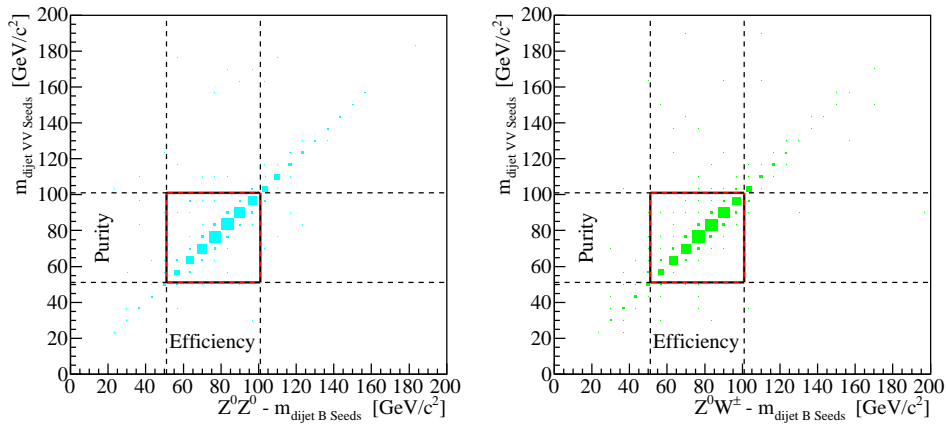


Figure 4.73: 2D plot between the Monte-Carlo Seeds dijet mass and the VV Seed Finder dijet mass in the window of $[56, 111]$ GeV/c^2 for the $Z^0 Z^0 \rightarrow b\bar{b} + \ell^+ \ell^-$ channel (left) and the $Z^0 W^\pm \rightarrow b\bar{b} + \ell^\pm \bar{\nu}_\ell$ channel (right)

4.7 Perspective

The significance, for a centre-of-mass energy $\sqrt{s} = 10$ TeV and for an integrated luminosity over one year $\int_{\text{year}} \mathcal{L} dt = 2 \text{ fb}^{-1}$, is $S/\sqrt{B} = 0.22$ ($S \sim O(1)$ event). The statistic is too low to expect any observation or hint in the channel $HW^\pm/Z^0 \rightarrow b\bar{b} + \ell$ within the LHCb experiment. Nevertheless several scenarii can be considered which will improve the results.

LO \rightarrow NLO: A point that is not displayed in the following plots and tables is the computation of the cross sections at NLO. The cross sections used in the thesis are provided by Pythia, i.e. at the Leading Order (LO); and are expected to increase [71] when higher orders are considered. This effect can be estimated to be in the range of 10 % to 50 %. Even if the background production increases by this amount, the ratio S/\sqrt{B} would still increase by roughly the root of the estimated enhancement, i.e. 5 % to 20 %

10 TeV \rightarrow 14 TeV: In the near future the LHC machine is planned to run at the nominal centre-of-mass energy of the pp collision of $\sqrt{s} = 14$ TeV. The production cross section of the various channels depends on pp collision centre-of-mass energy. Table 4.2 shows an increase by a factor of two at $\sqrt{s} = 14$ TeV, with a potential gain of $\sqrt{2}$ in significance. The complete analysis has been performed on events produced in these conditions. The expected number of events for the signal, HW^\pm/Z^0 , is 6.7 representing a gain factor of 2.3, while in the same time the background will pass from 170.3 events to 439.3. The background yield increases by 2.6, slightly larger than the signal increase. Nevertheless, the significance increases from 0.22 to 0.32, with a gain of 1.45 ($\sqrt{2.12}$). The significance will reach 0.72 after five years of exploitation whit $S \sim 35$ at a centre-of-mass energy $\sqrt{s} = 14$ TeV. This significance is still too low to observe anything by simple counting. Table 4.21 shows the numbers of events expected and the new significance for one year of data taking (third column).

Luminosity Upgrade: It is planned to increase the LHCb instantaneous luminosity to improve the integrated luminosity from 2 fb^{-1} to 5 fb^{-1} per year. Figure 3.3 shows that the number of collisions per bunch crossing still has its maximum probability for a single collision. The luminosity upgrade will also increase the statistics for the Higgs analysis. To test it, the full analysis has also been performed on simulated events produced with a centre-of-mass energy $\sqrt{s} = 14$ TeV and at this higher luminosity. The gain factor of the significance is roughly the expected $\sqrt{5/2}$. The significance reaches 0.5 for one year at $\sqrt{s} = 14$ TeV and with an integrated luminosity of 5 fb^{-1} . The number of Higgs events will be 13.4 for 726.7 background events. Finally the significance will reach 1.12 ($S \sim 70$) for five years of running in these conditions. Table 4.21 shows the numbers of events expected and the new significance for one year of data taking (last column).

Analysis Improvement: An improvement of the energy resolution using real b -jets could lead considering a smaller mass range. The dijet selection was tested with $90 \text{ GeV}/c^2 < m_{\text{dijet}} < 125 \text{ GeV}/c^2$, which reduces the number of background events. It is also reasonable to think of a better reconstruction which could lead to an achievable rejection of the combinatorial background by a factor of two. Both assumptions have been taken into account in a fourth scenario. The corresponding significance is 0.88 for one year of data taking at $\sqrt{s} = 14$ TeV and with an integrated luminosity of 5 fb^{-1} . The significance will reach ~ 2 after 5 years.

Table 4.22 shows all the different scenarii tested. The significance grows from 0.22 to 0.32, 0.5 or 0.88 for one year of data taking. Finally Figure 4.74 shows the evolution over the years of the different significances. The significance at 5 years have been marked.

		$\sqrt{s} = 10 \text{ TeV}$		$\sqrt{s} = 14 \text{ TeV}$	
		$\int_{\text{year}} \mathcal{L} dt = 2 \text{ fb}^{-1}$	$\int_{\text{year}} \mathcal{L} dt = 2 \text{ fb}^{-1}$	$\int_{\text{year}} \mathcal{L} dt = 5 \text{ fb}^{-1}$	
Nb of Evt's	HW^{\pm}/Z^0	2.9	\rightarrow	6.7	\rightarrow 13.4
	$t\bar{t}$	100.1	\rightarrow	294.0	\rightarrow 492.1
	$Z^0 Z^0$	3.7	\rightarrow	7.0	\rightarrow 14.1
	$Z^0 W^{\pm}$	4.0	\rightarrow	6.3	\rightarrow 15.2
	$\gamma^*/Z^0 + 2b$	37.9	\rightarrow	66.8	\rightarrow 105.1
	$W^{\pm} + 2b$	24.6	\rightarrow	65.2	\rightarrow 99.8
	S/\sqrt{B}	0.22	\rightarrow	0.32	\rightarrow 0.5

Table 4.21: Significances and expected numbers of events in the various scenarii).

Nb years	$\sqrt{s} = 10 \text{ TeV}$		$\sqrt{s} = 14 \text{ TeV}$		Analysis Improvement	
	$\int_{\text{year}} \mathcal{L} = 2 \text{ fb}^{-1}$	$\int_{\text{year}} \mathcal{L} = 2 \text{ fb}^{-1}$	$\int_{\text{year}} \mathcal{L} = 5 \text{ fb}^{-1}$	S/\sqrt{B}	$N_{\text{evt}}(HW^{\pm}/Z^0)$	
1	0.22	0.32	0.50	0.88	13.4	
2	0.31	0.45	0.70	1.24	26.8	
3	0.38	0.55	0.87	1.52	40.2	
5	0.50	0.72	1.12	1.97	67	
10	0.70	1.01	1.58	2.78	134	

Table 4.22: Significance over the years in the different scenarii.

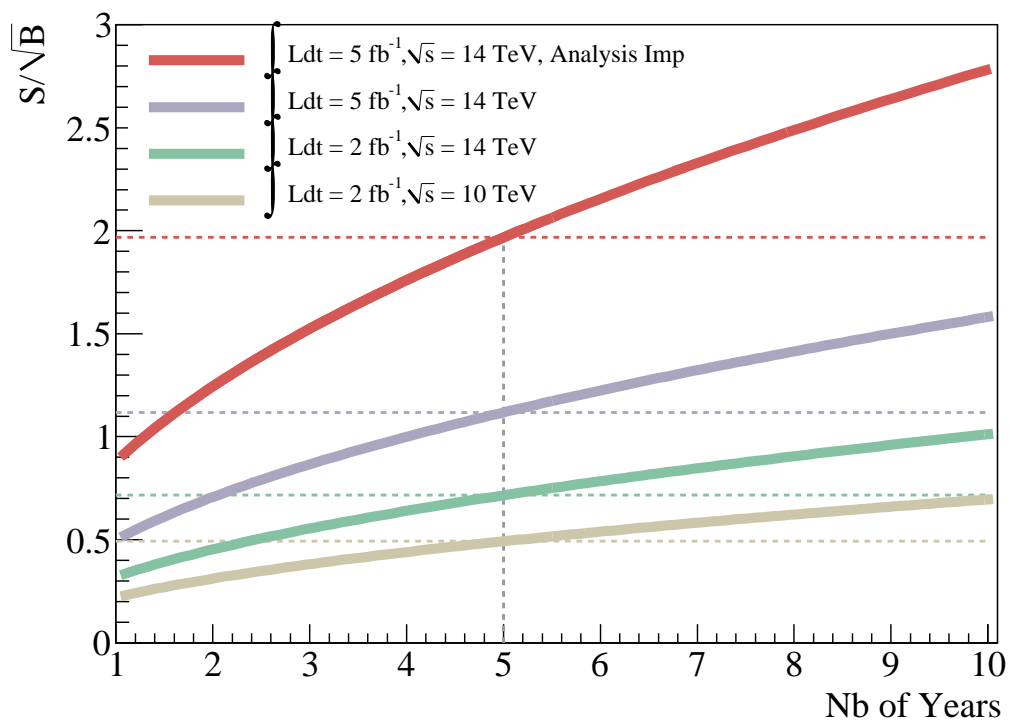


Figure 4.74: Significance over the years in the different scenarii. The Legend order corresponds to the drawn lines.

Standard Model-Like Higgs Boson: The latest Tevatron combined results set the limit on the cross section of Standard Model Higgs boson and from these upper limits, the yield can only be expected to be 2 times larger than the SM Higgs (figure 1.13 and Ref. [20]). Nevertheless, the current CDF experimental upper limits on the SM Higgs search in the associated production are at the level of 5.9 and 7.1 times that predicted within the SM, for $HW^\pm \rightarrow b\bar{b} + \ell^\pm \bar{\nu}_\ell^{(-)}$ and $HZ^0 \rightarrow b\bar{b} + \ell^+\ell^-$ respectively [75, 76]. These large ranges open the potential of this analysis to find a Standard Model-Like Higgs boson produced in association and decaying with a topology similar to SM HW^\pm/Z^0 .

Figure 4.75 illustrates the significance of the four scenarii as a function of the cross section after five years of data taking. In the case of a centre-of-mass energy $\sqrt{s} = 14$ TeV and after five years of data taking at the highest LHCb luminosity (5 fb^{-1} per year), a significance $S/\sqrt{B} = 3$ can be expected if the cross section is 2.7 larger than $\sigma_{pp \rightarrow HW^\pm/Z^0}^{SM}$. The expected number would be of the order of 200 signal events.

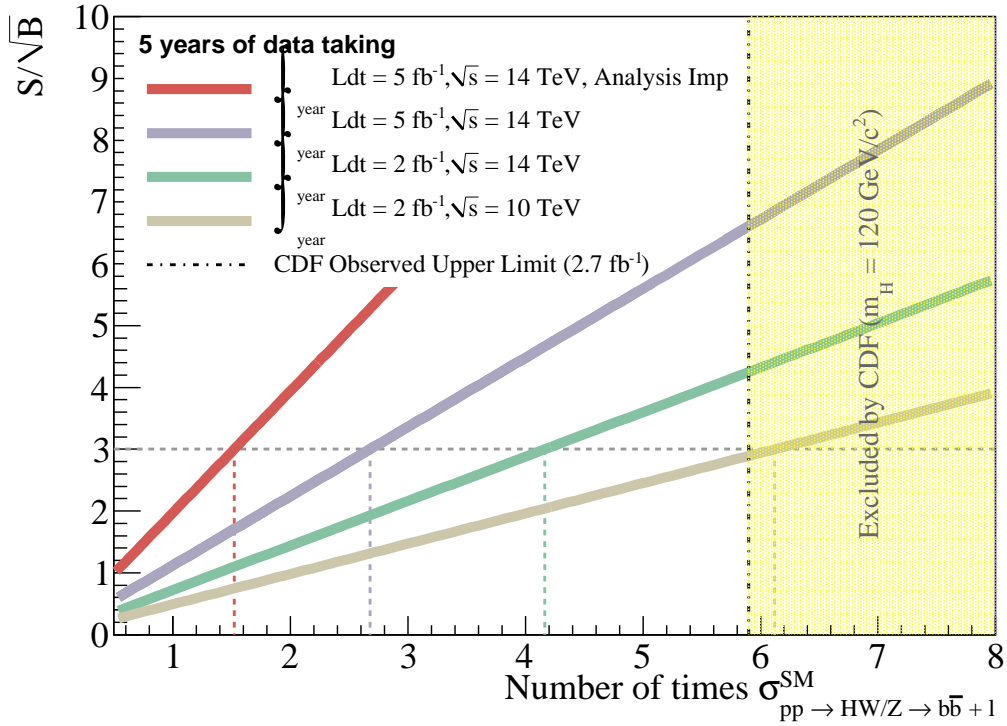


Figure 4.75: Significances after five years of data taking as a function of the cross section factor. The region above 5.9 has been excluded by the CDF collaboration in the channels $HW^\pm/Z^0 \rightarrow b\bar{b} + \ell$.

5

Software Integration of Data Acquisition Cards



The LHCb experiment has developed the Data Acquisition boards, built in Lausanne and called TELL1, on Field Programmable Gate Arrays technology. The TELL1s constitute the main component of the DAQ chain and are integrated in the global LHCb Experiment Control System. To that end, a software framework has been designed for the TELL1 to comply with the Supervisory Control And Data Acquisition (SCADA) tool chosen by CERN for the LHC experiments.

The LHCb detector operation is handled by the so-called online system. The three main components of the online system are the Timing and Fast Control (TFC) system that handles the distribution of the LHC beam-synchronous clock, trigger and resets, the Data Acquisition (DAQ) system in charge of streaming data from the FE electronics to the storage and the Experiment Control System (ECS). The latter is used for the configuration, control and monitoring of all the online system components. Figure 5.1 presents the general structure of LHCb online system.

This chapter presents the complete framework (internal structure, configuration, graphical user interfaces, etc...) developed to allow the integration of the TELL1 boards into the ECS of the LHCb experiment.

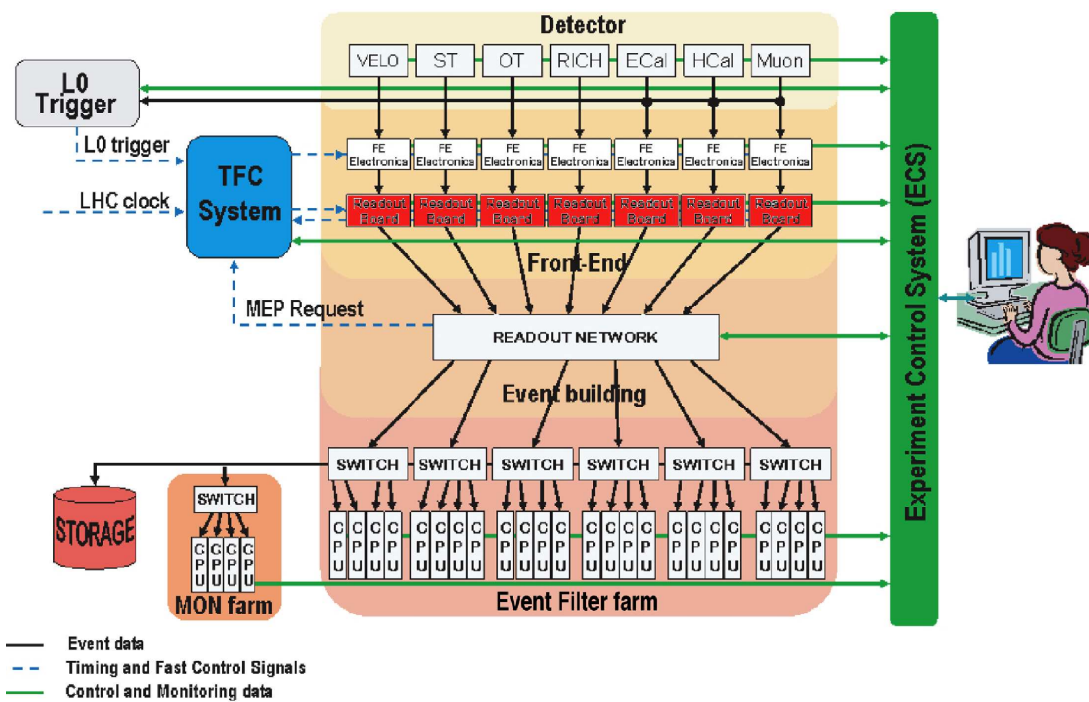


Figure 5.1: General architecture of the LHCb online system. The TELL1 readout boards are highlighted in red. The TELL1 boards are configured and monitored through the ECS, shown in green.

5.1 Data Acquisition Cards: TELL1

The LHCb detector consists of roughly one million detector channels. At the LHC bunch-crossing rate of 40 MHz the complete detector must be read out 40 million times every second. Due to limited power, space, material and financial budget requirements a fast pre-selection (trigger) of interesting events is implemented. During the time needed by the trigger algorithm to reach and distribute its decision, the majority of the data is temporarily stored in the FE electronics in a harsh radiation environment. Upon a first-level trigger accept decision the data is transferred over long (100 m) digital optical or specific for the VeLo 60 m analog copper links to the data acquisition boards called TELL1 (Trigger Electronics Level 1). A total of the order of 300 TELL1 boards are used by the different subdetectors (the RICH system is read with the so-called UKL1 readout board which has equivalent tasks as the TELL1 board). The TELL1 electronics is installed in the radiation-safe area in the shadow of a concrete shielding wall where standard electronic components can be employed.

Figure 5.2 shows a picture of the TELL1. It consists of a motherboard hosting several mezzanine daughter cards. A simplified block-diagram of TELL1 is presented in Figure 5.3.

While the data processing is different for each subdetector, the TELL1 card provides a common hardware and software framework for the implementation of customised algorithms. The subdetector specific adaptations are implemented on the Field Programmable Gate Arrays (FPGA). The main components of a TELL1 boards are:

Receiver Cards: Each TELL1 has four connectors accepting either four Analog Receiver mezzanines (*A-Rx*), or two Optical Receiver mezzanines (*O-Rx*). The receiver mezzanine system allows the TELL1 to cope with the two link systems. Due to the high radiation level and the tight space constraints in the proximity of the VeLo, an analog transmission of at least 10 to 15 m was estimated to be unavoidable before any digitisation could occur. Instead of this two step analog copper followed by digital optical system a complete analog link of a length of 60 m was chosen. This solution is more practical and cost effective. Consequently, the VeLo data is digitised only in the counting house by the TELL1. Thus, the TELL1 boards attributed to the VeLo are mounted with A-Rx mezzanines, which receive and digitise the signal. Each A-Rx card accepts 16 input channels of 10-bit ADCs sampled at 40 MHz. The other subdetectors opted for optical fibres to transmit their data, therefore they use O-Rx mezzanines that can have in total 24 channels per TELL1. The maximum data input bandwidth is 25.6 Gbit/s and 30.7 Gbit/s for the A-Rx and O-Rx versions, respectively. The L0DU TELL1 board uses in place of the receiver cards a daughter card which integrates three Field Programmable Gate Arrays to process the Level-O data.

Field Programmable Gate Arrays (FPGA): The data processing is performed on five large Altera Stratix I FPGAs [77]. Each FPGA has a total of 25'600 Logic Elements and 1'944 kbit of distributed on SRAM memory chip.

PP-FPGA: Four “Pre-Processor” FPGAs per TELL1 board receive on all links in parallel the L0 accepted data from the receiver cards. The maximal L0 accept rate is limited to 1.11 MHz corresponding to 36 LHC clock cycles event transmission period. All detectors have a constant L0 event frame length of 36 clock-cycles which is a basic LHCb requirement applying to all subdetectors. The first task of the PP-FPGAs is to synchronise and time-stamp the incoming parallel data with the help of the TFC information available from a on board TTC receiver chip. The next stage is the *pedestal* subtraction which brings the mean of each channel to zero, it is followed by the Common Mode Suppression filters. Finally Zero Suppression, clustering and encapsulation in a custom bank data format is performed.

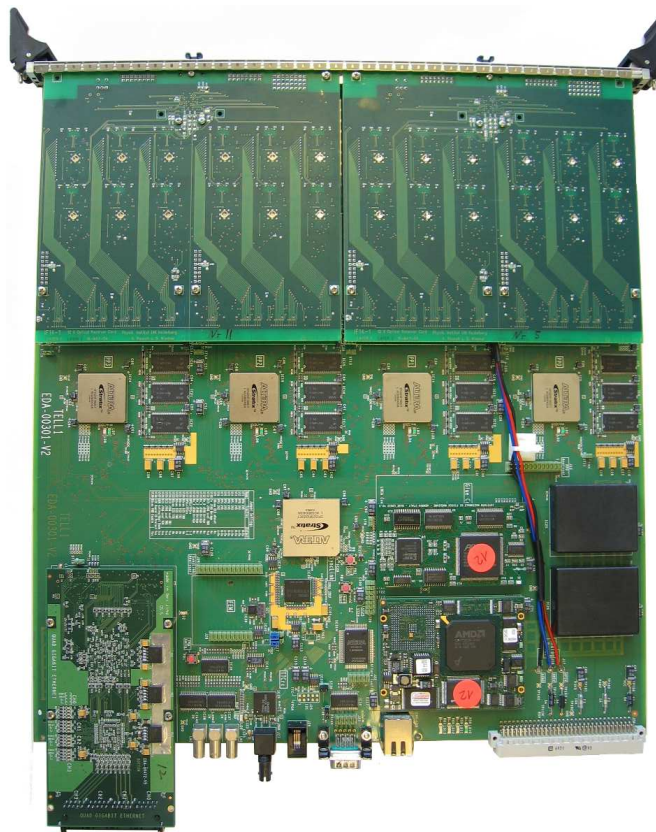


Figure 5.2: A photograph of the TELL1 board.

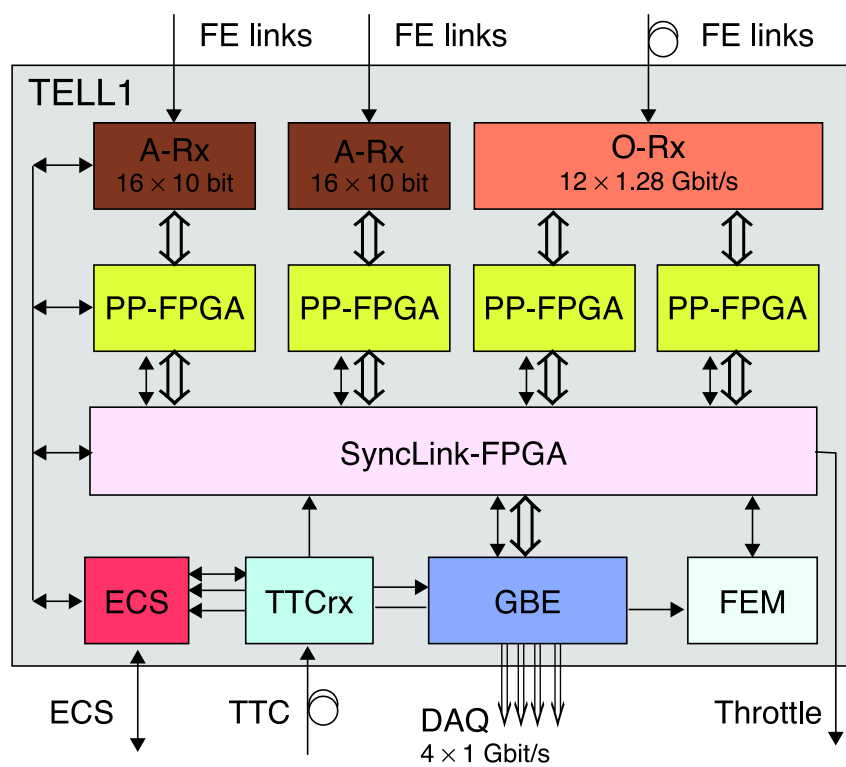


Figure 5.3: Simplified block-diagram of TELL1.

SyncLink-FPGA: The “Synchronisation and Link” FPGA is connected to the TTC receiver and distributes the synchronisation clock, trigger and resets signals for time-stamping (event identification) to the PP-FPGAs. Each PP-FPGA transmits the processed data in form of event banks to the SyncLink-FPGA which collects and merges them to form complete events and moreover multiple events. These so-called multi-event packets (MEP) are finally encapsulated into raw IP packets. The assembly of multiple events in MEPs is a measure taken to reduce the packet-rate on the network employed for the event building. The transmission to the event building network is implemented on standard Gigabit Ethernet technology. Figure 5.4 shows the multiple steps performed in the FPGAs for VeLo or ST signals.

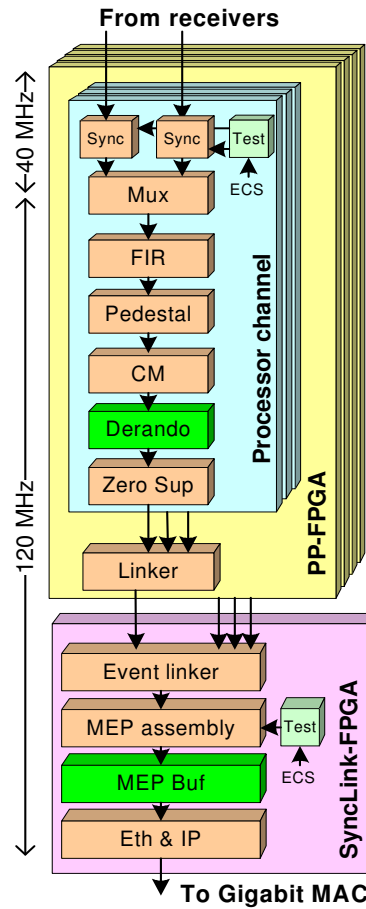


Figure 5.4: Signal processing chain in the VeLo and ST cases.

Quad Gigabit Ethernet: The readout network consists of a four-port Gigabit Ethernet (GBE) card. For each MEP a network destination address is distributed synchronously to all TELL1s over the TTC channel in order to dynamically select a node in the High Level Trigger CPU farm. This ensures that all the information corresponding to one event is directed to the same CPU for the event building process.

TTCrx: The TTC receiver obtains the fast control signals from the Readout Supervisor via optical interface. The fast control signals are the clock, reset, L0 trigger, trigger type, and the MEP destination address.

Throttle system: The overall size of an event depends on its charged track multiplicity and as

such is variable. De-randomising buffers are used to average the data rate and processing time. To protect from overflows during the de-randomisation operation, each buffer can send a special message called throttle to the Readout Supervisor, which will prevent further triggering until the de-randomisation can operate again.

CCPC: A PC (CCPC) [78], running Linux and possessing all the hardware necessary for disk-less operations, is embedded on the TELL1. It provides access for the slow control management, ECS, via a dedicated Ethernet Local Area Network, and it is used to configure, monitor and control the TELL1 board. The interface to the on-board chips is done with the so-called glue-card [79] built around a PLX PCI9030 PCI bridge, JTAG¹ and I²C controllers². The CCPC is booted from a server over NFS. The advantage of this approach is that each board has its own control path and the intelligence is decentralised.

As mentioned above the difference between the TELL1 boards of each subdetector lies in the program implemented on the four PP-FPGAs. A common software and firmware framework has been developed and is modified by the users to adapt the TELL1 to the specific needs of each subdetector in terms of data processing tasks.

Many small embedded dedicated memory blocks and distributed memory cells on the FPGAs are used to store the configuration values as pedestals, thresholds, lookup tables for divisions and square operations and simple single register values. Each TELL1 board represents a few hundred registers to be monitored continuously. Memory blocks of some hundred kilobytes need to be uploaded in a short time during configuration time.

5.1.1 The ECS Interface

As it has been seen above, the ECS interface consists of the CCPC and the dedicated glue-card with three physical interfaces. These interfaces are used to control, configure and monitor the resources on the TELL1 board.

JTAG is used to program the EEPROM³ that contains the firmware for the five FPGAs. Their Configuration is done indirectly through the dedicated EEPROM device, the content of the EEPROM remains after power cycling. Without re-programming the FPGAs are initialised at each power-up. JTAG on the board is also used for in-system connection verification called boundary scan. This is not foreseen to be used via CCPC and glue card.

I²C buses are used and shared among different destinations. The first bus is used to control the digital to analog converters (DAC) on the A-Rx cards. A second bus is used for the configuration of the TTCrx. The third is needed to control the FEM⁴. The last bus can be accessed for lab use to configure additional mezzanine cards as it is done for the trigger adaptor mezzanine card used to control a detector FE module directly from the TELL1. Many other small devices such temperature probes and EEPROMS on mezzanine cards are also accessed via the I²C buses.

Local Bus is provided via a PCI bridge and stands for a simple parallel bus. It is used to access the resources on the FPGAs and the GBE card. It is used in the 32-bit multiplexed mode

¹Joint Test Action Group.

²Inter-Integrated circuit Control bus.

³Electrically Erasable Programmable Read Only Memory.

⁴The Front End Emulator is used only for the VeLo to emulate the cycle accurate readout sequence of the Beetle readout chip. This is necessary to reconstruct the valid data of the readout sequence.

and 28-bit address space⁵ to access registers, FIFOs, RAMs and ROMs on the FPGAs. For the GBE card a region of the address space is reserved where the access is done in 16-bit non multiplexed mode. These different configurations are possible thanks to the flexible implementation of the PLX9030 PCI bridge.

5.1.2 Memory Map of the TELL1

The registers and RAMs for the FPGA are divided into two parts: the control registers part and the monitor registers part. The former registers are used to provide external control and setting signals to the internal TELL1 logic, therefore they are in a read/write memory space. The latter are read-only memories as they are used to monitor TELL1 information like counters, error, etc. Figure 5.5 illustrates the memory map of the FPGAs. Each PP-FPGA has dedicated control and monitor registers for the subdetector specific needs.

All the register descriptions can be found in the “ECS Interface Library User Guide” [80]. Table 5.1 is an example describing the PP_CTRL_REG0 (\$BA+0x0000004) which provides common and basic control signals for the PreProcessing. This example illustrates to which extend the functionality is customised to the application. Each data field is related to a work-around solution to a problem identified during the development of the detector. What is a Pseudo digital header high threshold value? For the Beetle readout chip, analog data transmission is used to encode the output of the values sampled on each detector channel. In addition to the detector signal which is a analog value some digital information as a bunch-crossing time stamp and some status flags should be transmitted. The problem is solved by encoding each bit of the digital information (16 bits in case of the Beetle) in a analog value. Where a high analog value is used for digital 1 and low analog value for 0. This encoding is named pseudo-digital encoding. In the TELL1 this encoding must be decoded again for synchronisation checks. A threshold needs to be defined which can be assumed to be the lowest limit for encoding 1, this limit is called PSEUDO_BIT_H_THR.

⁵“0x4, 0x5, 0x6, 0x70000000” for the four PP-FPGAs, and “0x10000000” for the SyncLink-FPGA

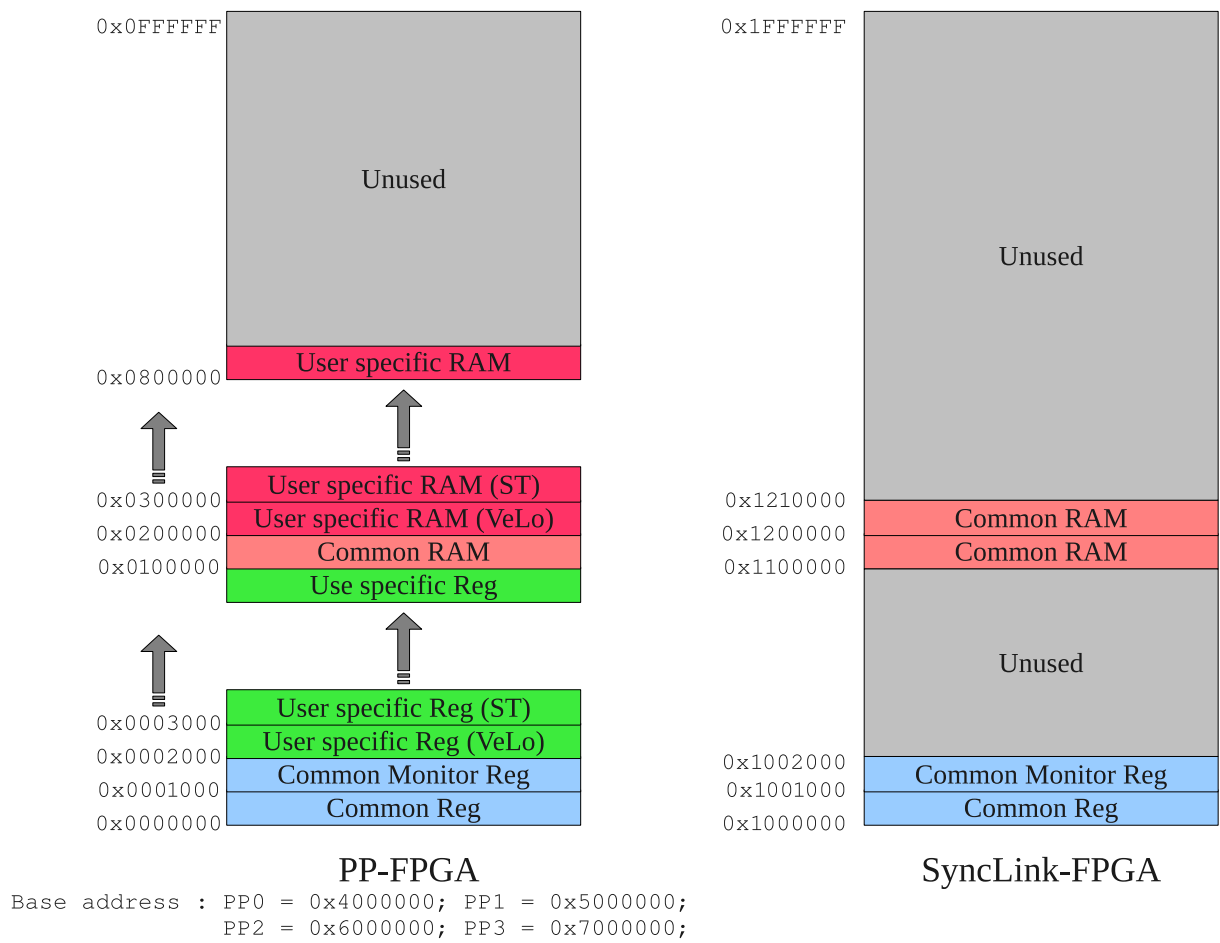


Figure 5.5: Memory map of the PP-FPGA and the SyncLink-FPGA.

Bit	Name	Description	Default
31-24	PSEUDO_BIT_H_THR	High threshold to generate pseudo-header bits. ADC values larger than this value is treated as logic '1'.	0xA0
23-16	PSEUDO_BIT_L_THR	Low threshold to generate pseudo-header bits. ADC values smaller than this value is treated as logic '0'.	0x90
15-12	READ_LINK_SEL	Monitor registers for each link sharing the same ECS address, these fields are used to select a certain link register to read out. (0-15 for A-Rx, 0-5 for O-Rx)	0
11	R_reorder	Choose the R-sensor reordering for VeLo.	0
10	Phi_reorder	Choose the ϕ -sensor reordering for VeLo.	0
9	ZS_EN	Enable/disable the zero suppression.	1
8	LCMS_EN	Enable/disable the common mode suppression.	0
7	BER_EN	Enable/disable the Bit Error Rate (O-Rx only).	0
6	DATA_GEN_EN	Enable/disable the internal data generator.	0
5	FIR_EN	Enable/disable the FIR (A-Rx only).	0
4	REORDER_EN	Enable/disable reordering (VeLo only).	0
3	PEDESTAL_UPDATE_EN	Enable/disable the pedestal auto-update feature, with which the pedestal can follow up the base line shift.	0
2	PEDESTAL_EN	Enable/disable the pedestal subtraction.	1
1-0	DATA_SCALE_MODE	After pedestal subtraction, determines how to scale the 11-bit down to 8-bit. 0: saturate from -128 to 127 (VeLo only) 1: bit(8..1) (LSB remove) 2: bit(9..2) (2LSB remove) 3: bit(10..3) (3LSB remove)	00

Table 5.1: PP_CTRL_REG0 (\$BA+0x0000004) provides common and basic control signals for the PP processes. Default value : 0xA0900204.

5.2 Introduction to the PVSS SCADA System

Historically the control of equipment not used directly for data acquisition is called “slow control” at CERN. The control framework (JCOP) [53] is based on a Supervisory Control and Data Acquisition (SCADA) system called Prozessvisualisierungs- und Steuerungs-System (PVSSII) [51, 52], interfaced to all experimental equipments. PVSS, from the Austrian company ETM, was selected after a formal tender process in 1999 for use in the slow control systems of all the LHC experiments. It offers a highly modular design with managers (e.g. processes) for multiple tasks developed upon a client-server architecture. The communication is based on a TCP/IP interface and is only active on demand. Figure 5.6 illustrates a typical PVSS application composed of multiple managers.

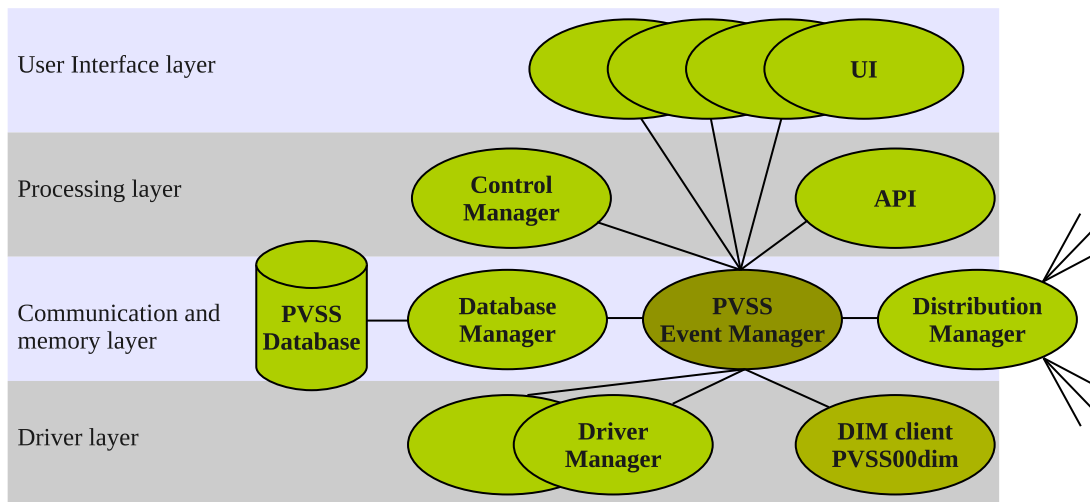


Figure 5.6: PVSS system design where all the managers are interconnected through the event manager.

PVSS offers a high scalability which is an important feature for detector systems with thousands of elements to control. It allows a device-oriented aspect and structured namespace to model the structure and control complex devices such as the TELL1s. Devices are not limited neither in number nor in complexity nor in the number of elements that composed them. Each device can be described as a *datapoint type* (DPT), which is the model for real devices, *datapoint* (DP), that are connected to the experiment. Figure 5.7 shows a part of the complexity of the datapoint of a TELL1 board. DTPs can be seen as classes in a object-oriented terminology. DP can have special attributes such as processing and alerts triggered on their values.

The main PVSS *Event Manager* is responsible for all communications. It receives data from drivers and stores the current value in its local memory as DP as well as sends it in the Oracle database connected through the database manager. It also eases the accessibility between the managers. Finally, it ensures the distribution of data to all the managers which have requested it.

The User Interface (UI) can get device data from the database, or acts on the device by sending data to the database to be sent to the device. It can have open connections to datapoints in the database to update its state. The Graphical UIs are the object that are manipulated by the LHCb shifters.

PVSS provides a platform independent scripting language for user-specific application developments running in the control managers. This language uses the same function as C language with additional PVSS internal function particularly providing better string manipulations. PVSS

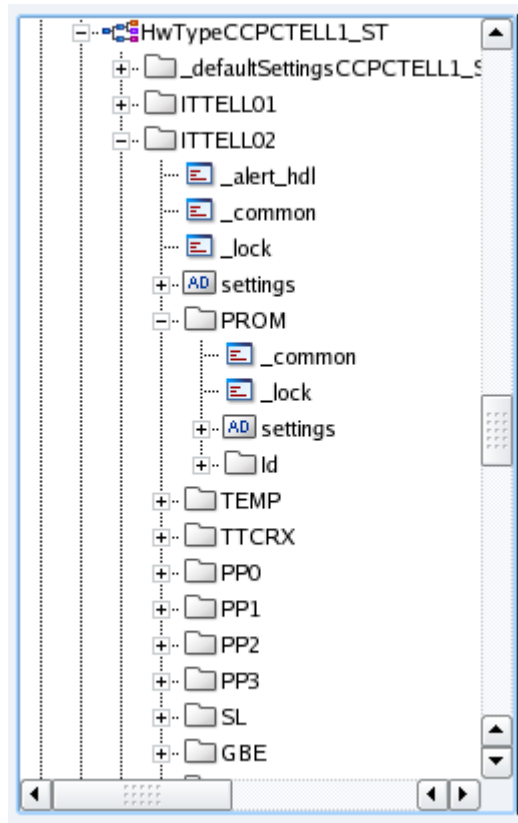


Figure 5.7: The complex TELL1 DP example.

allows Graphical User Interfaces (GUIs) development as well as scripts that run as daemon. It is possible to interface C++ libraries via an API interface to achieve more complex tasks.

The manager-based architecture of PVSS allows to design multi-CPU systems. The system can be distributed across multiple machines with the help of a dedicated manager. This special feature allows PVSS to be a cross-platform system highly distributed through the connected systems which can also run on different operating systems.

5.2.1 Recipes

The detector devices configuration data is stored in the Oracle database as special DP, called *Recipes*. Recipes consist in a set of predefined register settings which can be retrieved from the configuration database and uploaded to the readout boards. Different settings can be applied for different run conditions. Therefore additional managers are provided to define and operate on recipes.

An Application Programming Interface (API) manager is also provided for the communication with devices, either by PVSS or by the JCOP framework (like DIM as explained in section 5.2.3).

5.2.2 Finite State Machines

The LHCb ECS has adopted a hierarchical, tree-like, structure to represent the structure of the subdetectors, subsystems and hardware components. Figure 5.8 illustrates the hierarchical system with a single run control top node. This tree is composed of two principal types of nodes:

Device Units (DU) which are capable of accessing the hardware and Control Units (CU), that model the behaviour and the interactions between components.

A DU is always the leaf of a hierarchical tree and is directly attached to a DP, which is mirroring all the register and memory blocks values. DUs are grouped in subsystems, then in subdetectors.

Subdetectors are grouped by area of activity, DAQ or DCS and their states are combined with information received from external systems in order to compute a global decision. In LHCb the top of the hierarchy corresponds to the full experiment, allowing the shifter to have a global view of the experiment status and to act on all the different subsystems.

In this hierarchy commands flow down and status and alarm information flow up. Control and device units are typically implemented using Finite State Machines (FSM), which is a technique for modelling the behaviour of a component by the different states that it can occupy and the transitions occurring between those states. Figure 5.9 illustrates the transition paths for a FSM used inside the DAQ domain and Table 5.2 gives the corresponding semantic for DUs and CUs states in the DAQ domain.

SMI++ [55] has been integrated into PVSS for this purpose. Both PVSS and SMI++ can run on mixed-OS environments and allow for the implementation of large distributed systems, which is important due to the large scale of the system in terms of I/O channels.

The recovery from known error conditions can be automated using hierarchical control tools based on subsystems states. Since SMI++ is a rule-based system, errors can be handled and recovered by implementing rules. Scripts, which is translated to SMI++, it can be defined how the device units shall react upon the changing value of defined DP elements. Thus state transitions can be triggered if some important register values are changing. Also the other way around, actions can be performed on the DP upon receiving commands from a control unit.

Control units can act on a number of device units at once and thus allow for a better grouping and structuring of the hierarchical tree. If the state of any device units or sub-control units changes rules can be defined according to which the control unit may transit to another state. Commands propagate the hierarchical tree downwards, while statuses are propagating upwards the hierarchical tree allowing for a global overview of the whole experiment at the top

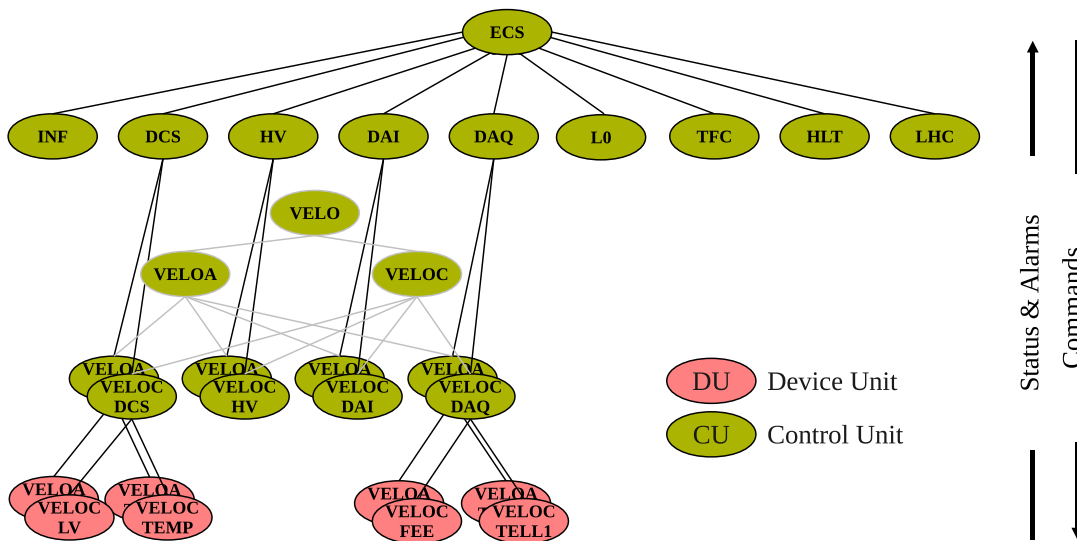


Figure 5.8: LHCb ECS architecture: the device units are connected to the real hardware, while the control units model the behaviour and the interactions between components.

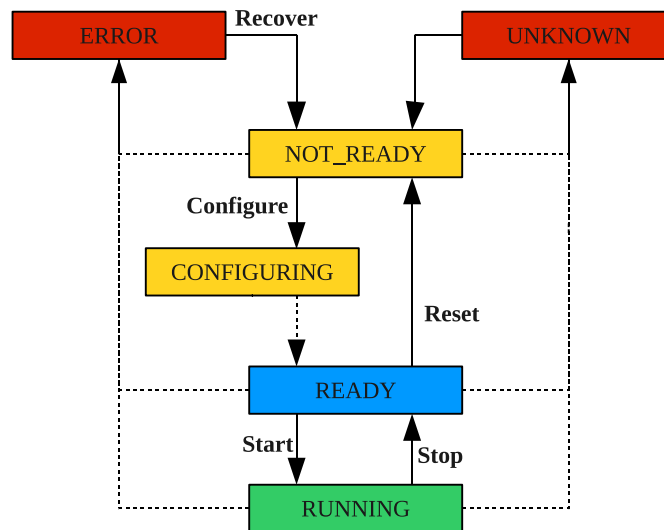


Figure 5.9: Transition paths for a FSM used in the DAQ domain. The transitions represented by dashed lines are automatic, i.e. they are not the result of a command. For a DU they are triggered by the monitoring device parameters, for a CU they are triggered by a state change in one of their children.

State	Semantic for DUs and CUs
UNKNOWN	Communication with the device is not possible. No information is available about it and no command can be applied to it. For example the driver process is dead.
NOT_READY	The device is under the control of the ECS but it needs to be configured before it can be used.
READY	The device is ready to take data. The Start command can, for example, clear some counters.
RUNNING	The device is fully configured and taking data. While in this state, its configuration can not be changed; it must be stopped before changing configuration.
ERROR	The device has detected an error, one of the error conditions flags in the status registers of the device has occurred.

Table 5.2: Semantic for DUs and CUs States in the DAQ domain.

ECS node.

Let's assume the occurrence of an error on the hardware. This will change the state of the corresponding device unit into ERROR. This state is then transported upwards by the CUs according to the rules until it reaches the ECS Run Control at the top. The run may be paused until the error recovery. However, an auto-recovery scenario may be implemented at DU level. Once the transition has reached the ERROR state, scripts can be invoked which check the hardware for standard errors and if it is identified launch routines to fix it. From another perspective, an action such as a "Configure" on a CU will be applied to all the unit attached to it. The state UNKNOWN is reachable from all states and defines the state when control is lost, e.g. when a communication problem occurs. In conjunction with the error recovery provided

by SMI++ the alarm handling tools provided by PVSS is used. In addition the system allows for partitioning, which is the capability of monitoring and/or controlling parts of the system independently and concurrently with the others in order to test, or perform calibration runs on a subsystem. This feature is represented in figure 5.8 where the VeLo subdetector can be released and controlled separately by its experts.

5.2.3 Distributed Information Management

The communication between the CCPC and the ECS uses the Distributed Information Management (DIM) [81, 82] protocol. DIM is a portable light-weight package for information publishing, data transfer and inter-process communication system based on TCP/IP.

DIM servers publish their available services on a DIM Name Server node (DNS). DIM clients can request services from the DNS node which hands over all necessary information about where to find this service to the client, e.g., IP address, so that a direct peer-to-peer connection can be established between server and client. Services are sent from server to client and in the other way around, commands can be sent from client to server. The advantage of this design lies in its high portability, as clients can be installed on any machine by just specifying the DNS node. It also increases the robustness of the whole system as crashed servers can easily republish their services on the DNS node.

A generic DIM server, *ccserv*, has been written to run on a CCPC. It has access to all the low level libraries containing the drivers to communicate with the hardware components. Especially it can perform all necessary actions such as write and read operations on registers and memory blocks, program the FPGA, monitor the registers, through the three different communication protocols (JTAG, I²C and PCI). On the client side, the JCOP framework provides a special API manager (PVSS00dim) which can act as a DIM client for PVSS.

A special set of functions can associate DPs to a DIM command or connect them to subscribed services. The *ccserv* service is started automatically started at the boot of the CCPC which publishes its services on the DNS node running on a support PC. The DNS node keeps the service coordinates and lets the PVSS clients request on these services. Services can be subscribed to either on change value or on a time basis which facilitates the communication on the LAN.

Figure 5.10 illustrates the communication process between the CCPC server and the ECS client via DIM.

A special framework component, *fwCcpc*, is provided for CCPC and is the client on the ECS

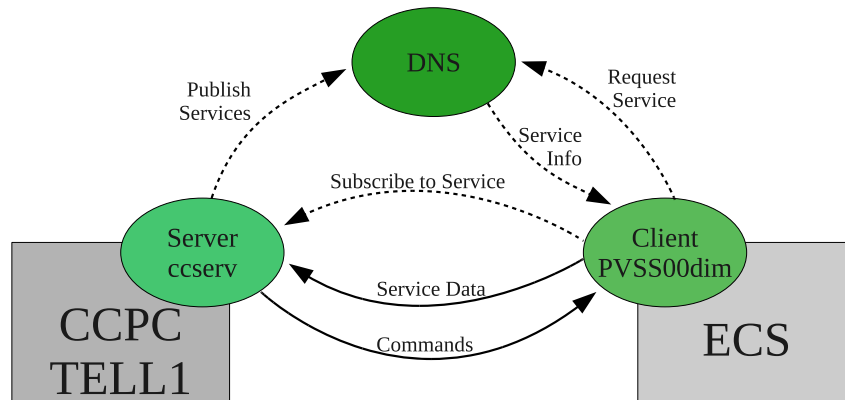


Figure 5.10: DIM protocol illustration.

side. A graphical user interface and basic functions to write and read the various registers are included in this framework. As an example, the basic function to do a Write/Read action on a PCI register is given by:

```
int fwCcpc_LBUSWriteRead(string pCCPC, int pAddress, int pType, int pSize,  
                        dyn_char pDataWrite, dyn_char pMask, dyn_char & pDataRead)
```

where `pCCPC` is the name of the CCPC, `pAddress` is the register address (`PP0_CTRL_REG0 = 0x4000004`), `pType` is the type of register on the PCI bus (8, 16 or 32-bit type), `pDataWrite` is the data to be written in “Byte” format and `pMask` the mask applied to the data and finally `pDataRead` is the data read out from the CCPC. Similar function are available to act on JTAG chain, I²C and GBE MAC chip.

The basic mechanism is that the whole representation of a register (bus type, address, register width, data, etc.) are written to specific DPs associated to a hardware type. These DPs are connected to the DIM API manager in such a way that upon writing of the data on the DP elements a DIM command is launched, sending the information to the server. On the server side a callback function is called. From within this callback function the hardware is accessed and an associated service is launched, sending the hardware information back to the client where it is written to a DP element. A change on this element can again call a PVSS callback function or raises an alert.

5.3 fwTELL1: Integration of TELL1 into PVSS and ECS

A complete component that is used by all the subdetectors (except the two RICH) was expected to control the TELL1. The PVSS system has to be used in order to integrate the TELL1 into the global ECS system. Therefore a complete framework, called *fwTell1*, was created. This section explains the main development of this framework, its functionality and its integration to the global ECS system.

The fwTell1 framework was created in close collaboration with the TELL1 developers and subdetectors users in order to release the best possible framework at that time. In order to avoid inconsistency in the descriptions, all the important parts of all the subdetector TELL1 type such as the DPT and DP or the definition of the recipes was developed in this framework. Some freedom was given to the user to tune specific panels, GUIs, in order to follow up some variables. The DPTs, DPs, recipe definitions and manipulations, FSM rules and commands, and main panels were developed for the eleven different types of TELL1s.

5.3.1 Datapoint and Datapoint Type Descriptions

The fwCepc provides the possibilities to communicate with the TELL1 via the representation of a register. This interface which requires the complete register information to be passed as parameters is cumbersome. In case only one bit of the register requires to be changed, while all other bits must be left untouched, the complete knowledge about the TELL1 register map for each access is required. Therefore an intermediate abstraction layer, *fwHw*, based on register names allows to model and clone the hardware inside the ECS in an intuitive manner.

The PVSS key-element is to store data inside DPs. It is distinguished between DP types (DPT), which define the internal structure, and DPs which can be seen as instantiations of a DP type. As PVSS has a non-flat namespace complex structures can be created. The fwHw tool allows to create for each register a DP containing for each register a well-defined set of DP elements connected to the DIM API manager.

The registers are represented by a DP with elements: writings, writingsStatus, readings, readingsStatus, operation and settings. This representation gives a hardware abstraction and it allows to monitor or to write to registers without having to know all the details (bus type, protocol, address, etc...) of the hardware. Once the registers are created and subscribed to the ccserv a set of framework functions allows for interaction in an abstract way by just passing the register name as parameter. The specific settings (e.g. addresses) are sent to the server where they are stored in a list. It also creates DIM services that are launched for reading and writing on the server side. A parameter can be written into the registers DP element “operation” which launches a DIM command, interpreted at the server side either as a write or a read command according to the parameter value passed. Therefore commands to trigger a writing or a reading do not have to send all the specific settings again.

Several type of register type exist in the fwHw framework. The register type used in the TELL1 project is the LBUS type, which control PCI bus registers, and the I²C type. To monitor some registers it is necessary to set some bits on control register (especially on the PP-FPGA). It is not possible to read directly the register in order to have the expected information. In the FPGA these registers are indirectly accessed via a setting of a multiplexer. Therefore in addition a special type of LBUS register have been added to the fwHw project in order to monitor for example this “realtime” registers of a TELL1 board. This special register type, called “UserSpecific”, first write on a defined register the bit that defined what it will be read out of this register. The GBE has also a dedicated type of register since its registers are accessed through a special protocol.

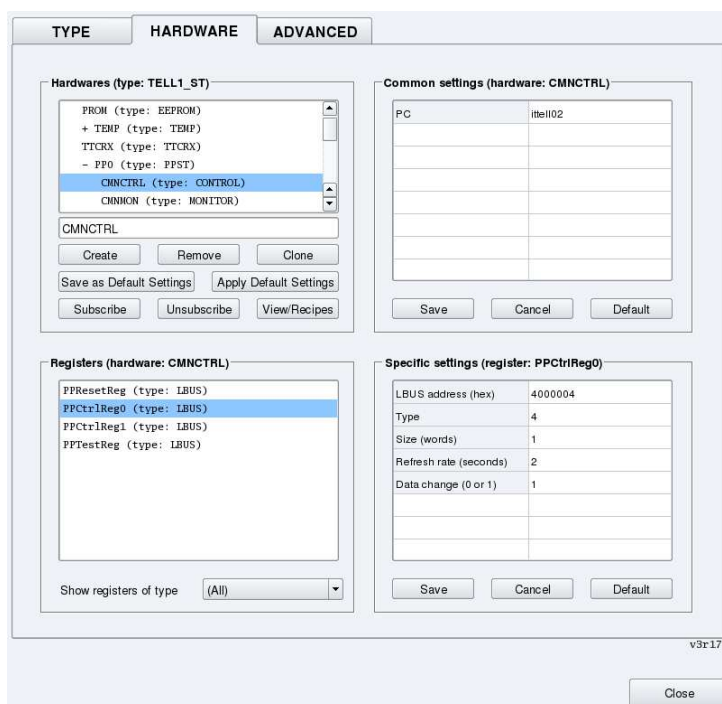


Figure 5.11: fwHw panel, a part of the structure of the ST TELL1 is visible on the top left window. On the top right a CCPC name/address is assigned, while on the bottom windows the registers belonging to the PP0/CMNCTRL and their setting are listed.

A hardware type can be then created by defining its registers. But also hardware type containing registers can be inserted to another hardware type. This feature has driven the conception of the complex TELL1 DP structure. Small hardware type representing the different mezzanines have been created with their own registers. The components are further inserted in other hardware type to finally form a complete electronic device. Each instantiation of such a structured DP type represents a TELL1 board. The fwHw allows to subscribe complete hardware to ccserv, but also to clone hardware in order to be more efficient in the creation of projects.

As example, the ST and VeLo TELL1s have respectively 689 and 701 registers that have been fully described with the local address, the bus type, the number of byte, etc. This works has been necessary to describe for each type of board (VeLo, ST, EHCAL, etc) each registers of the memory map. Table 5.3 shows the register maps in the VeLo (left) and ST (right) cases. These two boards were the first TELL1 to be described as DPs and therefore have guided the structure for all the project. The mezzanines have been created with substructures to help with the description.

These substructures, or abstract layers, were added to give a better view of the registers functions. These layers represent the common and specific parts of the TELL1 memory map. The common parts are used in all the different TELL1 types, therefore it was not necessary to describe them for each kind of TELL1, but only once. The registers or mezzanines in a TELL1 are:

PROM has a unique register with the PROM ID information. It is accessed via the I²C protocol at the address 0x50 on bus 0. It gives information about the system, the TELL1 type, VHDL and DAQ detector ID, version and serial numbers. This register is used to check

VeLo Register Map in PVSS			ST Register Map in PVSS		
Mezzanine	Substructure	Nb of registers	Mezzanine	substructure	Nb of registers
–	PROM	1	–	PROM	1
–	TEMP	2	–	TEMP	2
ARx	DACPP0	4			
	DACPP1	4			
	DACPP2	4			
	DACPP3	4			
TTCrx	–	15	TTCrx	–	15
FEM	–	24			
PP0	CMNCTRL	4	PP0	CMNCTRL	4
	CMNMON	25		CMNMON	25
	CMNMEM	6		CMNMEM	6
				ORX	37
	SPCREG	65		SPCREG	15
	SPCMEM	27		SPCMEM	50
PP1		127	PP1		137
PP2		127	PP2		137
PP3		127	PP3		137
SL	CMNCTRL	19	SL	CMNCTRL	19
	CMNMON	41		CMNMON	41
	CMNMEM	5		CMNMEM	5
	REALTIME	15		REALTIME	15
GBE	–	14	GBE	–	14
	PROM	1		PROM	1
	PORT0	10		PORT0	10
	PORT1	10		PORT1	10
	PORT2	10		PORT2	10
	PORT3	10		PORT3	10
total:		701	total:		701

Table 5.3: VeLo and ST TELL1 defined register summary tables.

REGISTERS	VELO	ST	OT	MUON	EHCAL	PSSPD
	Nb reg:	701	701	535	532	453
	L0PUS	L0CAL	L0MUON	L0DU	BCM	total:
	Nb reg:	441	445	445	301	351
						5358

Table 5.4: Number of registers, DP, per TELL1 types that have been defined in the project.

that the versions are correct and correspond to the TELL1 board to be used.

TEMP groups the registers of the two temperature probes which measure the temperature next to PP0 and under the GBE card. It is located on the third I²C bus at the addresses 0x48 (PP0) and 0x4A (GBE). The temperature probes can be used to set alarms to prevent failures.

ARX is a superstructure that group the four DACs used by the VeLo subdetector only. It was easier and natural to create a superstructure with the four DACPP0-3 which have the same registers. The DACPP0-3 have the dedicated I²C bus 2 and the addresses are 0x54, 0x55, 0x56 and 0x57. Data, offset and gain of the DAC can be set from these registers.

TTCrx groups the registers that control the TTCrx mezzanine. It is accessed also through the I²C protocol (address 0x58, bus 0). Fifteen registers can be read out, such as bunch and event number counters, but also the configuration is done there.

FEM represents the Front-end EMulator that is used only by the VeLo TELL1; its main purpose is to generate the DataValid signal which is not transmitted from the subdetector. It uses the I²C bus at the address 0x70, and all the setting of the FEM can be accessed.

PP0-3 controls the PreProcessing of signals. The DP description was done through substructure to avoid redundancy through the different kind of boards. The registers which are all accessed through the PCI bus are divided into:

CMNCTRL groups the four registers that are common to control all the PreProcessing settings such as enable or disable the pedestal suppression or the type of VeLo sensor. It is used by each TELL1 type.

CMNMON groups all the common registers that are used to monitor the PP-FPGA. It is composed of counter and FIFO information used by each type of TELL1.

CMNMEM groups six RAM blocks that are use to generate test data from the chip. Each block is 32-bit wide and 128-word depth used in Read/Write mode.

ORX registers are used by all the TELL1 type but VeLo. They are used to control and monitor the optical receiver attached to each PP-FPGA. Seven registers are used to control and configure the O-Rx channels. It can be noted that this PVSS DP development has driven the creation of a new register and the functionality behind, e.g. to enable or disable the O-Rx links in one go. The first UserSpecific register were used there to use correctly the ORX_PROBE_REG and ORX_SYNC_REG registers. For these registers it is necessary to select among the PP_CTRL_REG0 which O-Rx link has to be set or monitored. Each link has its two registers. This adds 12 registers. The 18 Bit Error Rate test registers are implemented in the same way (three per link).

SPCREG groups all the specific registers that control a given TELL1 type. Each board has a different set of specific registers which are well defined in these groups. These registers are of LBUS or UserSpecific types, and have a defined start addresses on the PP-FPGA as function of the TELL1 type. The VeLo specific registers are from \$BA+0x0002000 to \$BA+0x0002FFF, where \$BA is the PP-FPGA based address. (ST: 0x3000, OT: 0x4000, EHCAL: 0x5000, MUON: 0x6000, L0DU: 0x7000, LOPUS: 0x8000, L0CAL: 0xA000 and L0MUON: 0xC000).

SPCMEM is the substructure that groups all the specific memory register of a TELL1 type such as pedestal RAMs for ST and VeLo, or the different threshold that are

applied in the PreProcessing algorithms. The start address follows the same rules that the SPCREG but from \$BA+0x0200000 to \$BA+0x02FFFFFF for VeLo, etc.

SL groups together the registers assigned to the SyncLink-FPGA which are common to all the TELL1 types. These registers are also sub-grouped by activity:

CMNCTRL regroups the 19 control registers of the SyncLink-FPGA. **SL_CTRL_REG0** has the most important parameters such as the kind of trigger. It also indicates if the SyncLink- and the three PP-FPGA have been initialised which is an important information to check during the configuration of a TELL1.

CMNMON are the monitored registers. Eight registers probe the PP event numbers and are implemented as UserSpecific (controlled by **SL_CTRL_REG0**).

CMNMEM are the large RAM blocks as the complex MEP location RAM or IPv4 Header Ram that has the information about the destination and source IP addresses of the data.

REALTIME registers are essentially counters that can be synchronously read. This is implemented to check consistency among counters during a run. In order to read synchronously, it is necessary to “freeze” the registers. Setting the freeze bit copies the contents of all counters into ECS accessible registers. The freeze function can be called via ECS or via the TFC system.

GBE has 14 GBE type registers as the RxStatus or the MDIO Control register. In addition the four port have their own registers:

PROM is access through the I²C bus 3 under the 0x57 address.

PORT0-3 groups their own dedicated registers such as the PHY Control or Status.

Table 5.4 shows the 5’300 DPs that have been defined to reproduce all the registers of the 11 type of TELL1 boards. Even if some of the registers are common to all the types it has been necessary to create and maintain all the TELL1 to the current development. This work has been done in close collaboration with the TELL1 developers in order to fit to all the requirements. The DPs and DPTs were saved and distributed in the framework devoted to the TELL1 boards, fwTell1.

5.3.2 Graphical User Interfaces

PVSS allows for the development of Graphical User Interfaces (GUI) in a simple way, such interfaces are called panels. The functions of the objects composing a panle are described by C or PVSS scripts. Those can be executed upon user action, as a mouse click on the associated object representation for example. These functions can be connected to DP element (DPE) and can execute callback function upon DPE change. The function, called *dpConnect*, is particularly used for counters or registers that are frequently updated.

Numerous panels have been created for the *fwTELL1* framework and for the user purposes. They display the information coming out of the TELL1: counters, overflows, rates, etc. Other panels have been designed for debugging purpose.

The first panel that the user access is the panel for the CU ① that control the TELL1 boards, as pictured in Figure 5.12. By double clicking on a DU ②, the user access the panels to operate the board. The first panel to be displayed provides a the global overview of the main functionality and counters of the concerned TELL1. This main panel is displayed in Figure 5.13 in the case of a VELO TELL1 board. To avoid an overload of the ccscrv and of the transfer rate

between the CCPC and the ECS, each register that is shown on a panel is only subscribed when the panel opens-up and they are unsubscribed at the closing. Tab buttons allows to access to more specific information. The second panel 5.14 shows the data rates across the FPGAs.

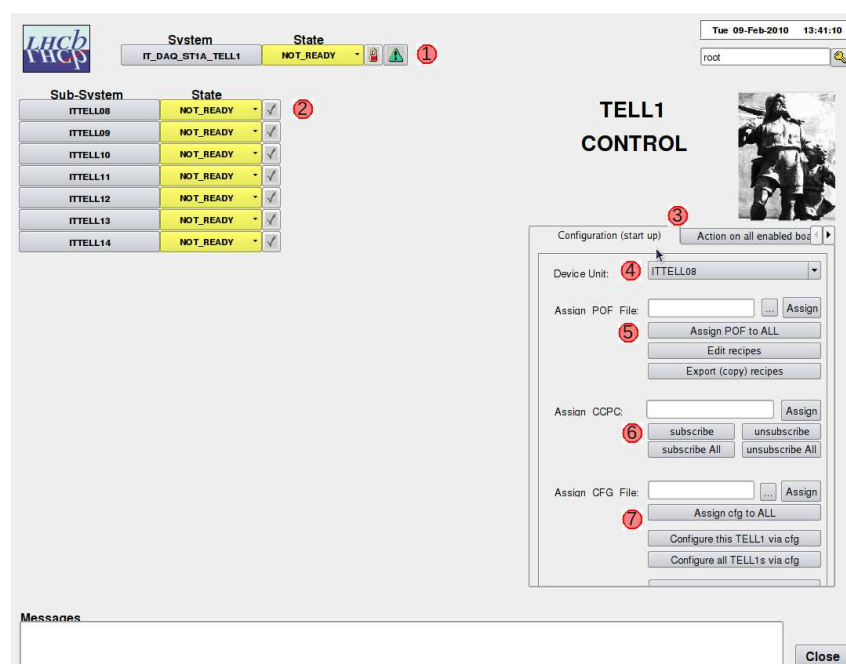


Figure 5.12: Tell1 CU unit display. It gives access to the boards (DUs ②) that belong to it and allows for their basic configuration (type of trigger, ...) ③. It is also possible to select a TELL1④:

⑤: assignment of the “.pof” file hat contains the FPGA firmware can be assigned from it and the path of the file is stored in a DPE attached to the TELL1 DP. The “.pof” file will be download on TELL1 on demand and load to the FPGA via the “EPC16” function these configurations.

⑥: set the CCPC name, subscribe the registers to the corresponding ccserv.

⑦: assignment of a “.cfg” file to configure the TELL1 with hard-coded functions.

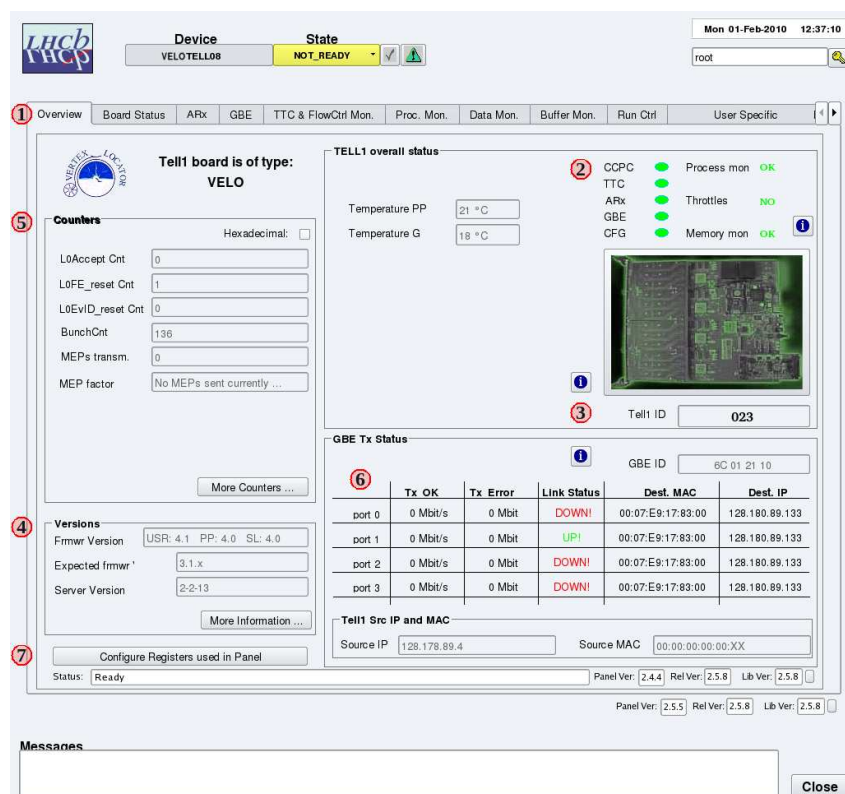


Figure 5.13: DU main monitoring panel of the fwTell1 framework in the case of a VELO TELL1 board. This panel is englobed in the main panel ① which changes depending the type of TELL1. The tabular contains the following panels: “Overview” which is the first and main panel; “Board Status” which is explained below; the “O-Rx” or “A-Rx” panels which shows information about the receiver cards; “GBE” shows the traffic on the GBE cards and the source and destination address; “TTC & FlowCtrl” has all the counters corresponding the the TTCrx and the FIFOs; “Processing” monitors the PP- and SyncLink-FPGA data processing counters; “Data Mon” gives access to the MEP buffer which can be decoded for specific TELL1 type (VELO case is displayed in Figure 5.17); “Buffer Mon” shows the status of all the buffer memories; “Run Ctrl” gives access to the main run control parameters, these parameters can be changed if the TELL1 is no receiving any triggers, “BER Test” is a panel to execute the Bit Error Rate test; “User Specific” displays the Subdetector specific value such as histograms or threshold’s RAMs, this panels is customisable by the user. Finally the last panels, “Recipes”, allows the creation and the configuration of recipes. The main monitoring panel displays:

- ②: The TELL1 overall status is displayed with the green or red lights on the top right. It shows the status of the different mezzanine in one look and also if the card is sending throttles, if the data processing is going well and finally if the FIFOs are not full. All these values are check.
- ③: If everything is going well, the TELL1 board is displayed green, while it turns red when one of the checked is not anymore valid.
- ④: The current version of the different firmware, configurations and ccserv are displayed to check the agreement between them.
- ⑤: When the cursor passes over one of the counters, it shows up some information about the registers that it uses. Clicking on the counters allows to configure (refreshing rate,...) the registers service that it belongs to. The MEP factor is calculated with the rate in and out of the SyncLink-FPGA.
- ⑥: The GBE rates and IP and MAC addresses are displayed as well as the link status.
- ⑦: Give possibility to configure all the registers services used in the panel, refreshing rate and data on change.



Figure 5.14: Data rates and overall status of the TELL1. At the opening the the states of the different mezzanines is checked. It illustrates the data flow as well as these states. As soon as one component flags a problem, its background colour changes to orange and the TELL1 goes to red. On the left the O-Rx link (or A-Rx DAC) states are displayed. When any mezzanine or the TELL1 is clicked on, its current state is rechecked. Finally the status of the four GBE ports is shown on the bottom right.

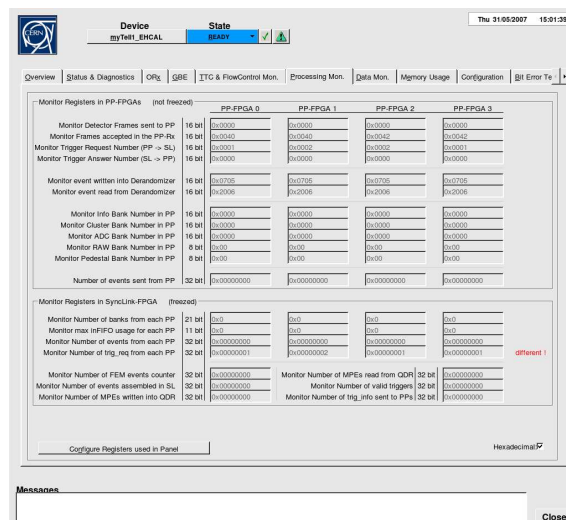
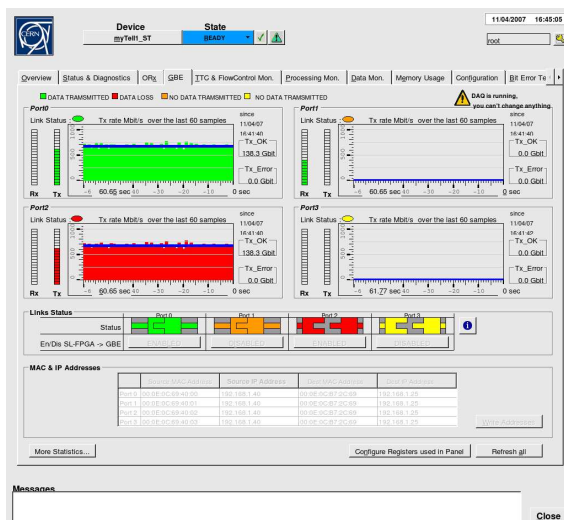


Figure 5.15: Left: GBE panel showing the current status and transfer rate across each link. The link status is also displayed.

Right: The Processing panel shows the counters on each PP-FPGA, cross-checks are done to ensure a full consistency between the different numbers. The SyncLink counters are frozen before read.

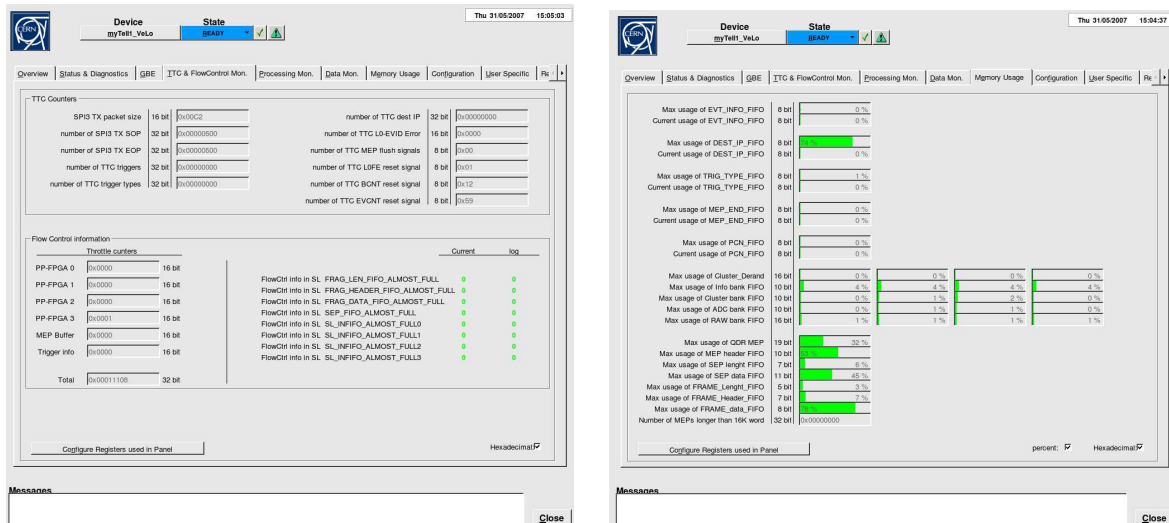


Figure 5.16: Left: TTC and Flow Control counters. Right: Memory Usage, the counters turn orange when the corresponding memory is close from being full (90%) and red upon reaching the limitation.

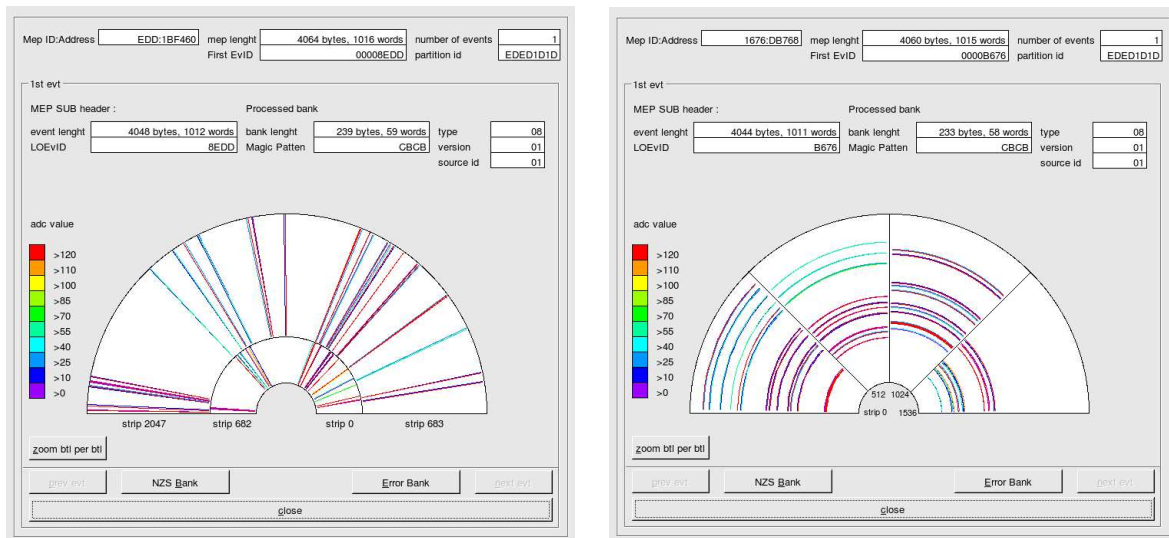


Figure 5.17: MEP decoding panel for VeLo sensors of type ϕ (left) and r (left). These panels are accessed from the DataMon panels of the main panel (see Figure 5.13). The MEP complex structure is decoded in the VELO and ST cases. To read the MEP buffer on the TELL1, it is necessary to freeze the processing, potentially creating throttles. Nevertheless as soon as the processing is frozen the MEP location map is read and the last 4 MEPs are upload into the panel variables. By clicking on one MEP, this MEP is completely decoded and allows the user to see all the information. Each bank can be decoded and displayed in a human readable way. These panels are useful for debugging or to the TELL1 developers. The access for data monitoring requires some access time to the data buffers and can therefore throttle the system.

5.3.3 Control Script and Check Functions

In order to check and control the TELL1 board via PVSS, a complete library (*fwTell1.ctl*) was created. This library uses of the fwHw and fwCcpc libraries. It contains several useful sets of functions that can be grouped by functionality:

Utility Functions are frequently used functions that are not network depended.

fwTell1_cloneManyTell1Boards clones many Tell1 boards from one original and assigns the credit card PC.

fwTell1_AssembleAndCreateRecipes assembles various sub-recipes into one single recipe. It takes care of masked operations, meaning that the bits can be set in one register by different sub recipes do not overwrite each other. This function is particularly used to create the global recipe for a specific TELL1 type.

fwTell1_BitsFromInt and **fwTell1_BitsFromString** are used to get some bits from a int or string (hexadecimal) value. It is useful to manipulate only some bits in register.

Common Hardware Functions are used to get fast answers from the hardware, these functions work with the hardware name (DP name) as parameters, but needs the TELL1 board to have been subscribed to the ccscrv. The functions return -1 if the registers could not be read on the board.

fwTell1_TypeOfBoard returns the TELL1 configuration type. TELL1 of different sub-detectors can be recognised by reading various bits of a special register **ConstantReg** implemented on every PP-FPGA.

fwTell1_enableMDIOCtrl sets second bit (0x2) in the MDIO-Control register (0x683) of the MAC chip to enable/disable the autoscan feature. The flag “true” (=default) enables the autoscan, “false” will disable the autoscan. It checks if the WriteRead function terminated successfully and compares the written bit with the value that was read back.

fwTell1_chkTriggers checks if Triggers are sent to Tell1 board. If so, Accessing the board e.g. applying recipes should be prohibited.

fwTell1_disableBoard disables the GBE ports on the SL (no data sent) and sets ECS as trigger source (no TTC triggers accepted). The TELL1 does not accepted TTC triggers anymore and does not sent any data to the Event Builder.

fwTell1_resetVeloSampleClockPhase resets the sample clock circuit and reinitialises all ADC clock phases in the VELO TELL1 type. This function has to be called after configuring the Tell1 board. If this operation is not performed the data from the A-Rx boards is not sampled correctly. The function is part of the FSM.

Common CCPC Functions have as input parameter the CCPC name (name of the server related to the Tell1 board). These functions work even when the board registers are not subscribed yet. Most of these function are used during the initialisation and the configuration of the TELL1 boards. Therefore to avoid timing and sequencing problems during this primordial phase, they are linked directly to the tell1lib provided with the C-code command line tools. These functions are mostly part of the FSM. The relevant functions are:

fwTell1_EPC16ToFPGA loads the FPGA from EPC16. The initialisation of the glue card, of the GBE and of the TELL1 is done with these hard coded functions. To properly configure of a TELL1 its initialisation function **fwTell1_iniTell1** must be called. In turn, it calls all the necessary hard-coded sequences directly on the server before applying the recipes.

TELL1 boards have to be reset at the end of each run, therefore two functions are implemented in this section. These functions are called in the RESET command of the FSM.

It is also possible to enable or disable all the links on receiver cards (O-Rx or A-Rx) in one command line.

Functionality Check Functions evaluate the status of the Tell1 boards. They are used for testing, whether the TELL1s are operational and functional. The input parameter of these functions will always be the hardware name (DP name) and these functions just work, if the board is subscribed. Most of These functions are used for the board evaluation on the device unit panels.

These functions check whether the CCPC is running (`fwTell1_chkCCPC`), as well as whether that the configuration was successful checking bits on SyncLink-FPGA registers (`fwTell1_chkCFG`) and that any GBE ports are enabled and not plugged, which would lead to a data loss (`fwTell1_chkGBE`) or if they are all disabled. A function checks that the TTCrx is operational (fibre is plugged) (`fwTell1_chkTTC`). The O-Rx and A-Rx have dedicated function to check that the O-Rx links that are enabled are not in state error and that the DACs are connected and accessible via ECS (`fwTell1_chkORx` or `fwTell1_chkARx`). The processing counter register on the FPGAs are frozen and compared to check that the processing may be not corrupted (`fwTell1_chkProcessing`). The data flow is checked on the TELL1 by looking if whether throttles are arriving or not. Therefore the throttle counter is read twice with a pause of 100ms in between (`fwTell1_chkFlow`). The two values are checked whether they are equal or not which would hint incoming throttles. Memory overflows occur if the number of bits used exceeds a certain limit of each RAM (`fwTell1_chkFlow`).

Further internal functions are used for string manipulation, for the creation and manipulation of internal functionality of the recipes and for FSM commands.

5.3.4 Recipes

As mentioned before the number of registers per TELL1 boards varies together with their name and functionality. In order to be configured some of these registers have to be set to the correct values. During the initialisation recipes are sent to important registers of the boards that have to be configured. Consequently the definition of recipes used depends on the TELL1 type.

In order to create recipes for a hardware, it was useful to use the defined function of the fwHw framework. These functions have multiple features. As recipes are DP in the PVSS point of view it is necessary to create their own type, therefore a function creates recipe types specifying which registers should be part of a recipe of this type. The recipe type does not get a type of board as parameter. Functions are also provided to delete or get the registers included in a defined recipe type. Table 5.5 gives the numbers of registers in each of the different recipe types, these types correspond to the TELL1 type.

Even if the definition of the recipe type is possible for very large number of registers in a simple way, it is not a user-friendly feature to set the data and mask value of the 308 registers that are used in the VELO TELL1 recipe. Therefore the idea was to create smaller recipes which are defined by the different controls that wanted the users.

To achieve this goal, the sub-recipes type definition were done in parallel to the development of GUIs which could be used for creation of specific recipes. It is from the “recipes” tabular of DU panel (see Figure 5.18 (right)) that the user can define and create his recipes. The recipes that are attached to the board are listed and can be assembled in a global one which will be

tagged with a configuration name (e.g. PHYSICS, COSMICS,...). The assembly function has to take care of the registers that are attached to each sub recipes. Several registers are used in multiple sub recipes, therefore it is necessary to use and check the associated masks in order to combined correctly the recipes. In a first step the recipe type is created, if it is nonexistent, with the register list that is passed as parameter.

This sub structure of recipes allows multiple configuration without the creation of the whole recipe, one can change some value of a sub recipe and reassemble a new global one.

The creation and parameter configuration are access for the different buttons. Figure 5.18 (right) shows the common control recipe panels, Figure 5.19 (right) illustrates the configuration of the network parameters. Figure 5.19 (left) shows the main panels to configure the specific VELO recipes.

Each panels allows to save the current status of the TELL1 as a recipes. It loads and displays all the parameters that belong to the sub recipes, the user can change some value or save it as recipe.

Another possibility is to export to or import from another TELL1 board recipes of the same type. Most of the TELL1 parameters used by a subdetector are the same, therefore these function permit a fast creation of all the recipes. In order to set correctly the register in the recipes, strict definitions of data and masks that are send were developed and tested in comparison to the the configuration of the TELL1 with the C-code.

These panels are mostly used in the development of the recipes for debugging purpose. The recipes for the individual configuration parameters for the 300 different boards must be generated automatically. Therefore when the configuration parameters are optimised in GAUDI job running in the VETRA project, they are parsed into XML files. These XML files are then saved in the condition database in a SQL format and also exported as recipes. It is then possible to apply the new recipes.

RECIPES	VELO	ST	OT	MUON	EHCAL	PSSPD	
	Nb reg:	308	293	64	100	56	72
		L0PUS	L0CAL	L0MUON	L0DU	BCM	total:
	Nb reg:	52	52	52	48	48	1145

Table 5.5: Number of registers that have to be configured during the configuration and therefore stored in the recipes per TELL1 types.

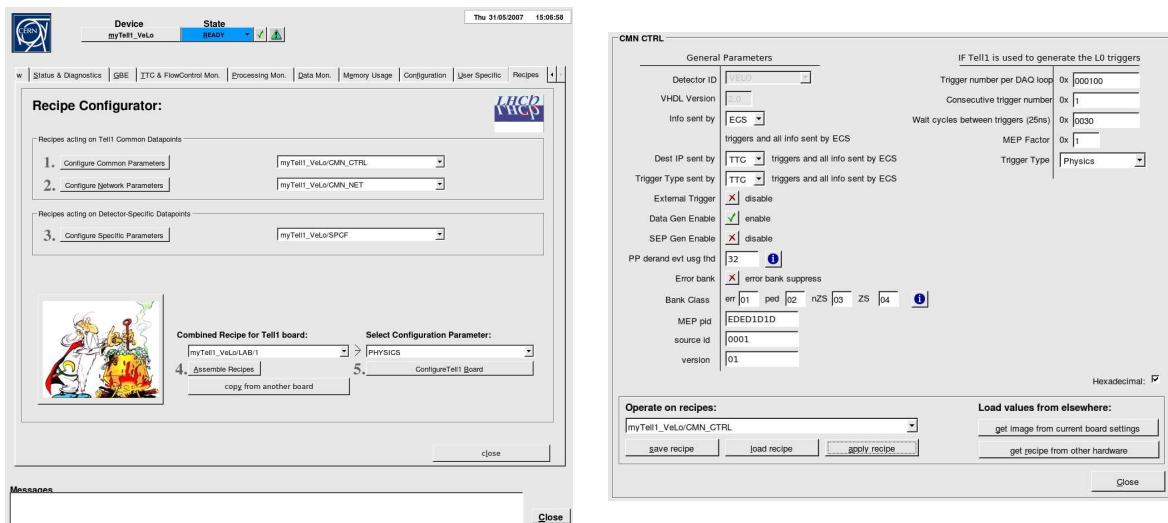


Figure 5.18: Left: DU Recipe main panel allowing access to sub recipes. A global recipe is defined and created in the panel itself. Right: Common control recipe panel creation and configuration. The main parameters of the run can be chosen.

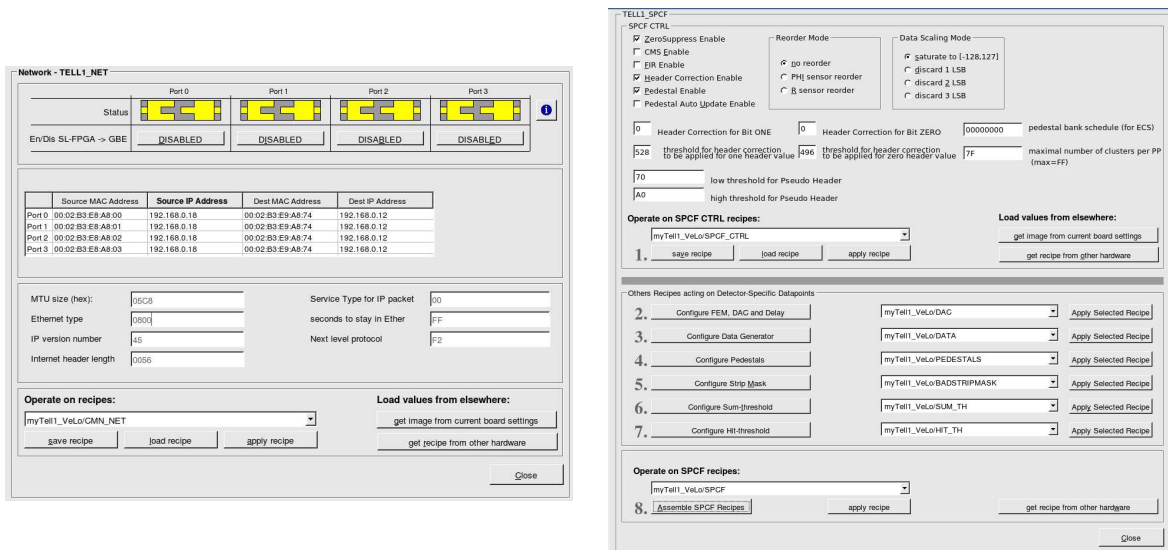


Figure 5.19: Left: Network recipe creation and manipulation. Right: The main panel to defined and create the VELO specific recipes.

5.3.5 FSM

The TELL1 configuration and state monitoring is done on the FSM. Multiple actions can be taken depending on the current state. As seen in Section 5.2.2 when the board state change from NOT_READY to READY, the “Configure” command is called. To do this configuration on a TELL1 board, the simple solution which is “apply the recipes onto the TELL1” was not possible due to the strict timing that have to be respected. Therefore, The definition of a sequence in order to initialise and configure correctly the TELL1 boards was required.

Figure 5.20 shows commands in details. All the commands start checking the TELL1 DPs existence, whether it has an assigned CCPC on which a ccserv is running and finally whether the TELL1 board type is determined. If either of these checks fails the DU goes to the ERROR

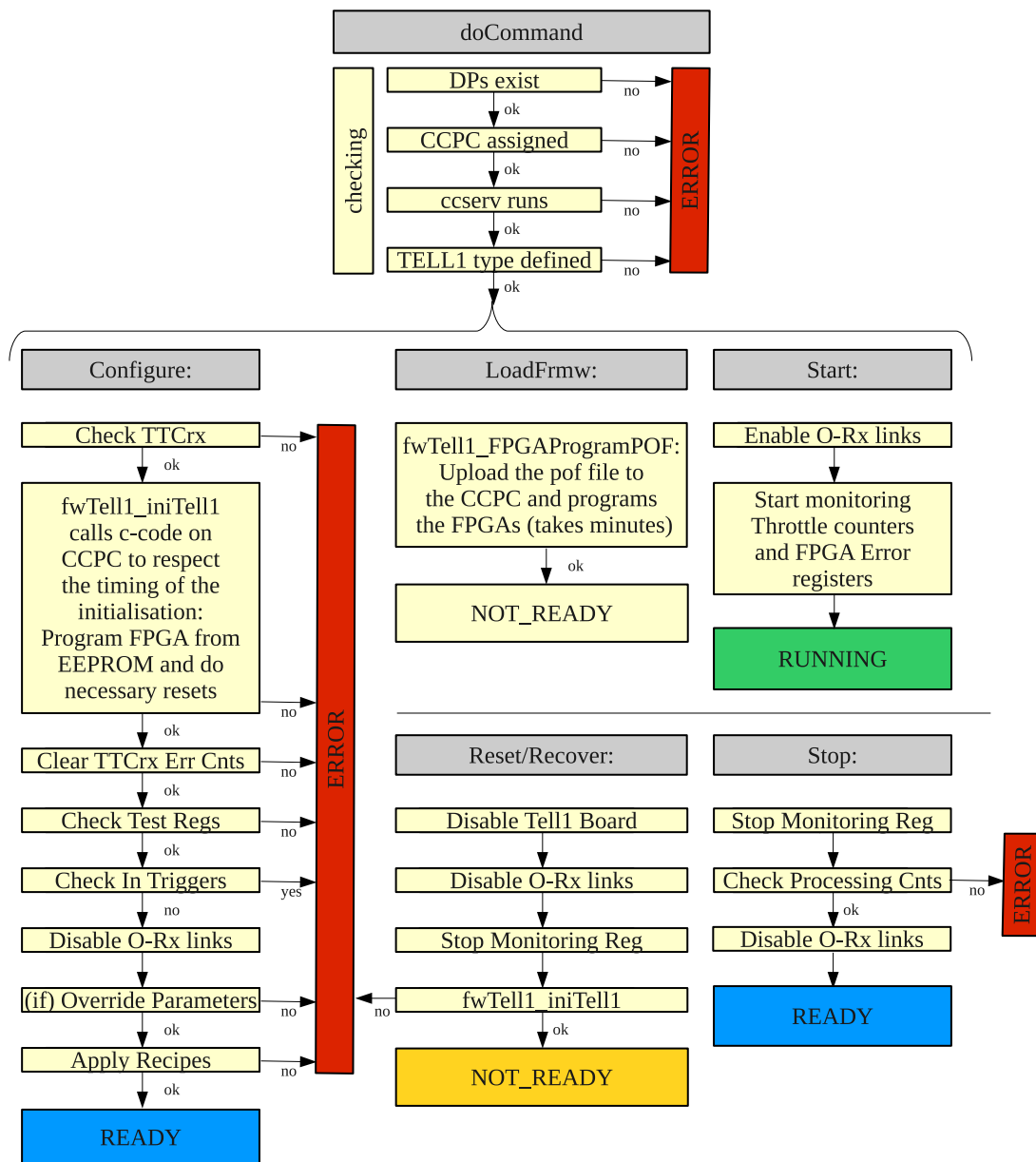


Figure 5.20: Details flow-chart of the Configure, LoadFrmw, Start, Stop, Reset and Recover commands and their actions available for a DU/CU TELL1.

state, and a message is printed in the shifter console stating the failure and the possible actions. Then all the commands take a different path:

Configure (NOT_READY → READY): The TTCrx connection is checked.

Then the main initialisation starts, calling a C-code function provided on the CCPC which initialises the FPGA from the EEPROM and doing the necessary resets. To respect the strict timing of the resets on the TELL1, the use of this hard-coded function is mandatory. Then the TTCrx Error counters are cleared.

It continues by checking the Test Registers performing a write/read operation on one dedicated register per FPGA. This action ensures that the ccserv, the subscription of the board and the firmware is loaded and work properly.

The configuration is not allowed if the TELL1 receives triggers. In this case its state is changed to ERROR. Therefore if triggers are sent to the TELL1 the next step puts its state to ERROR. Then all the O-Rx links (excepted for the VELO and L0DU TELL1 type) are disabled to ensure that no data is received during the configuration.

If some parameters have to be over-written, these actions take place at this step of the configuration.

Finally the appropriated recipes are applied to the board and upon successful operation the board state goes to READY.

Start (READY → RUNNING): When the TELL1 has been correctly configured and is in the READY state, a “Start” command can be applied, which enables the O-Rx links and starts monitoring throttle counters and FPGAs Error registers.

During the initialisation of the FSM DU the FPGA’s Error Mon registers (PPErrMonReg and SLErrMonReg) are “dpConnect-ed” to a callback function. As soon as an error occurs on the TELL1 one of these five registers would not be read as 0x00000000, therefore the callback function checks these value during the run and sets the TELL1 DU FSM state to ERROR if applicable.

The throttle counters are also connected to a callback function checking that the TELL1 does not send throttles.

These registers are used to continuously check that the TELL1 works fine.

Stop (RUNNING → READY): At the end of a run the “Stop” command is sent. The TELL1 DU stops monitoring the registers, the command checks that the processing counters are consistent and disables the O-Rx links. If the Processing counters are not equal the state goes to ERROR and a message is displayed for the shifter.

Reset (READY → NOT_READY): A “Reset” action has been implemented to ensure that the TELL1 do not send or receive signal anymore at the end of a run. The GBE ports on the SyncLink-FPGA and the O-Rx links are disabled, and the ECS is set as the trigger source on the TELL1 board. Finally the fwTell_iniTell1 function is called to reset correctly the TELL1.

Recover (ERROR → NOT_READY): The “Recover” action goes through the same path that the Reset command. It checks all the functionality of the project from the existence of the DPS to the initialisation of the TELL1.

LoadFrmw (NOT_READY → NOT_READY): A special command has been implemented to load the FPGA firmware. This action sends the pof files to the CCPC and executes the EPC16 Handling function.

Other commands can be send to the TELL1 such as a restart of the ccserv or a reboot of the CCPC. These commands executes system functions through the ccserv.

Conclusions

The studies presented in my doctoral thesis cover different aspects of the LHCb experiment reflecting my main contributions to the collaboration.

Due to its limited angular acceptance and the low LHCb instantaneous luminosity, the LHCb detector is not designed for the Higgs physics in particular. Nevertheless its capability to tag b -mesons and to trigger on high- p_T leptons has motivated the study of the Higgs boson produced in association with a gauge vector boson W^\pm or Z^0 .

In the first part of this thesis, a seed finder algorithm used to tag b -jets in this thesis, called VV Seed Finder, has been implemented in the LHCb software framework. The tests on simulated data prove that the algorithm presented in this thesis keeps 70 % of the b -jets and rejects 70 % of the c -jets and more than 90 % of the lighter quark jets. This algorithm configuration has been chosen to analyse the Higgs event type which were fully simulated. A Neural Network approach has also been developed to optimise the b -jet energy. This Neural Network is built using all the available information, from the tracking to calorimetry, within a cone of R-parameter of 0.45 around the b -seed direction. The final relative resolution of the dijet mass peak was improved from 54 % to 38 % after the application of the Neural Network to optimise the b -jet energy. This procedure allows to improve the separation between the signal and the irreducible background from the $Z^0 Z^0$ and $Z^0 W^\pm$ decays.

The channels $HW^\pm \rightarrow b\bar{b} + \ell^\pm \bar{\nu}_\ell^{(-)}$ and $HZ^0 \rightarrow b\bar{b} + \ell^+ \ell^-$ have smaller cross sections compared to the possible backgrounds sources. During one year of running at the centre-of-mass energy of $\sqrt{s} = 14$ TeV it is expected to have about 100 Higgs events with at least one high- p_T lepton within the LHCb detector, and 300'000 background events. The small relative yield reflects the big challenge of this analysis. To face this challenge it has been necessary to use a second Neural Network using kinematic, topological and global variables trained to remove $t\bar{t} \rightarrow bW^+ \bar{b}W^-$ events, in particular. The analysis has proved to be able to remove more than 99.8 % of the dangerous background and to keep 6.5 % of the signal events. After five years of data taking at a centre-of-mass energy of $\sqrt{s} = 14$ TeV and a yearly integrated luminosity of 2 fb^{-1} the expected number of events is $N_{\text{evt}}(HW^\pm/Z^0) = 33.5$ for a significance of $S/\sqrt{B} = 0.72$. Various scenarii have been analysed, they differ about the centre-of-mass energy and about the yearly integrated luminosity. The expected numbers of events and their significances remain low.

From the Tevatron data we can expect only a yield of about two times larger than for SM Higgs ($m_H = 120 \text{ GeV}/c^2$). Nevertheless it can be expected that this analysis might hint at the possibility of some non-SM particle with a topology similar to HW^\pm/Z^0 . The latest CDF experimental limits allow a factor of about six for the production cross section of such events.

During the second part of my thesis study, I developed an overall framework to integrate the TELL1 boards in the LHCb Experiment Control System. To accomplish this it was necessary to understand the general concept of configuration and monitoring and the specialities of the different subdetector types. The register map was translated into the PVSS internal structure and the different board types were continuously extended during the ongoing firmware development. Over seventy graphical user interfaces were designed, allowing to interact, spy and check the TELL1 boards. Furthermore, the recipe definitions were written and appropriate tools were developed to verify the correct configuration. Finally a complete Finite State Machines component for the DAQ boards was implemented. This project is now used by all the different subdetectors to configure, check and run their TELL1 boards.

References

- [1] C. Amsler *et al.* [Particle Data Group], *Review of Particle Physics*, Phys. Lett. B **667**, 1 (2008), and 2009 partial update for the 2010 edition.
- [2] D. Décamp *et al.*, *Determination of the Number of Light Neutrino Species*, Phys. Lett. **B231**, 519 (1989).
- [3] E. Noether, *Invariante Variationsprobleme*, Nachr. v. d. Ges. d. Wiss. zu Göttingen 1918 , 235 (1918).
- [4] J. H. Christenson, J. W. Cronin, V. L. Fitch, and R. Turlay, *Evidence for the 2π Decay of the K_2^0 Meson*, Phys. Rev. Lett. **13**, 138 (1964).
- [5] W. Pauli, *Niels Bohr and the Development of Physics*, McGraw Hill Book Company, Inc., New York (1955).
- [6] J. Gunion, H. Haber, G. Kane, and S. Dawson, *The Higgs Hunter's Guide* (Addison-Wesley, Reading, MA, USA, 1990).
- [7] A. Djouadi, *The Anatomy of Electro-Weak Symmetry Breaking. I: The Higgs Boson in the Standard Model*, Phys. Rept. **457**, 1 (2008) [hep-ph/0503172].
- [8] S. L. Glashow, *Partial-Symmetries of Weak Interactions*, Nucl. Phys. **22**, 579 (1961).
- [9] A. Salam, *Weak and Electromagnetic Interactions*, Proceedings Of The Nobel Symposium Held At Lerum, Sweden, 1968.
- [10] S. Weinberg, *A Model of Leptons*, Phys. Rev. Lett. **19**, 1264 (1967).
- [11] P. W. Higgs, *Broken Symmetries and the Masses of Gauge Bosons*, Phys. Rev. Lett. **13**, 508 (1964).
- [12] F. Englert and R. Brout, *Broken Symmetry and the Mass of Gauge Vector Mesons*, Phys. Rev. Lett. **13**, 321 (1964).
- [13] G. Guralnik, C. Hagen, and T. Kibble, *Global Conservation Laws and Massless Particles*, Phys. Rev. Lett. **13**, 585 (1964).
- [14] Y. Nambu, *Quasi-Particles and Gauge Invariance in the Theory of Superconductivity*, Phys. Rev. **117**, 648 (1960).
- [15] J. Goldstone, *Quasi-Particles and Gauge Invariance in the Theory of Superconductivity*, II Nuovo Cimento **19**, 154 (1961).
- [16] J. Goldstone, A. Salam, and S. Weinberg, *Broken Symmetries*, Phys. Rev. **127**, 965 (1962).
- [17] B. W. Lee, C. Quigg, and H. B. Thacker, *Weak interactions at Very High Energies: The Role of the Higgs-Boson Mass*, Phys. Rev. D **16**, 1519 (1977).

- [18] T. Hambye and K. Riesselmann, *SM Higgs mass bounds from theory*, (1997) [hep-ph/9708416].
- [19] G. Abbiendi, *Search for the Standard Model Higgs Boson at LEP*, Physics Letters B **565**, 61 (2003).
- [20] Collaborations, *Combined CDF and D0 Upper Limits on Standard Model Higgs- Boson Production with $2.1 - 5.4 \text{ fb}^{-1}$ of Data*, (2009) [hep-ex/0911.3930].
- [21] The LEP Electroweak Working Group, <http://lepewwg.web.cern.ch/>.
- [22] A. Collaboration *et al.*, *Precision Electroweak Measurements and Constraints on the Standard Model*, (2009) [hep-ex/0911.2604].
- [23] L. Evans and P. Bryant (Eds), *LHC Machine*, JINST **3**, S08001 (2008).
- [24] A. Team, Diagram of an lh dipole magnet, 1999.
- [25] C. Lefevre, The cern accelerator complex. complexe des acclrateurs du cern, 2006.
- [26] K. Aamodt *et al.* [ALICE collaboration], *The ALICE Experiment at the LHC*, JINST **3**, S08002 (2008).
- [27] G. Aad *et al.* [ATLAS collaboration], *The ATLAS Experiment at the LHC*, JINST **3**, S08003 (2008).
- [28] R. Adolphi *et al.* [CMS collaboration], *The CMS Experiment at the LHC*, JINST **3**, S08004 (2008).
- [29] A. Alves *et al.* [LHCb collaboration], *The LHCb Detector at the LHC*, JINST **3**, S08005 (2008).
- [30] O. Adriani *et al.* [LHCf collaboration], *The LHCf Detector at the LHC*, JINST **3**, S08006 (2008).
- [31] G. Anelli *et al.* [TOTEM collaboration], *The TOTEM Experiment at the LHC*, JINST **3**, S08007 (2008).
- [32] C. Eck *et al.*, *LHC computing Grid: Technical Design Report. Version 1.06 (20 Jun 2005)*, CERN Report lhcc-2005-024, 2005.
- [33] LCG web site.,
<http://lcg.web.cern.ch/LCG/> .
- [34] M. Brice, LHC Computing Grid Globe into the Computer Center, 2009.
- [35] P. R. Barbosa-Marinho *et al.* [LHCb collaboration], *LHCb VELO (Vertex Locator): Technical Design Report*, CERN Report LHCC-2001-11, 2001.
- [36] R. Antunes-Nobrega *et al.* [LHCb collaboration], *LHCb Reoptimized Detector Design and Performance: Technical Design Report*, CERN Report LHCC-2003-030, 2003.
- [37] P. R. Barbosa-Marinho *et al.* [LHCb collaboration], *LHCb Inner Tracker: Technical Design Report*, CERN Report LHCC-2002-29, 2002.

- [38] P. R. Barbosa-Marinho *et al.* [LHCb collaboration], *LHCb Outer Tracker: Technical Design Report*, CERN Report LHCC-2001-024, 2001.
- [39] S. Amato *et al.* [LHCb collaboration], *LHCb Magnet: Technical Design Report*, CERN Report LHCC-2000-007, 2000.
- [40] S. Amato *et al.* [LHCb collaboration], *LHCb RICH: Technical Design Report*, CERN Report LHCC-2000-037, 2000.
- [41] S. Amato *et al.* [LHCb collaboration], *LHCb Calorimeters: Technical Design Report*, CERN Report LHCC-2000-036, 2000.
- [42] P. R. Barbosa-Marinho *et al.* [LHCb collaboration], *LHCb Muon System: Technical Design Report*, CERN Report LHCC-2001-010, 2001.
- [43] R. Antunes-Nobrega *et al.* [LHCb collaboration], *LHCb Trigger System: Technical Design Report*, CERN Report LHCC-2003-31, 2003.
- [44] B. Adeva *et al.* [LHCb collaboration], *Roadmap for selected key measurements of LHCb*, (2009) [hep-ex/0912.4179].
- [45] M.-O. Bettler, *Construction of the Inner Tracker and Sensitivity to the $B_s^0 \rightarrow \mu\mu$ Decay at LHCb.*, PhD thesis, EPFL, Lausanne, 2010.
- [46] L. Nicolas, *Alignment of the LHCb Tracking Stations and Selection of $X(3872)$ and $Z(4430)^\pm$ in pp Collisions at 14TeV .*, PhD thesis, EPFL, Lausanne, 2009.
- [47] P. R. Barbosa-Marinho *et al.* [LHCb collaboration], *LHCb Online System, Data Acquisition and Experiment Control: Technical Design Report*, CERN Report LHCC-2001-040, 2001.
- [48] T. Nakada, E. Aslanides, A. Smith, and W. Witzeling, *Addendum to the LHCb Online System Technical Design Report*, CERN Report LHCC-2005-039, 2005.
- [49] G. Haefeli, *Contribution to the Development of the Acquisition Electronics for the LHCb Experiment*, PhD thesis, EPFL Lausanne.
- [50] G. Haefeli *et al.*, *The LHCb DAQ Interface Board TELL1*, Nuclear Instruments and Methods in Physics Research Section A: Accelerators, Spectrometers, Detectors and Associated Equipment **560**, 494 (2006).
- [51] PVSS-2 (Prozessvisualisierungs- und Steuerungs-System) SCADA tool, <http://www.pvss.com/>.
- [52] PVSS Service at CERN, <http://itcobe.web.cern.ch/itcobe/Services/Pvss/>.
- [53] A. Daneels and W. Salter, *The LHC experiments Joint COntrols Project*, ICALEPCS, Triste (1999).
- [54] SMI++ - State Management Interface, <http://smi.web.cern.ch/smi/>.
- [55] B. Franek and C. Gaspar, SMI++-object oriented framework for designing control systems, in *Nuclear Science Symposium, 1997. IEEE*, pp. 92–96 vol.1, 1997.
- [56] R. Antunes-Nobrega *et al.* [LHCb collaboration], *LHCb Computing: Technical Design Report*, CERN Report LHCC-2005-019, 2005.

- [57] G. Barrand *et al.*, GAUDI - *A Software Architecture and Framework for Building HEP Data Processing Applications*, Comput. Phys. Commun. **140**, 45 (2001), see also: <http://proj-gaudi.web.cern.ch/proj-gaudi/>.
- [58] I. Belyaev *et al.*, *Simulation Application for the LHCb Experiment*, (2003) [physics/0306035], see also: <http://lhcb-release-area.web.cern.ch/LHCb-release-area/DOC/gauss/>.
- [59] T. Sjostrand *et al.*, *High-Energy Physics Event Generation with PYTHIA 6.1*, Comput. Phys. Commun. **135**, 238 (2001) [hep-ph/0010017], see also: <http://projects.hepforge.org/pythia6/>.
- [60] D. J. Lange, *The EVTGEN Particle Decay Simulation Package*, Nucl. Instrum. Meth. **A462**, 152 (2001), see also: <http://www.slac.stanford.edu/~lange/EvtGen/>.
- [61] S. Agostinelli *et al.* [GEANT4 collaboration], *GEANT4: A Simulation Toolkit*, Nucl. Instrum. Meth. **A506**, 250 (2003), see also: <http://geant4.web.cern.ch/geant4/>.
- [62] LHCb collaboration, The BOOLE project, <http://lhcb-release-area.web.cern.ch/LHCb-release-area/DOC/boole/>.
- [63] LHCb collaboration, The BRUNEL project, <http://lhcb-release-area.web.cern.ch/LHCb-release-area/DOC/brunel/>.
- [64] LHCb collaboration, The DAVINCI project, <http://lhcb-release-area.web.cern.ch/LHCb-release-area/DOC/davinci/>.
- [65] C. Currat, *Direct search for Higgs boson in LHCb*, PhD thesis, Université de Lausanne, IPHE, 2001.
- [66] L. Locatelli, *Direct Search for Higgs Boson in LHCb and Contribution to the Development of the Vertex Detector*, PhD thesis, EPFL n. 3868, 2007.
- [67] V. Coco, *Reconstruction et identification de jets beaux dans l'expérience LHCb en vue d'étudier sa sensibilité à un boson de Higgs standard se désintégrant en paires $b\bar{b}$* , PhD thesis, Univ. de Savoie, Annecy, 2008.
- [68] D. J. Gross and F. Wilczek, *Asymptotically Free Gauge Theories. I*, Phys. Rev. D **8**, 3633 (1973).
- [69] H. D. Politzer, *Asymptotic Freedom: An Approach to Strong Interactions*, Phys. Rep. **14**, 129 (1974).
- [70] R. K. Ellis, W. J. Stirling, and B. R. Webber, *QCD and collider physics* (Cambridge Univ. Press, 2003).
- [71] K. A. Assamagan *et al.* [Higgs Working Group], *The Higgs Working Group: Summary Report 2003*, (2004) [hep-ph/0406152].
- [72] M. Cacciari and G. P. Salam, *Dispelling the N^3 Myth for the K_T Jet-Finder*, Phys. Lett. **B641**, 57 (2006) [hep-ph/0512210].
- [73] M. Cacciari, G.P. Salam and G. Soyez, <http://fastjet.fr/>.

-
- [74] A. Hoecker *et al.*, *TMVA - Toolkit for Multivariate Data Analysis*, (2007) [physics/0703039].
- [75] Richard Hughes, Ben Kilminster, Brandon Parks, Brian Winer, Rob Harr, Shalhout Shalhout, Bo Jayatilaka, Ashutosh Kotwal, Ravi Shekhar, Daniel Whiteson, *A Search for $ZH \rightarrow l^+l^-b\bar{b}$ in 2.7 fb^{-1} using a Neural Network discriminant*, CDF Public Note (2008).
- [76] The CDF Collaboration, *Combined $WH \rightarrow \ell\nu b\bar{b}$ search with 2.7 fb^{-1} of CDF data*, CDF Public Note (2008).
- [77] Altera web site, <http://www.altera.com>.
- [78] F. Fontanelli *et al.*, *Embedded Controllers for Local Board-Control*, IEEE Trans. Nucl. Sci. **53**, 936 (2006).
- [79] F. Fontanelli *et al.*, *CC-PC Gluecard Application and User's Guide*, CERN Report LHCb-2003-098, LPHE-2005-010, 2004.
- [80] TELL1 Homepage, <http://lphe.epfl.ch/tell1>.
- [81] C. Gaspar, M. Dönszelmann, and P. Charpentier, DIM, a Portable, Light Weight Package for Information Publishing, Data Transfer and Inter-process Communication, Presented at: International Conference on Computing in High Energy and Nuclear Physics (Padova, Italy, 1-11 February 2000).
- [82] C. Gaspar *et al.*, DIM web site, <http://dim.web.cern.ch/dim/>.

Curriculum Vitæ

Cédric Potterat

Laboratory for High-Energy Physics (LPHE)
Swiss Federal Institute of Technology (EPFL)
CH-1015 Lausanne, Switzerland

E-mail: `cedric.potterat@a3.epfl.ch`

Date of birth March 19, 1982
Nationality Swiss
Civil status Single

Education, Degrees obtained

May 2010 Ph.D. degree, EPFL
2005 – 2010 Ph.D. Thesis in High-Energy Physics on *Direct Search for Standard Model-Like Higgs Boson and Software Integration of Data Acquisition Cards*, LPHE, EPFL
 Thesis supervisor: Prof. Aurelio Bay
2005 – 2010 Member of the LHCb collaboration
Jan. 2008 CHIPP Ph.D. Winter School, Näfels, Switzerland
Apr. 2005 M.Sc. degree in Physics, EPFL
2004 – 2005 Master Thesis in High-Energy Physics on *Etude de la désintégration $B^\pm \rightarrow K^\pm \omega \gamma$ avec le détecteur Belle*, LPHE, EPFL
2000 – 2004 Physics Studies at EPFL

Other Work Experiences, Skills and Interests

2005 – 2010 System Administrator (Linux Cluster and Server) and Webmaster at LPHE
2002 – 2006 Member of the Communal Council, Cully, Switzerland
Sport Skiing, running (marathon)